Investigating the use of protein-targeted pegylated gold nanoparticle probes in the surface-enhanced Raman spectroscopy of cells

by

Conor P. Shaw
B.Sc., University of Victoria, 2005
M.Sc., University of Victoria, 2007

A Dissertation Submitted in Partial Fulfillment of the
Requirements for the Degree of

DOCTOR OF PHILOSOPHY

in the Department of Physics & Astronomy

Investigating the use of protein-targeted pegylated gold nanoparticle probes in the surface-enhanced Raman spectroscopy of cells

by

Conor P. Shaw
B.Sc., University of Victoria, 2005
M.Sc., University of Victoria, 2007

Supervisory Committee

Dr. A.I. Jirasek, Supervisor
(Department of Physics & Astronomy)

Dr. G. Steeves, Departmental Member
(Department of Physics & Astronomy)

Dr. W.A. Ansbacher, Departmental Member
(Department of Physics & Astronomy)

Dr. A.G. Brolo, Outside Member
(Department of Chemistry)

Supervisory Committee

Dr. A.I. Jirasek, Supervisor
(Department of Physics & Astronomy)

Dr. G. Steeves, Departmental Member
(Department of Physics & Astronomy)

Dr. W.A. Ansbacher, Departmental Member
(Department of Physics & Astronomy)

Dr. A.G. Brolo, Outside Member
(Department of Chemistry)

ABSTRACT

Currently, it is very challenging to accurately monitor the response of patients to radiation therapy over the course of treatment. The initial response to ionizing radiation occurs in the cells at a molecular level, and effects of the response are not typically noticeable on short time scales. Surface-enhanced Raman Spectroscopy, or SERS, has proven to be a useful technique in the analysis of tissues and cells at a molecular level. Specifically, the use of targeted SERS probes allows for the detection of specific proteins on the cell membrane. The work presented here looks to assess the feasibility of using targeted SERS probes and two-dimensional SERS microscopy to measure the response of tumour cells to ionizing radiation, by identifying changes in the distribution of membrane proteins following exposure to clinically relevant doses of ionizing radiation ($\leq 60Gy$).

Two different types of targeted SERS probes were investigated, based on the work of Grubisha *et al.* ([1]; Type I) and Qian *et al.* ([2]; Type II), both containing a gold nanoparticle core. In a simplified cellular experiment, biotin on the surface

of biotinylated OVCAR5 cells was targeted with streptavidin-SERS probes, and the Type-II SERS probes showed the most promising results. However, SERS maps still provided less characteristic spectral signal than expected, and challenges remain in the development of a reproducible cellular imaging technique.

Despite difficulties in cellular imaging, the functionality of the Type-II SERS probes was verified separately, using gold slides with a biotin monolayer in place of cells. Following verification, the SERS intensities provided by differently sized clusters of the SERS probes were characterized. To begin, both SERS maps and SEM images of gold slides were acquired after incubation with Type-II SERS probes for multiple times (1hr, 2hr, 3hr, 12hr). Data analysis of the SEM images provided a measure of the physical distribution of the SERS probes on the surface of the slide, while analysis of the SERS maps provided information about the spectral distribution of the probes. By relating the information provided by the SEM images and SERS maps, a simple polynomial relationship between SERS intensity and the number of clustered SERS probes providing the enhancement was determined, providing a framework for quantifiable SERS imaging.

Finally, an independent experiment was devised to ensure that exposure to clinically relevant doses of ionizing radiation would affect the ability of the targeted protein to bind to SERS probes, thus leading to measurable differences in SERS maps of irradiated and unirradiated cells. A series of experiments utilizing the *enzyme-linked immunosorbant assay* (ELISA) was performed to test the effect of ionizing radiation-induced damage on the ability of streptavidin to bind to biotin, and the results confirmed that a noticeable reduction in binding could be detected at doses as low as 10 Gy.

The results of this work demonstrate that following the development of a suitable cell/SERS probe incubation technique, Type-II SERS probes would be appropriate for use in quantifiable SERS imaging. Also, it is suggested that a measurable change in protein function will be present when comparing SERS maps of control cells to those of cells irradiated to clinically relevant doses.

Contents

List of Tables

List of Figures

ACKNOWLEDGEMENTS

This project provided many challenges, and I was very fortunate to receive support from many great people along the way. To begin I would like to thank my supervisor Dr. Andrew Jirasek for his patience and guidance throughout this long journey! Also, I would like to thank Dr. Alex Brolo for all of his guidance and support over the years and for connecting me to so many helpful people in the lab. My committee members Dr. Geoff Steeves and Dr. Will Ansbacher have also been great and our meetings have helped me through many challenges.

I spent a lot of time at the Deeley Research Centre while working on this thesis and I'd like to thank everyone there for being so accommodating. In particular I'd like to thank Rob Sahota for helping me get started in the lab and for many helpful discussions. Also thanks to Darin Wick and Siao Young for all of their help with my ELISA experiment.

Speaking of ELISAs, my sincere thanks to Becky Hof for being so helpful and for training me how to perform the assay. Thank you also to Alanna Roberts for suggesting that I speak with Becky in the first place!

I am deeply indebted to everyone in the Brolo group for all of their support and assistance in the Chemistry Lab. In particular Meikun Fan, Regivaldo Gomes, Rajan Nirwan, Chiara Valsecchi and Ting Yu for helping so often with cell culture and nanoparticle fabrication. I was also very fortunate to work with some wonderful co-op students during my PhD who worked very hard and spent a lot of time working with me on the cell experiments. Thank you very much to Garrett Barry, Chelsey Lane and Adele Duimering for all that you did!

I would also like to thank Dr. Elaine Humphrey and Adam Schuetze for their help with the SEM, Dr. Bob Chow for helping me with the Fluorescence microscope, Sean Adams from the Glass Shop for helping me anneal my gold slides, and Dr. Jeremy Wulff for the use of his lab. Thank you also to Chris Secord in the Physics machine shop for building me a specialized sample holder for the Raman microscope, and to the Chemistry machine shop for constructing the incubation device for the gold slides.

I also really appreciate the assistance given by Quinn Matthews when I started the project and needed to be trained on the Raman microscope. Thanks Quinn! And thank you also to Tim for your help with my streptavidin irradiation!

A big thank you also to everyone in the Medical Physics Department. It's nice to be a part of such a great team!

Last but not least I would like to thank my family for their love and support and for always believing in me.

DEDICATION

I would like to dedicate this thesis to my family: Mum, Dad, Dave, Kathy and my bro Chris!

Chapter 1

Introduction

The work presented in this thesis looks to develop the technique of surface-enhanced Raman spectroscopy (SERS) for the analysis of ionizing radiation-induced damage to cells. Further improvements in the treatment of cancer require a knowledge of the response of tissue to radiation at a molecular level, and techniques such as Raman spectroscopy and SERS provide that opportunity. The three main goals of this work were to: (1) develop a protocol for the imaging of the surface distribution of proteins on tumour cells using targeted SERS probes identifiable by Raman microscopy; (2) examine the SERS intensities provided by the probes and determine how to quantify the signal in terms of protein content and (3) ensure that ionizing radiation-induced damage had a measurable effect on the function of proteins. To achieve these goals, a knowledge of the response of living tissue to ionizing radiation, or *radiobiology* is required, so that it can be used to understand the biochemical information provided by molecular-level spectroscopic probes of cells. Also, an understanding of the practice of radiation therapy (RT) provides context within the larger framework of cancer treatment, and allows for an appreciation of the advances to RT that can be provided by radiobiology.

To begin, chapter 1 presents an introduction to the inter-related fields of Radiation Therapy and Radiobiology, and the challenges present in advancing both fields (section 1.1). An introduction to cellular biology is then provided (section 1.2), including a description of the cell cycle (section 1.2.1). The interactions of ionizing radiation with matter are then described (section 1.3), and the response of the cell to ionizing radiation is discussed, including information on DNA damage repair (section 1.3.1), the significance of damage to different parts of the cell (section 1.3.2), and the various cell death pathways (section 1.3.3). Various techniques for the analysis of

ionizing radiation-induced damage to biological material are then described (section 1.4), with a special focus on Raman spectroscopic techniques (section 1.4.1). Finally, the chapter concludes with a description of the scope of this work (section 1.5).

1.1 Radiation Therapy and Radiobiology

Since the first recorded use of x-rays in the treatment of cancer in the late 19th century, there have been tremendous improvements in the field of radiation therapy [6]. Early x-ray beams were of low energy (kilovoltage), and only capable of treating skin cancer and tumours close to the surface of the body. With the development of machines capable of delivering high energy x-rays (megavoltage), such as medical linear accelerators, the treatment of deep-seated tumours became possible [7, 8]. Advances in diagnostic imaging modalities including x-ray computed tomography (CT), magnetic resonance imaging (MRI), positron-emission tomography (PET) and ultrasound (US), allowed for the visualization of the tumour in three dimensions with a high degree of accuracy [9]. Based on 3D images of the tumour collected by the aforementioned imaging modalities, modern computerized treatment planning algorithms allow for the calculation of dose distributions highly conformal to the target, generated by multiple radiation fields of different sizes, delivered from a variety of angles, and potentially with modulated intensity distributions [7, 8]. Advanced treatment systems then allow the created treatment plans to be delivered to the target with a high degree of accuracy, and minimal damage to healthy tissue.

While many of the advancements in the delivery of radiation therapy have come through technology, much of the information regarding the efficacy of the treatment, and potential improvements, has been determined through the study of the effects of ionizing radiation on biological material, or radiobiology [10–14]. Both cancerous and healthy tissue are affected by ionizing radiation with differing responses, and it is the response of healthy tissue that is the limiting factor in radiotherapy. For treatment to be effective, it is important that damaging effects to healthy tissue are minimized, while still delivering a lethal dose to cancerous tissue. Radiobiological studies attempt to classify the damage caused to different types of tissue exposed to varying amounts of radiation, providing information about damage that is observed within weeks of treatment (*early effects*) and that which is noticed months or years later (*late effects*). With respect to radiation therapy, it is the goal of radiobiology to improve the therapeutic ratio of treatment, which is defined as the ratio of the

probability for tumour cure to the likelihood of normal tissue damage [15].

One of the earliest techniques that led to an increase in the therapeutic ratio of radiation therapy is known as *fractionation*. Since the early days of radiation therapy, it was noticed that more sparing of normal tissue damage occurred when radiation dose was delivered in multiple fractions over a period of time (typically days) rather than as a single dose. The explanation for the benefit of fractionation comes from radiobiology, which considers the ability of both normal and cancerous cells to respond to the damage caused by the radiation. Depending on the amount of time between fractions, surviving cells have the chance to repair non-lethal damage, and to continue through the cell cycle, repopulating damaged tissue. The irradiated cells move through the cell cycle at varying rates, resulting in the redistribution of cells in the target volume into different phases, some of which are known to be more radiosensitive than others. Further, the tumour cells, which typically are poorly supplied with oxygen, or *hypoxic*, may experience reoxygenation due to shrinkage of the tumour volume, allowing for better oxygen diffusion. Hypoxic cells are highly resistant to radiation, and the reintroduction of oxygen to tumour cells significantly increases the cell radiosensitivity.

The explanation for the benefit of fractionation came to be known as the four R's of radiobiology, referring to the *r*epair of sublethal damage, *r*epopulation by surviving cells, *r*edistribution of cells throughout the cell cycle, and the *r*eoxygenation of hypoxic cells that occurs between fractions [7]. To account for the inherent radiosensitivity of different cells, a fifth R was added for *r*adiosensitivity [16]. In modern radiotherapy, a typical fractionation regime is to deliver 2Gy of dose per fraction, 5 days per week, over a 6 week period [7, 15, 17]. However, alternative regimens are still investigated and sometimes prescribed based on the radiobiological response of different tissue and tumour types [15].

Recent advances in radiobiology continue to explore potential methods of improving the efficacy of radiation therapy. Due to a better understanding of the molecular pathways initiated by cells in response to stressors like ionizing radiation, it is possible to target and block certain pathways to increase the cell kill caused by radiation [14, 15, 18]. Promising results have been observed in clinical trials of the treatment of squamous cell carcinoma of the head and neck, when antibodies were used to target and block the epithelial growth factor receptor (EFGR) in conjunction with fractionated radiotherapy [19]. Other studies have looked to exploit tumour hypoxia using a variety of techniques, some of which include the introduction of molecules that become

toxic in the absence of oxygen [20], or compromise the vasculature of the tumour and increase hypoxia, eventually leading to cell death due to lack of oxygen [21]. Another focus has been on the mitigation of radiation-induced damage to normal tissue, attempting to reduce typically problematic late side effects caused by radiation therapy treatment [22–27]. Despite such advances, there are currently no accepted methods of predicting an individual's treatment response, or monitoring treatment response on short time scales.

However, radiobiology does shows promise in the development of individualized radiation therapy. Through the development of predictive assays, it will eventually be possible to characterize the response of an individual to radiation, both in terms of normal tissue and tumour response. Because of the multitude of factors that can influence tissue response including intrinsic radiosensitivity, growth rate, and the extent of hypoxia, it is important to have effective techniques that can measure the necessary parameters in a reasonable time frame. One of the most comprehensive ways to characterize tissue is to use genetic screening methods, which attempt to describe the genes that are expressed in tumour cells, how the genes differ from those of normal cells, and how the tumour's genome may affect its radiation response [15, 28–32]. However, the information obtained through genetics can be difficult to interpret, and there are many other possible techniques to characterize the radiation response of biological material, several of which will be discussed in section 1.4.

In the future, advances in radiotherapy treatment will come from both technological advancements and improvements in the understanding of radiobiology. However, while technological advancements may peak, further important developments in radiation therapy will be always be possible through an improved knowledge of radiobiology [14, 15].

1.2 Introduction to Cellular Biology

All tissue, healthy and cancerous, is made up of a collection of different types of cells. While there is remarkable variation in the functions of individual cells, all human (or, *eukaryotic*) cells share a common blueprint. A schematic of a basic human cell is shown in figure 1.1 [3]. The cell is surrounded by a cellular membrane, composed of a double phospholipid layer embedded with proteins. Water passes easily through the double phospholipid layer while the proteins serve a variety of functions, including acting as cellular identity markers, and controlling the passage of molecules and ions

through the membrane.

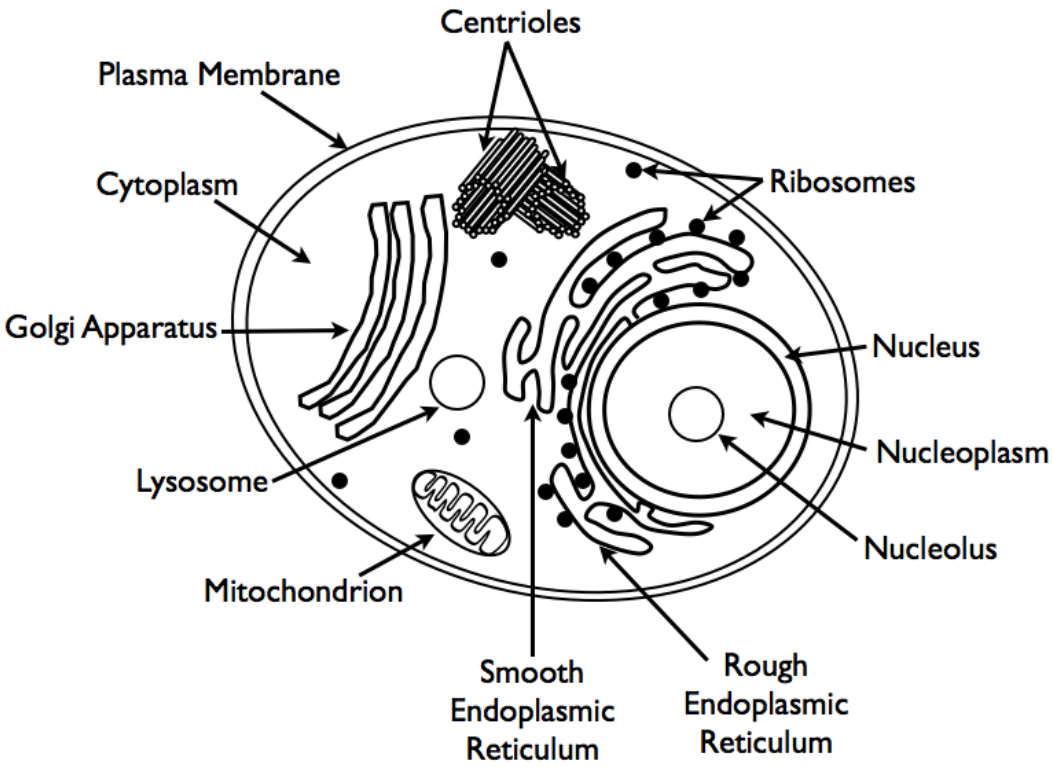

Figure 1.1: Schematic of a Eukaryotic cell [3].

Within the membrane is the cellular *protoplasm*, which is primarily water and contains proteins, amino acids (the building blocks of proteins), carbohydrates, lipids, nucleic acids and inorganic salts. The protoplasm is further subdivided into the *nucleoplasm*, which is contained within the nucleus of the cell, and the *cytoplasm*, which is outside of the nucleus. The nucleus is the control centre of the cell, and is enclosed by the nuclear membrane, which is similar to the cell membrane, but contains an inner and outer membrane. The outer membrane connects to a structure called the *endoplasmic reticulum* (ER), which has both a smooth, and a granular region. The rough, or granular ER is lined with tiny granules composed of ribonucleic acid and proteins, which are called *ribosomes*, and are the sites of protein synthesis. Inside the inner portion of the nuclear membrane is the nucleoplasm, which contains proteins, enzymes and other chemicals, as well as the nucleic acids (*deoxyribonucleic acid*, or DNA and *ribonucleic acid*, or RNA). Also found within the nucleus is the *nucleolus*,

which is a spherical structure primarily composed of DNA, RNA and proteins.

DNA contains all of the genetic information of the cell, and RNA, which is structurally similar to DNA, is involved in reading pieces of the DNA code, or *genes*, and performing protein synthesis based on the encoded instructions. Both DNA and RNA consist of two strands of a sugar-phosphate backbone which are connected by pairs of nitrogenous bases (see figure 1.2). The DNA and RNA molecule are grouped into a series of nucleotides, which consist of a phosphate group ($PO_4{}^{3-}$), a five carbon sugar called *deoxyribose*, and one of the bases. There are five nitrogen bases known as *adenine, thymine, guanine, cytosine* and *uracil*, and each base pairs with a specific partner. Adenine and thymine form one base pair (A-T) and guanine and cytosine form another (G-C). For RNA molecules, the base thymine is replaced with a base called uracil, which also pairs with adenine. The sequence of these base pairs on the molecule is important, as it is through this sequence that the genetic information of the cell is encoded in the DNA. In the nucleus, DNA is stored in the form of chromatin, which are long, fine strands of DNA molecules and proteins.

Other structures, or organelles, common to the cytoplasm of all eukaryotic cells are *mitochondria*, *lysosomes*, and the *Golgi apparatus*. Like the nucleus, the mitochondria have an inner and outer membrane. Each mitochondrion is a capsule like structure that produces energy for the cell through a chemical reaction on the folds of its inner membrane. Lysosomes are small, generally spherical structures containing digestive enzymes that can be used to breakdown cellular structures into their components for use elsewhere in the cell. The Golgi apparatus is a series of flat, membrane-bound cavities known as *cisternae*. Within the cisternae of the Golgi apparatus, compounds that will be secreted by the cell are collected and concentrated. Also, if carbohydrates are to be excreted by the cell, then they can be synthesized within the Golgi apparatus.

All organelles of the cell work together to keep the cell functioning properly, and all of the cellular processes are governed by the nucleus. Within the nucleus itself, many chemical reactions occur that are essential to the function and survival of the cell, including reactions related to both protein synthesis, and cellular reproduction.

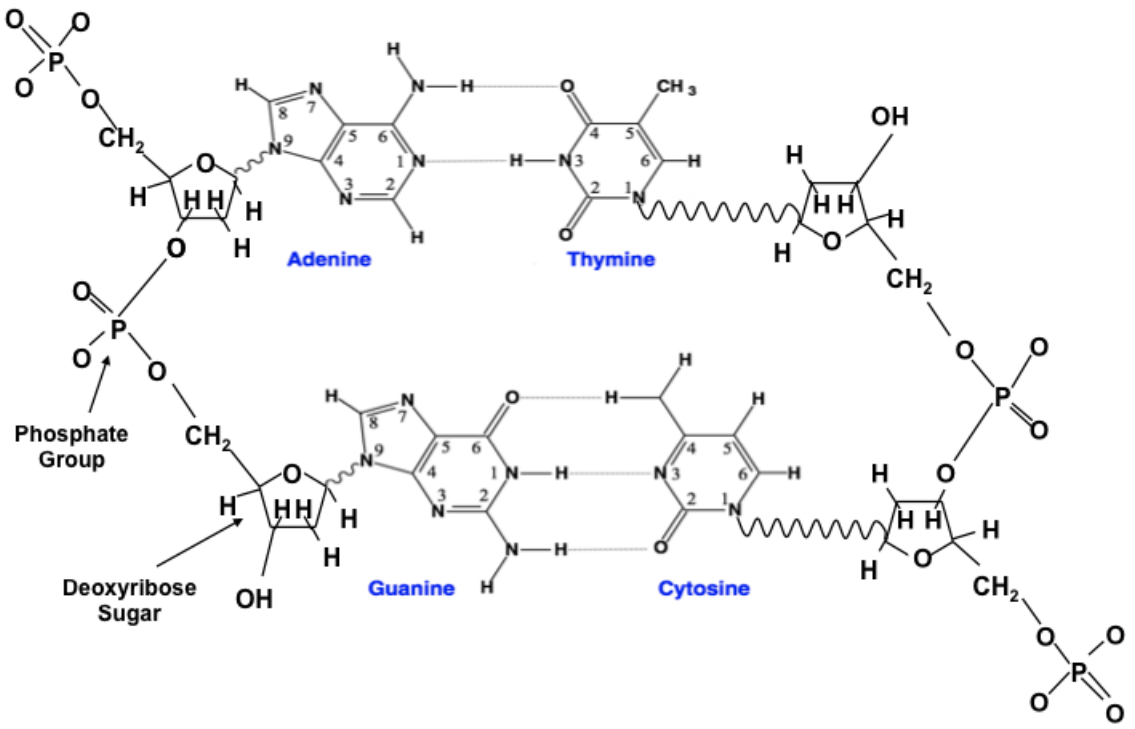

Figure 1.2: Schematic of DNA structure and nitrogenous bases.

1.2.1 Cell Reproduction

All eukaryotic cells undergo reproduction in a process called the *cell cycle*, resulting in two daughter cells genetically identical to the original [3, 33, 34]. The time taken to complete the cell cycle is highly variable depending on the type and function of the cell. In general, mammalian cells complete the cell cycle in ∼24 hours, but some cells rarely reproduce (such as liver, nerve or muscle cells) while others complete the cycle much more quickly (eg. approximately 20 minutes in a developing embryo) [3]. It is through the cell cycle that tissues in the body are able to grow and maintain themselves. The cycle itself is split into three stages called *interphase*, *mitosis*, and *cytokinesis*. Cells spend most of their time in interphase, which is also split into three subphases called growth one (G1), synthesis (S) and growth two (G2).

During the G1 phase, which takes up most of the cells lifespan, the cell grows, building organelles and performing its primary functions. In the synthesis (S) phase, the nucleus of the cell becomes particularly active, and all of the DNA is duplicated.

Helicase enzymes unwind each DNA molecule, and the separate strands are used as templates for their complementary strands with nucleotides added by the enzyme known as DNA polymerase. This results in two identical, or sister, strands of chromatin called chromatids connected at the centre of the strand by the *centromere*. Here, a disk of protein called the *kinetochore* pinches in and connects the two sister chromatids.

After the S phase, the G2 phase begins, during which the cell continues to grow and the final preparations for cell division are made. During this phase, two identical organelles known as *centrioles* finish forming, creating a pair called the *centrosome*. Each centriole is a system of microtubules, which are long, hollow, cylindrical fibers made of the protein *tubulin*. Alongside formation of the centrosome, mitochondria are also produced, and the strands of chromatin in the nucleus begin to condense and coil into tightly compacted forms known as *chromosomes*. The newly formed centrioles also begin to synthesize tubulin, to be used in the subsequent stages of the cell cycle.

Following the necessary preparations made during interphase, mitosis can begin. Through mitosis, two identical nuclei are formed. Mitosis consists of four stages known as *prophase*, *metaphase*, *anaphase* and *telophase*. During prophase, microtubules of tubulin form between the centrioles (called spindle fibers), pushing the organelles apart to opposite ends of the cell. Clusters of tubulin also begin to radiate outwards in all directions from each centriole, in a pattern called the *aster*. Concurrently, the nuclear membrane begins to break down and the nucleolus starts to dissipate. Microtubules from the centrioles then grow towards the centromeres of the chromosomes and attach to the kinetochores, connecting the sister chromatids to opposite poles of the cell.

As metaphase begins, the chromosomes start to align along the equator of the cell and the centromeres connecting the chromatid pairs then break. Anaphase occurs as the separated sister chromatids are pulled to opposite poles of the cell by the attached microtubules. The poles of the cell are also pulled apart by the action of the microtubules emanating from each centriole. Anaphase occurs relatively quickly, and is the shortest stage of mitosis.

During telophase, the final stage of mitosis, the identical sets of chromosomes at either pole of the cell begin to relax and uncoil back into strands of chromatin, as a new nuclear membrane forms around each group. The microtubules begin to break down into the tubulin protein, which will be used to construct the structure of the new daughter cells.

While mitosis divides the genetic material of the cell and forms two identical nuclei, the process of *cytokinesis* works to divide all other cellular material and actually separates the cell into two daughter cells. Cytokinesis can begin as early as anaphase, separating the cytoplasm of the cell in two. Filaments of a protein called *actin* are located around the cell membrane where it meets the equator on either side of the cell. Constriction of these filaments pinches in the cell on both sides, forming a *cleavage furrow*, and as this constriction continues the cells are eventually divided into two daughter cells. Cellular reproduction is now complete, and each daughter cell enters interphase, starting cell cycles of their own.

1.3 The interaction of ionizing radiation with biological material

When incident on cells and tissues, x-rays cause damage through interactions with molecules in the irradiated material. If an x-ray comes close enough to interact with a molecule, it undergoes a scattering event that can result in an electron being ejected from the molecule (*ionization*) as the photon scatters. The specifics of the reaction depend on the energy of the x-ray involved, but in the photon energies relevant for radiotherapy, the most common interactions are the *photoelectric effect*, *Compton effect*, and *pair production* [7, 8].

The photoelectric effect most commonly occurs at low energies (E) and in materials with a high atomic number (Z). The probability of occurrence of the photoelectric effect varies with $\frac{Z^3}{E^3}$. The photoelectric interaction occurs when an orbital electron absorbs the energy of an incident photon, gaining enough energy to escape from the atom (figure 1.3(a)). The ejected electron is known as a *photoelectron* and has a kinetic energy equal to the difference between the energy of the incident photon and the binding energy of the electron. By leaving the atom, the photoelectron has left a vacancy in one of the electron orbitals. The vacancy is filled by an electron in a higher orbital in a transition that releases a characteristic photon with energy corresponding to the difference in energy between the incident and final electron orbital. It is possible that the characteristic radiation may be absorbed by another electron in the atom, causing further ionization as the electron escapes the atom, now known as an *auger electron*. However, if the energy of the characteristic radiation is sufficiently high, it will escape the atom, causing ionizations at remote locations, along with the released

photo- and auger electrons.

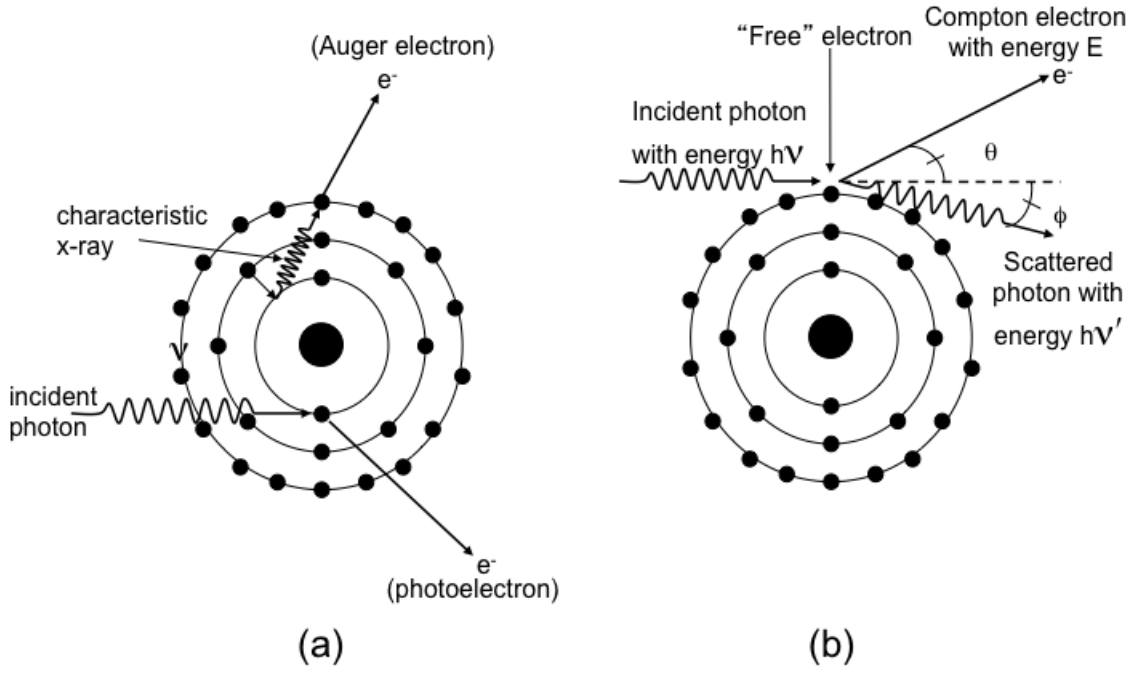

Figure 1.3: Basic diagram showing the interaction of an incident photon with an atom through (a) the Photoelectric Effect and (b) Compton Scattering.

At photon energies of $>$ 60 keV, Compton scattering begins to become important, acting as the dominant interaction between photons and matter for energies of 200 keV to 2 MeV.[7] Compton scattering occurs when an incident photon strikes a loosely bound, essentially free electron, as illustrated in figure 1.3(b). In the photon energy range that applies to Compton scattering, the binding energy of an electron in tissue is typically only a fraction of the incident photon energy, meaning that the electron behaves essentially as a free electron [7]. After the photon collides with the electron, some of its energy is transferred to the electron, and the photon and electron scatter at angles θ and ϕ, respectively. As photon energy increases, the amount of energy transferred to the electron as kinetic energy increases, with almost all of the energy being transferred for photon energies between 10 and 100 MeV. There is no dependence on atomic number for Compton scattering, and it occurs almost equally

frequently in a given mass, regardless of the material [7, 8].

Also occurring in the MeV energy range, pair production is an interaction between a photon and an atomic nucleus, resulting in the conversion of the photon into an electron and a positron (figure 1.4(a)). As a result, pair production can only occur if the incident photon has an energy greater than or equal to 1.02 MeV, which is twice the rest energy of an electron (or positron) [7, 8]. While less frequent, it is possible that a positron and electron can be produced by the interaction between an incident photon and atomic electron, freeing the bound electron from the atom in the process (figure 1.4(b)). Due to the interaction resulting in a positron and two electrons being set in motion, this is referred to as *triplet production*, and can occur if a photon has energy greater than or equal to 2.04 MeV [7, 8]. In the case of both pair and triplet production, any energy that the incident photon has in excess of either the 1.02 or 2.04 MeV threshold is divided amongst the charged particles set in motion as kinetic energy. The probability of occurrence of pair and triplet production increases with incident photon energy beyond the relevant thresholds, and varies according to the atomic number, Z, of a given mass. Both pair and triplet production are possible in the therapeutic energy range, but occur more frequently at higher energies, becoming the primary form of photon interaction for photons with incident energies between 50 and 100 MeV [7].

Regardless of the type of interaction that the incident photon undergoes, the scattered photon and charged particles that are released continue travelling through the medium and may result in further ionizations. In some cases, the initial ionization may have occurred at the site of a biomolecule, leading to biological damage through the *direct action* of radiation [35]. However, typically, the incident radiation produces ionization in non-critical targets, predominantly water, leading to the production of *free radicals*. Free radicals are atoms or molecules that contain an unpaired orbital electron in the outermost shell, and thus are highly reactive. Typically, free radicals go on to interact with critical sites in biomolecules, leading to biological damage in a process known as the *indirect action* of radiation [35].

As the electrons and positrons traveling through the medium begin to lose energy, interactions with molecules occur more frequently, resulting in clusters of ionizations and increased production of free radicals [36]. The clusters can be large enough to result in significant damage to biological material. Furthermore, in the case of a positron, when it is significantly slowed down through interactions with the medium, the positron will combine with a free or loosely bound electron, undergoing annihi-

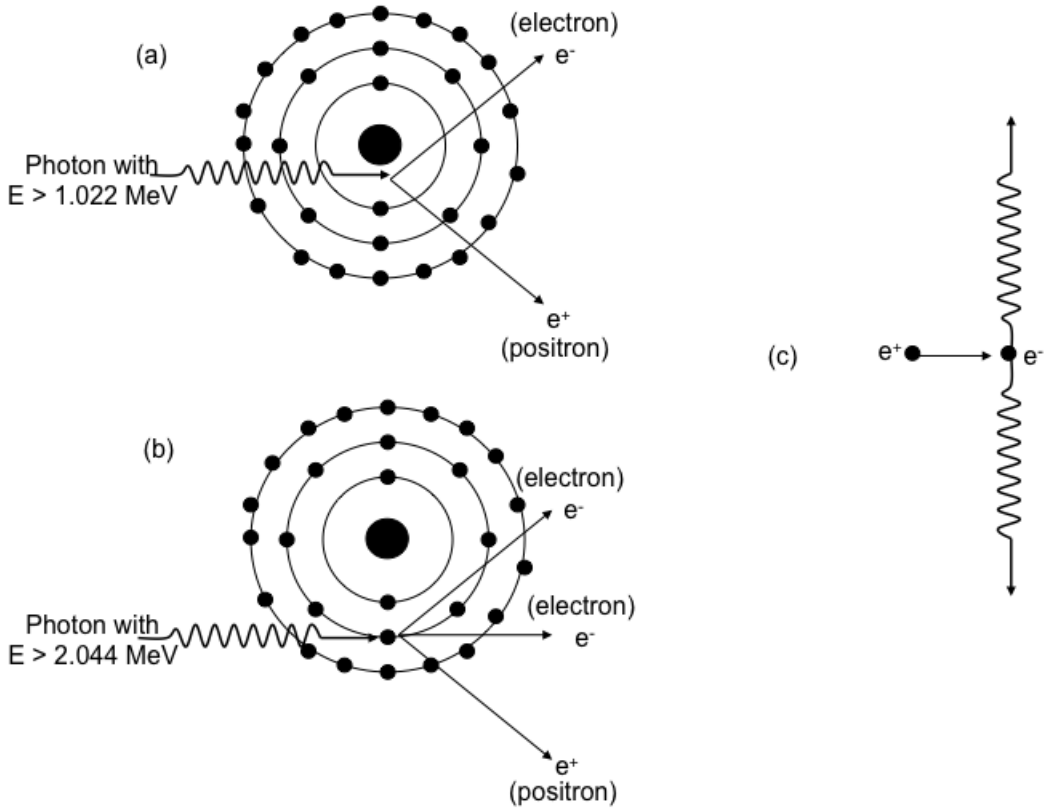

Figure 1.4: Basic diagrams showing an incident photon interacting with the nucleus to create a positron and electron via (a) Pair Production, and an interaction with an incident photon and an atomic electron setting two electrons and a positron in motion via (b) Triplet Production. The annihilation event that occurs when a positron slows down enough to interact with an electron is shown in (c).

lation and resulting in the production of two photons of equal energy radiating in opposite directions relative to each other to conserve momentum (as in figure 1.4(c)). The photons produced in an annihilation reaction will then continue through the medium, causing further ionization.

Damage caused due to clusters of ionization will occur to all parts of the cell, but for molecules that are present in multiple copies and/or produced regularly by the cell, such as water, RNA and proteins, the consequences of damage to a few such molecules are commonly believed to be limited [15]. Typically, due to the limited quantity of DNA in the cell, its large size, and importance in controlling metabolism, DNA is considered the principal target for cell killing [15, 35, 37, 38]. However, as will be discussed in section 1.3.2, many new studies suggest that damage to non-genetic

material such as proteins can also have a significant effect on cell survival.

1.3.1 DNA Damage Repair

In order to promote survival, cells have developed intricate systems that can detect DNA damage and initiate repair. The DNA damage response (DDR) is a highly complex system, consisting of a series of interrelated signaling pathways, regulated by specialized proteins. Sensor proteins constantly monitor the cell for DNA damage, and signal effector pathways, also regulated by proteins (as many as 700 [39]), that determine the response of the cell to the damage. Potential responses to DNA damage include damage checkpoints (which block cell cycle progress until the damage can be addressed), DNA repair pathways, and even programmed cell death (apoptosis).

Repair mechanisms for DNA damage are highly effective, but the success of repair is dependent on the type of damage that occurs. Exposure to ionizing radiation may result in damage to an individual base, a break in one of the backbone strands (single strand break; SSB), or disruption of both backbone strands, and cleavage of the DNA molecule (double strand break; DSB). Base damage and SSBs are most easily repaired via mechanisms known as base excision repair (BER) and single strand break repair (SSBR), respectively [15, 40]. DSB repair is more complicated and more likely to result in complications that can lead to cell death later on.

There are two types of DSB repair known as homologous repair (HR) and non-homologous end joining (NHEJ) [15]. Both begin with the detection of DSBs by sensor proteins, resulting in the phosphorylation of a protein known as histone H2AX [41], which is a component of chromatin, and is distributed throughout the nucleus. Phosphorylation of H2AX then extends in either direction from the DSB, over millions of bases, forming a region known as an ionizing radiation induced foci (IRIF). There are three known protein complexes (called kinases) that are able to initiate phosphorylation of H2AX at sites of DSBs [42].

Following the creation of the IRIF, the appropriate response is initiated based on the degree of damage. In some instances, apoptosis may be triggered to prevent the DNA damage resulting in mutations that could lead to the development of a tumour. If repair is possible, a checkpoint will be triggered, arresting the cell cycle and allowing the cell to focus on repairing the DNA damage.

If damage occurs in the S or G2 phases of the cell cycle, the preferred method of damage maintenance is homologous repair (HR). In fact, HR can only occur in

the S and G2 phases because it requires two copies of each DNA molecule to be available in the form of sister chromatids. Because HR uses identical undamaged DNA as a template to repair the damaged DNA, it is an error free method of repair [43]. After detection of a DSB (figure 1.5(a)), the repair process begins with the recruitment of other proteins that remove single stranded sections of DNA on either side of the break, leaving the overhanging complementary strands (see figure 1.5(b)). One of these strands then searches for a section of DNA identical to itself on the intact sister chromatid. Helicase enzymes then separate the strands of the undamaged sister chromatid in this region, and the single strand of the damaged DNA switches places with the identical section on the sister chromatid (see figure 1.5(c)). A crossover between the two DNA molecules is formed which extends until the gap left by the damaged single strand is filled by the corresponding undamaged strand of the sister chromatid (figure 1.5(d)). Single stranded sections of DNA are still missing on both sister chromatids, but each has an undamaged complementary strand to use as a template for repair. DNA polymerase enzymes synthesize the missing bases, and the molecules both become complete (figure 1.5(e)). However, the two sister chromatids are still connected in the crossover formation, and need to be separated. Specialized nuclease enzymes cut the molecules at the endpoints of the crossover, and the sister DNA molecules are separated. Depending on how the nucleases cut the endpoints (represented by the green arrows in figure 1.5(f) or (g)), the DNA molecules may swap identical sections beyond one of the crossover endpoints (figure 1.5(g)), but this does not affect the sequence of either chromatid, as both are identical. The entire process of homologous repair can take up to 6 or more hours to complete, but it is accurate and effective. In fact, due to the strength of HR as a repair mechanism, cells are most resistant to radiation in late S phase, when sister chromatids are present for almost all DNA, allowing for the repair of DSBs via HR [44].

In the G1 phase of the cell cycle, when a sister chromatid is not available to be used as a template, and to an extent in all other phases of the cycle, DSBs are repaired by a process called non-homologous end joining (NHEJ) [45]. The process involves reconnecting the ends of the DNA molecule on either side of the DSB. Typically, due to base damage at the site of the DSB, it is necessary to process the damaged ends so that it is possible for them to be reconnected [46]. If the damaged end is not blunt, and bases are missing from one strand, DNA polymerases can generate replacements, but it is also possible that some sections may have been removed altogether by the damage, resulting in deletions in the DNA molecule that would not be noticed without

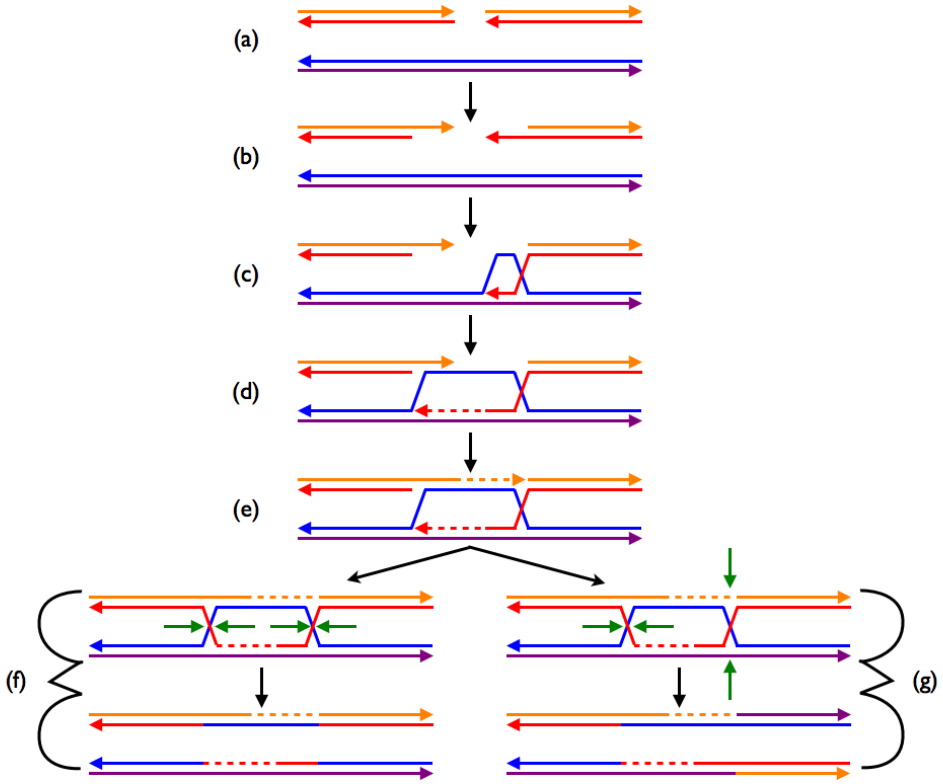

Figure 1.5: Schematic diagram representing homologous repair of a DNA DSB. (a) A DNA DSB occurs. (b) The ends of the damaged strands are processed by specialized proteins. (c) One of the overhanging strands of the damaged DNA invades the undamaged sister chromatid, forming a crossover. (d) The crossover structure extends until the undamaged DNA strand fills the gap left in the damaged DNA. (e) Using the undamaged strand as a template, DNA polymerase enzymes complete the opposite strand of the damaged DNA. The crossover structure is then separated by nuclease enzymes (represented by green arrows) according to the scheme shown in figure (f) or figure (g), resulting in two complete, identical sister chromatids.

a template for repair, as in HR. Therefore NHEJ, while faster than HR is less accurate, and can result in small deletions, or even insertions in the DNA molecule at the site of repair. Inaccurate repair such as this can cause mutations, the effect and severity of which depends on the section of the DNA molecule that is affected. Despite the problems with NHEJ, it is important for all cells and tissues, particularly those that divide rarely (or not at all), and don't often have sister chromatids available for HR.

1.3.2 Significance of damage to non-nuclear material

Despite the importance of DNA damage with regard to the cells response to ionizing radiation, damage occurs to all parts of the cell following radiation exposure. In many cases, the consequences of damage to parts of the cell other than DNA are believed to be less significant, due to the fact that most molecules appear in multiple copies, and have a rapid turnover during normal cellular function [15]. In some instances, however, it has been discovered that damage to molecules other than DNA can initiate cell death pathways. For example, in the endothelial cells of blood vessels, high doses of ionizing radiation ($>$ 15 Gy) cause damage to the cellular membrane, and result in the activation of an enzyme called ceramide synthase [47]. The large amounts of ceramide produced by this enzyme can trigger apoptosis, regardless of whether the DDR is successful or not [15].

Radiation-induced damage to cellular proteins is also potentially significant, due to the fact that proteins regulate many cellular functions, including the DNA damage response. As a result, damage to proteins will have an effect on cellular function, and while not yet well understood, it may have an effect on the survival of the cell. There are a variety of studies on the topic of radiation-induced protein damage, discussing both structural damage to proteins and the radiosensitivity of various amino acids [48–52]. The behaviour of proteins after exposure to ionizing radiation has also been studied and found to act as a biomarker indicating the progress of radiation-induced effects such as skin lesions [53–55], or the presence of DSBs in DNA [56–59] and chromatin rearrangement [60].

There is also evidence to suggest that radiation-induced damage to proteins plays an important part in cell death in bacteria and likely also in mammalian cells [61, 62]. The importance of protein damage in the outcome of the cell is still not completely understood, but a recent study suggests that it may be significant even at low doses of radiation ($<$ 10 Gy) [62]. In the study of radiation-induced cell death in bacteria, it is believed that radiation-induced protein carbonylation has a significant effect on cellular function, compromising processes such as DNA repair and ultimately leading to cell death [61]. The importance of protein damage in cell death suggests that attempts to regulate or de-regulate the expression of certain proteins could be a new avenue towards altering the radiosensitivity of cells and tissues [62].

Radiation-induced damage to DNA-protein complexes has also been studied, as the formation of these complexes is responsible for regulating the expression of struc-

tural genes that code for particular proteins [63–65]. Techniques such as *mass spectrometry* and *circular dichroism* were used to identify damaged products, and in all studies it was found that damage to the protein had the most significant effect on the formation of the DNA-protein complexes. In fact, it was suggested that the presence of the protein in the complex provided a degree of protection to the DNA molecule from the ionizing radiation [65]. Similarly, another study has found that the presence of protein in lipid membranes results in lipid-protein bonds that reduce the typically severe effects of ionizing radiation on cell membranes [66].

1.3.3 Ionizing Radiation-Induced Cell Death

Despite highly effective repair pathways, exposure of biological material to ionizing radiation may still result in cell death. As discussed in section 1.3.1, cell death may occur rapidly post-irradiation as a result of *apoptosis*, due to severe DNA damage. However, there are several other pathways for cell death following ionizing radiation-induced damage, known as *autophagy*, *senescence*, and *necrosis* [67]. The method by which a cell dies varies depending on cell type, and tumour cells have often mutated the pathways allowing for unmitigated proliferation.

Apoptosis is the highly regulated process that is most often associated with cell death, and is an important defence against the development of cancer. Activation of apoptosis can occur in response to damage within the cell, or from signals originating externally [68]. A balance exists between pro- and anti-apoptotic proteins within a cell, and conditions that lead to alterations in this balance, such as DNA damage, result in the activation of the pro-apoptotic proteins and the induction of apoptosis. Differences in the balance of the proteins affect the likelihood that apoptosis will be successfully triggered in a given cell or tumour type. Furthermore, the genes that regulate apoptosis are often mutated in tumour cells, and may prevent the initiation of apoptosis.

When apoptosis is successfully activated, it begins with the condensation and breaking apart of chromatin in the nucleus, while the body of the cell also starts to shrink. The nucleus and structures in the cytoplasm then begin to break apart, and small, membrane-bound apoptotic bodies begin to form. Due to the membrane surrounding the apoptotic bodies, leakage of cellular material is prevented, avoiding potential damage to other cells caused by the components of the dying cell. The apoptotic bodies are then engulfed and digested by *phagocytes*, which are cells designed

to remove harmful material from the body [3, 33, 34].

In contrast to apoptosis, necrosis is typically thought of as a form of accidental cell death. Necrosis will occur when a cell is exposed to conditions unfavourable to cell growth (such as ionizing radiation) resulting in damage from which the cell cannot recover. Typically, necrosis occurs when damage to the cellular membrane allows fluid to rush into the cell, resulting in swelling and the dissolution of cellular organelles. Eventually, the cell will burst and its contents will spill into the surrounding tissue, unlike in the case of apoptosis. Phagocytic cells will then attempt to clean up the debris and may initiate an *inflammatory response*, which is meant to create conditions that will mitigate further damage, but can also be harmful if allowed to persist [3, 33, 34]. Although necrosis was not originally believed to be a regulated form of cell death, recent studies provide evidence that like apoptosis, it may also be a controlled process [15].

While autophagy and senescence are also forms of cell death that can be initiated by ionizing radiation, these processes significantly differ in behaviour from apoptosis and necrosis. In fact, autophagy is primarily a process intended for cell survival. It involves the formation of structures called *autophagosomes*, which are double-membrane bound vacuoles that engulf cytoplasmic material [15, 69]. Autophagosomes fuse with lysosomes in order to digest the cytoplasmic components contained within in order to produce primary cellular building blocks and general energy for cell metabolism. Normally, autophagy occurs during times when a cell is deprived of nutrients and is starving, therefore it is initiated to provide the cell with enough energy to sustain basic metabolic function. However, autophagy also seems to behave as a tumour suppressor, and is known to be activated following the exposure of cells to ionizing radiation [70]. The relative importance of autophagy as a method of cell death is believed to be highly cell specific, and it is not clear whether cell death by autophagy is intended, or merely a failed attempt at cell survival [15, 69, 70].

Like autophagy, senescence is a process that is also not typically associated with cell death. However, it has been observed due to stress on cells as a result of ionizing radiation-induced DNA damage [71]. Senescence describes a situation in which a cell loses its ability to divide [72], and happens to all normal cells as part of the aging process. When caused prematurely as a result of ionizing radiation, the cytoplasm of the affected cell flattens and becomes more granular. The pathways that cause senescence are not completely understood, but in some cells, it occurs as a permanent extension of a checkpoint activated in the G1 phase of the cell cycle. As with the

apoptosis, necrosis and autophagy, the ability of different normal and tumour cells to initiate senescence is highly variable.

While cell death post-irradiation can occur by any of the methods described previously, it may not necessarily occur immediately (called early cell death, or *pre-mitotic*). In fact, in most instances, death occurs after multiple cell divisions (called late cell death, or *post-mitotic*). As a result, from a radiobiological standpoint, cell death is usually defined as the permanent inability of a cell to proliferate indefinitely after irradiation, referred to as the loss of *clonogenic survival*. A cell that has lost clonogenic ability will not contribute to the recovery of a tissue (normal or cancerous) following irradiation, but the effect of the damage to the cell will not be obvious until some time later. The cell may undergo reproduction multiple times, but if it has lost clonogenic ability, eventually death will be initiated later as a result of *mitotic catastrophe*, which is the inability of the cell to complete mitosis. The reason for this failure of mitosis is a result of the cell cycle being allowed to progress despite chromosomal errors due to damage caused by the ionizing radiation. Typically, any DNA damage would be repaired before mitosis begins (as mentioned in section 1.3.1), but in some cases the cell may not be able to properly regulate its cell cycle checkpoints, and in others the DNA may simply have been incorrectly repaired. Depending on the type of chromosomal aberrations present, mitosis may be able to occur successfully, or the duplication and separation of the chromosomes may fail, resulting in mitotic catastrophe [73]. Even if mitosis is successful, the aberrations may manifest themselves in the form of mitotic catastrophe many decades later. Regardless, whenever it does occur, mitotic catastrophe will cause cellular proliferation to cease and as a result, one of the other forms of cell death previously discussed may be triggered [74].

1.4 Analysis of ionizing radiation-induced damage to biological material

A great deal of work has been done to understand the response of biological material to ionizing radiation. Due to the significant role that DNA damage plays in determining the survival of the cell, much research has focused specifically on the effect of ionizing radiation on the DNA molecule. Many studies attempt to determine the number of radiation-induced DSBs in DNA using specialized assays such as *velocity sedimentation through sucrose gradients* [75, 76], *neutral and alkaline filter elution*

[77–82], or *agarose gel electrophoresis* [78, 81, 83–87]. All of the mentioned assays essentially involve the separation of fragments of DNA formed by DSBs based on their size. For example, when using *pulsed-field gel electrophoresis* (PFGE), irradiated cells are embedded in an agarose gel, lysed to release nuclear DNA, and exposed to an alternating electric field. The DNA molecules carry charge, and move under the influence of the field, separating based on their size. The number of detected DNA fragments can then be related to the number of ionizing radiation-induced DSBs. As an example, PFGE was used by Haveles *et al.* to determine how the number of double strand breaks in calf-thymus DNA exposed to gamma rays was affected by the presence of radical scavengers [86].

Studies have also attempted to quantify DNA damage by investigating radiation-induced base damage products. After irradiation, damaged bases are chemically cleaved from the DNA and then separated further according to their chemical properties. Often, *gas chromatography* (GC) is used in conjunction with *mass spectrometry* (MS) to identify the base products with a high degree of specificity [88, 89]. Gas chromatography separates the damaged base products based on their chemical properties as they pass through a capillary column, while mass spectrometry further classifies the products by breaking them into ionized fragments and separating them according to their mass-to-charge ratios. A specific application of the GC/MS technique involved the investigation of the types of base damage products produced in mammalian chromatin by free radicals generated by ionizing radiation in the presence of different gases such as argon and oxygen [88].

In the analysis of radiation-induced damage to proteins, techniques can be used that are similar to those used in the analysis of DNA damage. Early studies used two-dimensional paper chromatography to identify the amino acids still present after protein irradiation, and identified the acids that were particularly sensitive to radiation [48, 49]. More modern studies have used *polyacrylamide gel electrophoresis* (PAGE) to monitor the aggregation and fragmentation of proteins after exposure to oxygen radicals [50], and also to observe the structure of a DNA-protein complex post-irradiation [63]. Recently, the protein expression in the serum of mice after dorsal skin irradiation was monitored by *two-dimensional difference gel electrophoresis* (2D-DIGE) coupled with mass spectroscopy [54].

Other techniques that have proven useful in the identification of ionizing radiation-induced damage to proteins include *circular dichroism* [64], and *x-ray crystallography* [90–92]. Both circular dichroism and x-ray crystallography are spectral techniques

that provide structural information about proteins. Circular dichroism depends on a sample's differential absorption of left and right circularly polarized light [93], and has been used to study the structure of the binding portion of a protein in a DNA-protein complex after irradiation [64]. X-ray crystallography provides information about the three-dimensional structure of crystalline samples, including biomolecules, based on the diffraction of x-rays through the crystal [94]. Despite efforts to minimize damage to proteins by the x-rays inherent in the technique, results are still found to show evidence of radiation-induced structural damage [90–92]. However, because x-ray crystallography is performed on crystalline proteins at very low temperatures (77K), and involves very high radiation doses to the protein (10^7Gy) [95–98], findings from such studies of protein damage may not be representative of the response of physiological proteins to clinically relevant doses.

Alongside studies of ionizing radiation-induced damage at the molecular level, many other studies have focused on the effect of exposure to ionizing radiation on long term cell survival. Typically, cell survival is investigated through the use of a cell survival curve, which is a semi-log plot showing the surviving fraction of a cell culture after a given period of time as a function of dose [15, 35]. Cell survival curves measure clonogenic survival (see section 1.3.3), and take into account the fact that the survival of an individual cell post-irradiation does not mean that it will be able to successfully reproduce. While the standard form of a cell survival curve is well established [15, 35, 99], it is possible to detect differences relating to the type of cell irradiated, and the type of radiation delivered to the cell. There is particular variation in radiation response amongst tumour cells [35, 100], but the cells of normal tissues have also been found to show significant variations in radiosensitivity as well [101–104]. Through the use of cell survival curves, it has been found that cell radiosensitivity is dependent on the point in the cell cycle at which irradiation occurs [105–107], with cells being most sensitive during mitosis [15, 35]. Recently, investigations into the survival of a particularly radioresistant form of bacteria known as *deinococcus radiodurans* and different strains of *escherichia coli* have suggested that radiation damage to proteins can result in cell death even without damage to the cell's genetic material [61, 62].

1.4.1 Raman Spectroscopy in the analysis of ionizing radiation-induced damage to biological material

A technique that has proven to be particularly useful in the study of biological material at a molecular level, and shows promise in the analysis of ionizing radiation-induced damage to biomolecules is Raman spectroscopy (RS). Raman spectroscopy involves the collection of inelastically scattered light from a sample, with the difference in frequency between the incident and scattered light relating to energy absorbed by the sample to induce transitions between molecular vibrational energy levels. As such, a Raman spectrum provides information characteristic to the molecules in the sample, and the spectral peaks can be assigned to the vibrations of a specific type of molecule or group of molecules [108–110].

Currently, Raman spectroscopy has been successful in the analysis of radiation-induced damage to DNA [111, 112], protein [51, 66, 113–120], lipids [51, 66, 113–117, 120, 121], tissues [122–126], and cells [127, 128]. Unlike many of the techniques described in section 1.4, RS is unique in that it does not result in destruction of the sample, so long as an appropriate laser wavelength, power and exposure time are used [129–132]. RS can be used on live cells and tissues [129–137], and with the use of fibre optic cables, can provide measurements *in-vivo* [138]. The technique of RS provides highly specific molecular information about a sample, and allows for the analysis of multiple biomolecules within a sample in a single acquisition [110, 128, 139, 140]. Also, with the use of specialized focusing optics, Raman microscopy can provide spectral information at resolutions of 1μm or lower [127, 128].

Unfortunately, one of the drawbacks of RS is the inherently low intensity of Raman scattered light [110]. However, large increases in Raman intensity of more than six order of magnitude [141–143] can be obtained when scatter occurs in the presence of a rough metal surface, which has led to the technique of surface-enhanced Raman spectroscopy (SERS) [4, 108, 109]. Due to the ability of SERS to identify strong spectra from molecules even at low concentrations, it has been found to be particularly useful in the identification of biomolecules, and in the development of biological assays [144–149]. Also, through the introduction of metal nanoparticles to cell samples, SERS microscopy has provided an avenue for the two-dimensional mapping of the biomolecular content of cells [150–159]. Currently, SERS hasn't been used in the analysis of ionizing radiation-induced damage to biological material, but the success of Raman spectroscopy in investigating radiation-induced damage provides sufficient

motivation for the use of SERS in such studies. Further, SERS provides the benefit of high intensity signal at low sample concentrations, and the potential for the targeting of specific biomolecules using functionalized nanoparticles [1, 2].

The theory behind SERS and RS will be discussed in detail in Chapter 2, along with further detail on the use of SERS in the analysis of biological material, and the challenges associated with relating the measured intensity to a particular quantity of sample.

1.5 Thesis Scope

In the treatment of cancer it is critical to have a thorough understanding of the response of an individual to therapy. It is important that techniques are developed that can monitor patient response during treatment, ideally providing feedback that can be used to improve the treatment outcome. As mentioned in section 1.4.1, Raman spectroscopy has already shown great promise as a non-invasive, non-destructive technique in the analysis of ionizing radiation-induced damage to biological material. However, due to the large increases in scattering intensity provided by surface-enhanced Raman spectroscopy, and the proven ability of SERS to identify biomolecules with high specificity, the work described here attempts to assess the utility of SERS in the analysis of ionizing radiation-induced damage to biological material. Specifically, this work aims to develop a SERS microscopy technique to study the response of the membrane proteins of tumour cells to clinically relevant doses of ionizing radiation.

To begin, Chapter 2 provides a background in the theory of Raman Spectroscopy and SERS, while chapter 3 describes the materials and methods and data analysis techniques used in the studies presented in this work. A discussion of the challenges encountered in the attempt to develop a reproducible technique for imaging membrane proteins using targeted SERS nanoparticles follows in chapter 4. Chapter 5 then presents a promising SERS nanoprobe that has been rigorously characterized, and describes the results of a statistical technique (explained in chapter 3) that was developed to relate the number of SERS probes in an aggregated cluster at the spectral acquisition point to the measured SERS intensity at the point. The potential of the SERS probe in the use of quantifiable SERS microscopy is then discussed.

Due to the fact that a reproducible targeted SERS microscopy technique was not achieved in the time frame of this work, a previously established bioassay is used to determine whether changes in the binding of a protein can be identified at

clinically relevant doses. Chapter 6 describes the relationship of the binding ability of a representative protein to increasing radiation dose, and discusses whether a change in the ability of a protein to bind to its complement can be detected at clinically relevant doses.

Chapter 2

Surface Enhanced Raman Spectroscopy

In this chapter, an introduction to general Raman theory is provided (section 2.1), including discussions on Raman scattering (section 2.1.1), molecular vibrations and Raman-activity (section 2.1.3) and Raman spectroscopy (section 2.2). The theory of surface-enhanced Raman spectroscopy (SERS) is also provided (section 2.3), with descriptions of both the electromagnetic (section 2.3.1) and chemical (section 2.3.2) explanations of the effect. A general discussion of the metallic substrates used to provide SERS enhancement is also included (section 2.3.3), followed by a description of the difficulties in signal quantification of SERS, and some of the potential solutions that have been attempted (section 2.3.4). The chapter concludes with a discussion of the specific applications of SERS in the molecular imaging of cells (section 2.3.5).

2.1 Introduction to Raman Theory

2.1.1 Raman Scattering

When a light photon is incident on a molecule, it will be scattered both elastically and inelastically. Light that is scattered elastically has the same frequency as the incident photon, ν_0, and is known as Rayleigh scatter. Inelastically scattered light will experience a change in energy, and will thus have a different frequency ν'. The scattering interaction can be described classically, with the light source (typically a laser for Raman Spectroscopy) described in terms of its electric field strength, $\mathbf{E}$. Given the incident frequency of light, ν_0, the electric field strength as a function of

time, t, is given by:

$$\mathbf{E} = \mathbf{E_0} \cos 2\pi\nu_0 t \tag{2.1}$$

where $\mathbf{E} = (E_{0x}, E_{0y}, E_{0z})$ is the amplitude of the electric field. When the photon reaches the molecule, if its energy matches that of an energy difference between the ground state of the molecule and an excited state, the photon may be absorbed by the molecule, allowing it to achieve the higher energy state. However, if the energy does not match that of an electron transition, the photon will interact with the molecule and its electric field will distort the molecular electron cloud, forming a short-lived and unstable 'virtual state' (see figure 2.1), and also inducing a dipole moment, $\mathbf{P}$, given by:

$$\mathbf{P} = \alpha\mathbf{E} \tag{2.2}$$

where α is a constant of proportionality known as the *polarizability*. Written as a matrix in cartesian coordinates, equation 2.2 becomes:

$$\begin{bmatrix} P_x \\ P_y \\ P_z \end{bmatrix} = \begin{bmatrix} \alpha_{xx} & \alpha_{xy} & \alpha_{xz} \\ \alpha_{yx} & \alpha_{yy} & \alpha_{yz} \\ \alpha_{zx} & \alpha_{zy} & \alpha_{zz} \end{bmatrix} \begin{bmatrix} E_x \\ E_y \\ E_z \end{bmatrix} \tag{2.3}$$

In equation 2.3, the matrix containing the components of the polarizability is known as the *polarizability tensor*, and it is symmetric for normal Raman scattering [110].

Assuming that the charge separation in the molecule induced by $\mathbf{E}$ resulted in vibrations of the molecule's atomic nuclei, the displacement from equilibrium of the i^{th} nucleus can be written as:

$$q_i = q_{i0} \cos 2\pi\nu_n t \tag{2.4}$$

where q_{i0} is the maximum vibrational amplitude for the i^{th} nucleus, and ν_n is the frequency of vibration. The polarizability and the displacements of the atomic nuclei are related, and for small q_i, α is linear with q and can be expressed as follows:

$$\alpha = \alpha_0 + \left(\frac{\partial\alpha}{\partial q_i}\right)_0 q_i + \ldots \tag{2.5}$$

where α_0 is the polarizability at the equilibrium position of the molecule, and $(\partial\alpha/\partial q_i)_0$ is the rate of change of α with respect to q_i, evaluated at the equilibrium position.

Substituting equations 2.5 and 2.1 into equation 2.2 gives:

$$\begin{aligned}\mathbf{P} &= \alpha \mathbf{E_0} \cos 2\pi\nu_0 t \\ &= \alpha_0 \mathbf{E_0} \cos 2\pi\nu_0 t + \left(\frac{\partial \alpha}{\partial q_i}\right)_0 q_i \mathbf{E_0} \cos 2\pi\nu_0 t \end{aligned} \tag{2.6}$$

and inserting equation 2.4 into equation 2.6, the polarizability becomes:

$$\mathbf{P} = \alpha_0 \mathbf{E_0} \cos 2\pi\nu_0 t + \left(\frac{\partial \alpha}{\partial q_i}\right)_0 q_{i0} \mathbf{E_0} \cos\left(2\pi\nu_n t\right) \cos\left(2\pi\nu_0 t\right) \tag{2.7}$$

Finally, using the trigonometric identity $2\cos A \cos B = \cos(A+B) + \cos(A-B)$, equation 2.7 can be rewritten as:

$$\mathbf{P} = \alpha_0 \mathbf{E_0} \cos 2\pi\nu_0 t + \frac{1}{2}\left(\frac{\partial \alpha}{\partial q_i}\right)_0 q_{i0} \mathbf{E_0} \{\cos\left[2\pi(\nu_0 - \nu_n)t\right] + \cos\left[2\pi(\nu_0 + \nu_n)t\right]\} \tag{2.8}$$

Each of the terms in equation 2.8 can be explained in terms of Rayleigh and Raman scattering. The first term corresponds to Rayleigh scattering, and represents an oscillating dipole that scatters light at the same frequency as the incident light, ν_0. The second and third terms both correspond to Raman scattering, representing light that experiences a change in frequency. A scattering frequency of $\nu_0 - \nu_n$ is given by the second term, and a scattered frequency of $\nu_0 + \nu_n$ is expressed by the third term. The two different scattering frequencies represent two different types of Raman scatter; one corresponding to a loss in incident energy (related to frequency by $E = h\nu$, where h is Planck's constant), known as Raman Stokes scattering, and one corresponding to an increase in energy, known as Raman anti-Stokes scattering.

A schematic of the two different types of Raman scatter is shown in figure 2.1. In the figure, the ground and first excited state of the molecule are represented by Ψ_0 and Ψ_1, respectively. The vibrational energy levels of each state are represented by $v = (0, 1, 2, 3)$, the frequency of the incident light source is ν_0, and ν_{mn} represents the energy difference between the ground and first excited vibrational energy state of Ψ_0. As shown in the figure, Stokes scatter occurs when the molecule is in the vibrational ground state ($v = 0$), while anti-Stokes scatter occurs when the molecule is in an excited vibrational state ($v = 1$). Equation 2.8 and classical theory predict that the scattering intensity of Stokes and anti-Stokes are the same, but experiments show

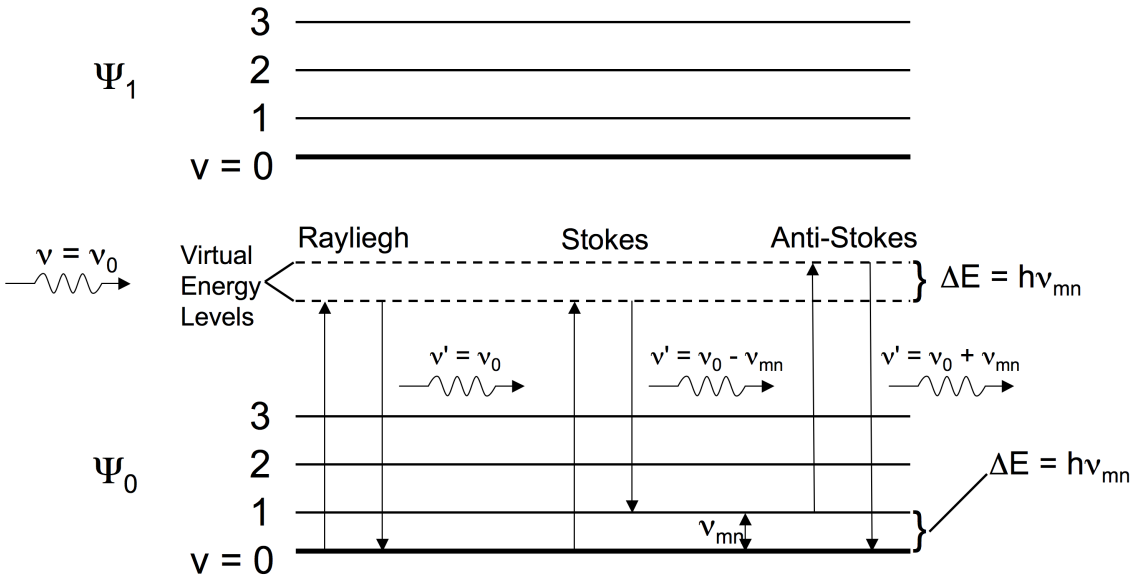

Figure 2.1: Schematic of Rayleigh scattering and Stokes and anti-Stokes Raman scattering.

that this is not the case. In fact, Stokes scattering is found to be much more intense than anti-Stokes [110], and the reason for the discrepancy from theory is related to the initial populations of the vibrational states. The Maxwell-Boltzmann law explains that at room temperature, the lower energy vibrational states are much more likely to be populated than the excited vibrational states [110]. As such, Stokes scattering is much more intense at room temperature, but since both Stokes and anti-Stokes scatter experience the same frequency shift of ν_n (written as ν_{mn} in figure 2.1), both types of scatter contain the same molecular information. Therefore, due to the higher intensity of Stokes scatter, it is Stokes that is typically the scatter measured in Raman spectroscopy.

Another important result of equation 2.8 is that if the partial derivative $(\partial\alpha/\partial q_i)_0$ is equal to zero for a given vibration, the dipole moment $\mathbf{P}$ will also be zero and no Raman scattering will be observed. As such, for a molecular vibration to be

Raman-active it must produce a non-zero change in at least one of the components of the polarizability tensor (equation 2.3). Further discussion of the Raman-activity of molecular vibrations will be provided in section 2.1.3.

2.1.2 Raman Scattering Intensity

Despite the fact that Stokes Raman scatter is of a higher intensity than anti-Stokes, both types of Raman scatter are much lower in intensity than Rayleigh scattering. Only one in 10^6-10^8 photons will scatter inelastically [108]. However, given the right experimental setup (see section 2.2) the Stokes Raman scattered light can still be detected. A general expression for the intensity of Stokes Raman scatter requires a quantum mechanical approach, and the details of such an approach can be found in standard texts [110, 160, 161]. Following a vibrational transition from state m to state n, the intensity of Stokes scattered radiation is given by [110]:

$$I_{mn} = C \cdot I_0 \cdot (\nu_0 - \nu_{mn})^4 \cdot \sum_{p\sigma} |(\alpha_{p\sigma})_{mn}|^2 \tag{2.9}$$

where C is a constant, I_0 is the intensity of the incident light source, ν_0 is the incident light frequency, ν_{mn} corresponds to the energy difference between states m and n (see figure 2.2), and α^2_{mn} represents the change in polarizability caused by the molecular transition from state m to n. The sum is over all p and σ which correspond to the x, y and z components of the polarizability tensor as shown in equation 2.3. An important aspect of equation 2.9 is that the intensity, I_{mn}, is proportional to both the incident intensity of the light source (I_0) and the fourth power of the frequency of the Raman scattered light ($\nu_0 - \nu_{mn}$).

To better understand equation 2.9, it is necessary to consider the $(\alpha_{p\sigma})_{mn}$ term in full, as described the Kramer Heisenberg Dirac (KHD) expression ([110]):

$$(\alpha_{p\sigma})_{mn} = \frac{1}{h} \sum_e \left(\frac{\langle \Psi_m | \mu_\rho | \Psi_e \rangle \langle \Psi_e | \mu_\sigma | \Psi_m \rangle}{\nu_{em} - \nu_0 + i\Gamma_e} + \frac{\langle \Psi_e | \mu_\rho | \Psi_m \rangle \langle \Psi_n | \mu_\sigma | \Psi_e \rangle}{\nu_{en} + \nu_0 + i\Gamma_e} \right) \tag{2.10}$$

in which ν_{em} represents the frequency corresponding to the energy difference between the initial molecular vibrational state m, and a given electronic excited state e, as represented in figure 2.2. Similary, ν_{en} relates to the energy difference between state e and the final vibrational state n. The $i\Gamma_e$ term is related to the lifetime of the excited

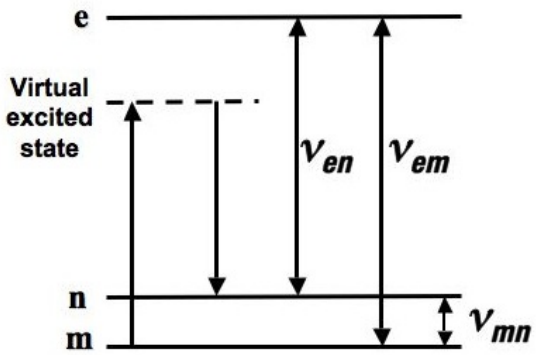

Figure 2.2: Energy Level Diagram: States m and n are vibrational states of the ground electronic state, and state e is an electronic excited state.

state, and is small compared to the other terms in the equation, but determines the natural width of Raman spectral lines [108]. Due to the relatively small magnitude of the $i\Gamma_e$ term, if the incident frequency of the light source is tuned to ν_{em}, the polarizability term in equation 2.10 becomes very large, leading to an even larger increase in intensity (equation 2.9) in a special type of process known as *resonance Raman scattering* [110]. However, in normal Raman scattering, the frequency of the incident light source is typically much less than ν_{em}, and the molecule is excited to a temporary virtual state rather than an electronic excited state. The integrals in the numerator of equation 2.10 (written in bra-ket notation) can be considered as terms that mix the wavefunctions of the ground (Ψ_m and Ψ_n) and excited states (Ψ_e) to describe the distorted electron configuration of the virtual state [108]. As an example, the bra-ket term mixing Ψ_m and Ψ_e can be written as an integral in the following way:

$$\langle \Psi_m | \mu_\sigma | \Psi_e \rangle = \int \Psi_m^* \mu_\sigma \Psi_e d\tau \tag{2.11}$$

where μ is the electric dipole moment operator along the coordinate specified by either ρ or σ.

Solving the KHD equation in full requires complex quantum mechanical operations (described elsewhere [108, 110]) and a knowledge of the wavefunctions of the molecule. Typically, the wavefunctions are not known, and an alternative method for determining the Raman activity of the molecule is implemented, which is discussed in section 2.1.3. However, detailed analysis of the KHD equation provides an inter-

esting result regarding whether or not a molecular vibration is Raman-active. It is found that the KHD equation will only have a finite result if there is one quantum of energy difference between the initial and final state of the molecule (ie. $m - n = 1$). The solution to the KHD equation also indicates that symmetric molecular vibrations produce the strongest Raman scattering [108]. A discussion of the symmetry of molecular vibrations is presented in section 2.1.3.

2.1.3 Molecular Vibrations

The vibrations of a given molecule can be very complicated, with each of the nuclei in a polyatomic molecule performing individual harmonic operations. As a result, it is not always obvious whether or not a given vibration is Raman-active. However, it is possible to consider the complicated vibrations of a polyatomic molecule as the superposition of a series of independent *normal vibrations*, or *normal modes*. It is the normal vibrations of a molecule that are detected by Raman spectroscopy, and the number of normal modes of a molecule are determined by the molecule's degrees of freedom. If a molecule consists of N atoms, then the number of degrees of freedom of motion is $3N$, since each atom can move in three dimensions (x, y and z). However, three of these degrees of freedom correspond to translational movement along the three dimensions, and another three correspond to rotations about the three principal axes (apart from linear molecules which only have two rotational degrees of freedom). This leaves $3N-6$ degrees of freedom that relate to possible vibrations, or 'vibrational degrees of freedom' ($3N - 5$ for linear molecules).

As an example, consider CO_2, which is a tri-atomic, linear molecule, and thus has $3(3) - 5 = 4$ degrees of freedom. Figure 2.3 shows the four normal vibrations of CO_2, with a symmetric stretch in figure 2.3(a), two bending, or deformation modes in figure 2.3(b), and an asymmetric stretch in figure 2.3(c). The two bending modes are known as *doubly degenerate* vibrations, due to the fact that both have the same frequency and move in the same way but in orthogonal directions. Only the vibrations in figure 2.3 that result in a change in polarizability (as shown in equation 2.8) throughout the oscillation will be Raman-active.

For simple molecules, the Raman-activity of a vibration can be determined by plotting the inverse of the square root of the polarizability ($1/\sqrt{\alpha_i}$ where $i = x, y$ or z) in all directions from the centre of gravity of the molecule. The resulting three-dimensional plot is known as the *polarizability ellipsoid*. In figure 2.4, the

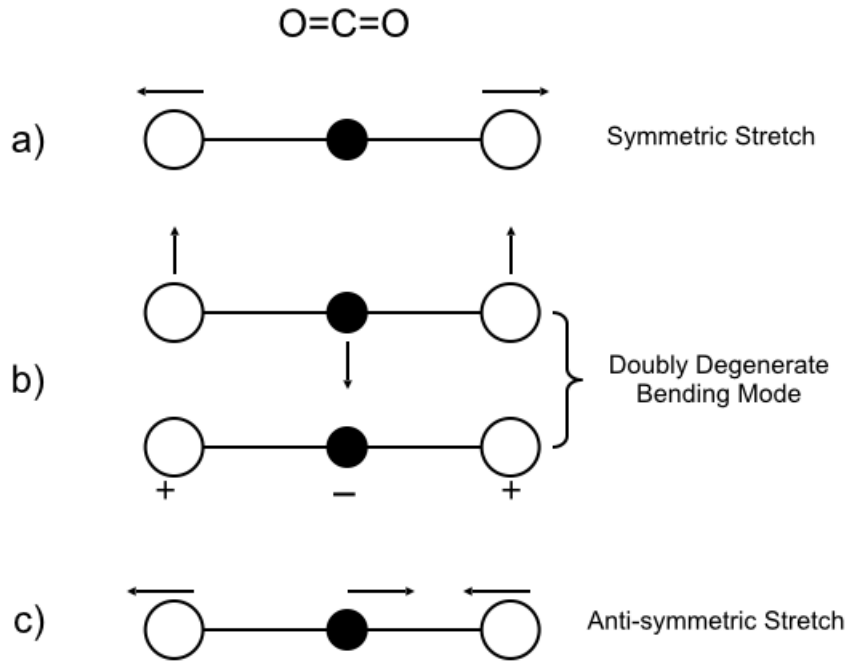

Figure 2.3: Normal modes of CO_2. In (b), the + indicates motion into the page and the − indicates motion out of the page in a direction perpendicular to the plane of the page.

polarizability ellipsoid is plotted at the equilibrium, maximum and minimum positions of each of the normal mode vibrations of CO_2. While the ellipsoid changes shape throughout each vibration, it is the same at the maximum and minimum positions for the bending and antisymmetric stretches (figures 2.4(b) and 2.4(c)). As a result, the slope of the polarizability as a function of the atomic displacement, q, is equal to zero at the equilibrium position (ie. $(\partial\alpha/\partial q_i)_0 = 0$) for these two vibrations. Since the polarizability does not change for small displacements from the equilibrium position, the bending modes and the asymmetric stretch both result in a dipole moment of zero (from equation 2.8) and are not Raman-active. In contrast, the polarizability ellipsoid of the symmetric stretch (figure 2.4(a)) changes in size from small to large in going from the maximum point of the stretch to the minimum. The change in polarizability for the symmetric stretch corresponds to a non-zero value of $(\partial\alpha/\partial q_i)_0$, and as such the vibration is considered Raman-active.

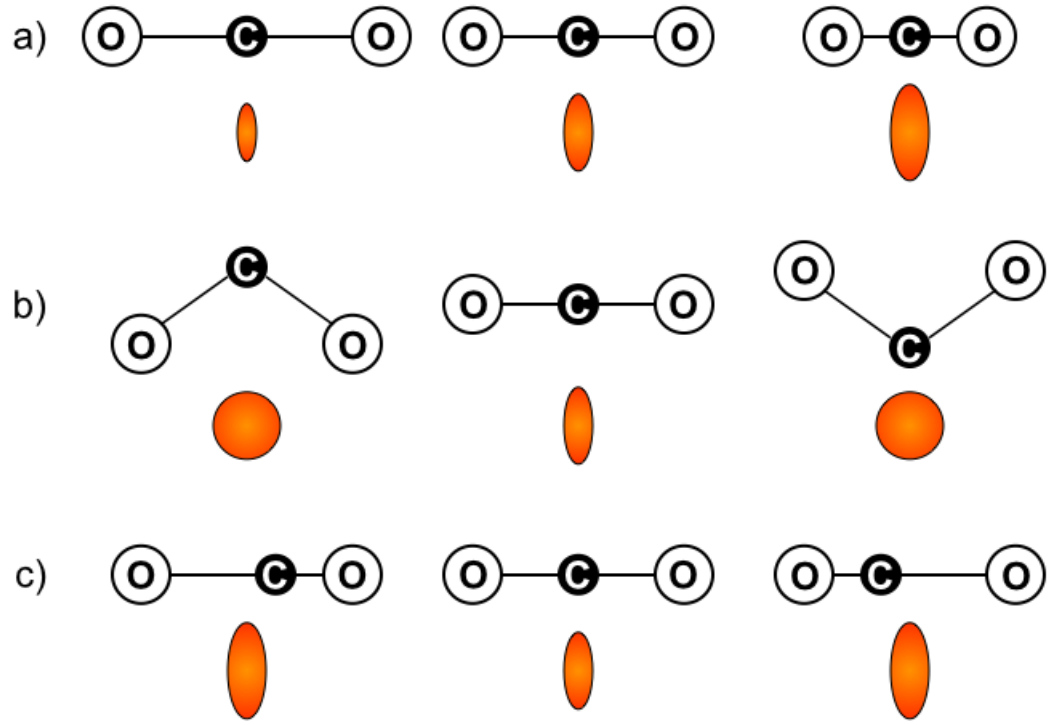

Figure 2.4: Polarizability ellipsoid ($1/\sqrt{\alpha_i}$, where $i = x, y, z$) for the normal vibrations of CO_2. In each case, the central configuration is the equilibrium position. (a) Symmetric stretch (b) Bending or deformation mode (c) Anti-symmetric stretch

For more complicated molecules, the analysis of the normal vibrational modes is not as straightforward, and requires the use of group theory [108, 110]. However, it is found that for all molecules with a centre of symmetry (such as CO_2), symmetric normal vibrations are always Raman-active and asymmetric normal vibrations are not. In the case of molecules without a centre of symmetry, a strict rule does not apply, but in general, symmetric vibrations are much more intense than asymmetric vibrations in Raman scattering [108].

2.2 Raman Spectroscopy

When a photon Raman scatters from a molecule, the difference between the wavelength of the incident and scattered light is directly related to the separation of

vibrational energy levels of the molecule. It is the molecular information, encoded within Raman scattered light, that is the basis for Raman spectroscopy. To perform this technique, a sample is excited by a light source (typically a laser) and the scattered light is collected through a series of optics that lead to a spectrograph, where the light can be separated into its component wavelengths, resulting in a Raman spectrum. An example of a basic Raman spectroscopic setup is shown in figure 2.5.

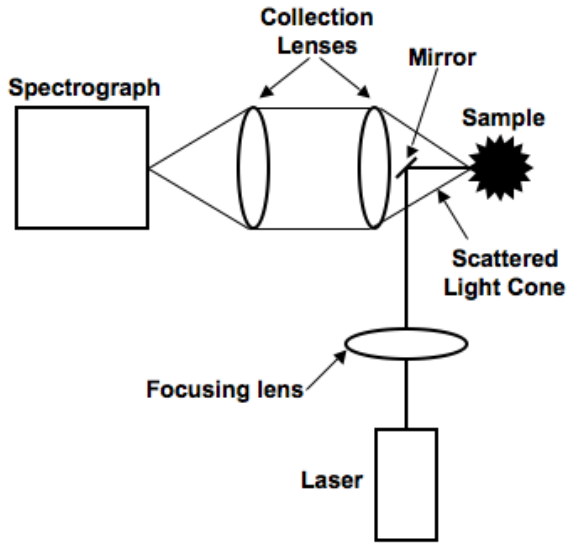

Figure 2.5: Sample Raman spectroscopic setup in a typical 180^o collection orientation (ie. laser excitation and collection occur along the same axis).

Since the change in energy of the Raman scattered light relative to the incident light is what provides the molecular information, it is this energy shift that is plotted in a Raman spectrum. It is standard in spectroscopy to plot a spectrum as a function of the *wavenumber* ($\bar{\nu}$) difference between the incident and scattered light (wavenumber is the inverse of the wavelength, expressed in cm^{-1}).

While the type of spectroscopic setup shown in figure 2.5 is used in many instances, it is not able to accurately provide spatially resolved information on a sample. To do so, it is necessary to direct the incident laser light onto a sample through a microscope. A microscope is very useful when trying to acquire the Raman spectrum of different parts of a sample with high precision. Typically, the sample is mounted on a high resolution motorized stage allowing the sample to be moved under the microscope with micrometer resolution. So long as the laser used is in the visible region, the light can be easily passed through the microscope optics. A basic schematic of a

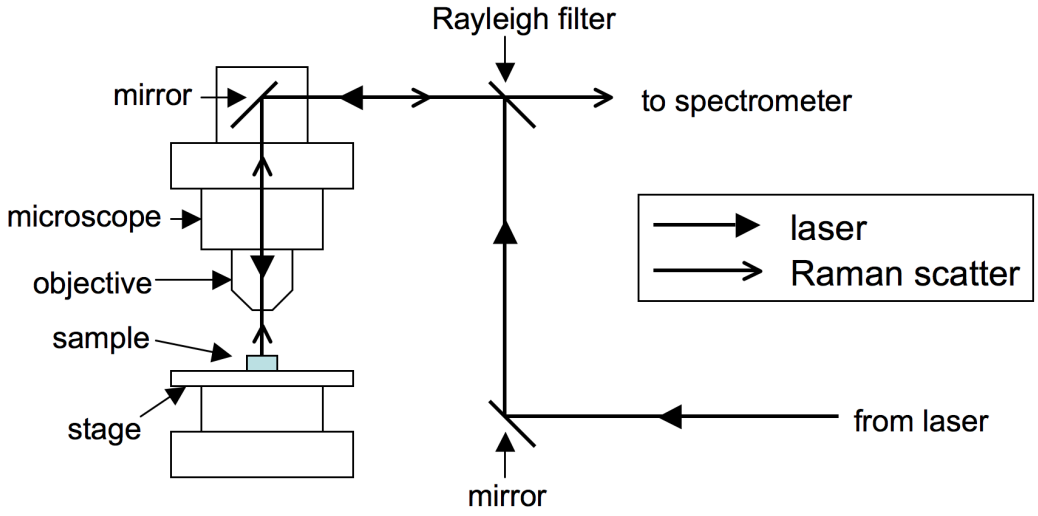

Figure 2.6: Basic schematic of a Raman microscope.

Raman microscope is shown in figure 2.6. It shows the laser being directed into the microscope via a series of mirrors, through the objective lens, and onto the sample positioned by the electronic stage. The Raman scattered light is collected through the same objective, directed back up through the microscope, and then passes through the Rayleigh filter into the spectrograph, while Rayleigh scattered light is reflected off of the filter.

The specific Raman microscope used in this research will be discussed in detail in the next chapter, but a description of the components of a typical Raman microscope is provided in the following sections. The laser excitation source is described in section 2.2.1, followed by a discussion of the optics of the objective in section 2.2.2. The spectrometer, which breaks the scattered light into its component wavelengths is described in section 2.2.3, and the charged coupled device (CCD) that converts the scattered light to an electronic signal is discussed in section 2.2.4.

2.2.1 Laser Excitation

Since the development of lasers in 1962 [162], lasers have proven to be excellent Raman excitation sources, and are a standard component of Raman microscope systems today. Lasers provide a high power, highly monochromatic source with minimal

beam divergence that can easily be collimated and focused to excite very small sample volumes [109, 110]. Typically, continuous wave (CW) laser are used instead of pulsed lasers, as pulsed lasers can provide extremely high instantaneous powers that increase the likelihood of sample damage and photochemical effects [109]. In contrast to pulsed lasers, CW lasers provide frequency stability, a low instantaneous power (but high power output) and a long operational lifetime [109].

The laser wavelength used depends on the application, and wavelengths from the hard UV (< 200 nm) to the near infrared (~ 1064 nm) have been employed in Raman spectroscopy [109]. For biological samples such as the cells imaged in this study, it is advised to use a longer wavelength (approaching infrared) in order to minimize sample damage and biological fluorescence [132]. While a longer wavelength results in weaker Raman scatter, it also allows for longer acquisition times which increases the collected signal intensity. Lasers that provide wavelengths suitable for biological applications include He-Ne (632.8nm) and diode lasers ($\sim$ 800 - 1500 nm) [109, 110].

2.2.2 Microscope Objective

A carefully chosen objective is a crucial component of a high performance Raman microscopy system. In order to prevent potential fluorescence, the objective must be of high optical quality with minimal impurities. The spatial and confocal resolution of the Raman microscope are largely defined by the objective, which is typically described by its numerical aperture (NA). The numerical aperture is defined as [163–165]:

$$NA = n \cdot \sin\theta \tag{2.12}$$

where n is the refractive index of the media surrounding the objective (*immersion medium*) and θ is the one half of the angle subtended by the cone of light collected by the objective (as shown in figure 2.7).

The minimum dimensions of the focused laser spot (and thus the sampling volume for Raman microscopy) are defined by the NA. The minimum width of the laser spot is given by [164, 165]:

$$r = \frac{\lambda}{2 \cdot NA} \tag{2.13}$$

where λ is the laser wavelength. The depth of penetration of the laser spot along the

beam axis, or the *depth of field* (DOF) is inversely proportional to the square of the NA, and is defined by [163–165]:

$$DOF = \frac{n \cdot \lambda}{NA^2} \tag{2.14}$$

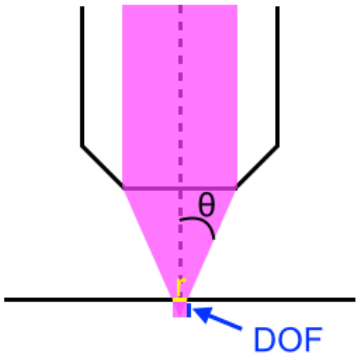

Figure 2.7: A schematic of a microscope objective showing the collected cone of light. The angle θ is one half of the angle subtended by the cone. The dimensions of the laser spot are indicated by r and DOF referring to equations 2.13 and 2.14 respectively.

Both equations 2.13 and 2.14 assume that the laser is perfectly aligned with the back aperture of the objective, and that the laser is perfectly collimated. While such assumptions are unrealistic experimentally, the equations are useful approximations when considering a choice of objective. Due to the relationship between r, DOF and NA, the smallest laser spot for a given wavelength and thus the highest spatial resolution is theoretically provided by an objective with a high NA. In addition, the highest collection efficiency (defined as the ratio of the solid angle subtended by the collected light cone and the solid angle for a sphere) is achieved with a high NA objective [163, 164].

While a high NA objective provides the best resolution for a RM system, it is important to consider the fact that a high NA may not be suitable when probing a weak Raman scatterer due to the small size of the sample volume. As a result, the choice of objective depends not only on the desired spacial resolution, but also the sample that is being analyzed.

2.2.3 Spectrometer

Scattered light that has been collected by the objective is passed to the spectrometer, where the signal is separated into its component wavelengths. For visible and UV excitation wavelengths, dispersive spectrometers are typically used, and while there are many different types, most modern spectrometers are based on the classic Czerny-Turner spectrograph [109]. A schematic diagram of a basic Czerny-Turner spectrograph is shown in figure 2.8. As illustrated in the figure, the collected light signal (ie. Raman scattered light) enters though the entrance slit, and reflects off the collimating mirror onto the diffraction grating, which has a series of evenly spaced grooves. The light is then reflected off of the grating at different angles depending on the wavelength of the light, and reflects off of the focusing mirror onto the focal plane. On the focal plane, the light is spatially separated by wavelength according to the *reciprocal linear dispersion* which is defined as:

$$\frac{d\lambda}{dl} = \frac{d \cdot \cos\theta}{mF_2} \tag{2.15}$$

where d is the groove separation of the grating, m is the order of diffraction, θ is the angle at which the diffracted light leaves the grating, and F_2 is the focal length of the focusing mirror (see figure 2.8). The reciprocal linear dispersion is typically in units of nm/mm, and written in terms of wavenumber ($\bar{\nu}$) the expression becomes:

$$\frac{d\lambda}{dl} = \frac{d(1/\bar{\nu})}{dl} = \frac{-1}{\bar{\nu}^2}\frac{d\bar{\nu}}{dl} \tag{2.16}$$

Inserting equation 2.15 into equation 2.16 gives:

$$\frac{d\bar{\nu}}{dl} = -\bar{\nu}^2\frac{d\lambda}{dl} = -\frac{d * \cos\theta * \bar{\nu}^2}{mF_2} \tag{2.17}$$

which leads to a non-linear relationship between the wavenumber of the light and the reciprocal linear dispersion at the focal plane.

In terms of the spectral information present at the focal plane, a low reciprocal linear dispersion results in a given wavenumber range being spread over a greater length at the focal plane, potentially allowing for fine spectral details to be resolved. If the wavenumber range present on the focal plane is not sufficient, a diffraction grating with a larger value of d can be used to increase the reciprocal linear dispersion, and thus spread a larger wavenumber range over the same length. However, the resolution of the spectrum would then be compromised. Instead it is more common to rotate the

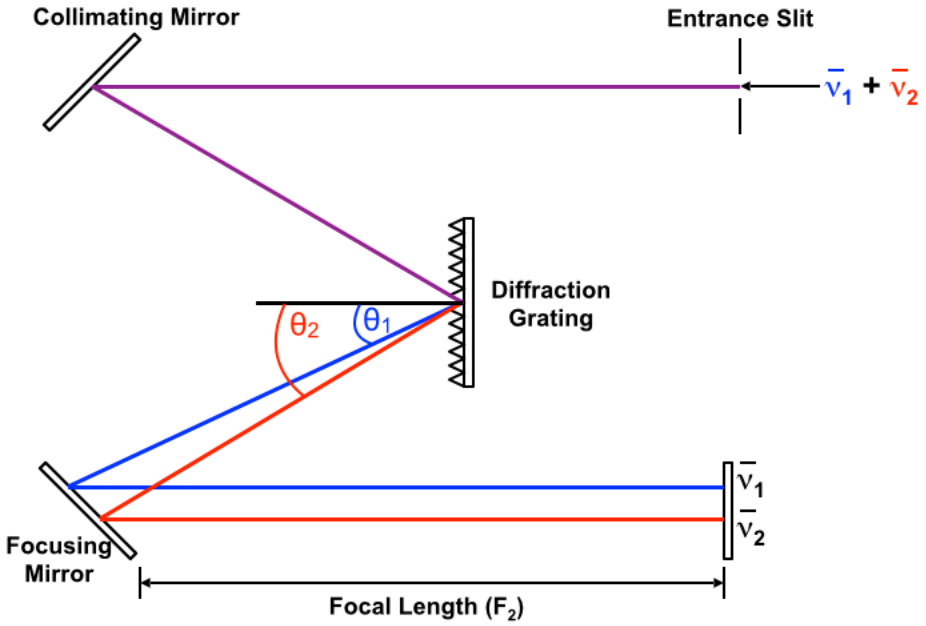

Figure 2.8: Schematic of a single grating Czerny-Turner spectrograph. Light composed of wavenumbers $\bar{\nu_1}$ and $\bar{\nu_2}$ is incident on the entrance slit, and split into it's component wavenumbers on the focal plane.

diffraction grating in a series of steps, focusing a different portion of the wavenumber range on the focal plane each time. The spectral windows acquired for each rotation then combine to generate a spectrum of the desired wavenumber range. In some modern spectrometers, the stepwise rotation of the diffraction grating is automated as a continuous scanning technique [166]. However, despite the wavenumber range present at the focal plane, the final spectral resolution is ultimately determined by either the width of the entrance slit or the pixel width of the charge-coupled device detector, as will be discussed in section 2.2.4.

2.2.4 Charge-Coupled Device

Typically, a charge-coupled device (CCD) is used in conjunction with a spectrometer to convert the spectrum into an electric signal [109, 110]. The CCD is placed at the focal plane of the spectrometer, and consists of a two-dimensional array of photosensitive diodes, usually composed of a silicon-metal-oxide semiconductor [167]. A circuit pattern of metal pads is deposited on the surface of the photosensitive elements, which

is held at a positive potential and defines the spatial grid of the detector. When light strikes the semiconductor array, photoelectrons are produced and are attracted to the nearest metal pad of the positively charged circuit array. The number of photoelectrons generated is related to the incident light intensity and the time of exposure to the light, or *acquisition time*. Since the photoelectrons are attracted to the metal pad, or *pixel* closest to their production, spatial information is retained.

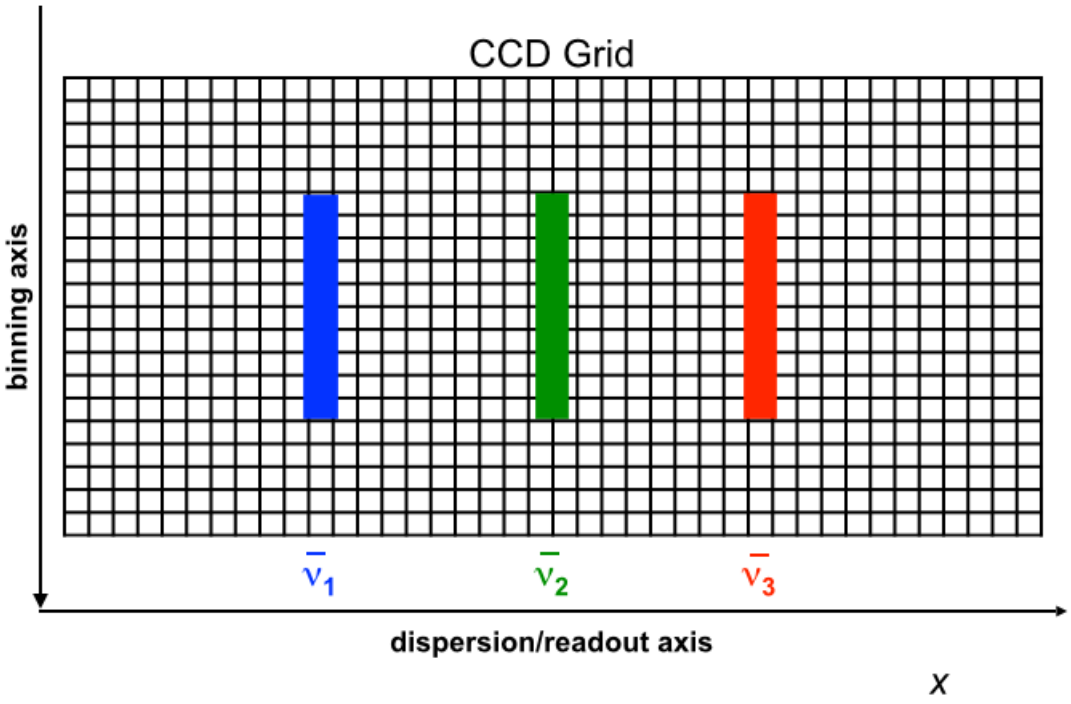

Figure 2.9: Schematic of a CCD Detector Array. Images of the spectrograph slit are spatially separated according to wavenumber ($\bar{\nu_1}, \bar{\nu_2}, \bar{\nu_3}$).

After passing through a spectrometer, light incident on the CCD grid is separated by wavenumber, as shown in figure 2.9. Typically, the height of the focal spot of a certain wavenumber (along the *binning axis* in figure 2.9) is longer than one pixel and depends on the dimensions of the spectrometer entrance slit. Since the pixels in a column along the binning axis all correspond to the same wavenumber, the signal from the entire column is often summed, or "binned", to generate maximum signal intensity for a given wavenumber. Binning occurs during the *readout* process, during

which the potentials of the metal pads on the circuit array are varied such that the signal is sequentially directed to the edge of the array along the binning axis, one pixel at a time. At the edge of the binning axis, the signal can be summed, or the two-dimensional pixel information can be recorded. The signal is then further shifted one pixel at a time along the *dispersion/readout axis* (see figure 2.9), where it is passed through an amplifier and then digitized by an analog-to-digital converter (ADC).

The digitized intensity can then be plotted as a function of pixel position to form a two-dimensional image, or a one-dimensional spectrum (if the columns have been summed). As the scattered light of different wavenumbers are spread out along the dispersion axis of the CCD, the pixel position along this axis is related to wavenumber, with a resolution that is limited by either the width of the spectrometer entrance slit or the CCD pixel width, depending on which is larger (see figure 2.9). Typically, a relationship between pixel position and wavenumber (ie. Raman shift) is determined by calibrating the CCD with the spectrum of a sample with a well-known Raman spectrum, such as tylenol or silicon [109]. After calibration, the spectrum can finally be plotted to show the intensity as a function of the wavenumber Raman shift.

2.3 The Theory of Surface Enhanced Raman Spectroscopy

While Raman spectroscopy is very useful in analyzing a multitude of substances, the Raman signal collected is typically of low intensity. Fortunately, there are several techniques that have been found to increase the intensity of Raman scattering from a sample. As can be seen from equation 2.9, these techniques would need to increase either the incident light intensity, I_0, its frequency, ν_0, or the change in the polarizability of the molecule, α_{mn}^2. The technique of surface enhanced Raman spectroscopy (SERS) is able to exploit increases in both I_0 and α_{mn}^2, and as such can provide enhancements in intensity of more than 10^6 times that of non-SERS Raman scattering.

SERS was originally discovered by Fleischmann *et al.* [168] in 1974, when it was found that molecules adsorbed on a rough metal surface produced intense Raman scattering. The reasons for this were a source of great debate, but today there are two generally accepted theories that are both consistent with the experimentally observed results, and it is believed that they both play a role in the dramatic enhancement

observed in SERS [4, 108, 169]. These theories, known as *field enhancement* and *chemical enhancement* are discussed in the following sections.

2.3.1 Field Enhancement

The theory of *field enhancement* is believed to be the most significant contributor to the large intensities observed with SERS [109]. This theory describes an increase in the electric field of the incident light source due to the field being scattered from a metal particle or rough metal surface. The enhancement comes from the interaction of the incident electric field with the conduction electrons surrounding the surface of the metal. This interaction results in the collective oscillations of the surface electrons across the surface of the metal, called *surface plasmons*. If the frequency of the laser incident on the metal matches the resonance frequency of a surface plasmon, the electric field at the metal surface becomes greatly enhanced.

A simple model to describe this phenomenon involves the scatter of light from a small metal sphere in the presence of a molecule from which Raman scatter will occur. In this case the sphere models the roughness features of a metal surface, and its radius must be much less than the wavelength of the incident light in order for this approximation to hold true [4]. A schematic diagram of this simple model is shown in figure 2.10. Essentially, the incident electric field distorts the cloud of surface electrons around the metal sphere and causes them to oscillate as a surface plasmon. These oscillations induce an electric field, E_r, at a distance r from the centre of the sphere which can be described by [108]:

$$E_r = E_0 cos\theta + g\frac{a^3}{r^3}E_0 cos\theta \tag{2.18}$$

where E_0 is the intensity of the incident electric field, a is the sphere radius, θ is the angle relative to the induced electric field, and g is given by:

$$g = \frac{\epsilon_1(\nu) - \epsilon_0}{\epsilon_1(\nu) + 2\epsilon_0} \tag{2.19}$$

In equation 2.19, ϵ_0 is the dielectric constant of the medium surrounding the sphere, and $\epsilon_1(\nu)$ is the dielectric constant of the sphere, which depends on the frequency of the incident radiation, ν. From this equation, it can be seen that the largest enhancement of the electric field occurs at the frequency for which $\epsilon_1(\nu)$ is equal to $-2\epsilon_0$. This resonance frequency varies according to the composition of the sphere

and nature of its surface, but for metals like silver and gold, the frequency is in the visible region, and thus silver and gold surfaces are very useful for SERS [108].

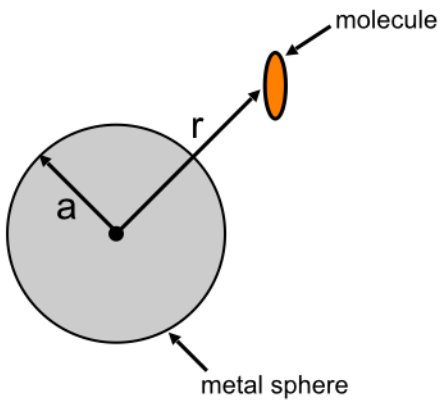

Figure 2.10: Schematic of the metal sphere used to describe the field enhancement theory of SERS

In this model, the sphere has become a radiating dipole, and as seen in equation 2.18, the field decays with distance from the sphere. As a result, the enhanced electric field is experienced by the molecule even if it is not adsorbed on the surface of the sphere. The intensity of the electric field experienced by the molecule is greater than it would have been in the absence of the metal sphere, and, as can be seen from equation 2.9, this will result in increased Raman scatter. Due to the fact that the induced electric field of the sphere is strongest perpendicular to its surface [108], the Raman scatter will be strongest from vibrational energy levels of the molecule that are polarized in this direction as well.

If the scattered light has a small enough Raman shift, the scattered photon will also resonate with the surface plasmon of the sphere and experience an enhancement in intensity in the same way as the incident light. This is called the "antenna effect", and the fact that *field enhancement* can be experienced by both the incident and scattered light leads to electromagnetic enhancement being the largest contributor to SERS enhancement [109].

While the model for *field enhancement* described above is very useful in understanding the concepts involved, it is important to remember that generally the surfaces involved in SERS are much more complicated. The metal used and the features of its surface have a very strong effect on the magnitude of the electromagnetic enhancement that is experienced (discussed further in section 2.3.3). For example, in the case of a collection of metal particles adsorbed on a surface, the greatest enhancement is not experienced on the surface of the particles, as suggested by equation 2.18, but in the regions between particles, or regions with clusters of particles [108]. While the explanation for these 'hot spots' is not fully understood, it is believed to be related to the coupling of surface plasmons between neighbouring particles, resulting in a shared plasmon with a unique resonance frequency [108].

2.3.2 Chemical Enhancement

Due to the fact that the effects of *field enhancement* are so significant, it can be difficult to separate out any other effects that may result in the large intensities of SERS. However, there is significant evidence to suggest the merit of another theory of SERS enhancement that is known as *chemical enhancement* [4]. This theory describes changes in Raman scatter intensity due to the interactions between a molecule from which Raman scatter occurs, and the metal surface. In this case, it is necessary that the molecule adsorbs onto the metal surface, with a chemical bond forming between the surface and the adsorbate (molecule). The bond between the adsorbate and surface creates a new complex which can result in the formation of new electronic states. When the incident light interacts with this new complex, significant enhancement can occur.

The enhancement provided due to the adsorbate/substrate bond is best described by *charge transfer theory* [109]. To understand this it is first necessary to discuss how the electronic states of the substrate and adsorbate differ. While the electronic states of the adsorbate molecule are separated by discrete energy levels, the energy separation between states in a metal is very small, such that the electronic states of a metal almost form a continuum. This is described in detail elsewhere [170], but briefly, the energy levels of a metal are separated into *bands*. The *valence band* consists of all of the orbitals that would be filled at absolute zero, with the maximum energy of the occupied orbitals being the *Fermi energy*, E_f. Any orbitals at an energy greater than E_f at absolute zero are part of the *conduction band*. Electrons in the

conduction band are less tightly bound to the nucleus than those in the valence band, and are free to move in an external electric field, resulting in the high conductivity of metals.

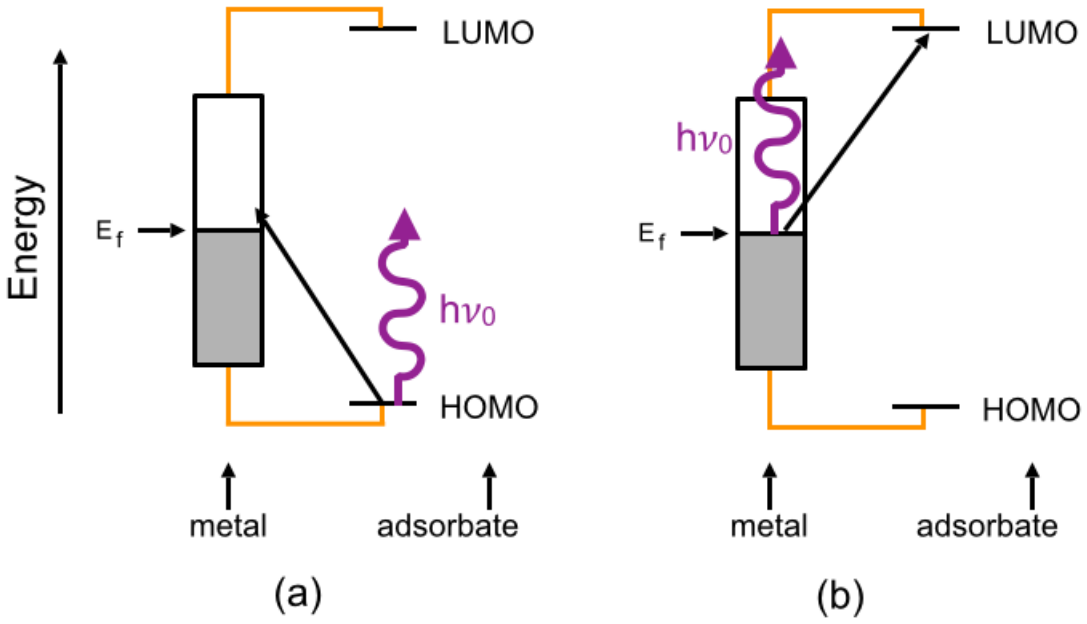

Figure 2.11: A representation of the (a) molecule-to-metal and (b) metal-to-molecule charge transfer that is possible due to the coupling (indicated by the orange lines) between the energy levels of a metal surface and an adsorbate molecule. Charge transfer theory is used to describes the chemical enhancement theory of SERS [4, 5] (*HOMO*: highest occupied molecular orbital, *LUMO*: lowest unoccupied molecular orbital).

Due to the chemical bond formed between the adsorbate and the metal, it is possible for electrons from the molecule to be transferred to the metal and vice-versa. Often, the fermi energy of the metal lies somewhere between the highest occupied molecular orbital (HOMO) and the lowest unoccupied molecular orbital (LUMO) of the adsorbate molecule [4] (see figure 2.11). In Raman spectroscopy, lasers used are typically of lower energy than the energy separation between the HOMO and LUMO of a molecule of interest [4]. However, the energy of these lasers would often

be sufficient to excite an electron in the ground state of the adsorbate molecule into the conduction band of the metal, in a process described as molecule-to-metal charge transfer [5] (see figure 2.11(a)). Similarly, an electron from the conduction band of the metal could be excited by a photon into the LUMO of the molecule in a process known as metal-to-molecule charge transfer [5] (see figure 2.11(b)). The excited electron would then drop down to its initial state either in the the ground state of the molecule or the conduction band of the metal, and its energy would be released as Raman scatter. In this situation, because of the coupling between the metal's conduction band and the molecules ground and excited states, the electron can be thought of as having been effectively excited to a higher electronic state by the incident light before it was scattered. As a result, the scattering intensity increases in a manner similar to resonance Raman scattering. Unlike resonance Raman scattering, however, which can lead to intensity increase $10^3 - 10^5$ times over that of normal Raman scattering [110], chemical enhancement only results in intensity increases on the order of 10^2 [108]. While comparing chemical enhancement and resonance Raman scattering is helpful in understanding the concept, a more detailed description of chemical enhancement and the intensity it provides is described by Lombardi *et al.* [5].

Ultimately, there is reason to believe that both *field* and *chemical enhancement* are accurate descriptions of SERS enhancement, and it is thought that both work together to provide the large intensities obtained by SERS [109].

2.3.3 SERS Substrates

There is a great variety of metallic surfaces that are capable of supporting SERS, and a significant amount of research has been performed to produce a SERS substrate that provides large, reproducible enhancement, as discussed in recent reviews [171–176]. Typically, the substrates are composed of metals such as gold, silver, or copper, as these metals are capable of supporting the excitation of surface plasmons when exposed to visible light [4, 169, 171]. The first observation of SERS was made using an electrochemically roughened silver electrode as a substrate [168], but the production of SERS substrates has advanced significantly in recent years. As the signal intensity of SERS is highly dependent on the surface structure of the SERS-active substrate [145, 169, 171–184], there has been a focus on creating regular surface features with a high degree of precision. For example, nanolithographic techniques such as electron

beam lithography [185, 186], and focused ion beam milling [187, 188] allow for the highly precise etching of regular nanostructures on a solid support, resulting in SERS substrates that are successful at providing highly reproducible scattering intensities. However, nanolithography requires access to expensive equipment and can be very time consuming. An attractive alternative is found in metal nanoparticles, which can be easily produced using wet chemistry at a low cost [189–195].

Recent developments in the manufacture of metallic nanoparticles have allowed for a great deal of control over their size and shape [171, 173, 190, 195], limiting extreme variations in the provided SERS enhancement. When used in SERS measurements, NPs may remain in solution, or can be immobilized on a solid support surface in a regular pattern. While the SERS intensities of scatter from NP surfaces can be highly reproducible [171, 173, 176, 196, 197], leaving the NPs in solution can be beneficial as it allows for more versatility in their use. In solution, a sample may be added to the solution for SERS measurement [198], or the NPs may be added to a sample, such as a cell culture [150]. Unfortunately, leaving the NPs in solution has the disadvantage of the potential aggregation of the NPs, and the aggregates can support very different SERS intensities than individual NPs [171–173, 175–178, 181, 182, 196, 197]. As a result, a great deal of effort has been afforded on producing reproducible SERS measurements when using NPs as a substrate, as will be discussed in section 2.3.4.

2.3.4 Quantification of SERS

Due to the well known dependence of SERS intensity on the structure of the SERS-active substrate and the challenges it provides [145, 169, 171–184], a great deal of research in the field has focused on obtaining reproducible measurements from a substrate. In particular, metal nanoparticles present a challenge as the size, shape, and inter-particle distance at the probed area all have a strong influence on the observed SERS intensity [172, 177, 178, 181, 182]. Despite the ability of modern techniques to provide a great degree of control over the size and shape of NPs [171, 173, 190, 195], the random degree of aggregation of SERS probes in solution, or even when deposited on a surface can potentially lead to high variations in SERS signal during an assay. There are methods, however, that address these difficulties, but their success depends very much on the experimental parameters. In the case of a SERS assay in which SERS probes are added to a sample that is in solution and assumed to have a relatively uniform target molecule (analyte) concentration,

the variations in measured SERS intensity can be addressed by simply performing spectral averaging throughout the sample [1, 149, 199–207], and quantification can be performed with a calibration curve. In these situations, normalization using an internal standard to correct for changes in the sample properties, SERS substrate, or laser beam intensity during the acquisition period can also be used for successful quantification [198, 208–210].

However, signal averaging might not be appropriate in attempts to use SERS probes to map an analyte that is non-uniformly distributed over a surface, as in the case of a planar assay platform or in the *in vitro* detection of cell membrane proteins. When mapping a surface, the SERS intensity at each acquisition point depends on the number of NPs at that point and how they are grouped (aggregated) relative to each other. In order to quantify the analyte at a given point in a sample, the measured SERS spectrum has to be related back to the number of SERS probes at the measurement point. It is then possible to determine the amount of analyte, assuming a linear relationship between the number of target molecules and the number of adsorbed SERS probes. However, determining the number of NPs that resulted in a particular SERS intensity is not straightforward and requires a specific understanding of the variability in SERS efficiency provided by differing groupings of clusters.

The variation in SERS intensity with NP aggregation is well known, and previous studies have monitored changes in intensity caused by the chemically induced aggregation of nanorods [211] and aggregation due to the deposition of multiple NP monolayers [212–214]. In general, it was found that an increase in particle aggregation leads to an increase in the average SERS intensity. A few groups have studied the SERS enhancement provided by individual NP clusters of varying size [177, 178, 182, 184]. For instance, Wustholz et al. [177] achieved a degree of control over the NP aggregations by using field flow fractionation [215] and stabilized the resulting clusters by individually encasing them in SiO_2 shells. After identifying individual clusters with transmission electron microscopy (TEM) and acquiring SERS and localized surface plasmon resonance (LSPR) measurements, they discovered that there is not necessarily an increase in SERS enhancement with the cluster size [177]. The results showed that a NP dimer can provide SERS intensities as high as that of a NP heptamer, with the enhancement much more dependent on the size of the inter-particle gap. Crevices formed in the junction between adjacent NPs act as hot spots dominating the overall enhancement provided by the cluster, and can result in signal over 10^8 times larger than that of normal Raman scattering [177].

In practice, the strong dependence on the inter-particle gap can be very problematic when attempting to quantify the results of SERS mapping. Typically, attempts are made to control the degree of aggregation of NPs by the introduction of a surfactant, such as cetyl trimethylammonium bromide (CTAB) [173], or the modification of the NP surface with a molecular coating, such as polyethylene glycol (PEG) [2]. However, these techniques cannot prevent aggregation entirely, and SERS intensity variation when using NP substrates remains a challenge. As such, further work is still required to understand the SERS intensities provided by different types of NPs, whether provided by the individual NP, or NP aggregates of varying size.

2.3.5 The role of SERS in imaging cells

SERS has long been useful in the study of biological materials, as the high signal it provides allows for the detection of molecules even at very low concentrations. It has been used to obtain spectra of many biomolecules such as amino acids, peptides and proteins [216–220, 220, 221] and DNA [222, 223] and is currently of great interest in the field of bioanalytics [144–149]. Of particular interest in this field is the identification of specific biomolecules within a volume. Due to improvements in the ability to control their size and shape [224, 225], gold and silver nanoparticles have shown promise as SERS substrates that provide reproducible enhancements, with gold nanoparticles having the benefit of being universally biocompatible [150, 155]. In some situations, nanoparticles are functionalized with a linker that will target a particular molecule [1, 226]. For example, Grubisha *et al.* [1] attached an antibody for the prostate specific antigen (PSA) to gold nanoparticles, and used them to detect PSA in human blood serum. To aid in the detection, a Raman active dye was adsorbed on the surface of the nanoparticles which gave a strong and distinct Raman signature.

Using a similar methodology, targeted SERS "nanoprobes" have been developed to identify cells that express a particular protein on their cellular membrane [2, 201, 227–229]. There is considerable variation in the design of the nanoprobes throughout the literature, with variations in the type and size of the nanoparticles used, the adsorbed Raman dye, and the antibody attachment method. Each design has its own advantages, and has proven useful in the detection of the membrane proteins. As an example, Kim *et al.* [201] successfully targeted the HER2 receptor on breast cancer cells, and the CD10 receptor on floating leukemia cells. In another instance, Lee *et al.* [228] were able to functionalize gold nanoparticles coated in silver in order to target

the PLCγ1 protein on the membrane of human kidney cells, which is believed to be associated with tumor development. Both of these examples used the strong SERS signal of Raman dyes adsorbed on the nanoparticle surfaces to locate the targeted nanoprobes.

There is also considerable interest in using SERS to study the internal structure of cells, as the ability of SERS to differentiate between different biomolecule signatures allows for the identification of various components of the cell cytoplasm [150–159]. Kneipp *et al.* [150] first used gold nanoparticles to probe biomolecules inside the cell with SERS. The nanoparticles were introduced to the cell growth media, and were uptaken by the cells. Raman mapping of the cells then indicated regions of strong signal enhancement due to the prescence of the gold nanoparticles. It is believed that the nanoparticles enter the cell through the *endocytotic pathway* [230, 231]. This involves the pinching in of the cell membrane, engulfing some extracellular material which may include the nanoparticles, and the formation of a vesicle within the cell. The vesicle (called an *endosome*) and its contents are then transported to other organelles such as *lysosomes*, or may be removed from the cell via *exocytosis*.

The SERS enhancement from the nanoparticles within the cell allowed for the identification of different cellular components, including proteins and nucleic acids. Recent studies have investigated how the SERS signal of the cells have varied with time as the gold nanoparticles aggregate [155], and how the distribution of nanoparticles varies within live and dried cells [158]. Some studies have used silver nanoparticles instead of gold [151, 153, 156], but, while there is some disagreement, gold nanoparticles are generally believed to be less cytotoxic to living cells [232–243]. In many cases, whether silver or gold, the metal nanoparticles have been labelled with a Raman dye to aid in their localization within the cells through the easily identified distinct peak of the dye [151, 153, 154, 156, 159]. In these instances, the nanoparticles still provided enhancement of Raman signal from molecular components of the cell in their immediate vicinity.

Through the use of both targeted and untargeted nanoparticle probes, SERS has shown great promise in detailed cell imaging. The use of targeted SERS probes provides information about specific proteins expressed on the membrane, while imaging with untargeted gold nanoparticles allows for a wealth of molecular infomation from the within the cell. However, the uncontrolled distribution of the gold nanoparticles within the cell can make the imaging of specific organelles difficult. The difficulty is compounded by the fact that the nanoparticles are confined to endosomes [155, 159],

and typically unable to cross the nuclear membrane. However, it is believed that the modification of the surface chemistry of the nanoparticles with various peptides will allow for better intracellular targeting in the future [244, 245].

Chapter 3

Materials and Methods

This chapter details the experimental techniques involved in the development of a procedure for the analysis of ionizing radiation-induced damage to tumour cells through the Raman microscopy of cell samples incubated with targeted SERS probes. The work was highly interdisciplinary, spanning the fields of chemistry, biology and physics. First, the details of the production of the two types of SERS probes used in this work are given in section 3.1. Preparation of cell samples and incubation of the cells with the SERS probes is then described in section 3.2. Experiments designed to verify the functionality of the SERS probes and the cell surface biotinylation are then discussed in section 3.3. Imaging techniques used in this work are described next, and include SERS microscopy, fluorescence microscopy, and scanning electron microscopy (section 3.4). Details of an experiment designed to determine whether ionizing radiation-induced damage affects the binding ability of streptavidin are then provided in section 3.5. Finally, a description of the data analysis techniques used to determine a relationship between SERS probe cluster size and SERS intensity is provided in section 3.6.

3.1 The Production of SERS Probes

Both types of SERS probes began with the synthesis of gold nanoparticles, described in section 3.1.1. Type I SERS probes (section 3.1.2) were used in early experiments, and consisted of a gold nanoparticle core linked to a targeting antibody via the molecule 5,5'-Dithiobis(succinimidyl-2-nitrobenzoate) (DSNB). Used in the majority of experiments, the Type-II SERS probes (section 3.1.3) also had a gold nanoparticle

core, but utilized a modified polyethylene glycol (PEG) molecule to link the nanoparticles to the targeting protein. Techniques implemented to verify the chemistry of the Type-II probes and characterize their SERS signal are described in section 3.1.4.

3.1.1 Synthesis of Au Nanoparticles

Colloidal gold nanoparticles were synthesized by the reduction of gold (III) chloride trihydrate ($HAuCl_4 \bullet 3H_2O$) with sodium citrate dehydrate in a glass beaker [189, 213, 246, 247]. To begin, 1 mL of a 1% solution of $HAuCl_4 \bullet 3H_2O$ ($\geq$ 99.9+% trace metals basis; Sigma Aldrich, Saint Louis, MO, USA) was added to 99mL of ultrapure water (UP-H_2O; Barnstead Nanopure ultrapure water purification system, 18.2 MOhm-cm resistivity; Thermo Scientific, Ottawa, Ontario, Canada), and the resulting solution was brought to a boil while stirring. Once boiling, 1mL of a 1% trisodium citrate dihydrate ($\geq$ 99%, FG; Sigma Aldrich) solution was added dropwise to the mixture. After boiling for another 5 minutes, the heat was turned off, and 1mL of a 5% sodium azide solution (ReagentPlus®, $\geq$ 99.5%; Sigma Aldrich) was added dropwise to the beaker. The mixture continued to stir as it was allowed to cool for about half an hour, after which point it was stored in the refrigerator.

3.1.2 Preparation of SERS Probes: Type I - DSNB

The first type of SERS probe produced in this work was based on the method described by Grubisha *et al.* [1]. A molecule known as 5,5'-Dithiobis(succinimidyl-2-nitrobenzoate) (DSNB) was used to link the gold nanoparticle and the targeting antibody, as shown in figure 3.1. The symmetric stretch of the NO_2 group of the DSNB molecule experiences strong Raman scatter, acting as a Raman reporter label. The intrinsic Raman label of DSNB allows for close proximity of the label to the nanoparticle and a high density of the label and antibody around the surface of the nanoparticle. DSNB was synthesized in the Brolo lab according to the method of Grubisha *et al.* [1].

To react the DSNB with the gold NPs of section 3.1.1, a 2.5 mM solution of DSNB was prepared in acetonitrile, and 100 μL of the solution was added to 1 mL of the $\sim$ 50 nm colloidal gold solution. The mixture was then allowed to react for 3-5 hours, during which time the DSNB attached to the nanoparticle surface through the thiolate of DSNB (see figure 3.1). Through centrifugation, the DSNB labelled colloids were separated from solution, and then resuspended in 1 mL of borate buffer.

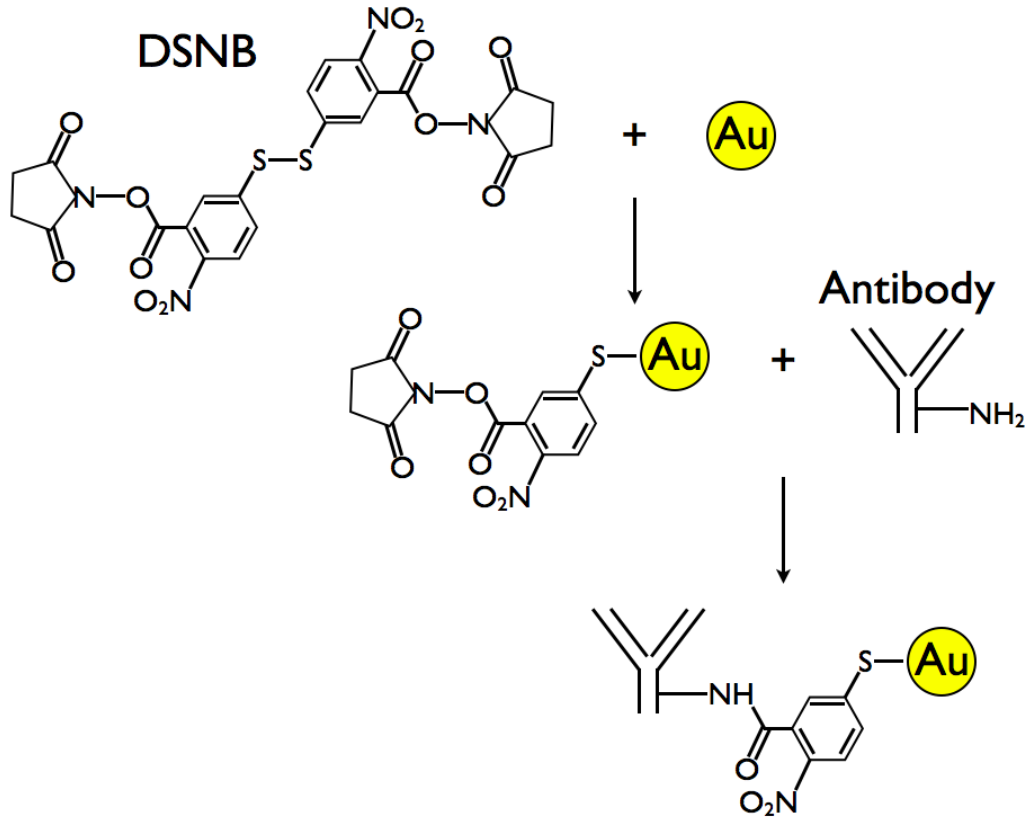

Figure 3.1: Schematic of the conjugation of a gold nanoparticle to an antibody using DSNB as the linker.

Both TACSTD2 antibody and streptavidin were used as targeting molecules for the DSNB SERS probes. TACSTD2 antibody is an antibody for the TACSTD2 protein on the membrane of the ovarian cancer cell line designated CaOV3. The antibody was produced by the Deeley Research Centre (DRC) at the British Columbia Cancer Agency - Vancouver Island Centre (BCCA-VIC). Streptavidin (essentially salt-free, lyophilized powder, $\geq$ 13 units/mg protein) was obtained from Sigma-Aldrich.

The targeting molecule attached to the NP via a reaction between the amine group (NH_2) of the antibody and the succinimide ester of the DSNB (see figure 3.1). A solution of the targeting molecule was added to the 1mL nanoparticle/DSNB solution to a final concentration of 35 μg/mL and allowed to react at room temperature for 1 hour. The targeted SERS probe solution was then centrifuged at 9700 rpm for 7 minutes at 4^{o}C, and resuspended in 1 mL of 2mM Tris buffer (Tris-HCL (pH 7.6), 1% bovine serum albumin (BSA); prepared from a stock solution at the DRC).

3.1.3 Preparation of SERS Probes: Type II - PEG

The second type of SERS probes used in this work were produced by modifying the NPs of section 3.1.1 according to an amended version of the method described by Qian *et al.* [2]. The nanoparticles were first coated with Nile Blue A perchlorate (NBA) dye (dye content 95%; Sigma Aldrich), followed by a polyethylene glycol (PEG) shell to which a targeting molecule was attached (see the schematic in figure 3.2; for this probe, only streptavidin was used as a targeting molecule). The PEG coating acts to stabilize the probe and reduce the non-specific binding of the SERS probes to sites other than the target.

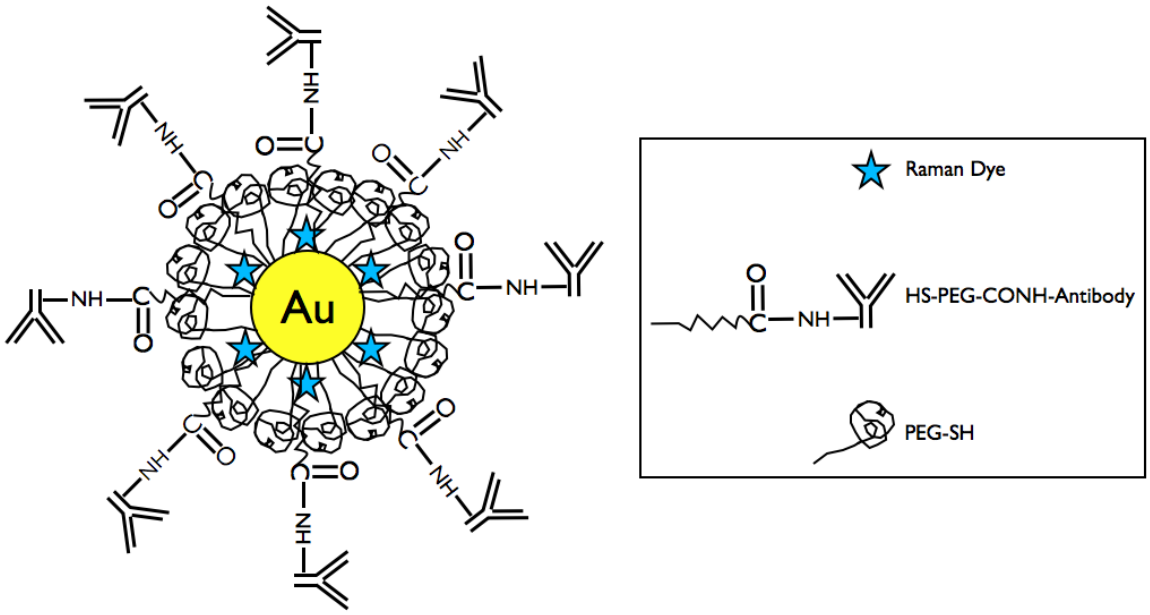

Figure 3.2: Diagram of the PEG coated nanoparticle probe. A Raman dye is adsorbed on the nanoparticle surface, along with HS-PEG-COOH, the COOH group of which connects to the NH_2 group of the antibody. PEG-SH coats any of the remaining surface of the nanoparticle to prevent non-specific binding to the gold surface. The final nanoprobe diameter is $\sim$ 90 nm in solution.[2]

To begin, 250-300μL of a 5μM NBA solution was slowly added, dropwise, to 2mL of a vigorously stirring NP suspension. The dye was allowed to mix with the NPs for 15 minutes, after which time 320μL of a mixed PEG solution was added to the rapidly stirring mixture. The mixed PEG solution was comprised of 0.5mL of a 200μM solution of HS-PEG-COOH (MW: 3000 Da; Rapp Polymere, Tuebingen, Germany) and 0.25mL of a 200μM methoxyl PEG-Thiol solution (PEG-SH, MW:

5000 Da; Jenkem Technology, Allen, Texas, USA), diluted to 1mL with UP-H_2O. The heterofunctional linker HS-PEG-COOH was included to attach to the streptavidin (targeting molecule), while the PEG-SH was to coat any areas of the gold NPs not covered by the linker.

After stirring for 20 minutes, the NP/NBA/PEG suspension was centrifuged twice at 13000 rpm for 7 minutes each time, and resuspended in 2mL UP-H_2O. To activate the COOH groups on the NP surfaces, 40μL of a 20mg/mL solution of ethyl dimethylaminopropyl carbodiimide (EDC; ProteoChem, Cheyenne, Wyoming, USA) was added, rapidly followed by 40μL of a 55mg/mL solution of sulfo-N-Hydroxysuccinimide (sulfo-NHS; ProteoChem). Following 40 minutes of stirring, 0.5 mL of phosphate buffered saline (PBS; diluted to 1x from a 10x concentrate; BioPerformance Certified; Sigma Aldrich) containing 1% Polysorbate 20 (Tween®20; Sigma Aldrich), or PBST, was added to the NP mixture to improve its solubility, and the suspension was stirred for a further 5 minutes. Excess reagent was then removed by two rounds of centrifugation (13000rpm for 7 minutes) and resuspension in 2mL PBST. At this point, 140μL of a 0.5mg/mL streptavidin solution was added to the nanoparticle suspension, resulting in a protein concentration of approximately 35μg/mL. The mixture was left to react overnight in the refrigerator at 4^{o}C.

After 24 hours, 0.5mL of PBST was added to the suspension before centrifuging (13000 rpm for 7 minutes) and re-suspending in 2mL of a PBS buffer with 0.1% Tween®20 and 100μg/mL of bovine serum albumin (BSA; $\geq$ 98% (agarose gel electrophoresis), lyophilized powder; Sigma Aldrich). The purpose of the BSA was to cap any unreacted activated COOH groups. After reacting for 20 minutes, the solution was centrifuged once more and resuspended in 2mL of PBST.

3.1.4 Characterization of PEG SERS Probes

The PEG SERS probes were used most frequently in this work, and needed to be routinely characterized to guarantee that samples from different batches used in the experiments had comparable physical and chemical properties. Such characterization techniques also assure that enough information about the samples is available for the eventual assessment of the results by other laboratories. The SERS probes were characterized at diverse stages during the synthesis by dynamic light scattering (DLS), ultraviolet/visible (UV/Vis) and surface enhanced Raman spectroscopy (SERS). These measurements were performed at four stages during the probe pro-

duction — on unmodified Au NPs; NPs after the addition of NBA and PEG; NPs with NBA/PEG/streptavidin; NPs with NBA/PEG/streptavidin/BSA. Results of the characterization process will be presented in sections 4.1.4 and 5.1.1.

Particle diameter was measured using a 90Plus Particle Size Analyzer (Brookhaven Instruments Corporation, Holtsville, New York) by dynamic light scattering (DLS). Through measuring variations in the intensity of laser light scattered from the particles in solution, the DLS technique yields the hydrodynamic diameter [248]. Effectively, the hydrodynamic diameter is the diameter of a sphere that would diffuse through the solution at the same rate as the particles being analysed. The measured hydrodynamic diameter includes contributions from molecules and ions attached to the surface of the particle, and as such it increases with the addition of the NBA, PEG and BSA layers to the NP core.

At least 0.5 mL of SERS probe solution was required for analysis, which was transferred to a plastic cuvette and inserted in the Particle Size Analyzer. Typically, two 3 minute runs of measurements of the hydrodynamic diameter were made and the results were combined, forming a multimodal distribution. A laser wavelength of 658nm was used and scatter was detected at an angle of 90^o. The 90Plus system required the viscosity and refractive index of the particle immersion medium, which were set to 0.890 centipoise (cp) and 1.33, respectively. For each SERS probe solution, the mean hydrodynamic diameter was recorded at each stage of production. The solution could be retrieved after measurement for experimental use.

The stability of the NPs during synthesis was monitored by UV/Vis spectroscopy, performed on the probe sample at each stage, using a Varian Cary 50 Scan Spectrophotometer (Agilent Technologies Canada Inc., Mississauga, Ontario). A 100 μL quartz cuvette filled with SERS probe solution was used for each measurement. The spectrophotometer measured the absorption of the solution from 650 nm to 400 nm in 1 nm steps. Unmodified NPs exhibited a characteristic spectral peak at approximately 530 nm. The probes were discarded at any stage if the 530 nm peak presented large red-shifts or broadening, since these are indicative of particle aggregation.

SERS of the probe suspension was carried out in all stages after the addition of the NBA to ensure that the spectral characteristics of the dye, including a strong peak at $\sim$595cm^{-1} [249], were always present. Raman spectroscopy was performed using an InVia Renishaw microscope (Renishaw Inc., Hoffman Estates, IL) with a 5x dry objective (Leica Microsystems, Wetzlar, Germany) and 1200 lines/mm diffraction grating. A 633nm Helium Neon Laser (Renishaw plc, Transducer Systems Division,

Gloucestershire, UK)) was used for sample excitation, and was focused on a drop of the SERS probe suspension centred on a glass slide. Spectra were acquired with a 5s exposure and a laser power of $\sim$ 1 mW at the sample. Laser power through the objective was measured using a Coherent FieldMax-TOP Laser Power/Energy Meter (Coherent Inc., Portland, Oregon, USA).

3.2 Cell Preparation

Details of the preparation of the cell samples for use in SERS microscopy are provided in the following sections and include descriptions of the cell culture protocol (section 3.2.1), cell fixation (section 3.2.2) and cell surface biotinylation (section 3.2.3). Incubation of tumour cells with unmodified gold nanoparticles is described in section 3.2.4, and cell incubation with Type-I and II SERS probes is discussed in section 3.2.5.

3.2.1 Cell Culture

Cell culture work for this project was initially performed in the Deeley Research Centre (DRC) at the British Columbia Cancer Agency - Vancouver Island Centre (BCCA-VIC), but eventually moved to the Chemistry Department at UVic in order to be closer to the Raman Lab. Three different cell lines were explored, each grown from frozen cell stocks at the DRC. The first cell line ('DU145') is derived from an epithelial prostate tumour. It is a robust cell line and its Raman spectrum as obtained with our Raman setup is well understood, as shown in previous studies [127, 128, 250]. The other two cell lines are both ovarian cancer lines ('CaOV3' and 'OVCAR5') and were chosen because it was possible to obtain an antibody specific to the cell lines for the targeted SERS probe study.

All cell culture work was performed in a laminar flow biological safety cabinet (BSC) to prevent contamination of the cell cultures. Each cell line was grown in a 10 cm tissue culture treated Falcon petri dish (BD Bioscences, Mississauga, ON, Canada). The dish was filled with approximately 15 mL of cell growth media containing 10% fetal bovine serum (HyClone, Logan, UT, USA). Both the DU145 and CaOV3 cells grew in Dulbecco's Modified Eagle Medium (DMEM) from HyClone and the OVCAR5 cells were grown in Roswell Park Memorial Institute (RPMI) 1640 media, also from HyClone. The cell lines were kept in an incubator conducive to cell

growth (37^o C in a 5% CO_2 atmosphere).

Every three to four days the cell growth would fill the base of the dish and the cells were near full confluency. Further growth was restricted due to overcrowding and the cells needed to be harvested and returned to fresh media at a lower cell concentration. The process was essentially the same for each cell line and began with removing the old media from the dish and washing the cells with a phosphate buffer solution (PBS; made by the DRC lab) to remove dead cell debris. The PBS was then removed and approximately 2 mL of the enzyme trypsin (HyClone) was added to the culture, which caused the cells to detach from the base of the dish. After incubation with the trypsin for approximately 10 minutes, the cells were almost completely detached from the dish. Approximately 5 mL of media was then added to the dish to deactivate the trypsin, and the cell solution was then transferred to a 15 mL Falcon tube (BD Biosciences) and centrifuged at 1200 revolutions per minute for 5 minutes. After centrifugation, the cells had settled at the bottom of the tube in a pellet, and the supernatant could be dumped in the waste. The cell pellet was then redissolved in 1 mL of media, and a fraction of the solution (typically from 1/4 to 1/8) was returned to a 10 cm dish containing approximately 15 mL of fresh growth media.

Prior to imaging, cells first needed to be transferred to a substrate appropriate for Raman spectroscopy. In this study, high purity quartz discs (Corning 7980 synthetic flame fused silica) were used as a growth substate. The discs were one inch in diameter, 2-3 mm thick, and were obtained from Technical Glass Products (Painesville Twp., OH, USA). High purity quartz was chosen due to its low Raman signal and the fact that the cells easily attach and grow on the discs [251]. Each disc was placed in a separate well of a six-well cell culture plate (BD Bioscences). To attach cells to a disc, a small volume of the 1 mL cell concentrate obtained from harvesting the cells was added to the disc after immersing it in $\sim$ 3 mL of fresh growth media. The discs then needed to be incubated for 24 hours to allow the cells to fully attach to the disc surface.

3.2.2 Cell Fixation

In order to image the cells with the standard dry objectives of the Raman microscope, it was necessary to fix and dry the cells on the quartz discs. The fixation procedure kills the cells, but essentially preserves their internal structure. Several methods

of cell fixing exist, but the one primarily used in this study is believed to be the most effective in maintaining the internal chemical composition of the cells [252] and involved the immersion of the cells in a formalin buffer solution.

To fix the cells on the quartz discs, the six-well plate was removed from the incubator, and each disc was rinsed with PBS and then soaked in approximately 5mL of a PBS solution containing 10% formalin for 15 minutes [251]. In one instance, a 1:1 mixture of methanol and ethanol was used to fix the cells instead of formalin. Approximately 5mL of methanol/ethanol solution was added to the well containing the cell-coated quartz disc, and the plate was then left for 10 minutes at -20^{o}C.

Following fixation, some cell-coated quartz discs underwent membrane permeabilization, which allowed for molecules to pass freely through the cell membrane. While the target sites for the SERS probes were on the cell membrane and not within the cell, permeabilization was still performed in some cases in order to be consistent with other published studies [2, 201, 227–229]. The permeabilization step is thought to be necessary as it will undo protein cross-links that are formed by the fixation process and can block the binding sites that the SERS probes will target [253]. After rinsing with PBS, the cell-coated quartz discs were permeabilized with the addition of approximately 5mL of PBS containing 0.2% Triton X-100 (Fisher Bioreagents; Ottawa, Ontario) for 10 minutes [228].

After fixation and/or permeabilization, the cells were rinsed again with PBS, and immersed briefly in deionized water to remove excess salts from the buffer. Once dried using compressed air, the slides were ready to undergo Raman imaging.

3.2.3 Biotinylation of Cells

In this work, cells were biotinylated either before or after fixation. In each instance, the process began with the preparation of a 6 mg/mL solution of EZ-Link Sulfo-NHS-SS-Biotin (Thermo Scientific, Rockford, IL) in deionized water. The cell-covered quartz discs were then washed three times in 1x-PBS. Each of the discs was then covered with 2mL of PBS mixed with 160 μL of the biotin solution. The cells remained in the biotin/PBS solution at room temperature for 45 minutes, followed by three washes with PBS. If biotinylation was performed on living cells, as was typically done, the cells were then fixed and prepared for imaging according to the procedure in section 3.2.2. If the cells were already fixed, then the slides were simply rinsed with deionized water and dried with compressed air.

3.2.4 Incubation of DU145 cells with Au NPs

Unmodified gold nanoparticles were introduced to DU145 prostate cancer cells growing on quartz discs via their growth media according according to two different procedures. The first was based on the work of Kneipp *et al.* [155] and involved the dilution of a 13 nm gold nanoparticle (NP) solution in DMEM to a concentration of 4 x 10^{-12}M. Four slides of the DU145 cells, each in one section of a six-well plate, were then covered with 4 mL of the DMEM/NP solution and placed in the cell incubator for 30 minutes. The discs were then removed from the incubator, and the DMEM/NP solution was replaced with regular DMEM solution. One of the slides was fixed in formalin and prepared for imaging immediately (as described in section 3.2.2), another after 2 hours of incubation in regular DMEM, and the other two after 24 hours of incubation time.

The second procedure of nanoparticle incubation with the cells was based on the work of Tang *et al.* [158]. In this case, an undiluted solution of 20nm nanoparticles was added directly to the DMEM solution covering DU145 cells growing on quartz discs. Each disc was coated with 4mL of DMEM, and a different volume of nanoparticle solution was added to the media covering each disc; 20 μL for the first disc, 200 μL for the second, and 500 μL for the third. The cells were then incubated in the DMEM/NP solution for 24 hours, after which they were fixed and prepared for Raman microscopy according to section 3.2.2.

3.2.5 Incubation of cells with SERS Probes (Type I and II)

Typically, cells were fixed before SERS probe incubation, but in some instances, probe incubation occurred prior to fixation. The only difference between the two techniques was that for unfixed cells, the SERS probe solution was diluted in cell culture medium, while for fixed cells, the SERS probes were diluted with PBS. Prior to introduction of the probes, the cell-covered quartz discs were washed three times with PBS, and the SERS probe solution (Type I or II) was mixed with the incubation medium (DMEM or PBS). Typically, for each disc, 400μL of SERS probe solution was added to 2mL of the incubation medium, although the probe volume did vary occasionally and will be stated explicitly alongside the results. Each cell-covered disc was then immersed in 2mL of the SERS probe/DMEM or SERS probe/PBS solution. The six-well plate containing the cell discs was then placed on a gently rocking table and probe incubation occurred at room temperature, typically for 2 hours.

Following incubation, unattached SERS probes were removed with extensive washing. Any cells that were alive during probe incubation would be fixed prior to the final washing step. Washing began with three changes of fresh PBS, each lasting for 5 minutes. A final wash with deionized water was then performed to remove excess buffer salts, lasting for 2 minutes. After removal of the water from the wells, the cell discs were typically allowed to air dry before undergoing Raman microscopy.

3.3 Independent Verification of Probe Functionality and Cell Biotinylation

Due to the complicated process of preparing a cell sample for SERS microscopy, two experiments were designed to separately verify different aspects of the procedure. In order to investigate the functionality of the SERS probes, samples for SERS microscopy were prepared with simplified surface chemistry, consisting of a biotin monolayer coated on a gold surface. Details of the sample preparation and SERS probe incubation are provided in section 3.3.1. An experiment to ensure that cell samples were being successfully biotinylated involved the preparation of cell samples for fluorescence microscopy. Both biotinylated cell samples and cell samples without biotin were incubated with a streptavidin/fluorophore conjugate as described in section 3.3.2.

3.3.1 Biotinylation of Gold Slides and SERS Probe Incubation

Glass slides coated with 100 nm gold films through a 5nm chromium (Cr) adhesion layer (EMF Corporation, Ithaca, New York, USA) were chemically modified with biotin in order to provide a surface to which the streptavidin-modified SERS probes (Type II) could attach. Each slide was first annealed, thoroughly rinsed with acetone (ACS reagent, $\geq$ 99.5%; Sigma Aldrich) and ethanol (Anhydrous ethyl alcohol; Commercial Alcohols, Brampton, Ontario, Canada), and placed in a clean 50mL glass beaker. A 1mM solution of biotinylated tri(ethylene glycol) undecane thiol (Whitesides Monothiol, Nanoscience Instruments, Inc., Phoenix, AZ, USA) was then prepared in 2mL of ethanol and added to the beaker. The beaker was sealed with Parafilm®M (Bemis Company, Inc., Neenah, Wisconsin, USA) as a monolayer

self-assembled on the Au surface for 12 hours.

The slide was then removed from the biotin solution, rinsed thoroughly with ethanol and UP-H_2O, and placed in a sealed beaker containing the SERS probe suspension for either 1, 2, 3, or 12 hours. After the incubation, the surface was washed thoroughly with PBST and UP-H_20 before being left to air-dry.

3.3.2 Preparation of Cell Slides for Fluorescence Microscopy

Fluorescence microscopy was to be performed on OVCAR5 cells both with and without biotin grown on quartz discs. Six discs were prepared in all, with five of the six slides biotinylated (as described in section 3.2.3), and one left as a non-biotinylated control. All six cell discs were fixed with formalin (see section 3.2.2) and washed with PBS prior to the addition of fluorescent dyes. Initially streptavidin-FITC dye (Rockland Immunochemicals Inc., Limerick, PA) was added to five of the discs, including the disc without biotin, and one biotinylated disc was left as a control. Streptavidin-FITC was added to the five discs at four different concentrations, diluted in PBS. The first two discs (one biotinylated and one without biotin) received a 1:125 dilution (16μL of dye in 2mL PBS), the third a 1:250 dilution (8μL of dye in 2mL PBS), the fourth a 1:500 dilution (4μL of dye in 2mL PBS), and the fifth a 1:1000 dilution (2μL of dye in 2mL PBS). The biotinylated control disc was immersed in 2mL of PBS, and all six discs were then placed on a gently rocking table in the dark at 4^{o}C for $\sim$ 25 minutes.

Following incubation with the streptavidin-FITC dye, the FITC/PBS solution was removed and each cell disc was covered with 2mL of PBS containing a 1:500 dilution of Hoechst 33342 dye (Life Technologies Inc., Burlington, ON) and a 1:1000 dilution of DRAQ5$^{\text{TM}}$dye (BioStatus Limited, Leicestershire, UK) to stain the cell nuclei. The cells incubated with the new dyes on a gently rocking table in the dark for $\sim$ 25 minutes at 4^{o}C. After incubation, each cell disc was washed with 2mL of PBS.

To prepare for imaging, the discs were removed from the PBS and a small amount of Shandon$^{\text{TM}}$Immumount$^{\text{TM}}$(Thermo Fisher Scientific, Ottawa, ON) was placed on the surface of each disc (Immumount$^{\text{TM}}$prevents the sample from drying out and resists fading of the fluorescence signal prior to imaging). A glass coverslip was then placed on each disc, with care taken to avoid the formation of bubbles under the glass. The discs were then returned to a six-well plate, covered with tinfoil and placed in

the refrigerator overnight to set. Small holes were punched in the tinfoil to allow air flow over the disc surfaces.

3.4 Imaging

Multiple imaging techniques were used in this work, and are described in the following sections. Details of the SERS Microscopy of cell samples are given in section 3.4.1, and fluorescence microscopy of the fluorescent cell samples (section 3.3.2) is discussed in section 3.4.2. The biotinylated gold slide samples of section 3.3.1 were imaged with both the SERS microscope and a scanning electron microscope (SEM), and details of these techniques are provided in sections 3.4.3 and 3.4.4, respectively. Analysis of the SERS maps and SEM images acquired of the biotinylated gold slide samples will be explained in section 3.6.

3.4.1 SERS Microscopy of Cells

Raman microscopy was performed with the InVia Renishaw microscope, using either a 50x or 100x dry objective (N.A. = 0.75; N.A. = 0.9) (Leica Microsystems, Wetzlar, Germany), 1200 lines/mm diffraction grating, and either a 633nm Helium Neon Laser or 785nm Diode Laser (Renishaw plc, Transducer Systems Division, Gloucestershire, UK). The resolution of the maps in the x and y direction could be entered manually and varied depending on the mapped area (from a single cell to tens of cells), but the maximum resolution was limited by the dimensions of the laser spot. The 633nm laser spot was measured to be approximately 1 x 1 x 2μm through the 100x objective, while the 785nm laser spot was found to be approximately 2 x 5 x 10μm. Most frequently, Streamline$^{\text{TM}}$Plus Raman imaging (Renishaw Inc., Hoffman Estates, IL) was used to ensure rapid scanning without compromising signal-to-noise ratio. Streamline$^{\text{TM}}$imaging is unique to the inVia microscope and involves raster-scanning a line-focused laser spot across the region of interest with acquisition and read-out occurring simultaneously (Product Note, Renishaw plc, 2008). When Streamline$^{\text{TM}}$imaging is used, the resolution in the y direction is fixed: 1.1μm for the 50x objective and 0.5μm for the 100x. The laser power at the sample could be adjusted via built-in filters of the inVia microscope, but the maximum power at the sample was $\sim$ 2mW for the 633nm laser and $\sim$ 50mW for the 785nm. The power density depended on the volume of the laser spot, and was lower when Streamline$^{\text{TM}}$imaging

was used due to the line-focused laser spot.

Prior to spectral acquisition, the laser spot was focused on the surface of the cell, and then the stage was brought closer to the objective by $\sim 2\mu$m. The focal point of the laser was typically also measured post-acquisition to ensure that there was minimal stage drift in the z-direction. For appreciable SERS signal, acquisition times of ~ 2 seconds/pixel were required for point-by-point mapping and ~ 5s/pixel for Streamline™ imaging. Two-dimensional SERS map data was presented with each pixel corresponding to the area under the characteristic peak of the SERS probe used ($\sim$1335 cm^{-1} [1] for Type I and $\sim$595 cm^{-1} [249] for Type II). For SERS maps of cells incubated with Type II SERS probes, the data was also typically presented as a histogram of SERS intensity. In these histograms, SERS intensity refers to the area of the NBA dye peak at 595 cm^{-1}.

3.4.2 Fluorescence Microscopy of Biotinylated Cells

Fluorescence microscopy was performed with a Nikon C1 Confocal Microscope (Nikon Instruments Inc., Melville, NY, USA) with 488 nm and 633 nm lasers. Images were acquired with the 20 and 100x objectives. Both fluorescence images and differential interference contrast (DIC) images were obtained of each disc. DIC microscopy is a technique typically employed to provide contrast in the images of nearly transparent samples, and the contrast is related to the optical path length of light that passes through the sample [254]. The DIC images were used to help identify the location of cells on the disc in a fashion similar to a bright-field image.

3.4.3 SERS Microscopy of Biotinylated Gold Slides

Raman spectroscopy was performed with the InVia Renishaw microscope using the 100x dry objective, 1200 lines/mm diffraction grating, and 633nm Helium Neon Laser. Streamline™ Plus Raman imaging was used, and maps of three randomly chosen regions were acquired on the gold slide corresponding to each SERS probe incubation time. The resolution of the maps was 1μm x 0.5μm, with each point exposed to $\sim$1 mW of laser power for 3 seconds. Each map covered an area of about 4000μm^2 and took approximately 15 minutes to complete. Two-dimensional SERS map data was presented with each pixel corresponding to the area under the NBA dye peak at 595 cm^{-1}. The three SERS maps for each slide were also combined and presented as a

histogram of SERS intensity. In these histograms, SERS intensity refers to the area of the NBA dye peak at 595 cm^{-1}.

3.4.4 SEM Imaging of Biotinylated Gold Slides

A Hitachi S-4800 field emission scanning election microscope (FESEM; Hitachi High-Technologies Canada, Inc., Toronto, Ontario) was used to acquire high resolution, high magnification images of the SERS probes on the surface of the gold slides. All images were obtained using an acceleration voltage of 1.0kV and a magnification of 20 000 x, covering an area of about 30 μm^2. A sampling of images of the SERS probes was acquired on the slide corresponding to each incubation time. At least 5 images were taken of each slide, with any differences in the imaged area of the slides accounted for in the analysis.

3.5 Study of Ionizing Radiation-Induced Damage to Streptavidin

This section details the experiment designed to determine whether ionizing radiation-induced damage affects the binding ability of streptavidin. The streptavidin irradiation procedure is described in section 3.5.1, followed by some brief background on the *enzyme-linked immunosorbant assay* (ELISA) in section 3.5.2, which is the test that was used to monitor the concentration of functional streptavidin in irradiated solutions. The specific procedures for each of the ELISAs performed are then provided in section 3.5.3.

3.5.1 Irradiation of Streptavidin

Solutions of streptavidin were prepared in 15mL Eppendorf vials, with one set of samples diluted in PBS (Type A) and the other in PBS with 3.5% BSA (Type B). The BSA was included in one set of solutions to mimic the high protein content of blood plasma, and the concentration was chosen based on that of human serum albumin, which is the most abundant blood plasma protein [255, 256]. All solutions of streptavidin were prepared at concentrations of 5 μg/mL. The streptavidin solutions were placed in a custom made irradiation phantom designed to fit in the accessory mount of a Varian 6EX linear accelerator (Varian Medical Systems, Inc., Palo Alto,

CA, USA) at the BCCA-VIC (see figure 3.3). Once placed in the accessory mount, the linac was rotated to a gantry angle of 270^o with the collimator at 90^o. Ion chamber measurements in the slots of the irradiation phantom had previously been performed and determined a conversion factor relating the number of monitor units (MU) delivered by the 6MV photons of the linac to the dose delivered to a vial in the phantom. Using the empirically determined conversion factor of 100 MU / 2.24 Gy, the number of MUs necessary to deliver doses between 5 and 240 Gy were calculated. For all irradiations, the x-jaws of the linac were set to 28 cm and the y-jaws were set to 30 cm. A dose rate of 600 MU/min was provided by the linac.

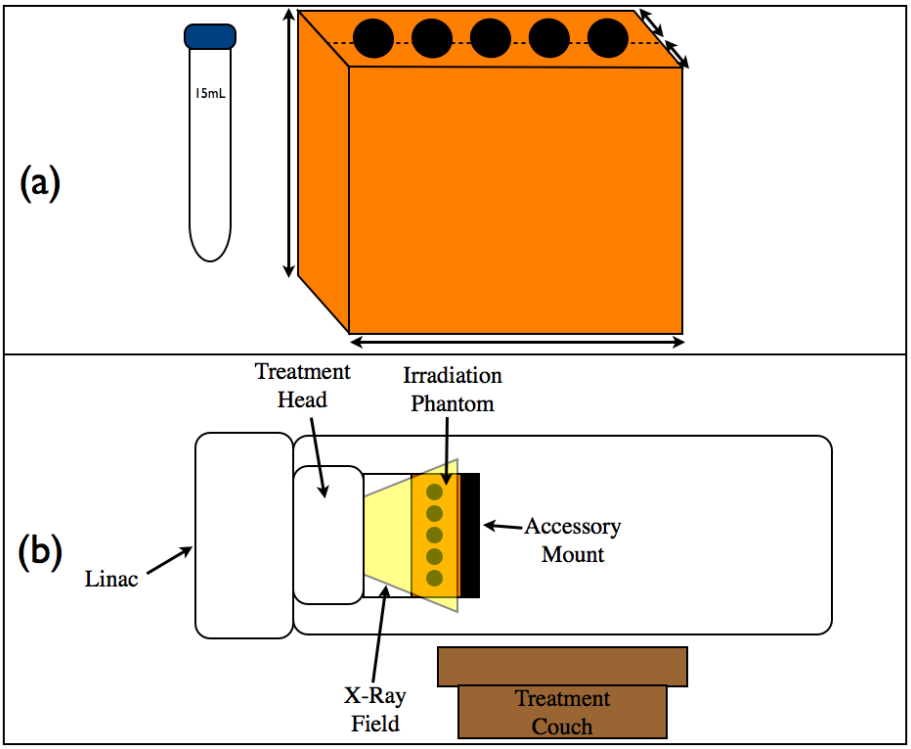

Figure 3.3: (a) Schematic of the phantom in which the 15mL vials containing streptavidin solution were irradiated. (b) Diagram of the phantom in the linac during irradiation.

3.5.2 ELISA Background

In order to detect ionizing radiation-induced damage to streptavidin via its ability to bind to its complementary protein biotin, an enzyme-linked immunosorbant assay (ELISA) was used. The ELISA is a commonly used biochemical assay that detects the

prescence of an antigen in a liquid sample. In this work, the direct "sandwich" ELISA technique is used, a schematic of which is shown in figure 3.4(a). Briefly, the well of a 96-well plate is coated with a *capture antibody*, specific to the antigen of interest. To prevent non-specific binding, a solution called a *blocking buffer* is added that contains a non-reacting protein to coat any areas of the surface not covered by the capture antibody. The solution containing the antigen is then added to the well and allowed to interact with the capture antibody. Any unbound antigen is then removed by the addition of a *wash buffer*. A solution of an enzyme-linked *detection antibody*, specific to the antigen, but different from the capture antibody, is then added to the well, attaching to the antigen from the top, "sandwiching" the antigen between the two antibodies. The well is then washed again to removed any excess secondary antibody. A chemical substrate is then added, which reacts with the enzyme producing a colour change in the liquid. An ELISA plate reader is then used to measure the absorbance of a particular wavelength of light through the liquid. The absorbance of the solution is related to the concentration of the secondary antibody, which is directly related to the concentration of the antigen. A quantitative result can be determined by comparing the measured absorbance to a standard curve that states the measured absorbance of wells containing a known antigen concentration.

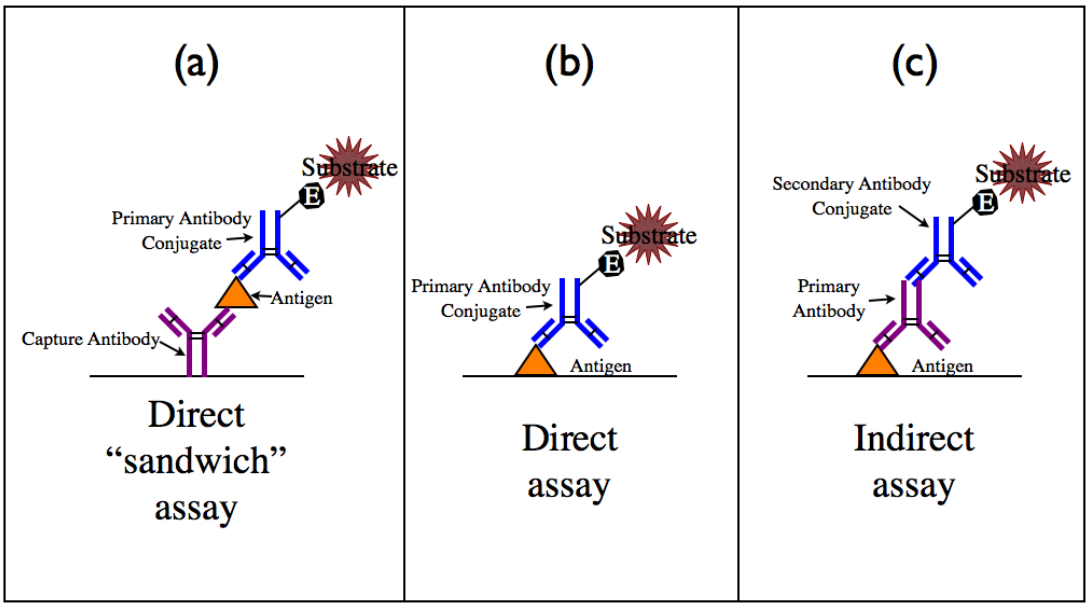

Figure 3.4: Schematic diagrams of a (a) "Direct" Sandwich ELISA, (b) "Direct" ELISA and (c) an "Indirect" ELISA.

A standard "direct" ELISA is also used in this work, which is very similar to the

sandwich ELISA described previously, but is used to detect an antigen directly coated on a surface, as shown in figure 3.4(b). A variation of the standard direct ELISA, called an "indirect" ELISA, is shown in figure 3.4(c), in which the detection antibody is not linked to an enzyme, and the addition of an enzyme-linked secondary antibody specific to the detection antibody needs to be included.

3.5.3 ELISA of Irradiated Streptavidin

Both standard direct and direct sandwich ELISAs for the irradiated streptavidin were performed at $\sim$ 2 hours and $\sim$ 30 hours post-irradiation, and two separate sets of irradiations were performed, referred to as "Experiment#1" and "Experiment#2". The same basic procedure was followed for the indirect and direct ELISAs each time, and the procedure is described below.

Standard Direct ELISA

To begin, 100μL of each 5μg/mL streptavidin sample was added to the wells of a Maxisorp$^{\text{TM}}$96 well plate (Sigma Aldrich, Saint Louis, MO, USA) according to the schematics shown in figures 3.1. The 96-well plate was then covered in plastic wrap and incubated at 37^{o}C for 60 minutes. Following incubation the streptavidin solution was removed from the wells and 200μL of PBS with 0.1% Tween20$^{\circledR}$and 1% BSA (referred to as *blocking buffer*) was added to each well. The plate was once again covered in plastic wrap and incubated at 37^{o}C for 60 minutes. The blocking buffer was then removed and the wells were washed 6 times with PBS with 0.1% Tween20$^{\circledR}$(referred to as *wash buffer*). Each well was then filled with 100 μL of a 100 ng/mL solution of anti-streptavidin horseradish peroxidase (HRP) conjugate (referred to as the *detection antibody*) diluted in blocking buffer. The plate was then covered with plastic wrap and incubated at room temperature for 60 minutes, followed by six washes with wash buffer. Finally, 100μL of Promega TMB One Solution (referred to as the *substrate*) was added to each well, and the plate was covered with aluminum foil.

After allowing the substrate to interact with the enzyme for $\sim$ 20 minutes, it was then possible to read the absorbance of the wells using an ELISA plate reader (Skanstacker 300; Molecular Devices, Sunnyvale, CA) at a wavelength of 600 nm. The absorbance values of duplicate wells were averaged and the results were plotted using Matlab (Mathworks, Inc., Massachussetts, USA).

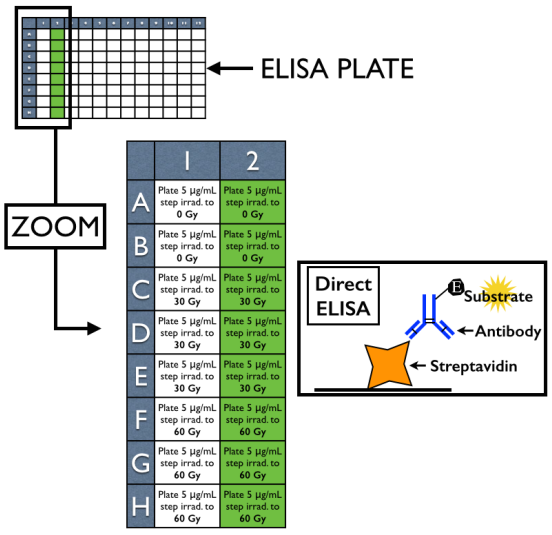

	1	2
A	Plate 5 µg/mL step irrad. to 0 Gy	Plate 5 µg/mL step irrad. to 0 Gy
B	Plate 5 µg/mL step irrad. to 0 Gy	Plate 5 µg/mL step irrad. to 0 Gy
C	Plate 5 µg/mL step irrad. to 30 Gy	Plate 5 µg/mL step irrad. to 30 Gy
D	Plate 5 µg/mL step irrad. to 30 Gy	Plate 5 µg/mL step irrad. to 30 Gy
E	Plate 5 µg/mL step irrad. to 30 Gy	Plate 5 µg/mL step irrad. to 30 Gy
F	Plate 5 µg/mL step irrad. to 60 Gy	Plate 5 µg/mL step irrad. to 60 Gy
G	Plate 5 µg/mL step irrad. to 60 Gy	Plate 5 µg/mL step irrad. to 60 Gy
H	Plate 5 µg/mL step irrad. to 60 Gy	Plate 5 µg/mL step irrad. to 60 Gy

(a)

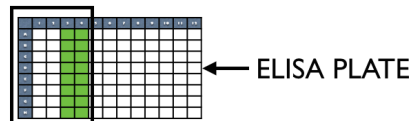

	1	2	3	4
A	Plate 5 µg/mL step irrad. to 0 Gy	Plate 5 µg/mL step irrad. to 0 Gy	Plate 5 µg/mL step irrad. to 0 Gy	Plate 5 µg/mL step irrad. to 0 Gy
B	Plate 5 µg/mL step irrad. to 0 Gy	Plate 5 µg/mL step irrad. to 0 Gy	Plate 5 µg/mL step irrad. to 0 Gy	Plate 5 µg/mL step irrad. to 0 Gy
C	Plate 5 µg/mL step irrad. to 30 Gy	Plate 5 µg/mL step irrad. to 30 Gy	Plate 5 µg/mL step irrad. to 30 Gy	Plate 5 µg/mL step irrad. to 30 Gy
D	Plate 5 µg/mL step irrad. to 30 Gy	Plate 5 µg/mL step irrad. to 30 Gy	Plate 5 µg/mL step irrad. to 30 Gy	Plate 5 µg/mL step irrad. to 30 Gy
E	Plate 5 µg/mL step irrad. to 30 Gy	Plate 5 µg/mL step irrad. to 30 Gy	Plate 5 µg/mL step irrad. to 30 Gy	Plate 5 µg/mL step irrad. to 30 Gy
F	Plate 5 µg/mL step irrad. to 60 Gy	Plate 5 µg/mL step irrad. to 60 Gy	Plate 5 µg/mL step irrad. to 60 Gy	Plate 5 µg/mL step irrad. to 60 Gy
G	Plate 5 µg/mL step irrad. to 60 Gy	Plate 5 µg/mL step irrad. to 60 Gy	Plate 5 µg/mL step irrad. to 60 Gy	Plate 5 µg/mL step irrad. to 60 Gy
H	Plate 5 µg/mL step irrad. to 60 Gy	Plate 5 µg/mL step irrad. to 60 Gy	Plate 5 µg/mL step irrad. to 60 Gy	Plate 5 µg/mL step irrad. to 60 Gy

(b)

	1	2	3	4	5	6
A	Plate 5 µg/mL step irrad. to 0 Gy	Plate 5 µg/mL step irrad. to 0 Gy	Plate 5 µg/mL step irrad. to 0 Gy	Plate 5 µg/mL step irrad. to 0 Gy	Plate 5 µg/mL step irrad. to 0 Gy	Plate 5 µg/mL step irrad. to 0 Gy
B	Plate 5 µg/mL step irrad. to 5 Gy	Plate 5 µg/mL step irrad. to 5 Gy	Plate 5 µg/mL step irrad. to 5 Gy	Plate 5 µg/mL step irrad. to 5 Gy	Plate 5 µg/mL step irrad. to 0 Gy	Plate 5 µg/mL step irrad. to 0 Gy
C	Plate 5 µg/mL step irrad. to 10 Gy	Plate 5 µg/mL step irrad. to 10 Gy	Plate 5 µg/mL step irrad. to 10 Gy	Plate 5 µg/mL step irrad. to 10 Gy	Plate 5 µg/mL step irrad. to 60 Gy	Plate 5 µg/mL step irrad. to 60 Gy
D	Plate 5 µg/mL step irrad. to 20 Gy	Plate 5 µg/mL step irrad. to 20 Gy	Plate 5 µg/mL step irrad. to 20 Gy	Plate 5 µg/mL step irrad. to 20 Gy	Plate 5 µg/mL step irrad. to 60 Gy	Plate 5 µg/mL step irrad. to 60 Gy
E	Plate 5 µg/mL step irrad. to 40 Gy	Plate 5 µg/mL step irrad. to 40 Gy	Plate 5 µg/mL step irrad. to 40 Gy	Plate 5 µg/mL step irrad. to 40 Gy	Plate 5 µg/mL step irrad. to 120 Gy	Plate 5 µg/mL step irrad. to 120 Gy
F	Plate 5 µg/mL step irrad. to 60 Gy	Plate 5 µg/mL step irrad. to 60 Gy	Plate 5 µg/mL step irrad. to 60 Gy	Plate 5 µg/mL step irrad. to 60 Gy	Plate 5 µg/mL step irrad. to 120 Gy	Plate 5 µg/mL step irrad. to 120 Gy
G	Plate 5 µg/mL step irrad. to 80 Gy	Plate 5 µg/mL step irrad. to 80 Gy	Plate 5 µg/mL step irrad. to 80 Gy	Plate 5 µg/mL step irrad. to 80 Gy	Plate 5 µg/mL step irrad. to 240 Gy	Plate 5 µg/mL step irrad. to 240 Gy
H	Plate 5 µg/mL step irrad. to 120 Gy	Plate 5 µg/mL step irrad. to 120 Gy	Plate 5 µg/mL step irrad. to 120 Gy	Plate 5 µg/mL step irrad. to 120 Gy	Plate 5 µg/mL step irrad. to 240 Gy	Plate 5 µg/mL step irrad. to 240 Gy

(c)

Table 3.1: Schematic of the ELISA plate for the Direct ELISA done (a) 2hrs and (b) 30hrs post-irradiation in experiment#1 and (c) 2 and 30hrs post-irradiation for experiment#2. White wells contained streptavidin dissolved in PBS (type A), and green wells contained streptavidin dissolved in PBS w/ 3.5% PBS (type B).

Direct Sandwich ELISA

For the sandwich ELISA, pre-blocked Pierce Biotin Coated Clear 8-well Strip Plates (Thermo Scientific, Ottawa, ON) were used. To begin, each well was washed 3 times with wash buffer, followed by the addition of streptavidin samples. In order to generate a standard curve consisting of the absorbance due to known concentrations of streptavidin, serial dilutions of unirradiated streptavidin in wash buffer were added to the wells (100μL per well), as indicated by the schematics in figures 3.2 and 3.3 (ie. column 1 and 4 of figure 3.3). Also, streptavidin samples corresponding to each of the doses were diluted to 0.005 μg/mL in wash buffer and added to the plate (100μL per well) according to the schematics of figures 3.2 and 3.3 (ie. the type A samples in columns 2-3, and type B samples in columns 5-6 of figure 3.2). The plate was then covered in plastic wrap and incubated for 60 minutes. Following incubation, each well was washed 6 times with wash buffer, and 100 μL of detection antibody at a concentration of 100 ng/mL in blocking buffer was added to each well. After covering the plate in plastic wrap, it was then incubated with the detection antibody for 60 minutes at room temperature. The wells were then washed 6 times with wash buffer, followed by the addition of 100 μL of substrate to each well. The plate was covered with aluminum foil and allowed to develop for $\sim$ 20 minutes.

The absorbance of the wells was then read with the ELISA plate reader at a wavelength of 600 nm. As with the results of the standard direct ELISA, the absorbance of duplicate wells was averaged and the results were plotted using Matlab. A standard curve of the absorbance of serial dilutions of unirradiated streptavidin was generated, and a linear fit to the data was calculated. According to the linear relationship, the absorbance values of both the indirect and sandwich ELISAs could then be converted to streptavidin concentrations.

ZOOM

	1	2	3	4	5	6
A	0.005 µg/mL strep. **0 Gy**	Control No strep.	Control No strep.	0.005 µg/mL strep. **0 Gy**	Control No strep.	Control No strep.
B	0.005 µg/mL strep. **0 Gy**	0.001 µg/mL strep.	0.001 µg/mL strep.	0.005 µg/mL strep. **0 Gy**	0.001 µg/mL strep.	0.001 µg/mL strep.
C	0.005 µg/mL strep. **30 Gy**	0.0025 µg/mL strep.	0.0025 µg/mL strep.	0.005 µg/mL strep. **30 Gy**	0.0025 µg/mL strep.	0.0025 µg/mL strep.
D	0.005 µg/mL strep. **30 Gy**	0.005 µg/mL strep.	0.005 µg/mL strep.	0.005 µg/mL strep. **30 Gy**	0.005 µg/mL strep.	0.005 µg/mL strep.
E	0.005 µg/mL strep. **30 Gy**	0.0075 µg/mL strep.	0.0075 µg/mL strep.	0.005 µg/mL strep. **30 Gy**	0.0075 µg/mL strep.	0.0075 µg/mL strep.
F	0.005 µg/mL strep. **60 Gy**	0.01 µg/mL strep.	0.01 µg/mL strep.	0.005 µg/mL strep. **60 Gy**	0.01 µg/mL strep.	0.01 µg/mL strep.
G	0.005 µg/mL strep. **60 Gy**	0.0125 µg/mL strep.	0.0125 µg/mL strep.	0.005 µg/mL strep. **60 Gy**	0.0125 µg/mL strep.	0.0125 µg/mL strep.
H	0.005 µg/mL strep. **60 Gy**	0.015 µg/mL strep.	0.015 µg/mL strep.	0.005 µg/mL strep. **60 Gy**	0.015 µg/mL strep.	0.015 µg/mL strep.

Table 3.2: Schematic of the ELISA plate for the Sandwich ELISA for experiment#1 done 2 and 30 hrs post-irradiation. White wells contained streptavidin dissolved in PBS (type A), and green wells contained streptavidin dissolved in PBS w/ 3.5% BSA (type B).

ZOOM

	1	2	3	4	5	6	7	8	9	10
A	0.005 µg/mL strep. 0 Gy	0.005 µg/mL strep. 0 Gy	0.005 µg/mL strep. 0 Gy	0.005 µg/mL strep. 0 Gy	Control No strep.	Control No strep.	0.005 µg/mL strep. 0 Gy	0.005 µg/mL strep. 0 Gy	Control No strep.	Control No strep.
B	0.005 µg/mL strep. 5 Gy	0.005 µg/mL strep. 5 Gy	0.005 µg/mL strep. 5 Gy	0.005 µg/mL strep. 5 Gy	0.001 µg/mL strep.	0.001 µg/mL strep.	0.005 µg/mL strep. 0 Gy	0.005 µg/mL strep. 0 Gy	0.001 µg/mL strep.	0.001 µg/mL strep.
C	0.005 µg/mL strep. 10 Gy	0.005 µg/mL strep. 10 Gy	0.005 µg/mL strep. 10 Gy	0.005 µg/mL strep. 10 Gy	0.0025 µg/mL strep.	0.0025 µg/mL strep.	0.005 µg/mL strep. 60 Gy	0.005 µg/mL strep. 60 Gy	0.0025 µg/mL strep.	0.0025 µg/mL strep.
D	0.005 µg/mL strep. 20 Gy	0.005 µg/mL strep. 20 Gy	0.005 µg/mL strep. 20 Gy	0.005 µg/mL strep. 20 Gy	0.005 µg/mL strep.	0.005 µg/mL strep.	0.005 µg/mL strep. 60 Gy	0.005 µg/mL strep. 60 Gy	0.005 µg/mL strep.	0.005 µg/mL strep.
E	0.005 µg/mL strep. 40 Gy	0.005 µg/mL strep. 40 Gy	0.005 µg/mL strep. 40 Gy	0.005 µg/mL strep. 40 Gy	0.0075 µg/mL strep.	0.0075 µg/mL strep.	0.005 µg/mL strep. 120 Gy	0.005 µg/mL strep. 120 Gy	0.0075 µg/mL strep.	0.0075 µg/mL strep.
F	0.005 µg/mL strep. 60 Gy	0.005 µg/mL strep. 60 Gy	0.005 µg/mL strep. 60 Gy	0.005 µg/mL strep. 60 Gy	0.01 µg/mL strep.	0.01 µg/mL strep.	0.005 µg/mL strep. 120 Gy	0.005 µg/mL strep. 120 Gy	0.01 µg/mL strep.	0.01 µg/mL strep.
G	0.005 µg/mL strep. 80 Gy	0.005 µg/mL strep. 80 Gy	0.005 µg/mL strep. 80 Gy	0.005 µg/mL strep. 80 Gy	0.0125 µg/mL strep.	0.0125 µg/mL strep.	0.005 µg/mL strep. 240 Gy	0.005 µg/mL strep. 240 Gy	0.0125 µg/mL strep.	0.0125 µg/mL strep.
H	0.005 µg/mL strep. 120 Gy	0.005 µg/mL strep. 120 Gy	0.005 µg/mL strep. 120 Gy	0.005 µg/mL strep. 120 Gy	0.015 µg/mL strep.	0.015 µg/mL strep.	0.005 µg/mL strep. 240 Gy	0.005 µg/mL strep. 240 Gy	0.015 µg/mL strep.	0.015 µg/mL strep.

(a)

	1	2	3	4	5	6	7	8	9	10	11	12
A	0.005 µg/mL strep. 0 Gy	0.005 µg/mL strep. 0 Gy	0.005 µg/mL strep. 0 Gy	0.005 µg/mL strep. 0 Gy	Control No strep.	Control No strep.	Control No strep.	0.005 µg/mL strep. 0 Gy	0.005 µg/mL strep. 0 Gy	Control No strep.	Control No strep.	Control No strep.
B	0.005 µg/mL strep. 5 Gy	0.005 µg/mL strep. 5 Gy	0.005 µg/mL strep. 5 Gy	0.005 µg/mL strep. 5 Gy	0.001 µg/mL strep.	0.001 µg/mL strep.	0.001 µg/mL strep.	0.005 µg/mL strep. 0 Gy	0.005 µg/mL strep. 0 Gy	0.001 µg/mL strep.	0.001 µg/mL strep.	0.001 µg/mL strep.
C	0.005 µg/mL strep. 10 Gy	0.005 µg/mL strep. 10 Gy	0.005 µg/mL strep. 10 Gy	0.005 µg/mL strep. 10 Gy	0.0025 µg/mL strep.	0.0025 µg/mL strep.	0.0025 µg/mL strep.	0.005 µg/mL strep. 60 Gy	0.005 µg/mL strep. 60 Gy	0.0025 µg/mL strep.	0.0025 µg/mL strep.	0.0025 µg/mL strep.
D	0.005 µg/mL strep. 20 Gy	0.005 µg/mL strep. 20 Gy	0.005 µg/mL strep. 20 Gy	0.005 µg/mL strep. 20 Gy	0.005 µg/mL strep.	0.005 µg/mL strep.	0.005 µg/mL strep.	0.005 µg/mL strep. 60 Gy	0.005 µg/mL strep. 60 Gy	0.005 µg/mL strep.	0.005 µg/mL strep.	0.005 µg/mL strep.
E	0.005 µg/mL strep. 40 Gy	0.005 µg/mL strep. 40 Gy	0.005 µg/mL strep. 40 Gy	0.005 µg/mL strep. 40 Gy	0.0075 µg/mL strep.	0.0075 µg/mL strep.	0.0075 µg/mL strep.	0.005 µg/mL strep. 120 Gy	0.005 µg/mL strep. 120 Gy	0.0075 µg/mL strep.	0.0075 µg/mL strep.	0.0075 µg/mL strep.
F	0.005 µg/mL strep. 60 Gy	0.005 µg/mL strep. 60 Gy	0.005 µg/mL strep. 60 Gy	0.005 µg/mL strep. 60 Gy	0.01 µg/mL strep.	0.01 µg/mL strep.	0.01 µg/mL strep.	0.005 µg/mL strep. 120 Gy	0.005 µg/mL strep. 120 Gy	0.01 µg/mL strep.	0.01 µg/mL strep.	0.01 µg/mL strep.
G	0.005 µg/mL strep. 80 Gy	0.005 µg/mL strep. 80 Gy	0.005 µg/mL strep. 80 Gy	0.005 µg/mL strep. 80 Gy	0.0125 µg/mL strep.	0.0125 µg/mL strep.	0.0125 µg/mL strep.	0.005 µg/mL strep. 240 Gy	0.005 µg/mL strep. 240 Gy	0.0125 µg/mL strep.	0.0125 µg/mL strep.	0.0125 µg/mL strep.
H	0.005 µg/mL strep. 120 Gy	0.005 µg/mL strep. 120 Gy	0.005 µg/mL strep. 120 Gy	0.005 µg/mL strep. 120 Gy	0.015 µg/mL strep.	0.015 µg/mL strep.	0.015 µg/mL strep.	0.005 µg/mL strep. 240 Gy	0.005 µg/mL strep. 240 Gy	0.015 µg/mL strep.	0.015 µg/mL strep.	0.015 µg/mL strep.

(b)

Table 3.3: Schematic of the ELISA plate for the Sandwich ELISA for experiment#2 done (a) 2hrs; and (b) 30 hrs post-irradiation. White wells contained streptavidin dissolved in PBS (type A), and green wells contained streptavidin dissolved in PBS w/ 3.5% PBS (type B).

3.6 Data Analysis and Statistical Approach for the Biotinylated Gold Slide Samples

This section describes the data analysis and statistical techniques used on SEM images and SERS maps of the biotinylated gold slide samples incubated with Type II SERS probes for four different time points. The samples were described in section 3.3.1, and the imaging of the samples was described in sections 3.4.3 and 3.4.4. Using the SEM images and SERS data, a statistical protocol was developed to evaluate the SERS probe and SERS intensity distributions on the slides, and to determine a relationship between the SERS probe cluster size and the SERS intensity of scatter from the cluster. All analysis was performed with Matlab (Matlab, Mathworks, Inc., Massachussets, USA). As a reference, figure 3.5 provides a schematic overview of the experiment and statistical approach used in the analysis of the SERS and SEM data.

Section 3.4.4 explains how SERS probe clusters on the biotinylated gold slides were identified and categorized through the analysis of SEM images. The number of SERS probes in each detected cluster was determined according to the technique described in section 3.6.2. Further analysis of the SEM images described in section 3.6.3 determined a statistical representation of the number of SERS probes excited by the laser spot in a given spectral acquisition. Finally, the development of a system of equations relating the SERS probe cluster size to the measured SERS intensity is explained in section 3.6.4

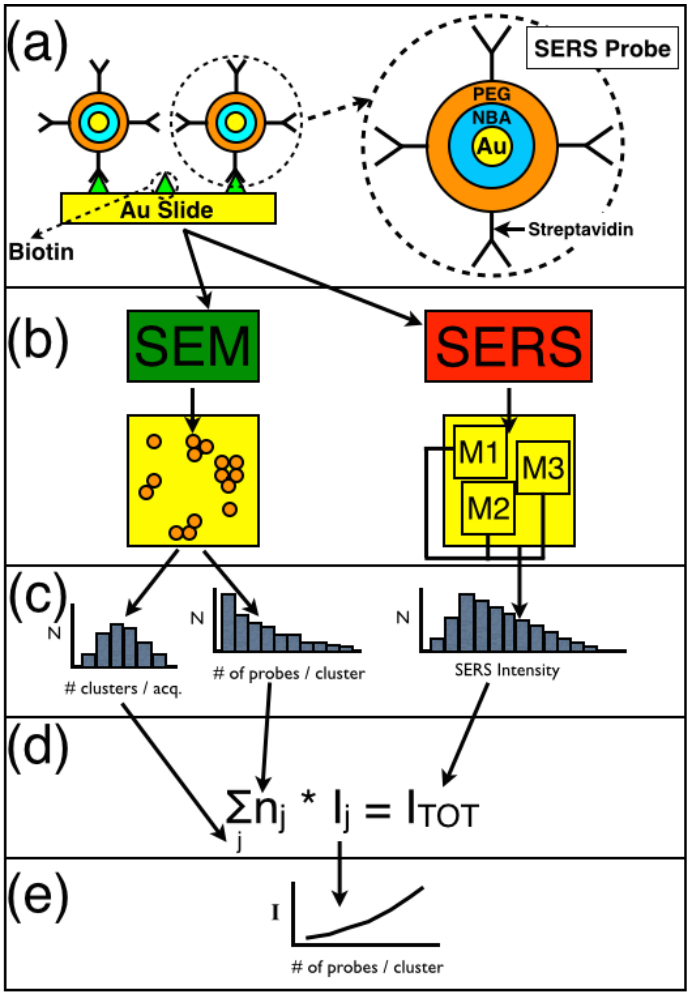

Figure 3.5: Process outline showing the (a) SERS probes bound to the surface; (b) SEM and SERS data acquisition (M1 = Map 1, etc.); (c) statistical distributions generated from the SERS and SEM data; (d) general equation for the total SERS intensity, generated using the distributions from (c); (e) relationship between SERS intensity and SERS probe cluster size.

3.6.1 Detection and Analysis of SERS Probe Clusters in SEM images

In order to identify the nanoparticle clusters in the SEM data, each image was first processed with a 20x20 pixel^2 standard deviation filter (figure 3.6(b)). All pixels above a threshold equal to twice the mode intensity were then set to 1, while the rest were set to 0, creating a binary image (figure 3.6(c)). The threshold was empirically chosen such that only high intensities corresponding to the nanoparticles would remain. Groups of connected non-zero pixels in the binary image were identified by Matlab and the number of pixels in each group, or "pixel area" was recorded (figure 3.6(d)). The identified groups corresponded to individual clusters of SERS probes.

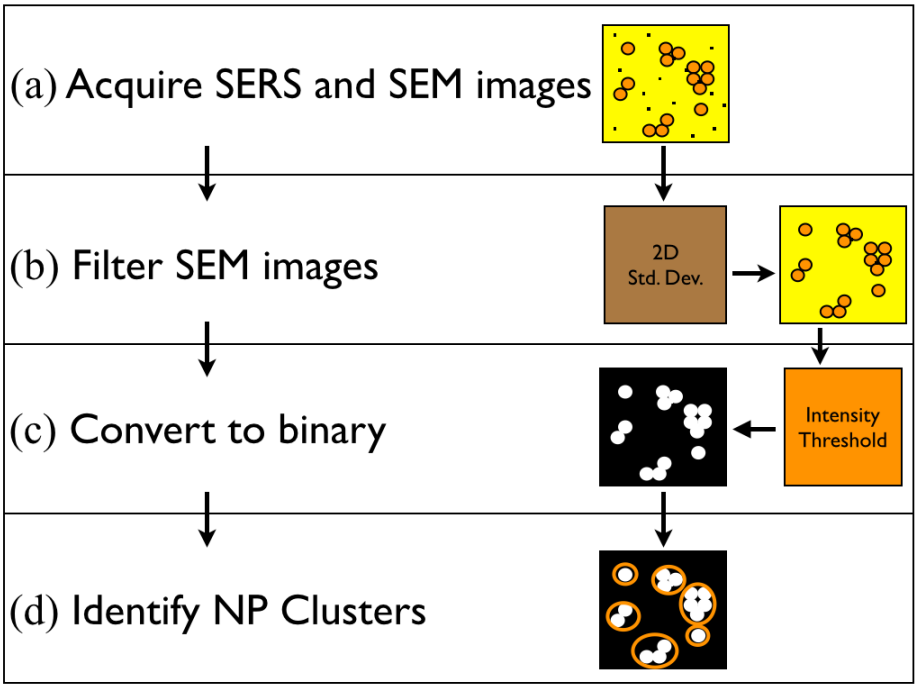

Figure 3.6: Flow chart showing the processing of SEM images, from acquisition to cluster identification.

3.6.2 Conversion of Cluster Area from Pixels to # of SERS probes

To determine the number of SERS probes contained in the identified clusters, the number of pixels in a single probe had to be calculated. Due to their intrinsic size

variation, the size of a single probe was represented statistically. All SERS probe clusters consisting of only one probe were identified (figure 3.7(a)), and a histogram of the pixel area of each of these regions was generated, and fit with a Gaussian curve (figure 3.7(b)). The Gaussian fit was then sampled according to a random number generator developed in Matlab, and each sampled value corresponded to a pixel area for a single SERS probe ($PA_1|_i$ in figure 3.7(c)). The pixel area of each cluster detected in the SEM images (^kPA in figure 3.7(d)) was then divided by the sampled single probe pixel area, and the resultant number of SERS probes in each cluster was recorded ($^kSPC|_i$ in figure 3.7(d)). The Gaussian was sampled a total of 1000 times, and each time all pixel areas were divided by the newly sampled single probe pixel area, generating a new set of values of the number of probes in each cluster (figure 3.7(e)). From the results of the 1000 trials, the average number of probes in each identified cluster was calculated (figure 3.7(f)), and a histogram of the number of probes per cluster was generated (as indicated in figure 3.5(c).

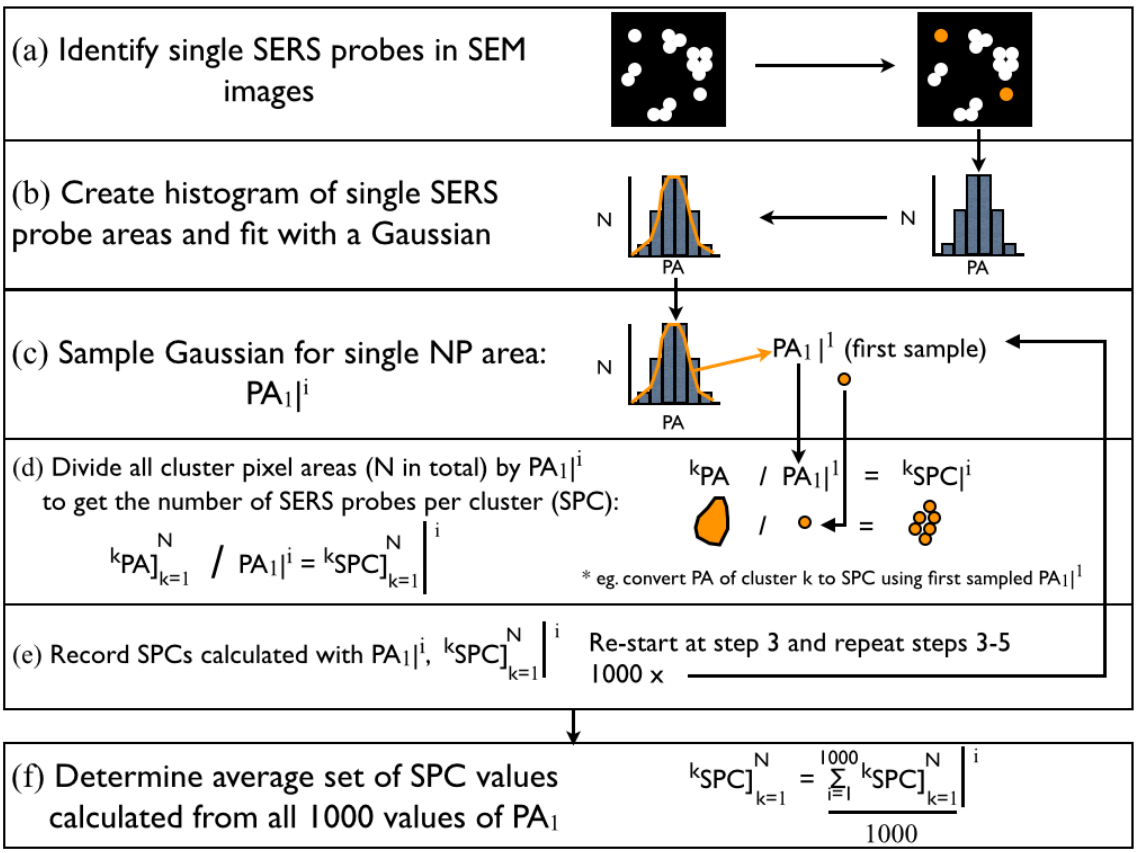

Figure 3.7: Chart demonstrating the determination of the number of SERS probes in each identified cluster.

3.6.3 Determining the # of SERS probes under the laser spot

In order to statistically represent the number of SERS probes excited by the laser spot during each spectral acquisition, all of the binary SEM images were divided into 1μm x 1μm grids, with each grid point approximating the size of the laser spot (figure 3.8(a)). The number of clusters in each square was counted, according to position of the cluster centroid (figure 3.8(b)). After pooling the results from each SEM image for a given slide, a histogram of the cluster count under the laser spot per acquisition was generated (figure 3.8(c)).

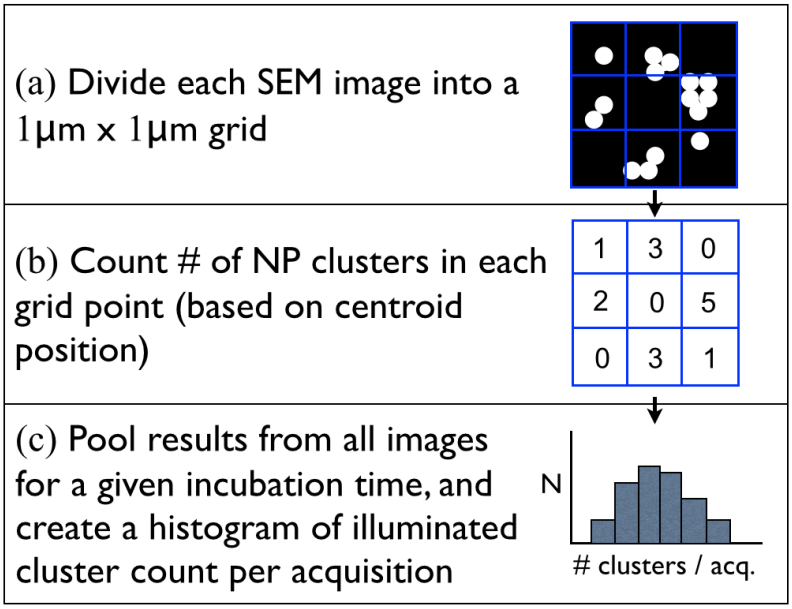

Figure 3.8: Chart demonstrating the creation of the histogram for the illuminated cluster count per acquisition.

3.6.4 Expressing SERS intensity in equation form

Following the analysis of the SEM images, it was now possible to generate a series of equations relating the measured SERS intensity at a given point on the slide to the SERS probe clusters contributing to the signal. Assuming that there are n_j clusters containing j SERS probes illuminated by the laser spot, then the total SERS intensity at a pixel can be described as follows:

$$\sum_{j} n_j * I_j = I_{TOT} \tag{3.1}$$

where the sum is over the series of integers, j, that represent the size (in SERS probes) of each of the clusters contributing to the total intensity. For a given incubation time, using the SERS intensity histogram and the distributions described in the preceding sections (see figure 3.5(c)), a series of equations in the form of equation 3.1 was generated as is suggested in figure 3.5(d).

To begin, a value for I_{TOT} was sampled from the histogram of total SERS intensities (figure 3.9(a)). The number of clusters (N_{clust}) that produced I_{TOT} was then statistically determined by sampling the histogram of illuminated cluster count per acquisition (figure 3.9(b)), setting the number of terms in the equation. The size of each cluster was then determined by sampling the histogram of cluster sizes, providing the set of integers, j (figure 3.9(c)). The SERS intensities, I_j, produced by each cluster were left as unknowns (figure 3.9(d)). To solve for the unknowns, it was necessary to generate a linearly independent set of m equations, where m represents the largest cluster size present after the given incubation time (3.9(e)). With a maximum cluster size of m SERS probes, then all intensities, I_j, could be determined by solving the m x m system of equations. When solving the system, only unique, non-zero, monotonically increasing solutions were accepted, otherwise a new system of equations was generated.

Results of the analysis of the SERS and SEM data acquired from the biotinylated slides corresponding to each of the SERS probe incubation times are presented in Chapter 5. Also, the results for each incubation time are combined and a final relationship between cluster size and measured SERS intensity is calculated and discussed.

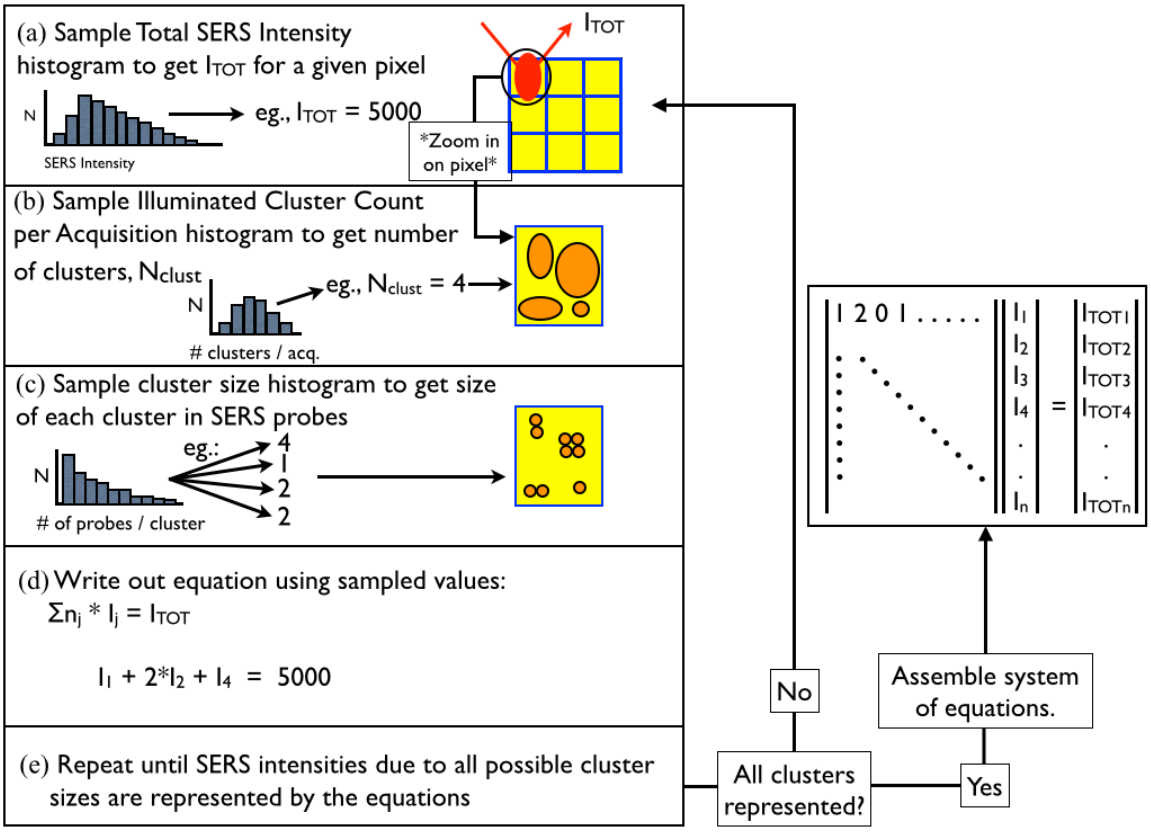

Figure 3.9: Chart showing the construction of the system of equations used to solve for the SERS intensities due to the various SERS probe cluster sizes.

Chapter 4

Results and Discussion I: SERS of Tumour Cells

This chapter presents the results of experiments performed regarding the development of SERS probes labelled for proteins in tumour cells. The SERS probes were intended to be used to monitor ionizing radiation-induced damage to the cells. Prior to the development of labelled SERS probes, initial studies investigated the standard Raman spectrum of a tumour cell, followed by the acquisition of SERS spectra from cells incubated with unmodified gold nanoparticles. Targeted Type-I SERS probes were then manufactured (section 3.1.2), initially conjugated with an antibody for the TACSTD2 protein (developed at the DRC) of CaOV3 cells. SERS maps of CaOV3 cells provided minimal signal from the probes, leading to the development of SERS probes targeted to the protein biotin, which was artificially coated on the surface of OVCAR5 cells (section 3.2.3). Such probes were conjugated to streptavidin, and were initially of the Type-I variety, later changing to Type-II probes (section 3.1.3). Low signal from the probes persisted, and a thorough investigation of the Type-II probes was performed (section 3.1.4), considering the manufacturing process of the probes, and the ability of the probes to attach to the protein biotin. Despite a reproducible manufacturing technique, and demonstrated probe functionality, the probes continued to provide poor results when incubated with biotinylated OVCAR5 cells.

4.1 Results

4.1.1 Raman and SERS spectroscopy of DU145 Tumour Cells

Before beginning analysis of SERS data, it was important to have an understanding of the standard Raman spectrum of a cell. Figure 4.1(a) shows the Raman spectrum of a DU145 prostate cell obtained by the Raman microscope using a 633nm laser at 100% power through the 100x objective with a 20s acquisition time. Despite a relatively short acquisition time, the result agrees well with the known Raman spectrum of DU145 [250]. The most well defined peaks in the spectrum of figure 4.1(a) are at 1003cm^{-1} and 1450cm^{-1}. At 1003cm^{-1}, the peak corresponds to the symmetric ring breathing mode of phenylalanine, one of the amino acids [131, 250], while the peak at 1450cm^{-1} is actually composed of several overlapping peaks, namely the peaks at 1438, 1450 and 1460 cm^{-1}. The peak at 1438 cm^{-1} corresponds to a CH_2 deformation mode in lipids, and the peaks at 1450 and 1460 cm^{-1} both correspond to a CH deformation mode found in proteins and lipids [131, 250].

In order to illustrate the information provided by a standard Raman map of a cell, figure 4.1(b) shows a map of the peak intensity at 1003 cm^{-1} throughout the cell, and figure 4.1(c) shows a map of the intensity at 1450 cm^{-1}. Map data was obtained with a 633nm laser at 100% power through the 100x objective on a 1μm x 1μm mapping grid and 20s per acquisition. In both figures 4.1(b) and (c) the outline of the cell is visible, but in figure 4.1(b) high intensities are spread relatively uniformly throughout the cell, while in figure 4.1(c), the high intensities are concentrated in the upper portion of the cell. The difference between the two maps is due to the fact that phenylalanine (represented by the 1003 cm^{-1} peak) and other amino acids are spread throughout the cytoplasm of the cell, while proteins and lipids (represented by the 1450 cm^{-1} peak) are particularly highly concentrated in the nucleus of the cell, indicated by the high intensity region of figure 4.1(c).

Following investigation of the Raman spectrum of the DU145 cells, initial SERS studies began of cells incubated with gold nanoparticles. As described in section 3.2.4 two different incubation techniques were used, according to the work of Kneipp *et al.* [155] and Tang *et al.* [158]. The first technique (described by Kneipp *et al.* [155]) involved a 30 minute incubation in live cells of a 4 x 10^{-12}M concentration of 13nm gold NPs in cell growth media. Following the incubation (referred to as an NP pulse),

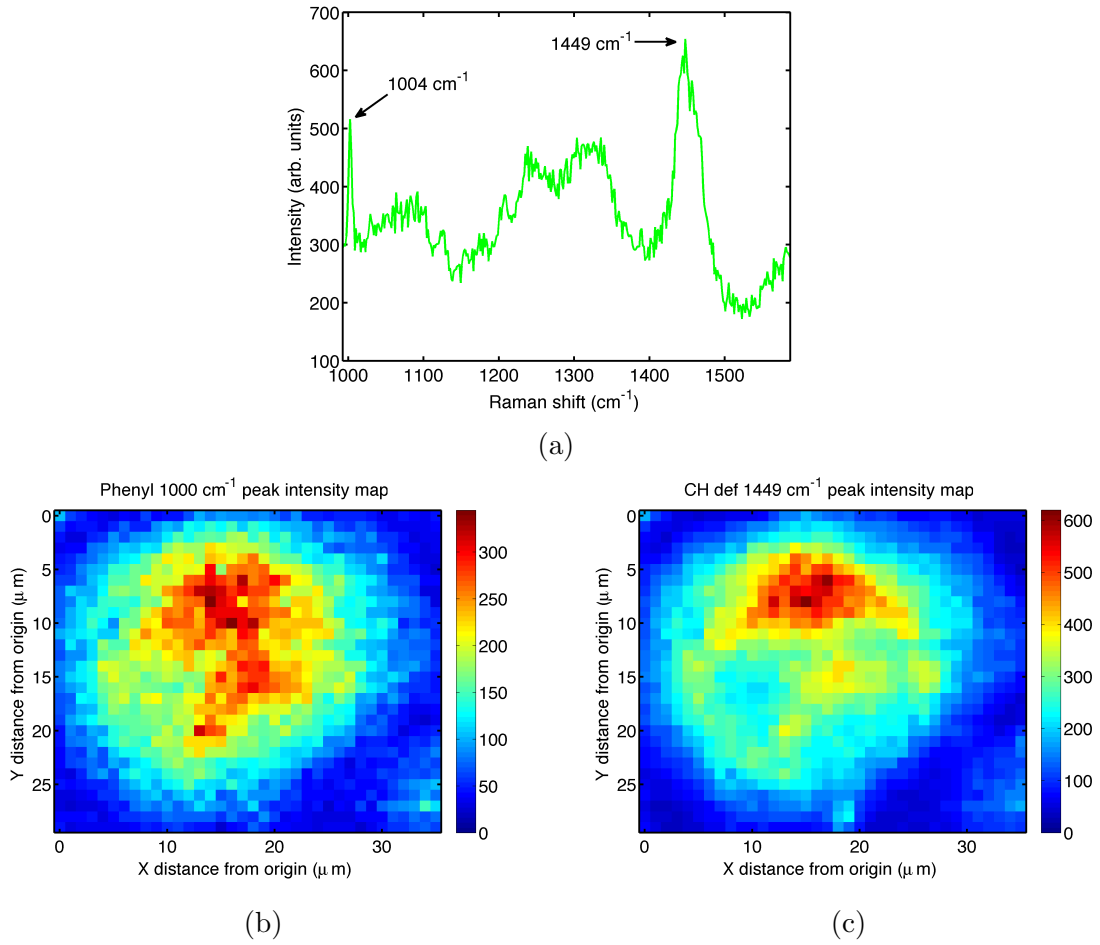

Figure 4.1: (a) Sample Raman spectrum of the DU145 cell, obtained using a 633 nm laser at 100% power through the 100x objective with a 20s acquisition time. (b) Intensity map of the 1004 cm^{-1} peak. (c) Intensity map of the 1449 cm^{-1} peak. Map grid is 1μm x 1μm.

the cells continued to grow for various times before fixation and imaging (0hrs, 2hrs and 24hrs post NP incubation). For the technique based on the work of Tang *et al.* [158], different volumes of an undiluted 20nm NP solution were added directly to the cell culture media covering four separate quartz discs coated with live DU145 cells. All of the discs were then incubated with the NPs for 24 hours prior to fixation and imaging.

Upon SERS mapping of the samples using the first technique, very few SERS spectra were identified, with a significant amount of signal only observed in the cells allowed to grow for 24 hours post-incubation. In the work of Kneipp *et al.* [155], multiple SERS spectra were present in maps of cells imaged immediately after the

NP-incubation, with maximum intensities observed 1.5 hours post-incubation. The reason for the difference between our results and those of Kneipp *et al.* is unclear, but may be related to the different types of cells used in each study. Kneipp *et al.* worked with immortalized rat renal proximal tubule cells (IRPT) and mouse macrophage J774 cells, and it is highly likely that the rate of the endocytotic uptake of NPs by the aforementioned cells differs from that of the DU145 cells used in the current study.

The low rate of NP uptake alone, however, does not explain why SERS signal was only noticed after 24hrs. Each of the samples was exposed to the NPs for the same amount of time, and cell cycle progression post-NP pulse would not have affected the number of NPs that entered the cell during the pulse. However, in the time after the NP pulse, the cells would have had time to process the NPs and allow them to distribute throughout the cytoplasm. The cells allowed to live for 24hrs after NP-incubation would likely have the most evenly distributed NPs, and therefore Raman imaging is more likely to probe multiple regions containing a NP.

SERS mapping of the samples prepared using the second technique yielded significantly more SERS signal when imaged with the Raman microscope. The increased amount of identifiable SERS signal is likely due to the longer NP incubation time of 24hrs, and higher NP incubation concentration, allowing many more NPs to be taken up by the cells prior to fixation. Unsurprisingly, the cell samples that had the largest volume of NP solution added to their culture media (500μL of NP solution in 4mL of DMEM) exhibited the most SERS spectra when imaged.

Due to the fact that the SERS signal is highly dependent on the biomolecule distribution in the immediate vicinity of the NPs, the identified SERS spectra were highly variable, and it proved difficult to efficiently map the distribution of the enhancement throughout the cells. Despite high spectral variability, the peak located at 1532 cm^{-1} was regularly noticed in spectra acquired from the DU145 cells. The 1532 cm^{-1} peak corresponds to vibrational modes of the nucleic acids adenine, thymine and guanine (A, C, G)[155]. A SERS map of the peak intensity at 1532cm^{-1} for a DU145 cell is shown in figure 4.2(a). To indicate the spectral variability, several sample SERS spectra from the map in figure 4.2 are shown in figures 4.2(b)-(e). The spectrum in figure 4.2(d) shows a strong fluorescence signal that was commonly observed during mapping and was difficult to exclude from peak intensity maps due to the high intensity of the fluorescence at all wavenumbers. The origin of the signal is likely due to biological photodamage caused by the laser, which results in the decrease of most Raman signal (allowing fluorescence to dominate) and an increase in the characteristic

D peak of carbon at $\sim$1360cm^{-1} [257–259].

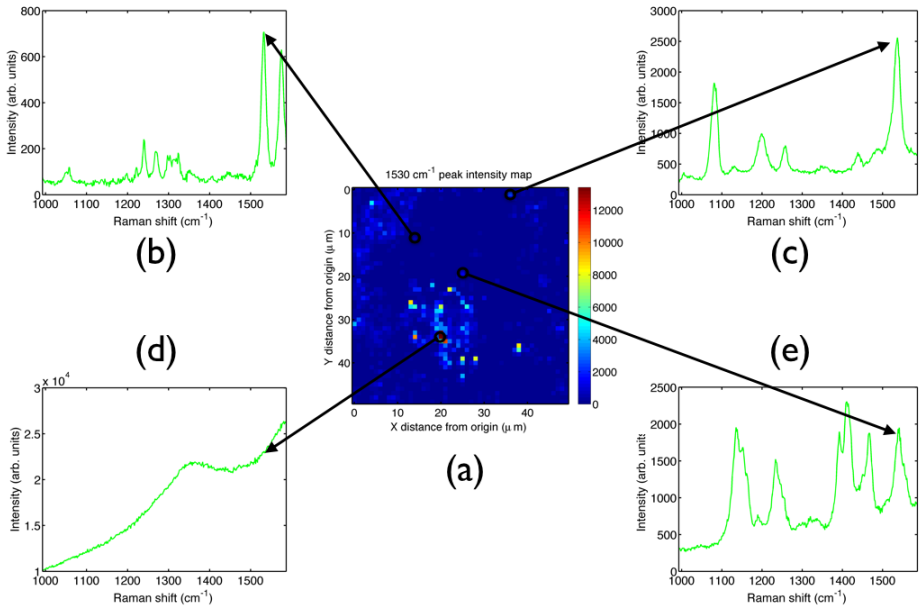

Figure 4.2: (a) Intensity map of the 1532 cm^{-1} peak for a DU145 cell incubated with 20nm gold nanoparticles. (b) - (e) Sample SERS spectra with their locations in the map indicated by arrows. Each spectrum was obtained using a 633 nm laser at 100% power through the 100x objective with a 2 second acquisition time. Map grid is 1μm x 1μm.

Ultimately, the uptake of NPs by the cells, and the presence of measurable SERS signal further demonstrated the promise of SERS mapping of cells incubated with NPs that had been previously established by earlier studies[155, 158]. However, the variability of the SERS signal made it difficult to interpret the information provided, and gave motivation for the development of targeted cellular SERS probes with a definitive Raman signature that would allow for improved visualization of the NP distribution within the cell.

4.1.2 Incubation of Cancer Cells with TACSTD2-targeted Type-I SERS Probes

The first experiments with targeted SERS probes used Type-I probes that were targeted to the TACSTD2 protein on CaOV3 cancer cells. Efforts initially focused on

determining the proper protocol for incubating the probes with the cells. It was possible to add the SERS probes either to the live cells, or to the cells after fixation and/or permeabilization (as described in section 3.2.2). As a first attempt, probes were added to the cell culture before fixation, after fixation, and after fixation and permeabilization of the cell membrane.

SERS maps of live cells incubated with probes before fixation (400 μL probe solution in 4mL of cell culture media) are shown in figure 4.3. The maps were acquired using a point-by-point acquisition with the 633nm laser at 100% power through the 100x objective with 2s/acquistion on a 1μm x 1μm grid. In the maps shown, regions of high peak intensity are sparsely distributed throughout the cell and also appear outside of the cell. The optical images of the mapped regions also show that crystalline structures can be seen irregularly distributed on top of the cells and in the surrounding regions. Most likely these are salt crystals that have condensed out of the buffer within the nanoparticle solution. As can be seen in the lower left corner of the map in figure 4.3(c), it appears that the salt crystals may be non-specific sources of NP signal. To ensure that this signal did not contaminate the samples, the nanoparticle solution was passed through a 0.2 μm filter prior to incubation with the cells for the remainder of the first experiment.

Figure 4.4 shows SERS maps of cells that were incubated with filtered Type-I SERS probes after fixation, and figure 4.5 shows maps of cells incubated with probes after fixation and cell membrane permeabilization. Each sample was incubated with 400μL of probe solution in 4mL of PBS, and the maps were acquired with the same parameters as those of figure 4.3. Due to the filtering of the probes the salt crystals are not present in the images of figure 4.4 and 4.5, however there is also a dramatic reduction in the amount of pixels with signal from the SERS probes. The reduction may be due to the loss of SERS probes in the filtering process, however the 0.2 μm filter should be more than large enough to allow the $\sim$50nm probes to pass through with ease. It is more likely that the maps in figure 4.3 had significant signal from SERS probes that were present on the buffer salt crystals due to non-specific binding. Regardless, very little signal from the SERS probes is identifiable in the maps of figures 4.4 and 4.5.

In order to confirm the results of the first experiment, another six samples were prepared and were all incubated with filtered Type-I SERS probes. In this case, both CaOV3 cells (positive for TACSTD2) and OVCAR5 cells (negative for TACSTD2) were incubated with the probes. Multiple parameters were varied in each of the sam-

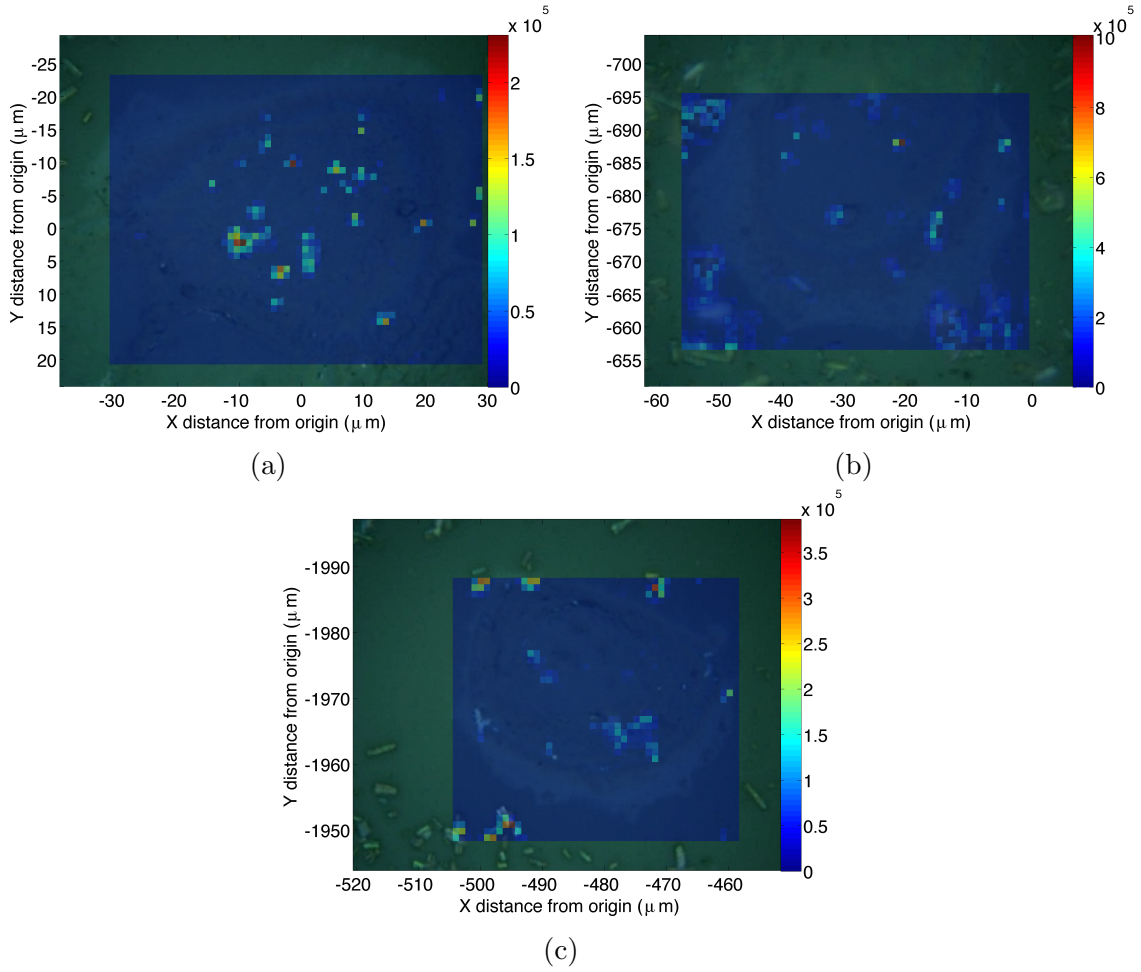

Figure 4.3: Sample maps of CaOV3 cells incubated with Type-I SERS probes prior to fixation. Regions of high intensity (warmer colours) are associated with the 1335 cm^{-1} SERS peak of DSNB. Maps were acquired with the 633nm laser at 100% power through the 100x objective and 2s/acquistion on a 1μm x 1μm grid.

ples, including fixation technique, length of the permeabilization step, and whether the cells were incubated with the probes before or after fixation. For each sample, 200μL of probe solution was added to 2mL of PBS covering the cells. A full description of each of the samples is shown in table 4.1, and a representative map of each sample is shown in figure 4.6.

For each of the maps in figure 4.6, a point-by-point scan was performed with the 633nm laser at 100% power through the 100x objective and an acquisition time of 2s per pixel on a 1μm x 1μm grid. Also, the maps are taken over a much larger area ($\sim 5000 - 24000\mu m^2$) than those in figures 4.3 - 4.5 ($\sim 1800 - 2600\mu m^2$) and each contains multiple cells in the mapped region. By mapping more cells, it was

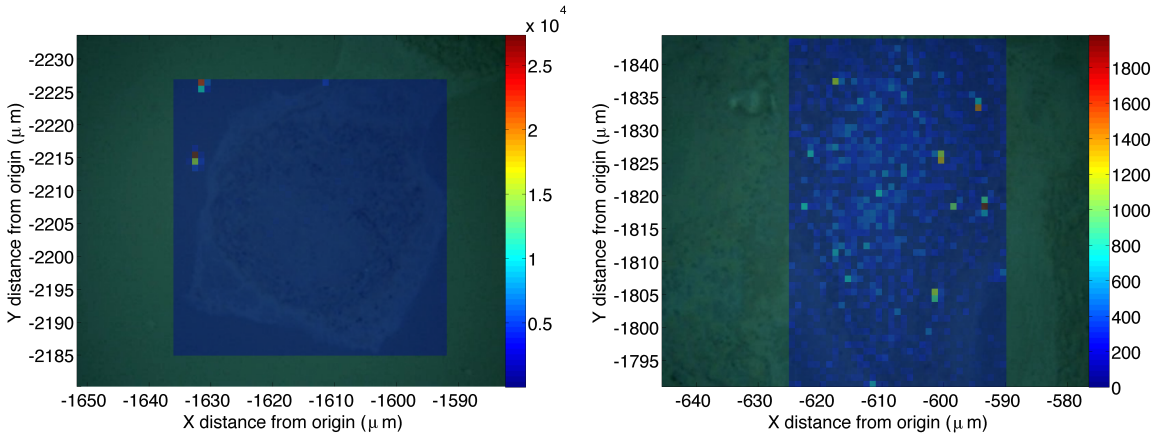

(a) (b)

Figure 4.4: Sample maps of CaOV3 cells incubated with Type-I SERS probes after fixation. Regions of high intensity (warmer colours) are associated with the 1335 cm^{-1} SERS peak of DSNB. Maps were acquired with the 633nm laser at 100% power through the 100x objective and 2s/acquistion on a 1μm x 1μm grid.

Sample	Cell Type	Probe Addition	Fixation Technique	Permeabilization Technique
1	CaOV3	Before Fix.	Formalin	N/A
2	CaOV3	After Fix.	Formalin	1x Triton for 10 mins.
3	CaOV3	After Fix.	Formalin	1x Triton for 20 mins.
4	CaOV3	After Fix.	Methanol/Ethanol	N/A
5	OVCAR5	Before Fix.	Formalin	N/A
6	OVCAR5	After Fix.	Formalin	1x Triton for 10 mins.

Table 4.1: Summary of Sample Parameters for Experiment 2 with Type-I SERS Probes

hoped that a more representative map of the SERS probe distribution would be obtained. Generally, the maps of figure 4.6 do show more pixels with signal from the filtered SERS probes than in figures 4.4 and 4.5. In particular, figures 4.6(b) and 4.6(c), which correspond to cells formalin-fixed and permeabilized prior to probe incubation show an encouraging amount of probe signal, as does figure 4.6(d) which corresponds to cells that were fixed with an ethanol/methanol mixture instead of formalin. However, the maps of figures 4.6(e) and 4.6(f), which were designed as controls for figures 4.6(b) and 4.6(c) respectively, also show appreciable signal. The

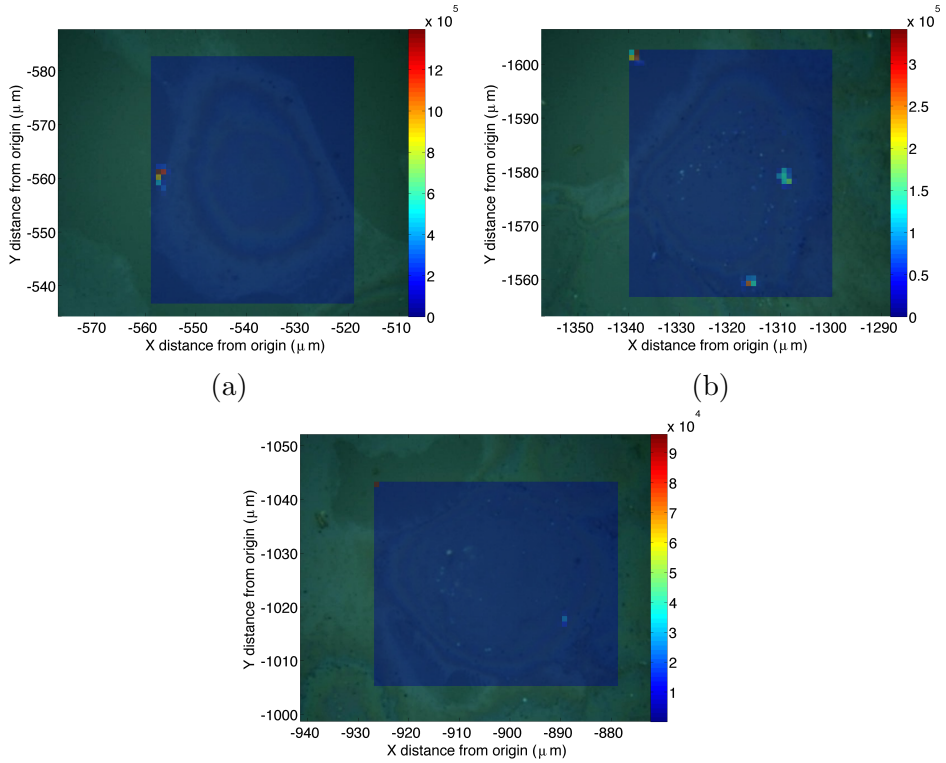

Figure 4.5: Sample maps of CaOV3 cells incubated with Type-I SERS probes after fixation and permeabilization. Regions of high intensity (warmer colours) are associated with the 1335 cm^{-1} SERS peak of DSNB. Maps were acquired with the 633nm laser at 100% power through the 100x objective and 2s/acquistion on a 1μm x 1μm grid.

cells in figure 4.6(e) and 4.6(f) are OVCAR5 cells, which do not contain the TACSTD2 protein, and the presence of probe signal in the maps of these cells implies that the Type-I SERS probes experience significant non-specific binding.

While a control was not included for figure 4.6(d), non-specific binding was likely an issue here as well, as it is unrelated to the method of fixation. Also, as can be seen from the optical image of the cells in figure 4.6(d), it appears that the cellular structure was not preserved as well by the ethanol/methanol fixation as it was by the formalin method. As such, further experimentation with ethanol/methanol fixation was not conducted, and formalin fixation was used exclusively.

Due to the fact that the TACSTD2 antibody had not been extensively studied, and it was not clear how much of the protein to expect in the CaOV3 cells, an attempt to simplify the SERS probe targeting was explored. It was decided that in future

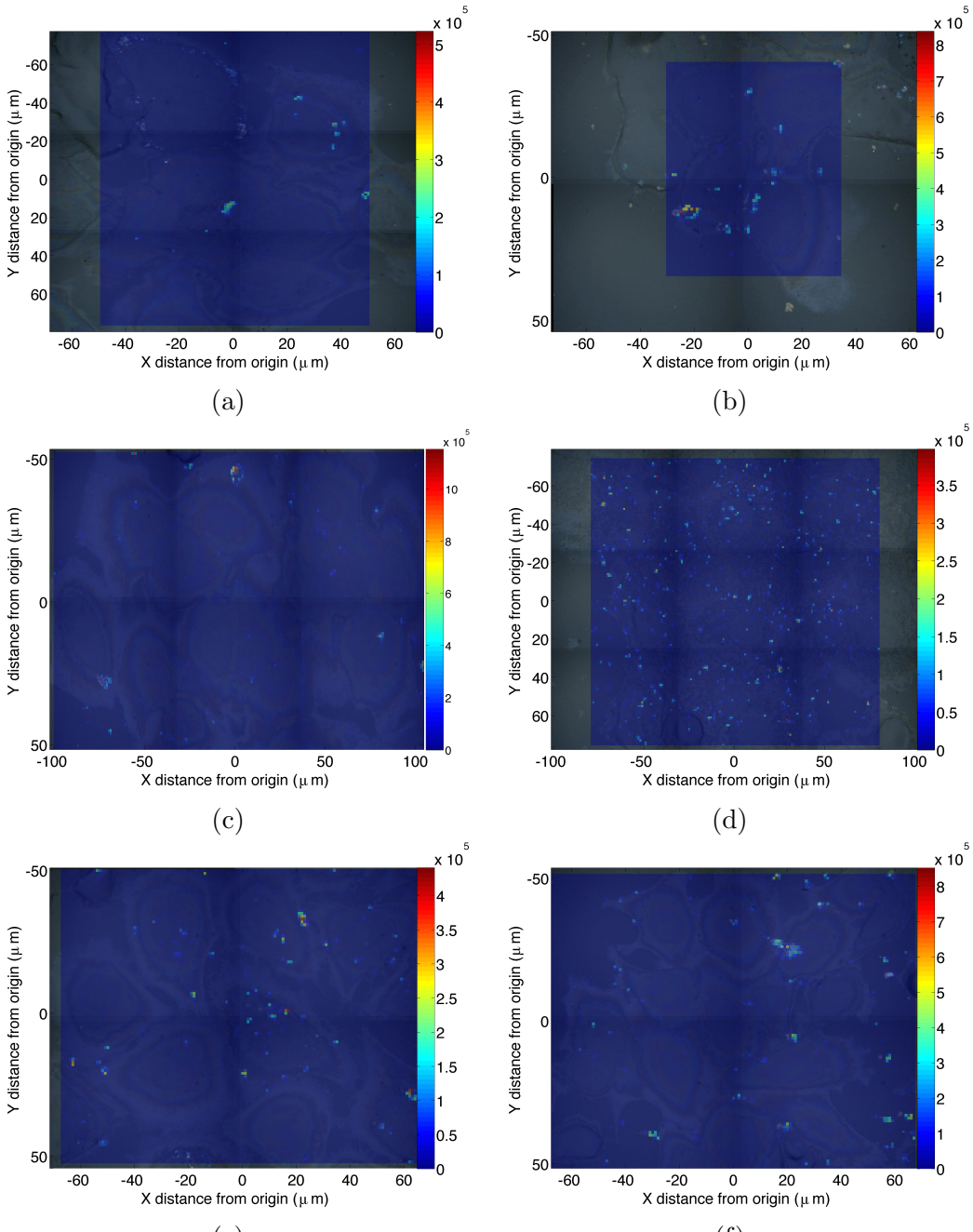

Figure 4.6: CaOV3 cells incubated with filtered Type-I SERS probes: (a) prior to formalin fixation; (b) & (c) following formalin fixation and permeabilization; (d) following fixation with a Methanol/Ethanol solution. OVCAR5 cells incubated with Type-I SERS probes: (e) prior to formalin fixation (as a control for (a)); (f) following formalin fixation and permeabilization (as a control for (b) & (c)). Maps were acquired with the 633nm laser at 100% power through the 100x objective and 2s/acquistion on a 1μm x 1μm grid.

experiments, OVCAR5 cells would be coated with biotin, a widely available protein, and the SERS probes would be conjugated to streptavidin, a protein that is known to bind strongly with biotin [260, 261] (OVCAR5 cells were used for the biotinylation process rather than CaOV3 cells simply due to the fact that they were found to grow more readily in culture). Also, in order to obtain large maps more quickly, streamline imaging was often used as opposed to point-by-point acquisitions.

The results of the first attempt to biotinylate OVCAR5 cells and then target the biotin with Type-I SERS probes conjugated to streptavidin are shown in figure 4.7. For each sample, 600μL of probe solution was added to 3mL of PBS covering the cells for 1hr, and all maps were obtained with a 633nm laser at 100% power through the 100x objective, streamline imaging on a 1μm x 0.53μm grid, and a 5s streamline acquisition time. Figure 4.7(a) shows a SERS map of biotinylated cells incubated with SERS probes after fixation, and figure 4.7(b) shows a SERS map of cells without biotin added, acting as a control to the latter and also incubated with probes post-fixation. A small amount of probe signal is present in figure 4.7(a), while no appreciable signal is present in the control (figure 4.7(b)).

While a larger amount of signal was expected in figure 4.7(a) due to the fact that biotin was expected to cover all of the cells completely, the contrast between figures 4.7(a) and 4.7(b) was encouraging. As such, the experiment was repeated, with the resulting SERS maps shown in figure 4.8.

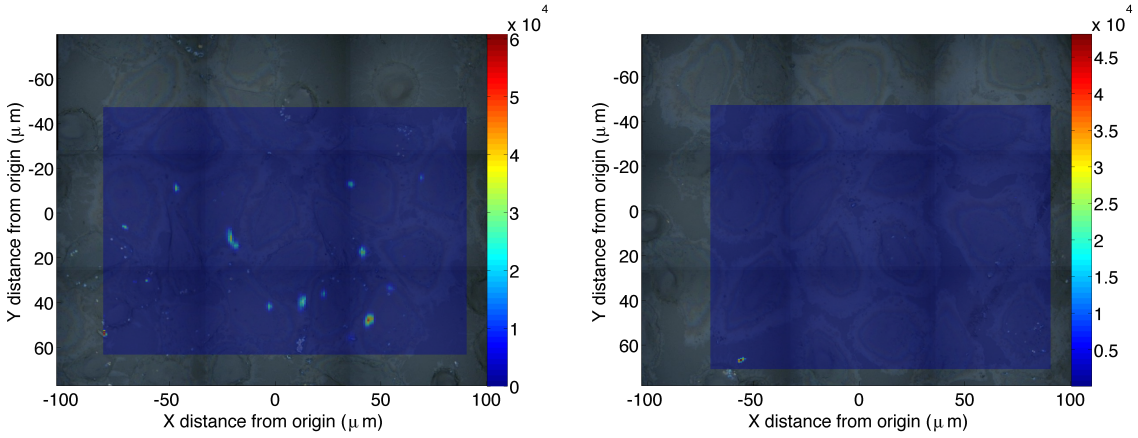

(a) (b)

Figure 4.7: SERS maps of (a) biotinylated and (b) unbiotinylated (control) OVCAR5 cells incubated with Type-I SERS probes conjugated to Streptavidin post-fixation. Maps were obtained with a 633nm laser at 100% power through the 100x objective, streamline imaging on a 1μm x 0.53μm grid, and a 5s streamline acquisition time

In the next experiment, three samples were prepared with varying initial conditions. The first sample consisted of biotinylated OVCAR5 cells incubated with SERS probes while the cells were alive, prior to fixation (350μL of probes in 2mL PBS for 1hr; figures 4.8(a) and 4.8(b)); the second sample consisted of biotinylated OVCAR5 cells incubated with SERS probes post-fixation (350μL of probes in 2mL PBS for 1hr; figures 4.8(c) and 4.8(d)); and the third sample was a control, consisting of non-biotinylated cells incubated with SERS probes post-fixation (300μL of probes in 2mL of PBS for 1hr; figure 4.8(e)). For all samples, unfiltered Type-I SERS probes were used. While it was known that unfiltered probe solution included salt crystals that seemed to provide non-specific signal, the filtering process was abandoned due to concerns that it was also removing SERS probes from the solution. As with the previous experiment, the maps in figure 4.8 were acquired using a 633nm laser at 100% power through the 100x objective, streamline imaging on a 1μm x 0.53μm grid, and 5s per streamline acquisition.

As can be seen from figures 4.8(a) - 4.8(d), the amount of probe signal is still very sparse in the SERS maps. Also, some signal does appear in the control map, shown in figure 4.8(e). Since the biotinylation process coats the entire surface of the cells in biotin, it was expected that SERS probes would completely cover the cells, and that probe signal would be frequently detected throughout the mapped region. From the small amount of signal observed in the maps, it was clear that there was an error in the experimental procedure and that either the SERS probes or the biotinylation was not working efficiently. As a first attempt, use of the Type-I SERS probes was halted, and efforts focused on introducing Type-II SERS probes to the process.

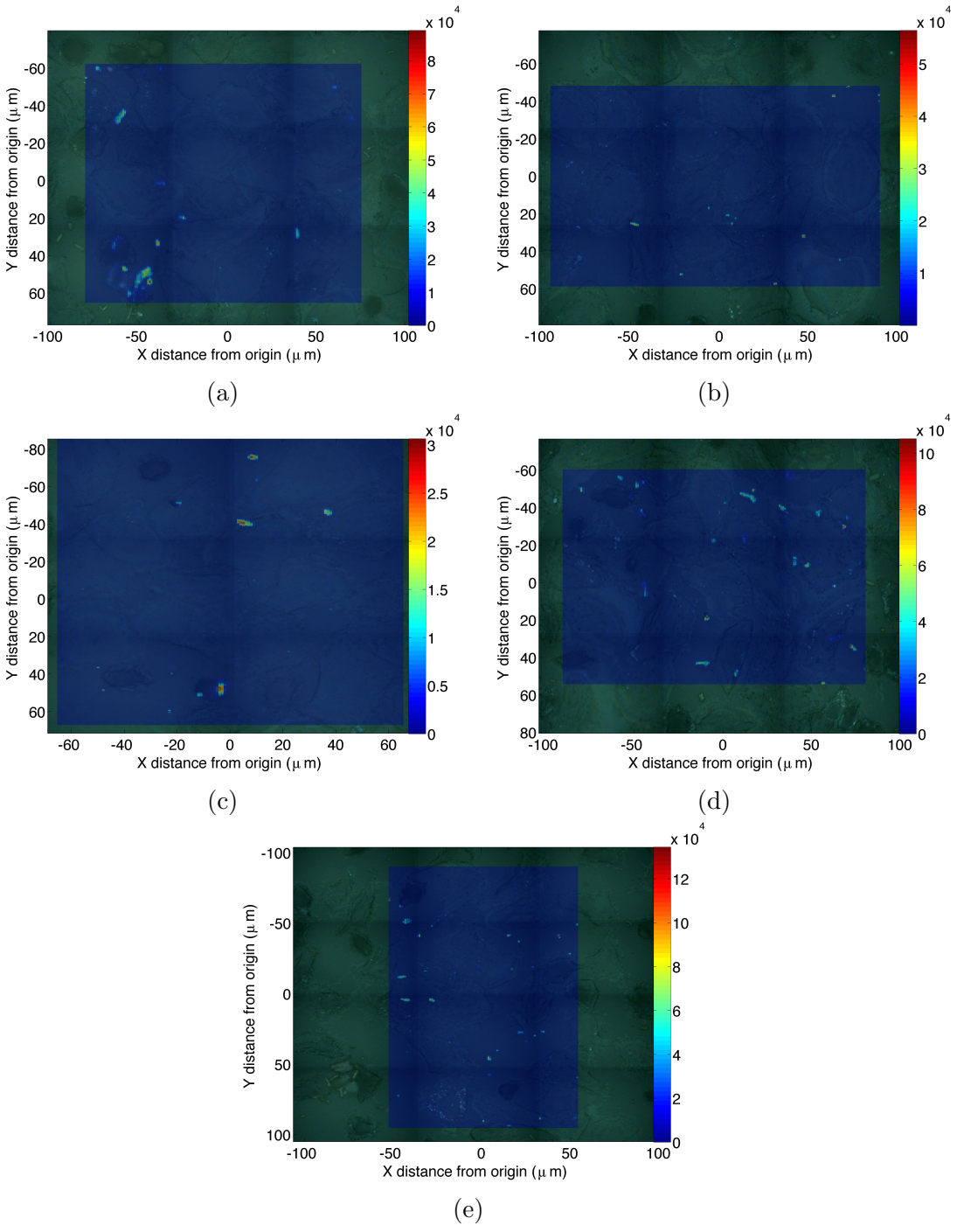

Figure 4.8: Biotinylated OVCAR5 cells incubated with Type-I SERS probes conjugated to Streptavidin: (a)&(b) prior to formalin-fixation; (c)&(d) post formalin-fixation. (e) Non-biotinylated OVCAR5 cells incubated with Type-I probes post formalin-fixation. Maps were acquired using a 633nm laser at 100% power through the 100x objective, streamline imaging on a 1μm x 0.53μm grid, and 5s per streamline acquisition.

4.1.3 Incubation of Biotinylated Cancer Cells with Type-II SERS Probes

In order to determine whether the lack of signal observed in previous SERS maps was due to an inefficiency of the Type-I SERS probes, experiments with the biotinylated cells were repeated using the Type-II SERS probes. The Type-II probes also had a polymer coating that improves probe stability and helps to prevent non-specific binding [2], which had been an issue in many of the SERS cell maps acquired of the Type-I probes. Initial results using the Type-II SERS probes to target the biotin on the surface of OVCAR5 cells were mixed. In many cases very little signal was seen in the cell maps, much like in section 4.1.2, but there were some promising exceptions. For example, a map of biotinylated cells incubated with Type-II SERS probes overnight is shown in figure 4.9(a), next to a control map of non-biotinylated cells incubated with the same probes in figure 4.9(b). Both maps were obtained with streamline imaging using the 633nm laser at 10% power through the 50x objective on a 0.8μm x 1.1μm grid with a 5s streamline acquisition. Regions of high intensity signal are clearly visible in figure 4.9(a), while there is no obvious signal in the control map. The difference in the amount of SERS signal between the biotinylated and control cells is better illustrated in the histogram shown in figure 4.10.

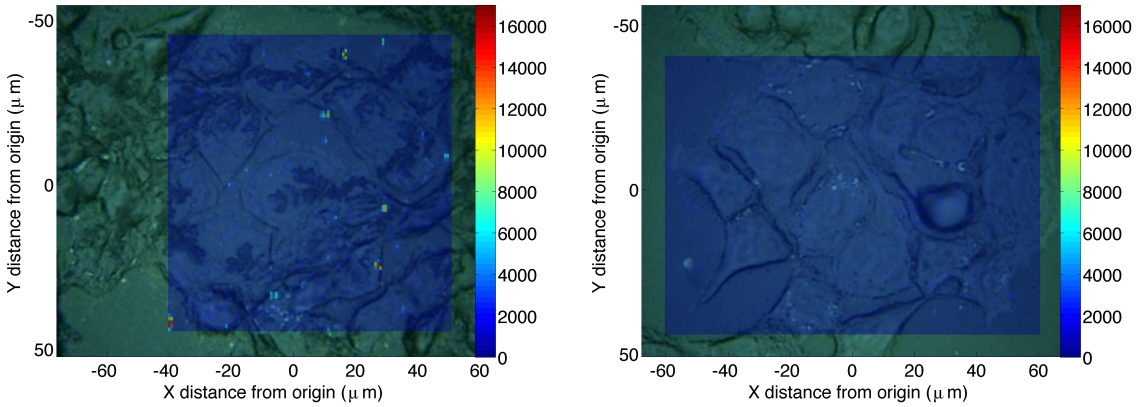

(a) (b)

Figure 4.9: (a) Biotinylated and (b) Control OVCAR5 cells incubated with Type-II SERS overnight; 633nm laser, 10% power, 5s streamline acquisition, 50x obj., 0.8 x 1.1 μm pixels.

At this point in the research, a histogram of the SERS peak areas collected from all maps of a given sample (as described in section 3.4.1) was typically considered

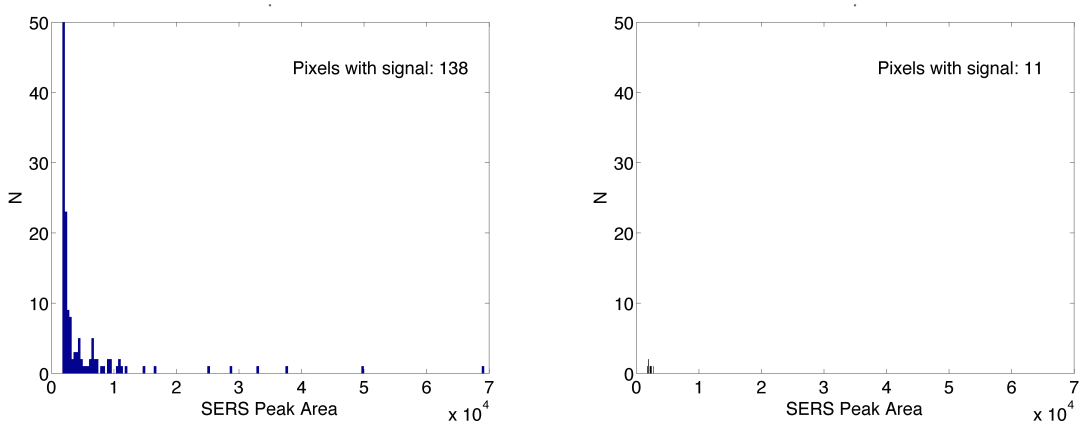

(a) (b)

Figure 4.10: SERS Peak Area Histogram for Maps in Figure 4.9. (a) Biotinylated cells; (b) Control cells. A zero signal cutoff of 1800 was chosen for these maps.

alongside the two-dimensional SERS maps as it was found to be very helpful in illustrating the prescence or lack of SERS signal. Only SERS peak areas above a designated cutoff were considered to exclude contributions from spectral noise. The cutoff was chosen based on inspecting multiple spectra from the data set and the corresponding peak area values. For the histograms of figure 4.10, the cutoff is 1800 (in arbitrary units) and it can be seen that the histogram of the biotinylated cells (figure 4.10(a)) has a number of SERS intensities above the cutoff, while the histogram for the control shows almost none (figure 4.10(b)).

Unfortunately, the results shown in figures 4.9 and 4.10 were not found to be reproducible, and other experiments with the Type-II probes were not as promising. In an attempt to better detect SERS probe signal that may have been missed by the 633nm laser, SERS maps were acquired using the 785nm laser. With the larger laser spot size of the 785nm laser ($\sim$ 3x8 μm with a 50x objective), it was possible to coarsely map larger cell regions using the point-by-point technique. While there was a loss in resolution compared to the 633nm maps, it was believed that the larger surface area probed by the 785nm laser spot would be able to detect probes that may have a weak signal.

Some examples of 785nm SERS maps are shown in figure 4.11. The cells in figure 4.11(a) were biotinylated and then fixed, while the cells of figures 4.11(b) were controls and were fixed without being biotinylated. All cell samples were incubated with 2mL of SERS probe solution for 2 hours. In this particular experiment, some aggregation

was intentionally induced in the SERS probes during the addition of the Nile Blue-A dye [185]. The SERS probes were aggregated in order to increase the intensity of the probes while mapping.

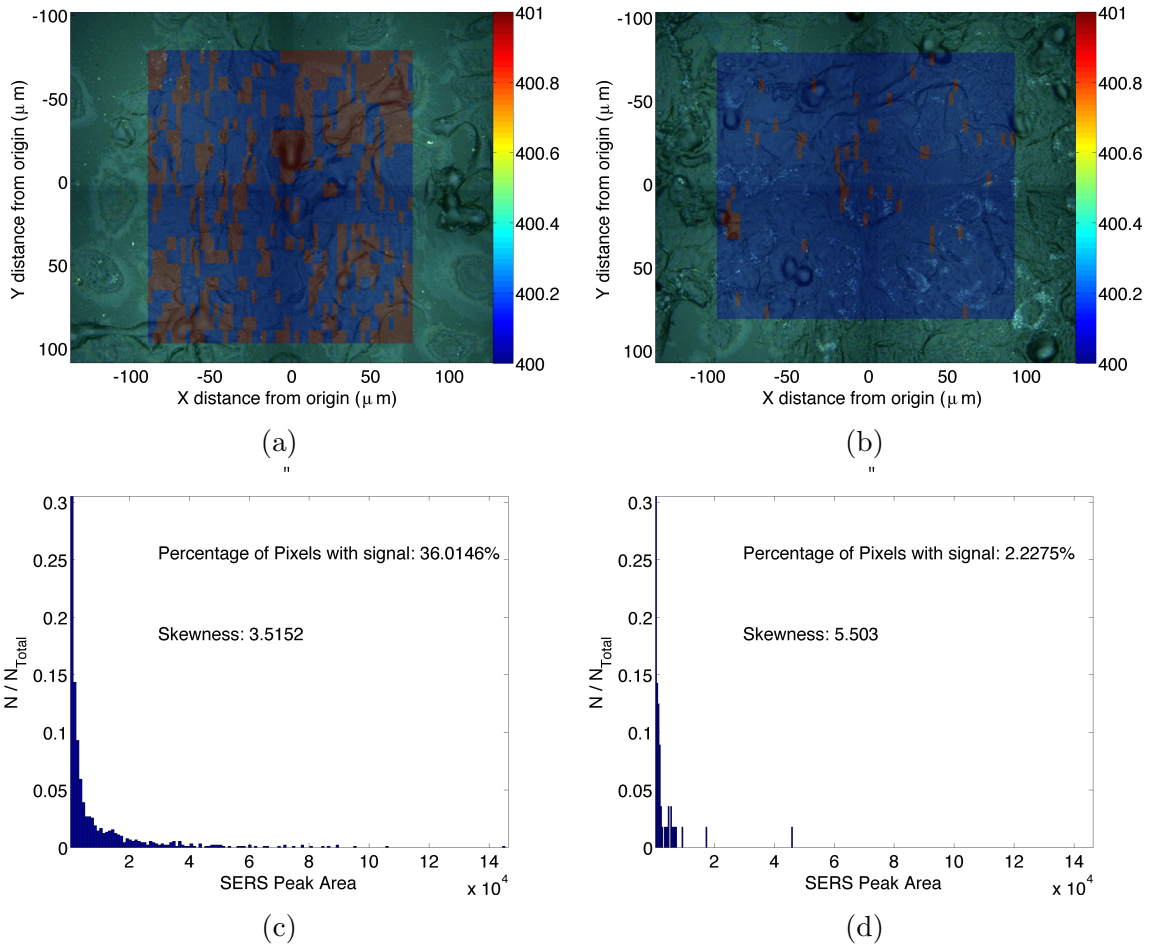

Figure 4.11: Fixed (a) biotinylated and (b) control OVCAR5 cells incubated with 2mL of aggregated Type-II SERS probes for 2hrs; 785nm laser, 50% power, 2s/acquistion, point-by-point mapping, 50x obj., 3 x 8 μm pixels. Also shown are histograms of the peak area for the (c) biotinylated and (d) control cells. The chosen cutoff value for the histograms is 400.

Rather than the colour map of intensity that was used in previous figures, the maps in figure 4.11 are displayed in a binary sense with each pixel being considered either to have SERS signal (red) or not (blue). A cutoff peak area was chosen based on the inspection of a sampling of spectra from the maps, and any pixel with a corresponding SERS peak area above the cutoff is considered to be SERS active. For the maps in figure 4.11 the cutoff area was chosen to be 400 (in arbitrary units) and

upon inspection it is clear that there is significantly more signal present in the maps of the biotinylated cells as opposed to the control cells. The histograms in figure 4.11(c) and (d) summarize the results and include data from one other map of the biotinylated sample and one other map of the control sample (not shown). In total, it was calculated that 36% of the pixels from the biotinylated cell maps were SERS active, as opposed to only $\sim 2\%$ of the pixels from the control maps, and the difference in the number of measured SERS intensities is clear when comparing the histograms in figure 4.11(c) and (d).

As with previous experiments, however, the results shown in figure 4.11 were not reproducible. Further repetition of the experiment was conducted in an attempt to develop a reproducible procedure. Eventually, an additional modification was made to the SERS probes that seemed to show some promise. In an attempt to simplify the chemistry of the SERS probes, streptavidin was conjugated directly to the gold NPs without the addition of the HS-PEG-COOH layer that was typically used (see section 3.1.3). Also, the ratio of EDC to NHS in the SERS probe mixture was changed to 3:1 according to a recommendation in the paper by Keng et al. [262]. Despite these minor modifications, the production of the SERS probes remained the same, but without the HS-PEG-COOH linker molecule, there were gaps in the PEG coating of the nanoparticle surface. The effect of the gaps on the stability and efficiency of the probe was not clear, but was decided to be an acceptable alteration due to the seemingly low binding efficiency of the original Type-II SERS probes to the cells.

An example of an experiment using the modified Type-II SERS probes is shown in figure 4.12. The cells of this experiment were grown on a gold slide rather than quartz in an effort to reduce non-specific binding to the cell growth substrate. The cells in figure 4.12(a) are biotinylated and fixed, while the cells in figure 4.12(b) are fixed controls. As in figure 4.11, the maps are presented with a binary colour map, where white pixels are considered SERS active, and black pixels are not. In total, nine maps of the biotinylated cells and six of the control cells were obtained, and the results are summarized in the histograms of figures 4.12(c) and (d). While SERS signal is present in both samples, there is significantly more present in the biotinylated cell sample with 94% of pixels registering as SERS active, compared to only 63% of the control maps' pixels.

Despite the clear difference between the SERS signal in the biotinylated and control samples, the amount of non-specific binding is still significant, perhaps due to the modification in the production of the SERS probes. Regardless, further study did

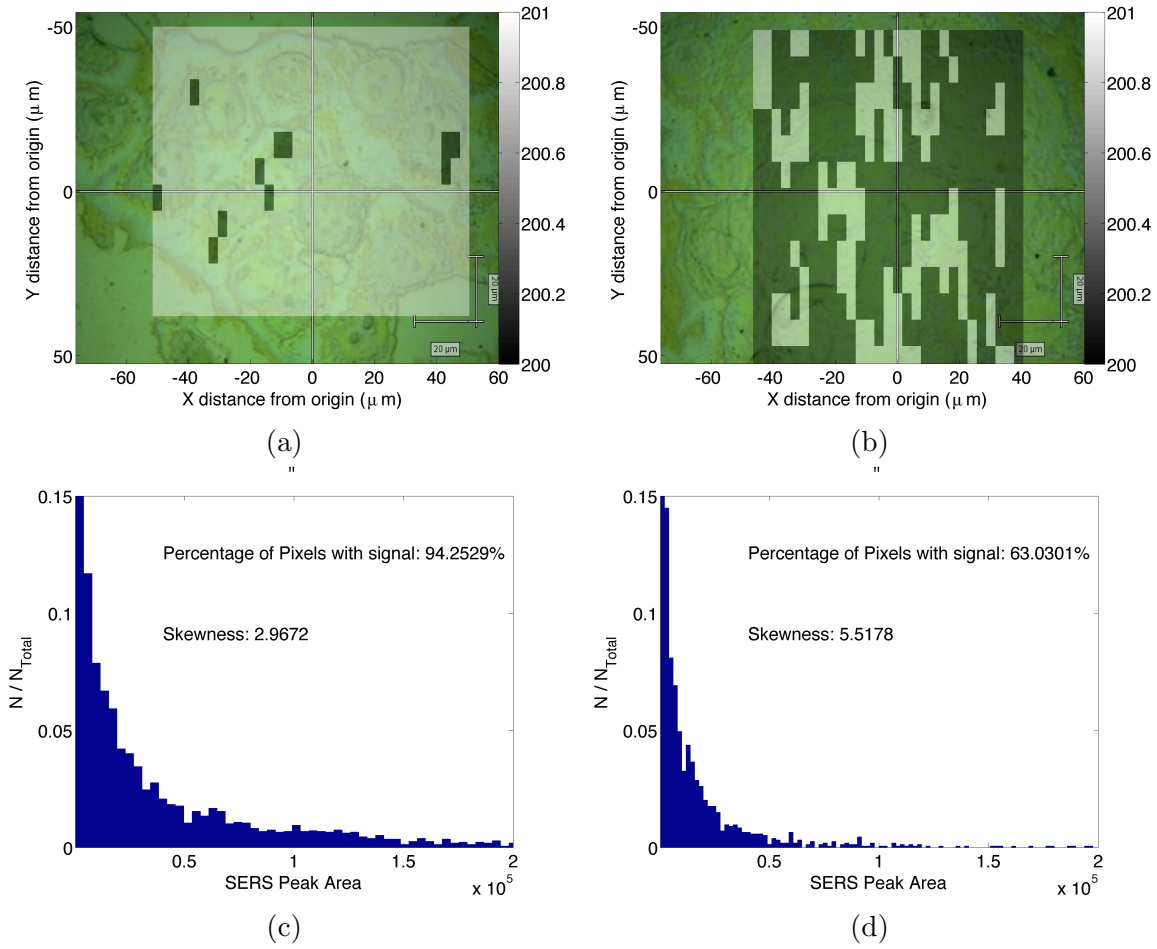

Figure 4.12: Fixed OVCAR5 cells grown on gold slides and incubated with Type-II SERS probes (w/o HS-PEG-COOH) for 8hrs. (a) Biotinylated cells; (b) Control cells; SERS Peak Area Histograms of the (c) nine biotinylated cell maps and (d) six control cell maps obtained; 785nm laser, 50% power, 2s/acquistion, point-by-point mapping, 50x obj., 3 x 8 μm pixels.

not yield reproducible results.

While the reasons for the unsuccessful targeting of biotin with the streptavidin-conjugated Type-II SERS probes was unclear, significant efforts were made to understand where the procedure was going wrong, and these efforts are detailed in section 4.1.4.

4.1.4 Confirmation of the Type-II SERS Probe Chemistry

In order to determine the reason for the low amount of signal detected from the SERS probes in our cellular SERS maps, it was necessary to troubleshoot the entire procedure including both the production of the SERS probes and the biotinylation of the cell membrane. To verify that biotin was present on the membrane of the biotinylated OVCAR5 cells, fluorescence microscopy was used, and the results are described below. Also described are tests of the binding ability of the Type-II SERS probes using a biotinylated gold surface and the monitoring of the manufacturing process of the probes at multiple stages using DLS and Raman microscopy.

Fluorescence Microscopy

As described in section 3.3.2, streptavidin conjugated to the fluorophore FITC was incubated with biotinylated, fixed OVCAR5 cells, and the prepared samples were then imaged with a fluorescence microscope. Multiple samples were prepared for fluorescence imaging, and the first are shown in figure 4.13. The fixed cells in figure 4.13 were also incubated with Hoechst 33342 and DRAQ5 dye, which bind to DNA and delineate the cell nucleus in fluorescence images. In figure 4.13, the purple colour corresponds to the nuclear dyes, while the green corresponds to fluorescence from the streptavidin-FITC. While cell nuclei are present in both figures 4.13(a) and 4.13(b), green from the streptavidin-FITC is only present in the image of the biotinylated cells in figure 4.13(a). The entire cell membrane appears green implying that streptavidin-FITC is present all over the surface of the cells. Since the green membrane only appears in figure 4.13(a) it is clear that the streptavidin-FITC is successfully binding to biotin present on the surface of the biotinylated OVCAR5 cells.

In order to better visualize how the entire membrane is coated with streptavidin, a higher magnification image of the biotinylated and fixed cell sample is shown in figure 4.14. Figure 4.14(a) shows an image of the cells filtered to only show the contribution from the streptavidin-FITC dye, while figure 4.14(b) shows fluorescence contributions from the nuclear dyes as well. In figure 4.14(a), the green membrane can clearly be seen and is particularly intense around the edges of the cell. The green colour is duller in the cell interior due to the fact that a highly confocal fluorescent microscope was used and only a thin slice of the cell is visualized in the image.

It was clear from figures 4.13 and 4.14 that our traditional method of biotinylation was effective, but in order to investigate the sensitivity of the biotinylation procedure

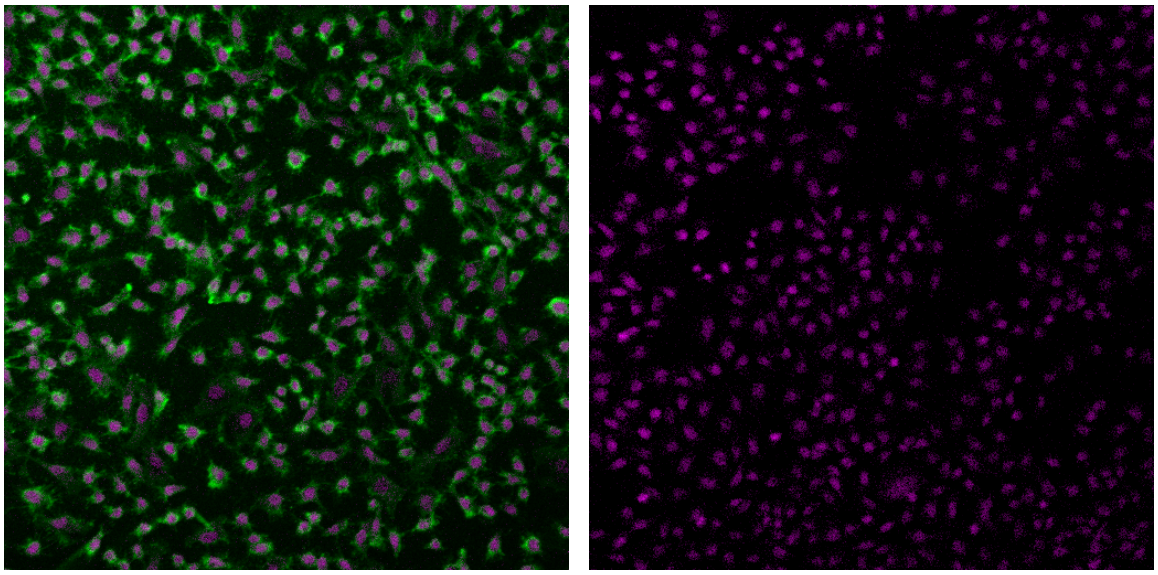

(a) Fixed Cells Biotinylated on Quartz Disc (b) Fixed Control Cells

Figure 4.13: Fixed OVCAR5 cells grown on quartz discs and incubated with Streptavidin-FITC (1:125 dilution in PBS), Hoechst 33342 (1:500 dilution) and DRAQ5 (1:1000 dilution) dye for 25 mins.; Fluorescence Imaging done with 488nm laser and 20x objective.

to variations in technique, a second sample was prepared. For the second sample, the cells were biotinylated while in solution and were then allowed to attach to the quartz discs overnight before being fixed and then incubated with streptavidin-FITC for 45 minutes. A control for this sample was prepared that consisted of non-biotinylated cells allowed to attach to a quartz disc overnight, and the control was also incubated with streptavidin-FITC for 45 minutes. Figure 4.15(a) shows an image obtained using differential image contrast (DIC) microscopy that clearly shows a region of biotinylated cells. A fluorescence image of the same region is shown in figure 4.15(b) indicating the presence of streptavidin-FITC all over the surface of the cells. Comparatively, a DIC image of the control cells is shown in figure 4.15(c) and the corresponding fluorescence image is shown in figure 4.15(d). Despite the abundance of control cells in figure 4.15(c), only faint patches of green are present in figure 4.15(d) indicating only slight non-specific binding of the streptavidin-FITC to the control sample.

Whether biotinylated in solution or when attached to a quartz disc, it is clear that the biotinylation procedure is successful, and that streptavidin is able to bind to the biotin present on the surface of fixed OVCAR5 cells.

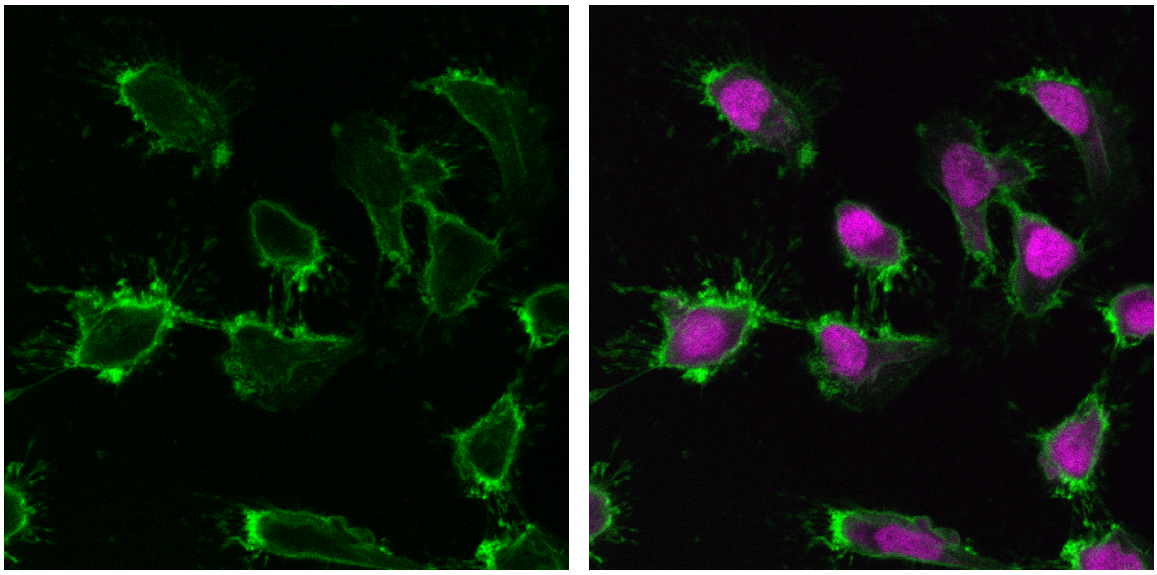

(a) (b)

Figure 4.14: Biotinylated, fixed OVCAR5 cells grown on quartz discs and incubated with Streptavidin-FITC (1:125 dilution in PBS), Hoechst 33342 (1:500 dilution) and DRAQ5 (1:1000 dilution) dye for 25 mins; Filtered fluorescence image obtained with 50x objective showing (a) the cell nuclei (Hoechst 33342 and DRAQ5 dye) and (b) both the cell nuclei and bioitnylated cell membrane (Strep-FITC dye).

SERS Mapping of Biotinylated Slides

While the fluorescence microscopy was able to verify the biotinylation of the OVCAR5 cells, a separate experiment was developed to determine whether the Type-II SERS probes were able to bind successfully to biotin. As described in section 3.3.1, a gold surface was coated with biotionylated tri(ethylene glycol) undecane thiol to act as an artificial biotinylated cell membrane. Another gold slide was coated with a hydroxy-terminated hexa(ethylene glycol), which would not bind to streptavidin and acted as a control. After a 24 hour incubation with the Type-II SERS probes, the slides were washed and mapped with the Raman microscope.

A SERS map of the biotinylated slide is shown in figure 4.16(a) and a map of the control slide is shown in figure 4.16(b). The map of the biotinylated slide exhibits SERS signal over the entire mapped area (represented by the red regions), while only a small amount of SERS signal is identified in the map of the control slide, due to non-specific binding. Histograms of the SERS peak areas obtained from the biotinylated and control gold slide are shown in figures 4.16(c) and (d), respectively. Each histogram combines the results from three separate maps of the slides. While

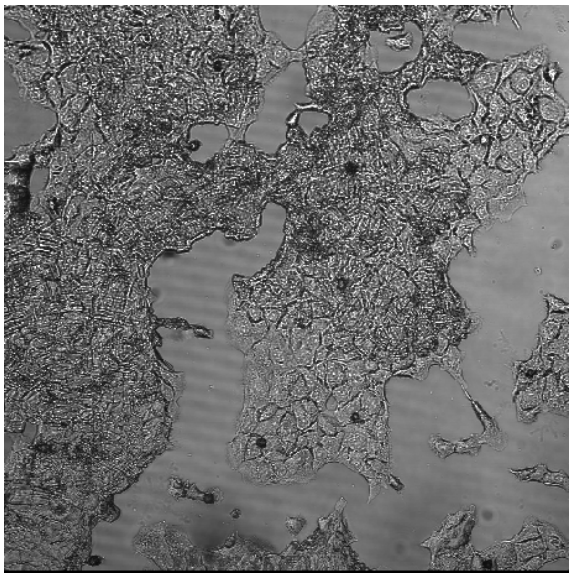

(a) Biotinylated Cells - DIC Image

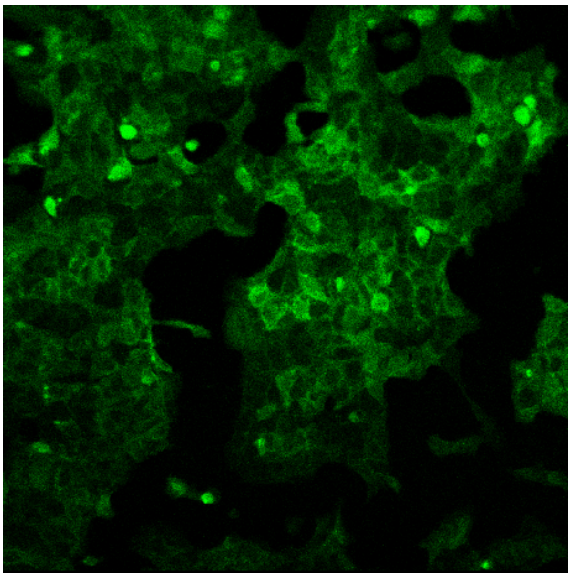

(b) Biotinylated Cells - Fluorescence Image

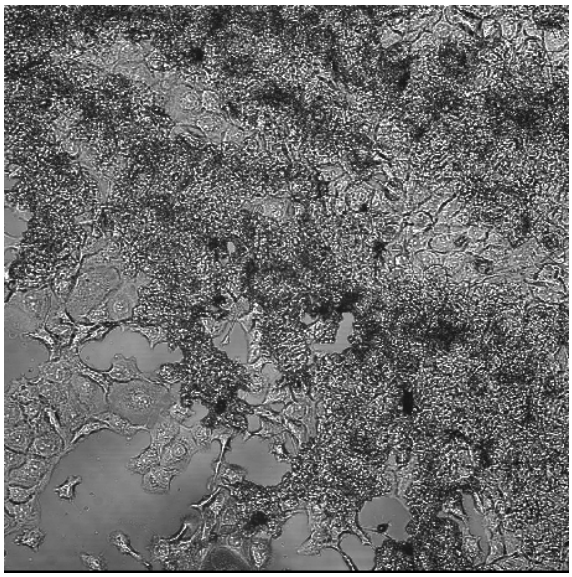

(c) Control Cells - DIC Image

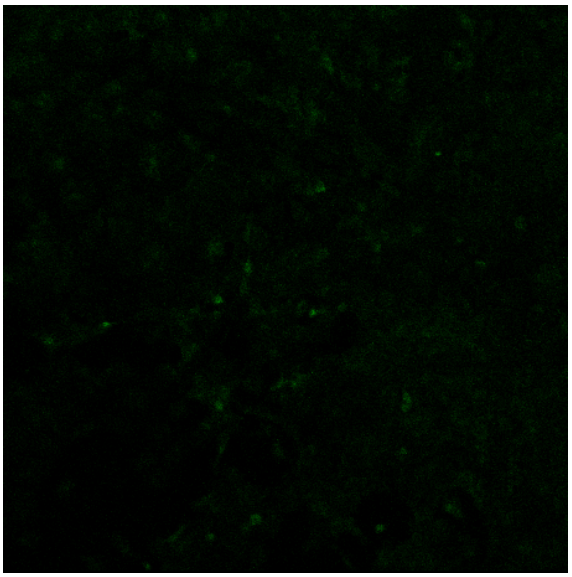

(d) Control Cells - Fluorescence Image

Figure 4.15: OVCAR5 cells biotinylated in solution and control cells, grown on quartz discs, fixed and incubated with Streptavidin-FITC (1:125 dilution in PBS) for 45 mins; Fluorescence Imaging done with 488nm laser.

a small number of low SERS intensities are present on the control, a significant shift in the SERS intensity to higher values is seen on the biotinylated slide. Further, only 8.6% of the control slide is SERS-active, compared to 93% for the biotinylated slide.

It should be noted that the Type-II SERS probes incubated with the gold slides had BSA added in the final step of the manufacturing procedure to block any unre-

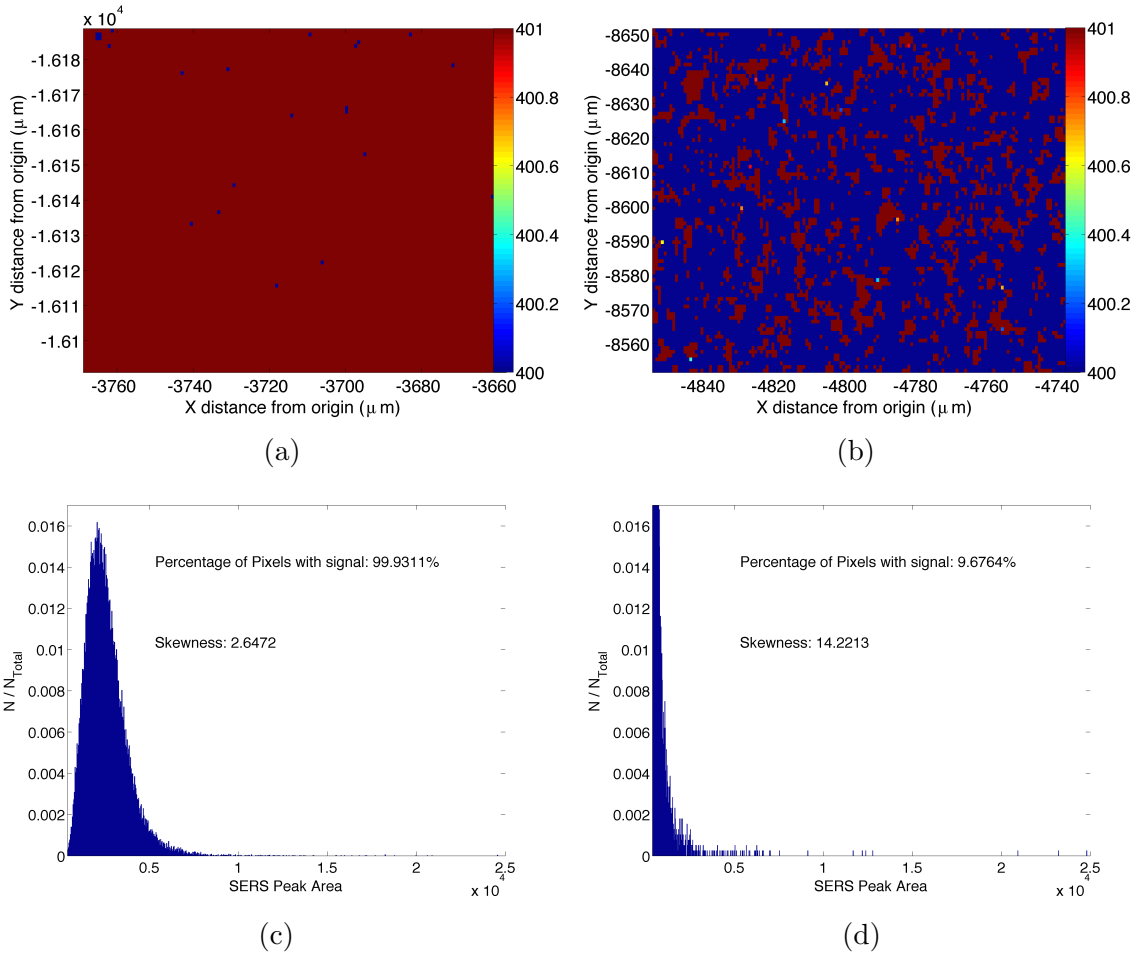

Figure 4.16: SERS maps of (a) biotinylated and (b) control gold slides incubated with Type-II SERS probes for 24hrs. Also shown are SERS Intensity Histograms combining the results of three maps obtained from the (c) biotinylated and (d) control slide. Raman Microscopy performed with 633nm laser at 50% power, 3s streamline acquisition, 50x objective, Intensity Cutoff of 400.

acted sites on the nanoparticle core, and thus minimize non-specific binding of the probes. BSA was typically not added to the SERS probes used in the cell experiments because the general lack of binding to the cells meant that non-specific binding was not a significant concern. It was only when the probes were successfully able to attach to the biotinylated gold slides that a reduction in non-specific binding due to the addition of BSA was found to be beneficial.

Nonetheless, the results of figure 4.16 confirm that the Type-II SERS probes are functioning properly and are able to bind to a biotinylated surface with only a small amount of non-specific binding.

DLS Measurements of the Type-II SERS Probes

In order to verify the chemistry of the Type-II SERS probes during and following production, DLS was used at multiple points during probe manufacturing to measure the average hydrodynamic diameter of the particles in the probe solution. Measurements were typically made of the unmodified NPs, after the addition of the PEG, after the addition of the streptavidin, and after the addition of the BSA (when applicable). After performing DLS measurements on multiple samples during production, an average range of hydrodynamic diameter was determined for each step. These ranges are displayed in table 4.2.

Table 4.2: Range of Hydrodynamic Diameters at multiple stages in production of Type-II SERS probes

Bare AuNPs	w/ NBA/PEG	w/ NBA/PEG/Strep.	w/ NBA/PEG/Strep./BSA
∼40-60 nm	∼70-90 nm	∼105-140 nm	∼105-140 nm

As can be seen from table 4.2, there was generally an increase in hydrodynamic diameter at each stage in the process, which was expected as each stage effectively adds a new molecular coating to the probe. When BSA was added, the hydrodynamic diameter typically did not change significantly, however, due to the fact that BSA was used to bind to unreacted sites on the NP core in order to prevent non-specific binding. As such, BSA did not provide an additional coating of molecules to the entirety of the probe surface.

During the SERS probe production, DLS measurements were closely monitored, and if they deviated significantly from the experimentally derived results of table 4.2, the probes were not used for cell incubation studies.

SERS Imaging of the Type-II SERS Probe Solution

As a final check of the suitability of the SERS probes for cell incubation studies, all Type-II SERS probe solutions were imaged with the Raman microscope to ensure that they provided an easily identifiable SERS signature. For the Type-II SERS probes a distinct Raman peak due to NBA dye was expected at 595 cm^{-1}. The probes would only be used in cell experiments if the characteristic NBA peak could be detected in the solution by the Raman microscope. An example of a Type-II SERS probe spectrum acquired using the 633nm laser can be seen in figure 4.17(a), while a

spectrum acquired using the 785nm laser is displayed in figure 4.17(b).

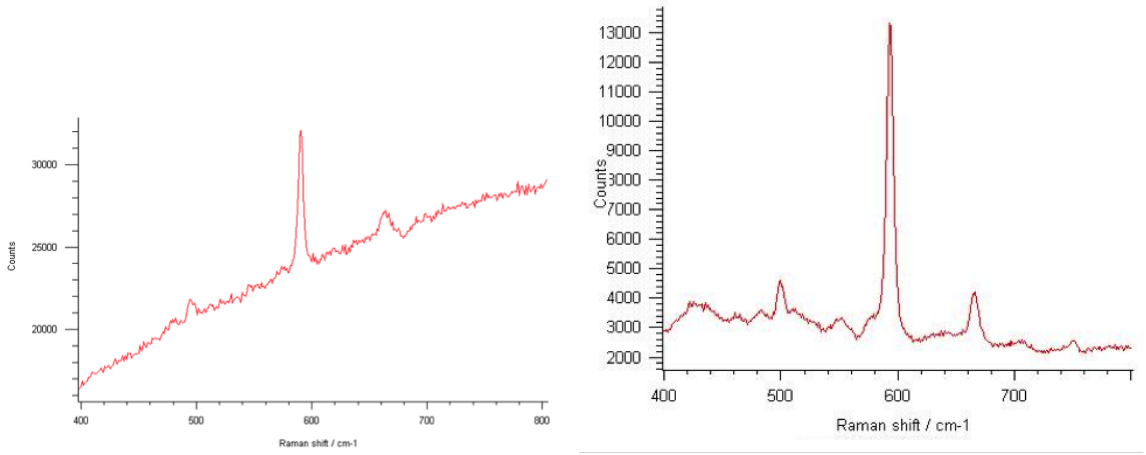

(a) 633nm (b) 785nm

Figure 4.17: SERS spectrum of Type-II SERS Probe Solution acquired with the (a) 633nm (at 10% power) and (b) 785nm (at 100% power) lasers. Both spectra were acquired with the 50x objective with a 5s acquisition time.

As an example of the type of enhancement provided by Type-II SERS probes, figure 4.18 is included. The spectrum in figure 4.18(a) is of a 100μL drop of a 5μM solution of NBA on a glass slide, while the spectrum in figure 4.18(b) is of a 100μL drop of Type-II SERS probe solution. Both spectra are the cumulative result of five 5s acquisitions with the 5x objective and 633nm laser at 100% power. NBA has an absorption spectrum that peaks at around 627nm [249, 263, 264] which is very close to the laser wavelength, and so resonance Raman scattering is expected.

As mentioned in section 3.1.3, the Type-II SERS probes contain only 250-300μL of 5μM NBA dye per 2mL of probes. Despite containing a higher concentration of NBA than the SERS probes, the spectrum of the drop of 5μM NBA in figure 4.18(a) is dominated by fluorescence, and the peak at 595 cm^{-1} appears only a few hundred counts above the baseline. In the spectrum of the SERS probes shown in figure 4.18(b), the 595 cm^{-1} peak is clearly visible, and is about 2×10^5 counts above the background. Due to the laser wavelength, the dye on the SERS probes actually experiences surface enhanced *resonance* Raman scattering [249, 263, 264], and the peak in figure 4.18(b) shows an enhancement on the order of 10^2 times that of the peak due to normal Raman scatter from the dye in figure 4.18(a).

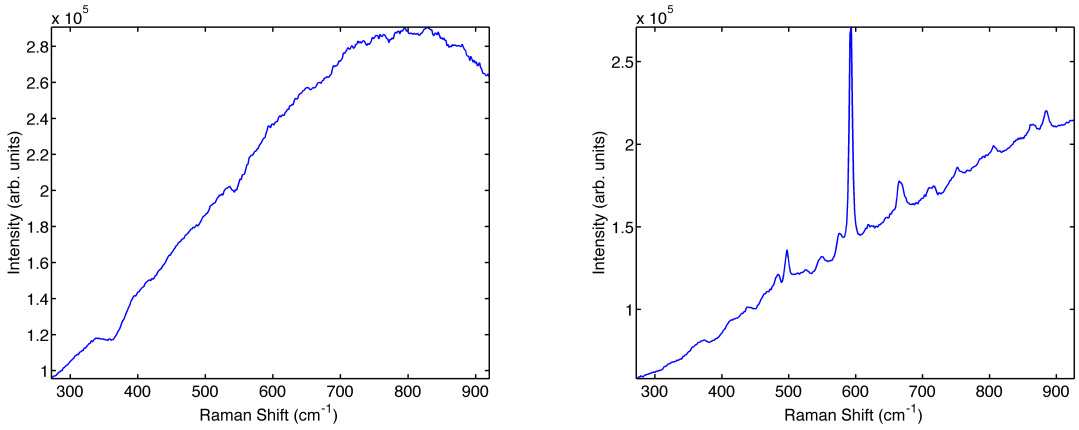

(a) (b)

Figure 4.18: (a) Raman spectrum of a 100μL drop of 5μM NBA dye on a glass slide and (b) SERS spectrum of a 100μL drop of Type-II SERS probe solution. Each spectrum is the cumulative result of five 5s acquisitions with the 633nm at 100% power through the 5x objective.

4.2 Discussion

It is still not clear why SERS mapping was unable to successfully utilize the targeted SERS probes to image the protein distribution on cancer cells. Both the Type-I and Type-II probes have been successfully used by other groups in the past [1, 2], yet we were not able to reproduce the results of their studies. There have also been a number of similar studies using different types of SERS probes that have reported successful results in the past, as described in section 2.3.5. When reading results published by other groups, it was clear that there are a number of different protocols used for experiments with targeted SERS probes. Such differences include the substrate on which the cells are grown, the target, fixation technique, and whether or not a permeabilization step is included.

Our early studies with the Type-I probes attempted multiple protocols, including experiments with and without permeabilization, and with different fixation techniques (formalin fixation and methanol/ethanol fixation). However, regardless of protocol, no significant differences were noticed in the results. Due to the fact that SERS probe characterization did not begin until experiments with the Type-II SERS probes, it is possible that there was a problem with the chemistry of the Type-I SERS probes and they were not functioning properly. The learning curve was steep in the early experiments, but after beginning experiments with Type-II SERS probes, character-

ization of the probes became more and more rigourous, ultimately leading to the results described in section 4.1.4.

It is clear from the fluorescence microscopy results that the biotinylation process successfully coated the OVCAR5 cells, and fluorescent streptavidin was able to bind to the biotin with specificity. The fluorescence images were obtained of cells grown on quartz discs, biotinylated and fixed in the same way that they are prepared for SERS probe incubations. As such, there does not appear to be a problem with the cell growth substrate or the biotinylation process. The cells did not undergo a membrane permeabilization step (see section 3.2.2) prior to incubation with the fluorescent streptavidin, and the successful results of the fluorescence microscopy demonstrate that permeabilization was not necessary for our purposes.

According to the results with the biotinylated gold slides, it is also clear that the Type-II SERS probes were functioning correctly, and were able to bind with specificity to a biotinylated surface. The DLS results and Raman microscopy of the SERS probe solution further verified the chemistry of the probes, indicating that the necessary chemicals were conjugated at each step of the manufacturing process, and that the solution exhibited an easily identifiable characteristic Raman signature.

Nonetheless, when the Type-II SERS probes were incubated with the biotinylated cells, Raman microscopy produced SERS maps with only sparse regions of SERS signal. Modifications to the production of the Type-II SERS probe such as probe aggregation and removal of the PEG shell initially resulted in promising results but were ultimately not reproducible. Further, according to the results of section 4.1.4, modifications to the SERS probe recipe were not necessary, as the traditional recipe was verified to be functional. However, despite many attempts, the SERS maps of biotinylated cells incubated with the probes displayed minimal SERS signal, and were often indistinguishable from the controls.

Regardless, based on the success of the results with the biotinylated gold slides, the Type-II SERS probes clearly warrant more investigation, and show significant promise for use in targeted SERS experiments. In the process of completing the experiments described in this chapter, a great deal of experience was gained in dealing with cells, and in the production of SERS probes, and despite closely following previously established protocols, there is obviously a fundamental flaw at some point in the technique used. Previously published results rarely describe the sample preparation and experimental procedure in great detail, and after performing the extensive trials with the probes described in this work, it is likely that in future studies it will be

necessary to contact groups that have used the probes successfully, namely Qian *et al.* [2]. With the current experimental infrastructure already in place, it will likely be straightforward to implement the necessary adjustments to the procedure suggested after collaboration with other groups.

Chapter 5

Results and Discussion II: Statistical Correlation between SERS Intensity and Nanoparticle Cluster Size

The work presented in this chapter was previously published in the *Journal of Physical Chemistry C* in the article "Statistical Correlation Between SERS Intensity and Nanoparticle Cluster Size" [265]. The chapter begins with section 5.1.1 presenting the results of the characterization tests of the Type-II SERS probes that were incubated with a biotinylated gold slide for four different incubation times (1hr, 2hr, 3hr, 12hr). Section 5.1.2 follows showing sample results of the SERS mapping of the experimental slide, along with a histogram of the SERS intensities measured from the regions of the slide corresponding to each incubation time. Sample SEM images of the gold slide after each probe incubation time are presented in section 5.1.3, as well as the multiple histograms generated from analysis of these images, with references to the analytical procedures outlined in section 3.6. Section 5.1.3 ends with an overview of the linearly independent series of equations generated from the data (first described in section 3.6.4) that relate the measured SERS intensity to the individual SERS probe clusters. Solving the system of equations is described in section 5.1.4 and a graph showing the relationship between SERS intensity and the size of the cluster probed by the laser is presented. Section 5.2 then includes a discussion of the results followed by a summary of the significant conclusions in section 5.3.

5.1 Results

5.1.1 Characterization of the Type-II SERS probes

The SERS probes were characterized throughout their production with the use of dynamic light scattering (DLS), ultraviolet/visible (UV/Vis) and surface enhanced Raman spectroscopy (SERS), as described in section 3.1.4. DLS was used to monitor the hydrodynamic diameter of the probes, UV/Vis spectroscopy indicated whether excessive particle aggregation had occurred, and SERS spectra of the probe solution confirmed the presence of the characteristic spectral peak of the dye adsorbed on the probe surface. Measurements of each type were made before modification of the NPs (bare Au-NPs; Stage I), after the addition of NBA and PEG (NP/NBA/PEG; Stage II), after the addition of streptavidin (NP/NBA/PEG/Strep; Stage III) and finally after the addition of BSA (NP/NBA/PEG/Strep/BSA; Stage IV).

Figure 5.1 shows measurements of the average hydrodynamic diameter of the SERS probes made at each stage of production. The average hydrodynamic diameter was seen to increase significantly as the Au-NPs were modified, from 50nm at Stage I, to 140nm at Stage IV. The general increase in hydrodynamic diameter implies the successful coating of the NP core with a molecular coating at each stage. The reason for the decrease in hydrodynamic diameter between Stage III and IV is unclear, but as the two points are almost within one standard deviation of each other, it was not considered to be cause for concern.

Figure 5.2 shows the UV/Vis spectrum of the probes at each of the four stages. As mentioned in section 3.1.4 of Chapter 3, the unmodified Au-NPs should show an absorption peak at about 530nm, and the presence of the peak is confirmed by the blue curve of figure 5.2. While the figure shows that the peak decreased and broadened slightly as the stages progressed, it remained distinctly identifiable at $\sim$ 530nm, indicating that excessive particle aggregation did not occur.

Finally, figure 5.3 shows the SERS spectrum of a drop of the SERS probe solution at each point in the modification process. After the NBA dye was added to the NP solution in stage II, the characteristic NBA dye peak at $600cm^{-1}$ was visible, as shown by the blue curve of figure 5.3. The peak remained visible at stage III and stage IV of the SERS probe production, despite a slight intensity decrease and an increase in the fluorescence background.

Taking all of the aforementioned results into consideration, the SERS probe pro-

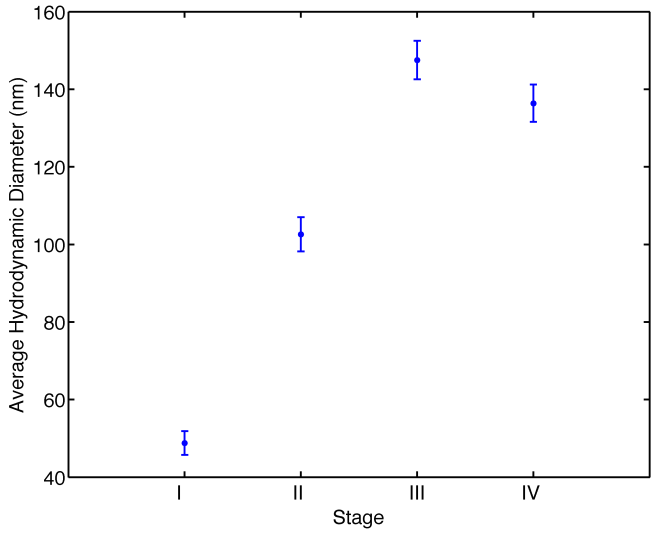

Figure 5.1: DLS measurements of average hydrodynamic diameter of the SERS probes at Stage I (bare Au-NPs), Stage II (NP/NBA/PEG), Stage III (NP/NBA/PEG/Strep) and Stage IV (NP/NBA/PEG/Strep/BSA). Error bars correspond to $\pm 1\sigma$.

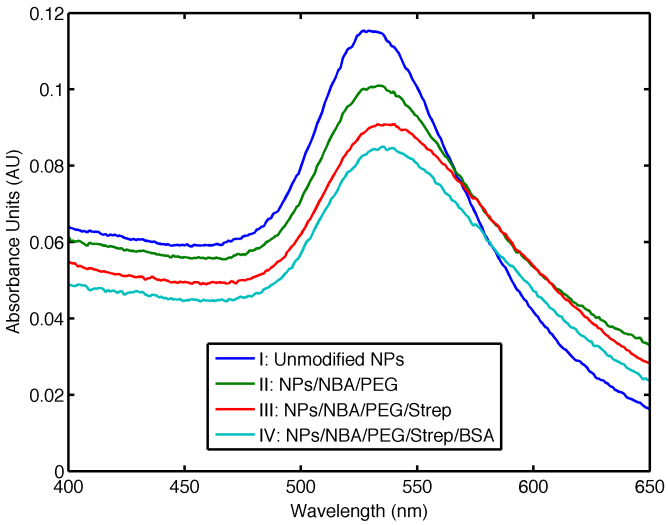

Figure 5.2: UV/Vis spectrum of the SERS probe solution at each of the four stages of production.

duction was determined to have been successful, and the resultant batch of probes was incubated with the biotinylated gold slide as described in section 3.3.1 of Chapter 3.

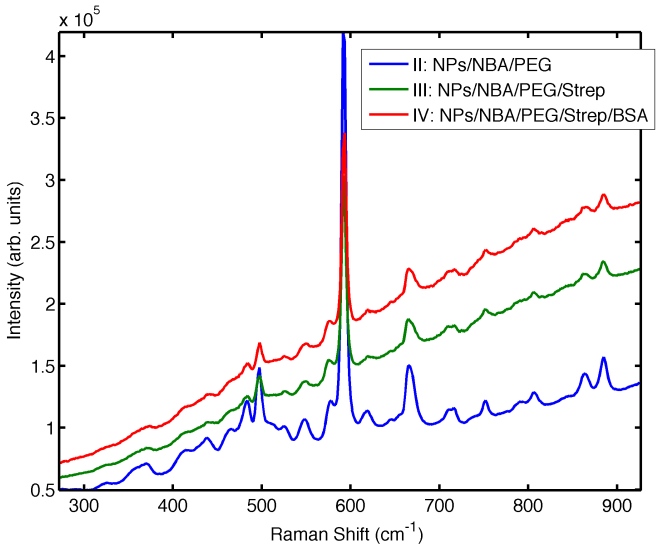

Figure 5.3: SERS spectra of the probe solution at stages II, III and IV after the NBA dye has been added. The signature NBA dye peak at 600 cm^{-1} is visible in each spectrum. Spectra acquired with the 633nm laser at 50% power through the 5x objective. Each spectrum is the cumulation of five 5s acquisitions.

5.1.2 SERS Mapping and histograms

Figure 5.4 shows sample SERS maps of the gold slides coated with SERS probes for 4 different incubations times (1 - 12hrs). The SERS mapping at low incubation times (Figure 5.4(a)) shows a large spatial variation in SERS intensities, due to the sparse coverage of the gold surface by SERS probes. The intensity maps become more uniform as the incubation time increases (Figure 5.4(b) - 2(d)). In those cases, the overall SERS probe surface coverage increases, as does the number of probes illuminated at each mapped point. These observations are corroborated in Figure 5.5, where the distributions of SERS intensities corresponding to each incubation time are represented as histograms. Each count in the histogram corresponds to the SERS intensity (integrated SERS peak) obtained under a laser-illuminated area during mapping. The histograms were generated by combining the data from 3 large area (76 x 53 μm^2) maps obtained from random positions in every slide, leading to a large sample of SERS intensities. Zero intensity events were defined by a cutoff which varied based on the intensity distribution of the data set, but was typically on the order of 100 to 300 counts. After discarding the intensities below the cutoff, the final sample sizes for the histograms varied from approx. 7000 for the 1hr data to over 23000 for the 12 hour data. Following a common treatment of error on histograms,

the measured number of counts in each bin (N_{bin}) is assumed to be the mean of a Poisson distribution, with the error bars corresponding to $\pm N_{bin}^{1/2}$, which represents one standard deviation (1σ) [266, 267] (the Poisson treatment of error is used for all histograms in this thesis).

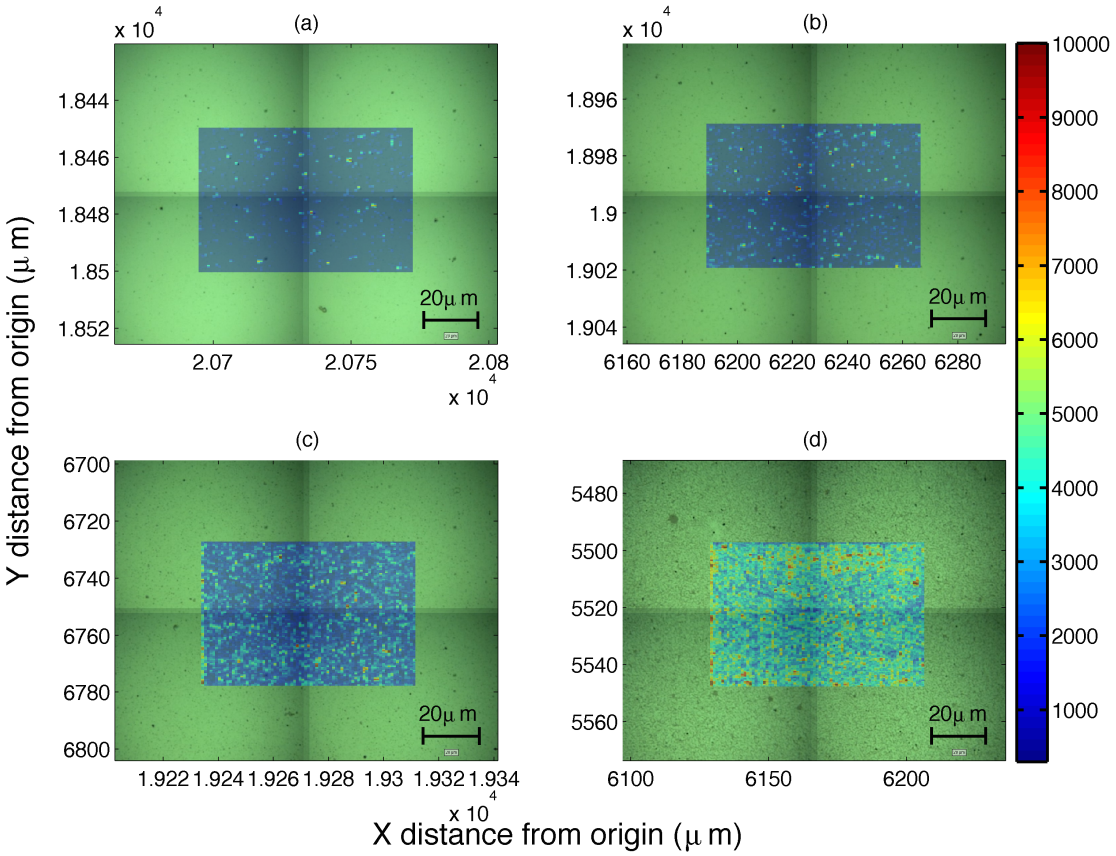

Figure 5.4: SERS map of the gold slide surface after a SERS probe incubation of (a) 1hr; (b) 2hrs; (c) 3hrs; (d) 12hrs.

The results for the shortest incubation time (Figure 5.5(a)) show a tailed distribution, with a skewness of 10.1 (skewness values can provide a quantitative assessment regarding the symmetry of the distribution [268]), and a high number of low intensity events. These correspond to illuminated areas that contained low efficiency probes that produced Raman signal near the detection limit of the system. Even at this low coverage regime, however, a small number of events presented a relatively high SERS intensity (∼1000 counts). The distribution clearly spread to higher intensities as the incubation time increased (Figure 5.5(b)) and the number of regions with low SERS intensity decreased. When the incubation time reached 3 hours (Figure 5.5(c)), the

number of low signal events became small and a peak clearly develops in the distribution. This result is consistent with a larger coverage and a higher probability of SERS probes being found under each laser illuminated area during mapping. Finally, in Figure 5.5(d), the least skewed distribution, a peak forms at higher intensities than in figure 5.5(c). Based on its low skewness value, the distribution in figure 5.5(d) is more symmetric than the others (figures 5.5(a)-(c)), appearing almost Gaussian in shape [268]. This result is consistent with a higher surface coverage of SERS probes and, consequently, a larger probability of several NPs being interrogated by the laser in each particular mapped spot.

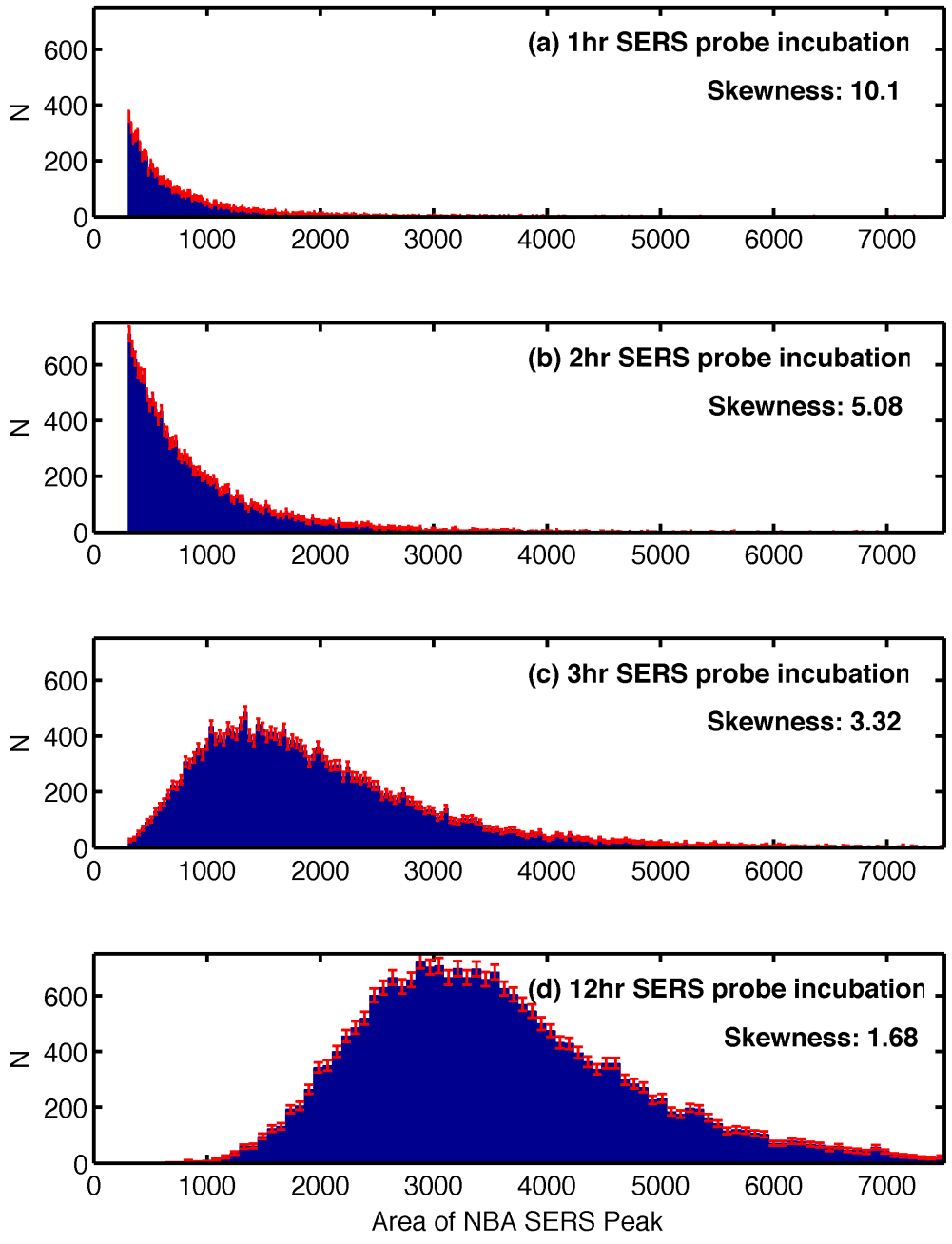

Figure 5.5: Histogram of integrated SERS peak of Nile Blue-A ($\sim 600cm^{-1}$) measured on the slide surface incubated with SERS probes for (a) 1hr; (b) 2hrs; (c) 3hrs; (d) 12hrs. Error bars correspond to $\pm 1\sigma \quad (N_{bin}^{1/2})$.

5.1.3 SEM Imaging and histograms

Sample SEM images of the gold slide incubated with SERS probes for different times are shown in figure 5.6. The scale of the images in figure 5.6 was chosen so as to provide the largest surface area possible, displaying a large number of clusters while still allowing for the identification of individual probes. As an example of the spacing between the SERS probes in a cluster, figure 5.7 shows two high magnification SEM images of pegylated SERS probes produced in an identical fashion to those described in this work, but for an earlier trial of the experiment. The images show three large clusters, each consisting of a single layer of probes on the gold slide surface, and most of the individual probes within the clusters are clearly identifiable. There is some blurring in the images due to the high magnification (130,000x in figure 5.7(a) and 200,000x in figure 5.7(b)), and the slight interaction of the electron beam with the gold slide surface underneath the probes, but it is possible to get an idea of the spacing between the probes. Many probes appear to be separated by approximately 10 to 20 nm, although larger gaps are visible, particularly in figure 5.7(b).

In order to identify all clusters of SERS probes visible in the SEM images of the gold slide, such as those shown in figure 5.6, analysis of the images was performed as described in section 3.6.1. To illustrate, figure 5.8(a) shows a raw SEM image of the gold slide (after the 12hr probe incubation), and figure 5.8(b) shows the same image in its binary form with identified clusters outlined in blue. While the blue outlines of figure 5.8(b) enclose areas of the slide not covered with SERS probes, only the number of pixels in the white regions shown in figure 5.8(b) are included in the pixels areas of the clusters.

After identifying the SERS probe clusters in all of the SEM images, all of the regions that corresponded to a single SERS probe were flagged, and a histogram of the pixel areas of all imaged single SERS probes was generated and fit with a Gaussian. The histogram, along with the fitted Gaussian curve is displayed in figure 5.9. By sampling the Gaussian for the pixel size of a single SERS probe, it was possible to convert the pixel areas of the identified clusters into the corresponding number of probes per cluster, as outlined in section 3.6.2. The resultant histogram of the SERS probe cluster size distribution corresponding to each probe incubation time is presented in Figure 5.10. Due to the fact that a different number of SEM images were obtained of each region of the slide corresponding to a particular incubation time, each histogram in figure 5.10 has been normalized by the total imaged surface

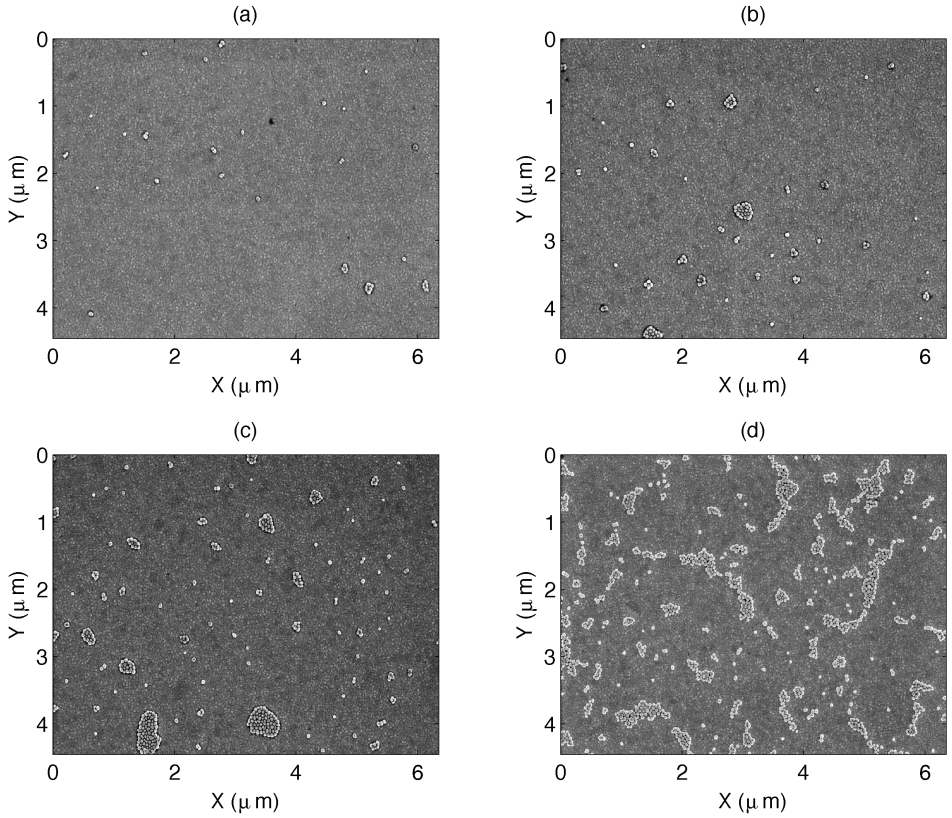

Figure 5.6: Sample SEM images of the gold slide surface after SERS probe incubation of (a) 1hr; (b) 2hrs; (c) 3hrs; (d) 12hrs.

area of the corresponding region (A^t_{SEM}; t = 1hr, 2hr, 3hr or 12hr). The normalized histograms show a clear increase in the number of SERS probes in the aggregated clusters with the incubation time, although some large clusters, with more than 10 SERS probes, were also observed in the 1hr incubation experiment. Notice that the number of single particles and small clusters (less than 5 SERS probes) still dominates the distribution even after 12 hrs. This is a strong indication that the PEG-layer efficiently protects the SERS probes against aggregation; meaning that the SERS probe adsorption is likely driven by the specific interaction with the surface, rather than by particle-to-particle attraction.

Our final goal is to correlate the SERS intensity from each illuminated spot obtained from the SERS map histograms (Figure 5.5) with the number of SERS probe clusters at that spot. In order to achieve that, a new set of histograms, shown in Figure 5.11 were obtained from the SEM images, as described in section 3.6.3. In

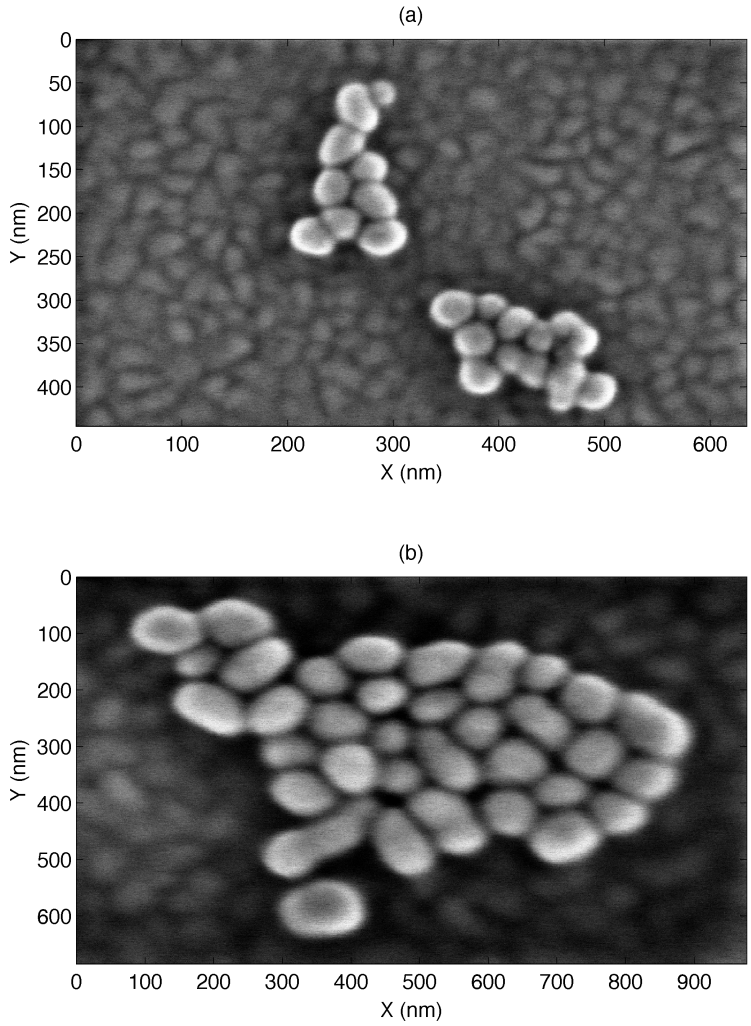

Figure 5.7: High magnification SEM images of pegylated SERS probe clusters (a) 1.0kV; 130 000x, (b) 1.0 kV; 200 000x.

the case of Figure 5.11, the histograms considered the number of SERS probe clusters illuminated per acquisition (i.e., the number of SERS probe clusters in a 1 x 1 μm^2 SEM imaged area). As expected, the histograms in Figure 5.11 show that each laser-illuminated area is mostly populated with either 0, 1 or 2 SERS probe clusters for the lower incubation time (1 hr; figure 5.11(a)). On the other hand, most of the mapped SERS intensities were generated by illuminating 2 to 5 SERS probe clusters when the incubation was 12 hrs (figure 5.11(d)).

In order to relate the SERS and SEM results to determine the SERS intensity due

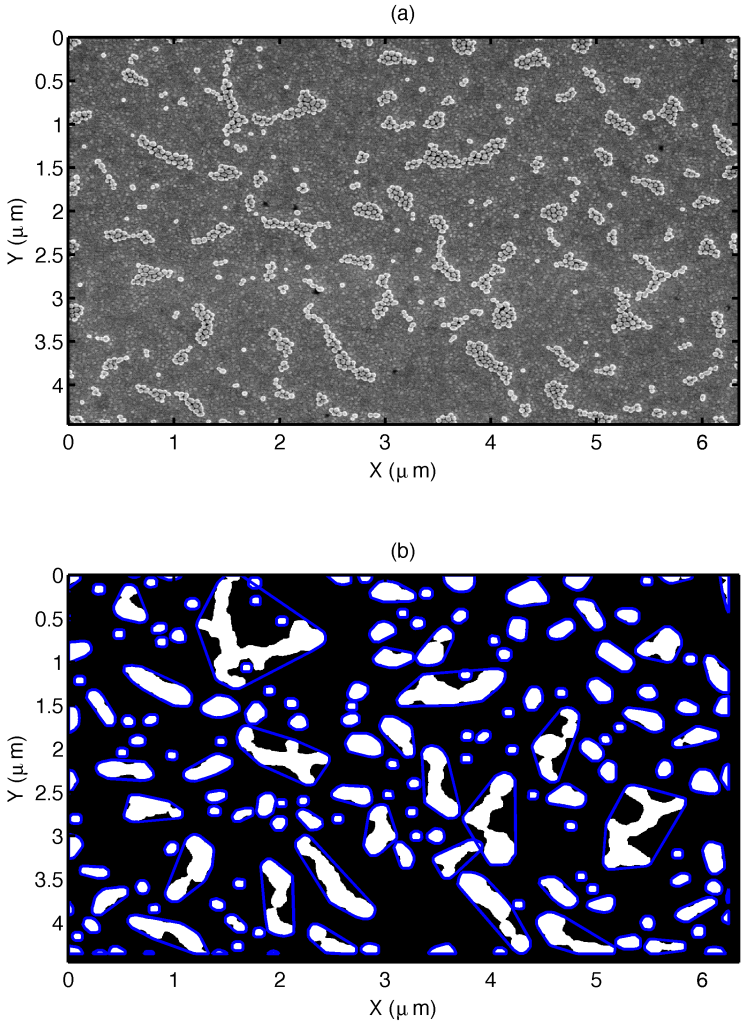

Figure 5.8: Sample SEM image of the region of the slide incubated with the SERS probes for 12 hrs in its (a) original and (b) binary format. Identified NP clusters are outlined in blue.

to an individual SERS probe cluster, a system of equations was generated according to the method laid out in section 3.6.4. Briefly, a relationship was developed by first sampling the histogram in Figure 5.5 to provide a SERS intensity from a random spot on the slide sampled by the laser. The probability that the sampled intensity was from a certain number of clusters was then generated from Figure 5.11 and the possible size of these clusters (number of SERS probes per cluster) was revealed by sampling the distribution in Figure 5.10. A relation between the measured SERS

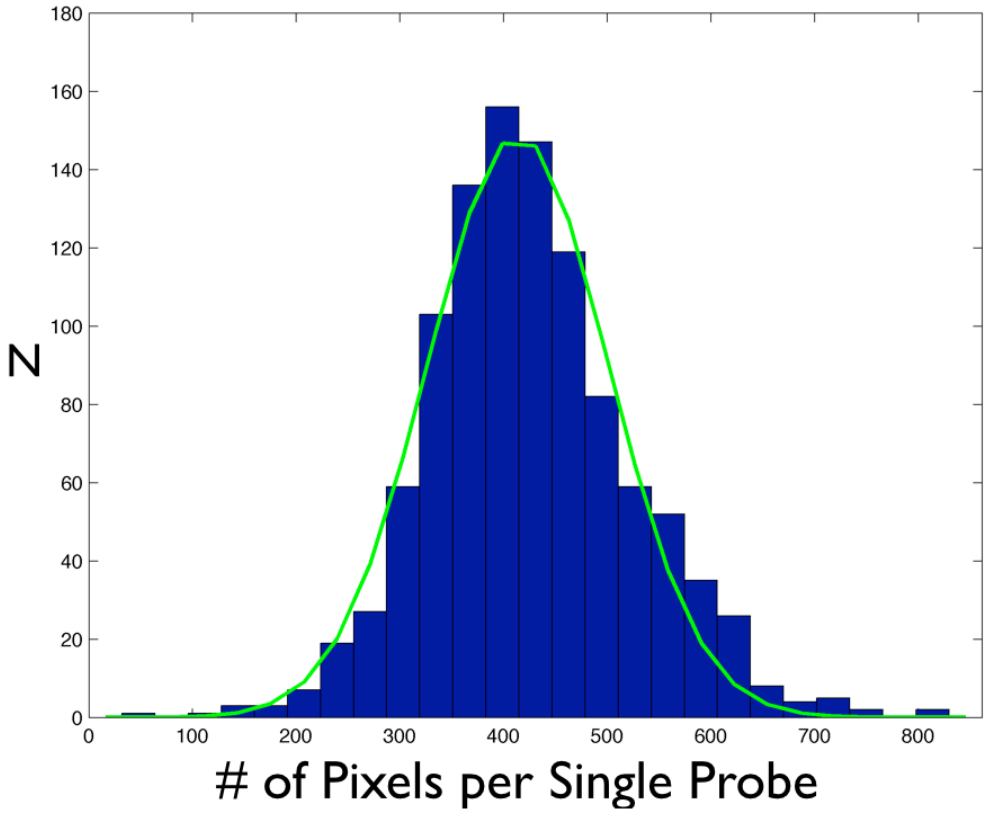

Figure 5.9: Histogram showing the distribution of single SERS probe size in pixels, and a Gaussian fit to the data (in green).

intensity and the SERS probe clusters in the sampled area was then defined, according to equation 3.1. By sampling the distributions of Figure 5.5, 5.10 and 5.11 many times, a linearly independent system of equations was produced fully describing the relationship between the measured SERS intensities and the clusters probed by the laser. The representative system of equations provided a statistically robust result, determined from sampling the histograms as much as 1000 times or more.

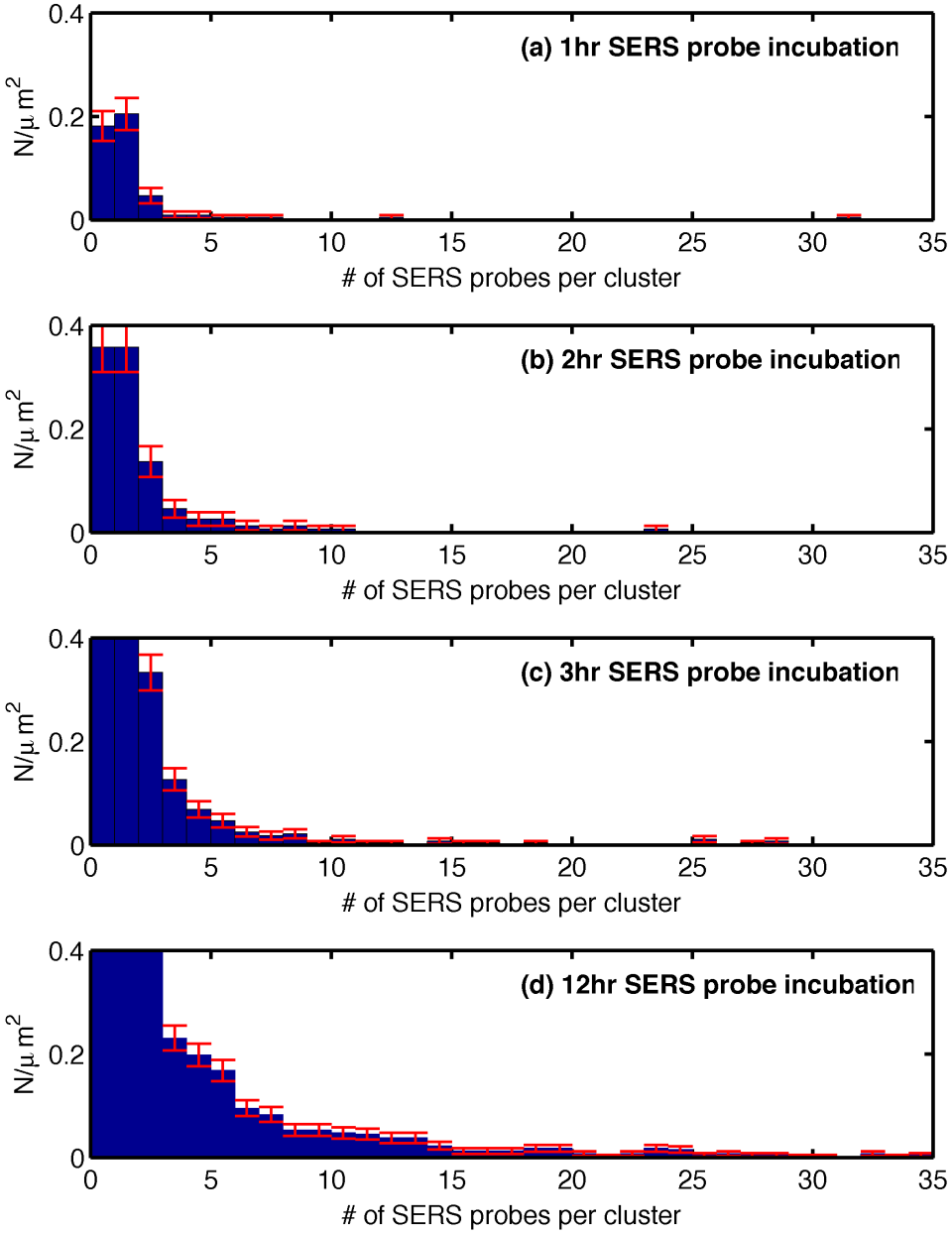

Figure 5.10: Histogram showing the distribution of cluster sizes (measured in the number of SERS probes per cluster) for the region of the slide incubated with SERS probes for (a) 1hr; (b) 2hrs; (c) 3hrs; (d) 12hrs. The histograms are each normalized by the area of the slide imaged with the SEM for the corresponding region (A^t_{SEM}; t = 1hr, 2hr, 3hr, 12hr). Error bars indicate $\pm 1\sigma$ $\quad (\frac{1}{A^t_{SEM}} * N^{1/2}_{bin})$.

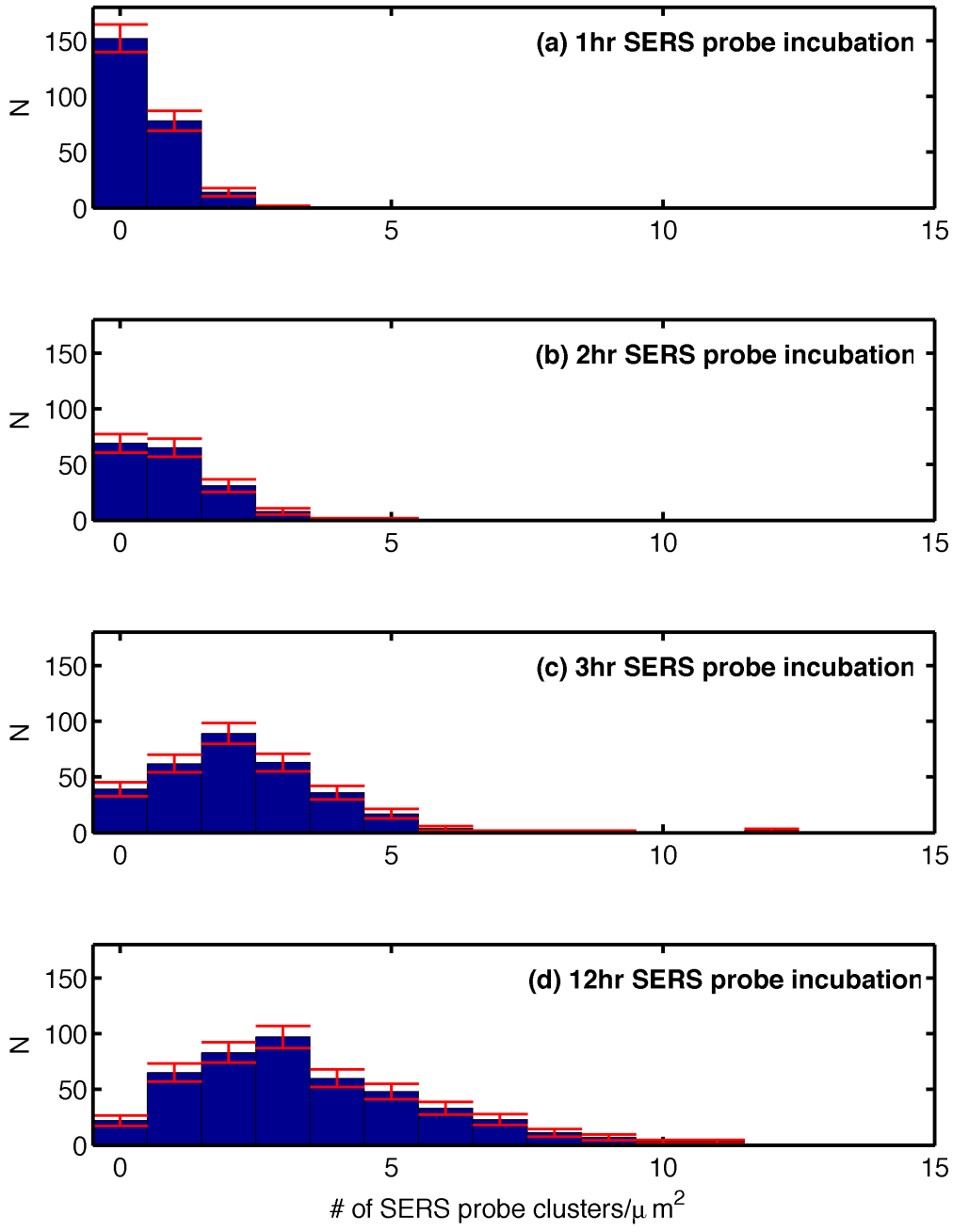

Figure 5.11: Histograms showing the distribution of illuminated SERS probe clusters per acquisition for the data corresponding to the (a) 1hr; (b) 2hr; (c) 3hr; (d) 12hr probe incubation times. Error bars correspond to $\pm 1\sigma \quad (N_{bin}^{1/2})$.

5.1.4 Solving systems of equations for the SERS Intensity Ratios

As described in full in section 3.6.4, the SERS intensity at each illuminated area was correlated to the number of SERS probe clusters and their size in that same area. In other words, the total SERS intensity from a particular spot was treated as a linear sum of SERS intensity contributions from each cluster (as in equation 3.1). The individual intensities from each cluster were unknown, and for each incubation time a linearly independent set of equations was generated to allow for the SERS intensity attributed to each SERS probe cluster size to be evaluated. The system of equations for each SERS data set contained m variables, with m being the maximum cluster size for a particular set. Due to the fact that very large SERS probe clusters (> 15 probes) were rarely detected, particularly for the shorter probe incubation times (see figure 5.10), it was decided that the total SERS intensity distributions could be described by only considering SERS probe clusters up to a maximum cutoff value, m_{max}. For each incubation time, a different value for m_{max} was chosen, based on the cluster size distributions of Figure 5.10.

Starting with the 1hr incubation time, a value of $m_{max} = 6$ was chosen (based on where the histogram begins to approach zero in figure 5.10(a)), and a 6×6 system of equations was generated. This procedure is illustrated in Figure 5.12. The solutions to the 6×6 system of equations provided values for I_1 to I_6, corresponding to the SERS intensity due to clusters from 1 SERS probe (I_1) to 6 SERS probes (I_6) in size. To account for variability in these solutions, 500 6×6 systems of equations were generated for the 1hr data set and solved, giving 500 independent sets of solutions (figure 5.12(b)). All solutions for I_1 to I_6 were then averaged and the uncertainties on the mean values were calculated (figure 5.12(c)). To provide an idea of the variability in the values of these intensities, seven independent calculations of I_1 to I_6 for the 1 hr incubation experiment have been overlain in Figure 5.13. In Figure 5.13, the solution for I_6 is seen to have a high uncertainty compared to the first five SERS intensity solutions due to the fact that it contains contributions from the relatively small number of NP clusters larger than 6 that form after a 1hr incubation. As a result, I_6 was recalculated from the equations for the 2hr incubation, while $I_1 - I_5$ were treated as known values.

For the 2hr incubation, a system of equations was generated with an m_{max} set to be equal to 9 (based on figure 5.10(b)). In this case, as only $I_6 - I_9$ were unknowns,

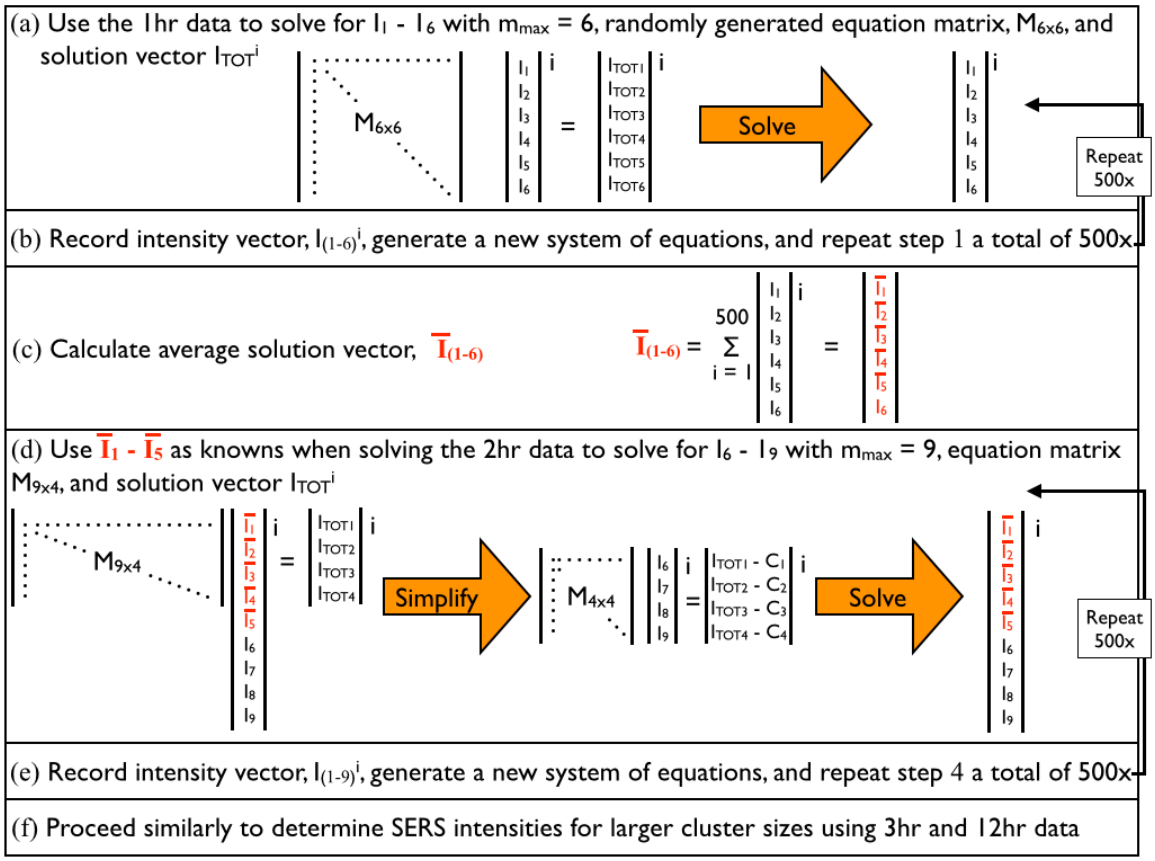

Figure 5.12: Chart describing the method used to solve the system of equations for the SERS intensities due to each SERS probe cluster size.

only four linearly independent equations were required (see figure 5.12(d)). Any contributions from terms involving $I_1 - I_5$ in the equations were known values, and could be subtracted from the vector of I_{TOT} values, simplifying the system as shown in figure 5.12(d). The resultant 4×4 system of equations could then be solved to give solutions for the SERS intensities due to clusters up to 9 probes large (figure 5.12(d)). The process was again repeated 500 times, as discussed in figure 5.12(e), and an average of the solutions was found. The 3hr probe incubation data was then similarly used to find intensity solutions for clusters up to 12 probes large (this time with I_1 to I_8 as known values), and the 12hr probe incubation data was used to find solutions for SERS intensities produced by clusters up to 15 probes large (with I_1 to I_{11} as known values). The final results of the calculations are found in figure 5.14, where the average SERS intensities normalized to the intensity due to a single probe ($\frac{I}{I_1}$) are plotted against the number of SERS probes per cluster. A polynomial fit to

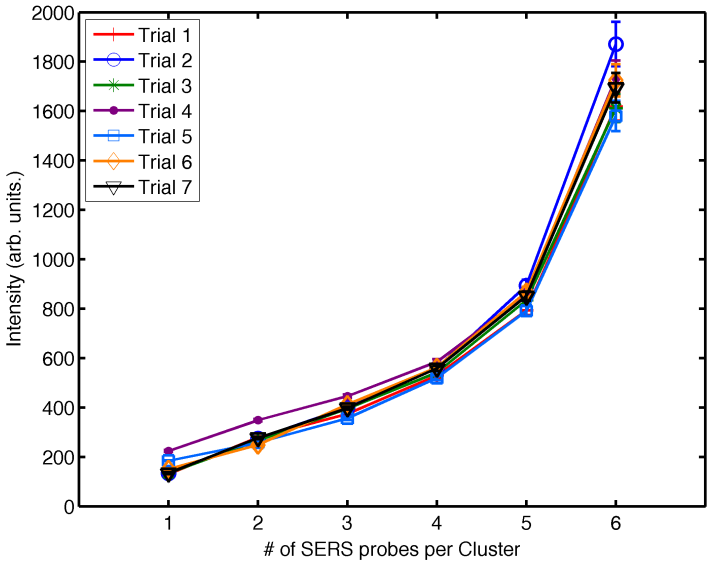

Figure 5.13: Seven independent calculations of the SERS intensities due to the first six cluster sizes.

the data in figure 5.14 is also provided.

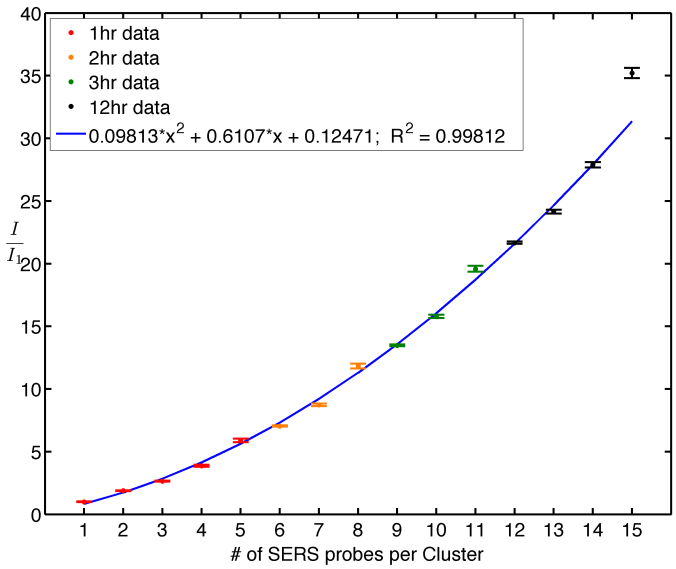

Figure 5.14: SERS intensity ratio solutions due to clusters from 1 to 15 SERS probes in size. The data set used to calculate each of the values is indicated. A polynomial fit of the first 14 intensity ratios is included.

High reproducibility of the calculated SERS intensities of figure 5.14 is suggested

by the strong agreement ($p < 0.05$) between the seven sets of independent calculations of the SERS intensities for the first six cluster sizes shown in Figure 5.13.

5.2 Discussion

When using NPs as a substrate in SERS, the specific enhancement to the Raman signal of the sample provided by the NPs can be highly variable and difficult to control. In general, it is known that an irregular surface allows for the greatest enhancement, and that a collection of NPs provides greater enhancement than a single NP [169]. Studies that observe the change in the SERS intensity as a function of random NP aggregation have shown an increase in intensity with aggregation [211–214], and the polynomial relationship shown in Figure 5.14 supports this idea. However, the gradual increase in SERS intensity with SERS probe cluster size is somewhat unexpected considering that studies of multiple depositions of NP monolayers show a more rapid increase in average SERS intensity as the number of layers (and thus NP aggregation) increases, eventually reaching a plateau [212–214]. Similarly, studies of individual NP clusters [177, 182] found a very sharp increase in intensity (as much as 4 orders of magnitude) between single and dimer NPs. However, the study by Wustholz *et al.* [177] highlights the importance of inter-particle spacing when it comes to SERS enhancement, noting that an increase in the cluster size does not necessarily result in a larger potential SERS enhancement. In fact, their results suggest that a pair of NPs with a sufficient spacing can produce a hot spot which can potentially result in a SERS enhancement as large as that provided by bigger clusters.

The gradual rise of the curve in Figure 5.14 seems to suggest that the type of hot spot that would result in a 4 orders of magnitude increase in SERS intensity between a single and dimer SERS probe was not observed in this work, or at least didn't occur frequently enough to influence the average SERS intensities for each cluster size. Likely, this is due to the fact that the distance between the Au-NP cores of the SERS probes used to generate Figure 5.14 was mediated by the PEG coating. The pegylation of the Au-NPs and their functionalization with streptavidin to form the SERS probes provided a relatively thick coating that limited the distance of closest approach between the Au-NP cores which was not present on the Au-NPs used in the work of Wustholz *et al.* [177]. Due to this fundamental difference, we cannot expect that our work will compare directly with that of Wustholz *et al.* [177]. However, the systematic attempt to correlate SERS intensities to NPs cluster

sizes performed by Wustholz *et al.* [177] does mirror the study described here. In our case, the molecular coating provided by the PEG seems to have prevented the conditions necessary for the formation of the type of hot-spots formed in between the NPs of the Wustholz study that provided such significant rises in SERS intensity, and likely had an effect on the rapid increase in SERS intensity found in the studies of multiple depositions of NP monolayers [212–214] and of nanorod aggregation [211]. Indeed, in high magnification SEM images of clusters of the SERS probes (as can be seen in figure 5.7), there is a clear separation of 10-20 nm between many of the probes within the clusters. It is possible that the separation between the NPs in the SERS probe clusters causes the probes to provide surface-enhancement somewhat independently of each other, and the intensity due to a cluster is the cumulative result of the intensity due to each probe in the cluster. However, this would suggest a linear relationship, which is not what is seen in Figure 5.14. While the exact reason for the non-linear nature of the relationship in Figure 5.14 is unclear, it does imply that there may be some degree of hot-spot interaction between the probes in the cluster. Similarly, it is possible that the SERS intensity produced by the clusters is affected by a relationship between the gold slide surface and the SERS probes, whether that be due to a hot-spot interaction, or simply reflection of Raman scattered photons towards the objective that would otherwise have been lost. Nonetheless, the polynomial relationship between SERS probe clusters and their resultant SERS intensity is extremely well defined ($R^2 = 0.99812$) and reproducible (see Figure 5.13), and a non-linear component to the relationship is entirely possible.

Given confidence in the reproducibility and accuracy of the results shown in Figure 5.14, the polynomial relationship that the figure displays will prove to be useful in experiments that use PEG NPs as SERS probes. The exhibited relationship between cluster size and the resultant SERS intensity is unique to the PEG NP probes described in this work, and these probes, based on those in the paper by Qian *et al.* [2], are specifically designed for targeted SERS imaging, such as in the identification of proteins within cells and tissues. As discussed in section 2.3.4, determining the quantity and distribution of the target within the SERS maps of a sample remains challenging. However, considering the simple relationship between cluster size and SERS intensity shown in Figure 5.14, PEG NP SERS probes seem ideally suited for quantifiable SERS mapping. For example, a simple technique would involve first determining the average SERS probe cluster size formed after the chosen incubation time, using information such as the histograms shown in figure 5.10. Knowing the

average cluster size, the SERS intensity at a given point would be known to be a multiple of the intensity due to a single cluster. It would then be straightforward to determine the number of clusters contributing to the total SERS intensity at the given point and thus the number of targeted sites could be determined at that location.

5.3 Conclusion

The work presented in this chapter provides a novel technique that relates 2D SERS intensity maps to SEM images of SERS probes on a biotinylated gold surface, allowing for the calculation of SERS intensities due to SERS probe clusters of varying size. In order to examine a variety of cluster sizes, targeted SERS probes were incubated with biotinylated surfaces for several time periods prior to the acquisition of SEM and SERS images. Using the SEM images and SERS maps, statistical descriptions of both the SERS probe cluster distribution and SERS intensities on the surface were developed. Based on the statistical relationships, linearly independent systems of equations relating the measured SERS intensity to the distribution of SERS probe clusters on the slide were devised. Solutions to the equations provided the SERS intensities resulting from enhancement due to clusters from 1 to 14 SERS probes in size.

A simple polynomial relationship between SERS probe cluster size and resultant SERS intensity was found, suggesting the utility of pegylated SERS probes in targeted SERS mapping. By simply controlling the probe incubation time to limit the distribution of cluster sizes formed in a targeted SERS sample, quantification of targeted sites within a sample would be relatively straightforward. The ability to quantify targeted sites in a sample would make targeted SERS mapping a viable technique for imaging protein distribution within cells and tissues, providing a quantifiable, high-resolution alternative to methods such as immunohistochemistry.

Chapter 6

Results and Discussion III: Determining Ionizing Radiation-Induced Damage to Streptavidin using a Streptavidin/Biotin ELISA

The results presented in this chapter are from two separate experiments that look to determine how the binding ability of a protein (namely streptavidin) is affected by exposure to various doses of ionizing radiation. An enzyme-linked immunosorbant assay (ELISA; see section 3.5.2) was used to determine the concentration of bound streptavidin in solutions exposed to doses between 0 and 250 Gy. Two separate batches of streptavidin solutions were irradiated and investigated using the ELISA. The results of the first experiment are presented in section 6.1, and those of the second experiment are shown in section 6.2. Each experiment included two sets of protein solutions, one with streptavidin dissolved in PBS, and one with streptavidin dissolved in PBS with 3.5% BSA (in order to mimic a physiological total protein concentration). Two ELISAs were designed to investigate the effect of ionizing radiation on the binding ability of streptavidin. As described in section 3.5.3, a direct sandwich ELISA tested the ability of the irradiated streptavidin to bind to biotin, and a direct standard ELISA tested the ability of the irradiated streptavidin to bind to anti-streptavidin (the detection antibody). The results of the sandwich ELISA are

described in section 6.1.1 for the first experiment, and section 6.2.1 for the second experiment. A discussion of the results is presented in section 6.1.3. Sections 6.1.2 and 6.2.2 describe the results of the standard ELISA for experiments 1 and 2, respectively, followed by a discussion in section 6.2.3. Finally, the chapter concludes with a summary of the results and a potential extension of the work in section 6.3.

6.1 Results of First Series of ELISA Experiments

For the first set of ELISAs, three solutions of 5μg/mL strepavidin in PBS were prepared (type A), as well as three solutions of 5μg/mL streptavidin in PBS with 3.5% BSA (type B). One of each set of solutions was left as an unirradiated control (0Gy), and the other two of each set were irradiated to 30 and 60 Gy, respectively. A direct sandwich ELISA to test for the ability of the irradiated streptavidin to bind to biotin was performed 2 and 30 hrs post-irradtion (section 6.1.1) as were direct ELISAs to test for the ability of the irradiated streptavidin to bind to anti-streptavidin (section 6.1.2). Details of the procedure for the direct standard ELISA are provided in section 3.5.3 of chapter 3.

6.1.1 Biotin ELISA to test binding of Irradiated Streptavidin

Both of the direct sandwich ELISAs were performed according to the schematic of the 96-well plate shown in table 6.1. Columns 2 and 3 were duplicates containing serial dilutions of streptavidin, and the absorbances of these columns were averaged along the rows and used to generate the type A standard curve (relating streptavidin concentration to absorbance) for the ELISA done 2 hrs post-irradiation (shown in figure 6.1(a)) and the ELISA performed 30 hrs post-irradiation (figure 6.1(b)). The standard curves for the type B samples were generated using the averaged absorbances of columns 5 and 6, and are shown in figure 6.1(c) for the 2 hrs post-irradiation ELISA and figure 6.1(d) for the ELISA performed 30 hrs post-irradiation. Each of the standard curves were fit with a line using a least-squares fit algorithm in Matlab, and the equation of each line is shown in the corresponding figure.

Columns 1 and 4 of the plate shown in table 6.1 contained the irradiated streptavidin samples at a concentration of 0.005 μg/mL (in the middle region of the standard curves shown in figure 6.1). Each column contained two duplicates of the 0 Gy sample, three duplicates of the 30 Gy samples and three duplicates of the 60 Gy samples.

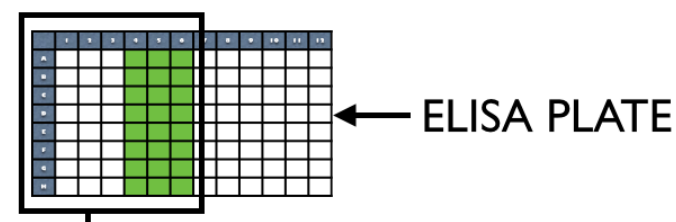

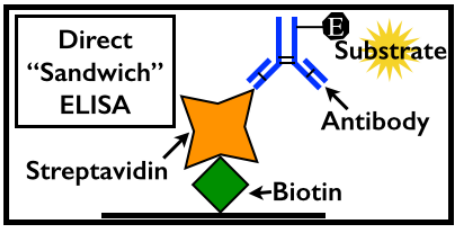

ZOOM

	1	2	3	4	5	6
A	0.005 µg/mL strep. **0 Gy**	Control No strep.	Control No strep.	0.005 µg/mL strep. **0 Gy**	Control No strep.	Control No strep.
B	0.005 µg/mL strep. **0 Gy**	0.001 µg/mL strep.	0.001 µg/mL strep.	0.005 µg/mL strep. **0 Gy**	0.001 µg/mL strep.	0.001 µg/mL strep.
C	0.005 µg/mL strep. **30 Gy**	0.0025 µg/mL strep.	0.0025 µg/mL strep.	0.005 µg/mL strep. **30 Gy**	0.0025 µg/mL strep.	0.0025 µg/mL strep.
D	0.005 µg/mL strep. **30 Gy**	0.005 µg/mL strep.	0.005 µg/mL strep.	0.005 µg/mL strep. **30 Gy**	0.005 µg/mL strep.	0.005 µg/mL strep.
E	0.005 µg/mL strep. **30 Gy**	0.0075 µg/mL strep.	0.0075 µg/mL strep.	0.005 µg/mL strep. **30 Gy**	0.0075 µg/mL strep.	0.0075 µg/mL strep.
F	0.005 µg/mL strep. **60 Gy**	0.01 µg/mL strep.	0.01 µg/mL strep.	0.005 µg/mL strep. **60 Gy**	0.01 µg/mL strep.	0.01 µg/mL strep.
G	0.005 µg/mL strep. **60 Gy**	0.0125 µg/mL strep.	0.0125 µg/mL strep.	0.005 µg/mL strep. **60 Gy**	0.0125 µg/mL strep.	0.0125 µg/mL strep.
H	0.005 µg/mL strep. **60 Gy**	0.015 µg/mL strep.	0.015 µg/mL strep.	0.005 µg/mL strep. **60 Gy**	0.015 µg/mL strep.	0.015 µg/mL strep.

Table 6.1: Schematic of the ELISA plate for the Sandwich ELISA. White wells contained streptavidin dissolved in PBS (type A), and green wells contained streptavidin dissolved in PBS w/ 3.5% BSA (type B).

The mean and standard deviation of each set of duplicates were calculated, and the absorbance values were converted to streptavidin concentration according to the relevant standard curve. Figure 6.2(a) shows the concentration of streptavidin bound to biotin after irradiation to each dose for both type A (red) and type B (blue) samples in the 2 hr - ELISA, and figure 6.2(b) shows the same for the 30 hr - ELISA.

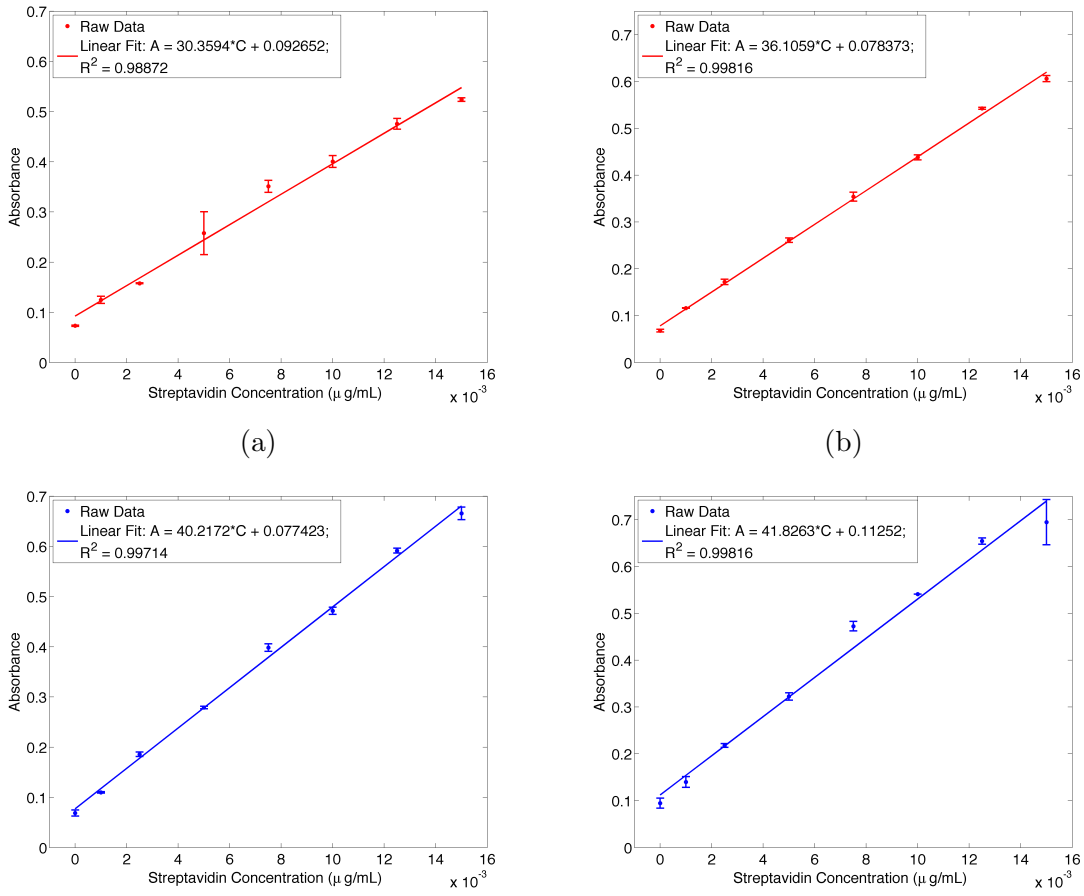

Figure 6.1: Standard Curves for the Sandwich ELISA done (a) 2hrs post-irradiation with streptavidin in PBS (type A); (b) 30hrs post-irradiation with streptavidin in PBS (type A); (c) 2hrs post-irradiation with streptavidin in PBS w/ 3.5% BSA (type B); and (d) 30hrs post-irradiation with streptavidin in PBS w/ 3.5% BSA (type B).

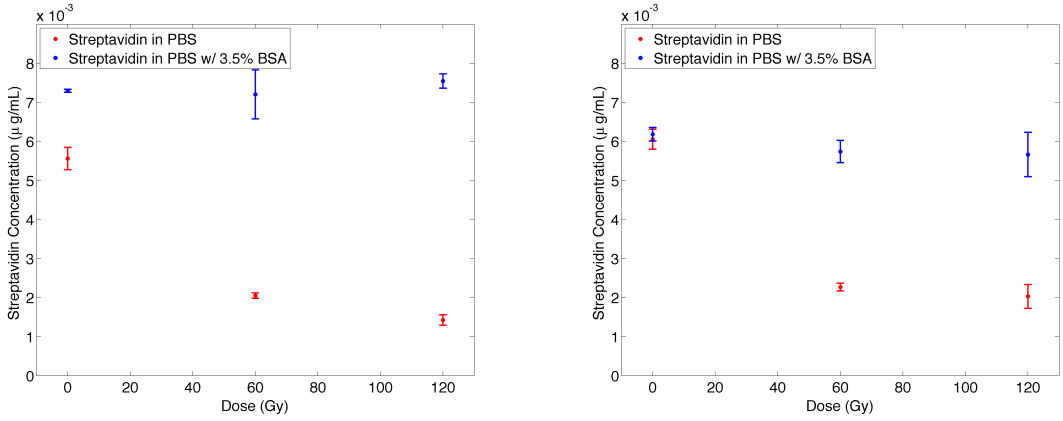

(a) (b)

Figure 6.2: Concentration of streptavidin in PBS (type A; red) and streptavidin in PBS with 3.5% BSA (type B; blue) detected in the direct Sandwich ELISA (a) 2 hrs and (b) 30 hrs after irradiation to various doses.

6.1.2 Irradiated Streptavidin ELISA to test binding of Anti-Streptavidin

The schematics of the plates for the direct ELISAs designed to test the ability of irradiated streptavidin to bind to anti-streptavidin are shown in table 6.2. The schematic differs slightly for the ELISAs performed 2 hrs (table 6.2(a)) and 30 hrs (table 6.2(b)) post-irradiation. For the 30 hr - ELISA a duplicate of each of the columns in the 2 hr - ELISA was included to improve the statistics of the result. As a result, for the 2-hr ELISA, there were 2 duplicates of the 0 Gy sample, 3 duplicates of the 30 Gy sample, and 3 duplicates of the 60 Gy sample. For the 30 hr - ELISA, the number of duplicates for each dose point was doubled.

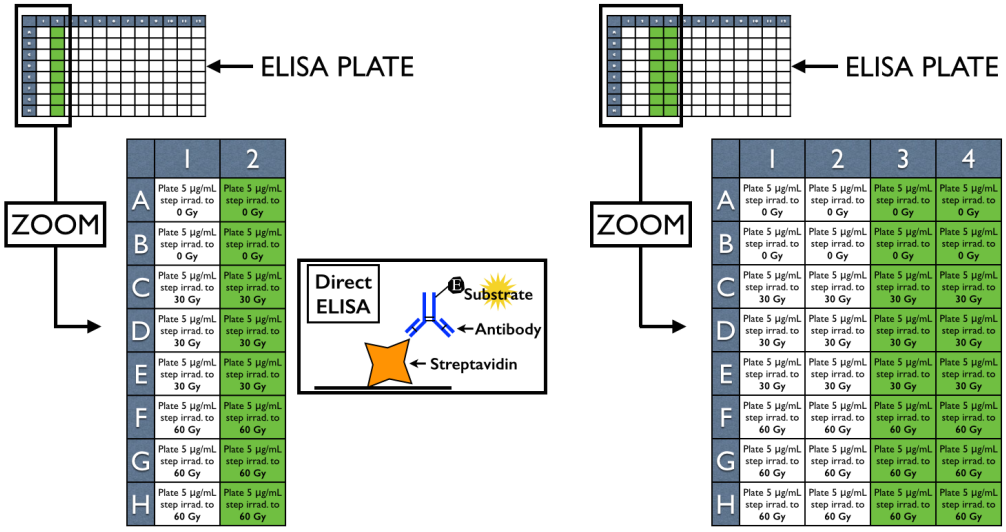

(a) (b)

Table 6.2: Schematic of the ELISA plate for the Direct ELISA done (a) 2hrs and (b) 30hrs post-irradiation. White wells contained streptavidin dissolved in PBS (type A), and green wells contained streptavidin dissolved in PBS w/ 3.5% PBS (type B).

The average absorbance measured at each dose point ($\pm 1\sigma$) is shown in figure 6.3(a) for both the type A (red) and type B (blue) samples in the 2 hr - ELISA, and in figure 6.3(b) for the 30 hr - ELISA.

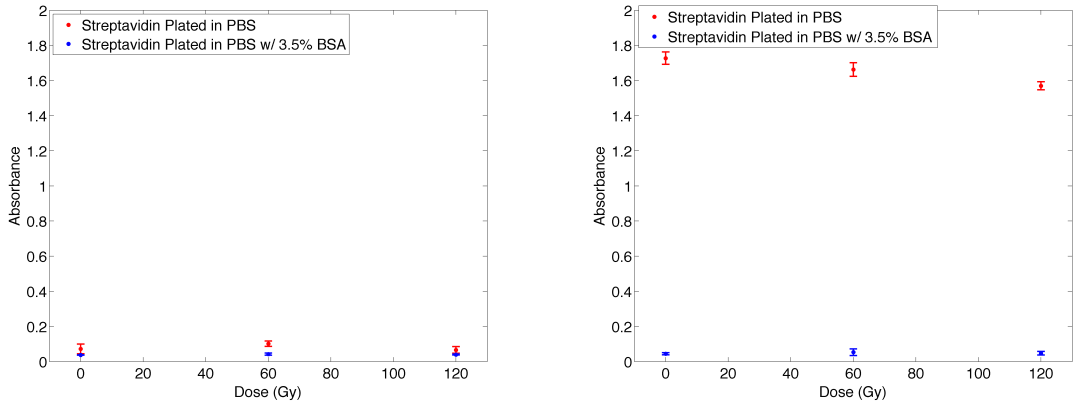

(a) (b)

Figure 6.3: Absorbance of streptavidin in PBS (type A; red) and streptavidin in PBS with 3.5% BSA (type B; blue) detected in the direct Standard ELISA (a) 2 hrs and (b) 30 hrs after irradiation to various doses.

6.1.3 Discussion of Results

In preparation for the ELISAs performed in the first experiment, several test ELISAs were run to determine a range of streptavidin concentrations in which the relationship between absorbance and concentration could be represented by a linear fit. As can be seen in figure 6.1, the R^2 values of the linear fits to the standard curves verify the assumption of linearity.

Upon consideration of figure 6.2(a), it can be seen that the concentration of bound streptavidin from type A samples (red) detected in the sandwich ELISA performed 2 hrs post-irradiation decreases significantly between the 0 Gy and 30 Gy samples, and continues to decrease (albeit less significantly) for the 60 Gy sample. The same trend is noticed for the type A samples in the 30 hr - ELISA as well (figure 6.2(b)). It is not expected for there to be a difference in the results of the 2 hr and 30 hr - ELISAs, as damage to the protein will occur within milliseconds of irradiation [15] and no repair will occur post-irradiation as the samples are not alive. However, comparing the results of the ELISAs at each time point is useful in order to check for any errors in experimental technique (discussed further in section 6.1.4).

For the type B samples (blue), in both figure 6.2(a) and (b), there appears to be little change in the detected concentration of bound streptavidin between dose points. The streptavidin concentrations for each type B sample essentially lie within uncertainty of the nominal streptavidin concentration present at 0 Gy. As such, it

appears that the streptavidin in the irradiated type B samples is undamaged by the radiation, and able to bind to biotin as well as if they had not received any dose. The reason that the streptavidin molecules remain functional is likely due to the high concentration of BSA present in the type B samples. Due to the abundance of BSA molecules in the type B solutions (present at 0.035g/L compared to streptavidin at 5μg/mL, in a ratio of 7000:1), most of the free radicals generated in the samples after irradiation would have interacted with a BSA molecule before ever reaching a streptavidin molecule. Essentially, the surrounding BSA acts to "shield" the streptavidin from ionizing radiation-induced damage.

When there was a change in the detected concentration of streptavidin between the dose points in figure 6.2 it was assumed to be due to damage to the streptavidin molecule resulting in a change in the ability of the protein to bind to its complement biotin. However, if radiation-damage affected the ability of the streptavidin to bind to anti-streptavidin (the detection antibody), a reduction in detected streptavidin would also be observed. In fact, it is possible that the streptavidin molecule could be damaged in such a way that it was able to bind to the biotin coating the ELISA plate, but it would not be detected because the damage resulted in an inability to bind to anti-streptavidin. As such, the results of the sandwich ELISA confirm that the binding of the streptavidin is affected by exposure to ionizing radiation, but it does not specify precisely which binding site on the streptavidin molecule was damaged.

The direct ELISA described in section 6.1.2 was designed as a control to determine with specificity whether the ability of streptavidin to bind to anti-streptavidin was affected by exposure to ionizing radiation. Figure 6.3 shows the results of the direct ELISAs performed 2 hrs and 30 hrs post-irradiation, displaying measured absorbance as a function of sample dose. The figures do not show streptavidin or anti-streptavidin concentration as a function of dose due to the fact that the standard curves of figure 6.1 were generated from sandwich ELISA plates and thus only apply to those plates. However, variations in absorbance are still directly related to variations in concentration and are sufficient for the purpose of the direct ELISAs as controls.

In figure 6.3(a), it can be seen the absorbance corresponding to the samples at each dose point for both the type A and B samples are very low. These absorbances essentially correspond to no binding of streptavidin to anti-streptavidin, and this is due to the fact that for the 2 hr - direct ELISA, the wells of the 96 well plate were rinsed with blocking buffer before being plated with the streptavidin samples. The Maxisorp$^{\text{TM}}$plates used for the direct ELISA have a high affinity for protein, and it

is likely that BSA in the blocking buffer bound to all of the available sites in each well, leaving nowhere for the streptavidin to bind. As a result, the results in figure 6.3(a) are not useful, and it is only possible to consider the results of the 30 hr - direct ELISA.

When considering the results of the 30 hr - direct ELISA shown in figure 6.3(b), it can be seen that the absorbances for the type B samples are still very low. Since the type B samples contain 3.5% BSA (even more than the 1% BSA in the blocking buffer), all of the binding sites in the wells of the Maxisorp™ plate have again been filled by BSA instead of streptavidin. As such, useful information from the direct ELISA can only be determined for the type A samples, containing streptavidin dissolved in PBS with no BSA. However, this is not a significant disadvantage, as the results of the direct sandwich ELISA for the type B samples already implied that the binding ability of streptavidin was not significantly affected by the radiation, due to the high concentration of BSA also present in the samples.

For the type A samples, however, figure 6.3(b) shows that a slight decrease in absorbance, and thus the concentration of anti-streptavidin that binds to streptavidin, appears to occur as the dose to the sample increases. As the sensitivity of the relationship between absorbance and anti-streptavidin concentration is not known for the direct ELISA, a straightforward comparison with the direct sandwich ELISA is not possible. However, as an approximation, it is useful to compare the results of figure 6.3(b) with the raw absorbance data of the direct sandwich ELISA for the Type A samples. In figure 6.3(b), the percent difference in absorbance between the 0 and 60 Gy samples is only about 9%, compared to the $\sim$ 50% difference in absorbance between the 0 and 60 Gy type A samples in the direct sandwich ELISA (calculated from the raw data). The significant increase in % difference for the type A samples in the direct sandwich ELISA seems to imply that the majority of the changes in the detected concentration of streptavidin between dose points is due to radiation damage affecting the ability of streptavidin to bind to biotin, and not its ability to bind to anti-streptavidin. This result is not entirely surprising, as polyclonal [269] anti-streptavidin was used, which consists of a collection of antibodies that each recognize a different binding site (known as an *epitope*) on streptavidin. Due to the abundance of epitopes on streptavidin that anti-streptavidin can recognize, it is likely that the antibodies will still be able to identify some functional epitopes on the irradiated streptavidin molecule.

In comparison, streptavidin only has four binding sites for biotin [270]. Also,

a complex network of molecules are involved in the bond between streptavidin and biotin, all of which are important in forming a strong bond that almost completely encloses the biotin molecule [271]. Specifically, the binding site is considered as a system of amino acid *residues*, which are what remains of individual amino acids after binding together to form the *polypeptide* chains of a protein [269]. At each binding site, biotin is tightly bound to streptavidin through a series of hydrogen bonds and Van Der Waals interactions with the amino acid residues [271–274]. Hydrogen bonds are formed by amino acid residues of serine, aspartic acid, tyrosine, and asparagine, while Van Der Waals contacts primarily occur at residues of tryptophan [271–274]. The importance of both types of bonds have been verified by previous studies involving selective mutagenesis of the streptavidin binding sites [275–279], and it has been found that changes to select amino acid residues can significantly affect the integrity of the streptavidin/biotin bond. As a result, ionizing radiation-induced damage to any of the amino acid residues at the streptavidin binding sites could affect the ability of streptavidin to bind to biotin. Alternatively, damage to residues outside of the streptavidin binding site could affect the conformation (structure) of the protein which is known to also have an effect on the binding ability [280–287]. Due to the multiple factors that can affect the binding ability of streptavidin, while the ELISA technique can determine whether the streptavidin binding sites have been compromised, it is not possible to determine the specific residues that have experienced damage from the ELISA technique alone.

6.1.4 Errors in ELISA technique

In regards to variation between the results of the 2 hr and 30 hr ELISAs, it was generally observed that the same trends were identified at each time point. However, as mentioned earlier, comparisons between the ELISAs at each time point are useful in identifying errors in experimental technique. Error predominantly occurs during the pipetting stages of the ELISA, and while each well is intended to receive 100 μL of sample, a slight variation in volume is inevitable. As a result, some of the error bars on the data points are larger than others, while any systematic errors in technique may result in over or underestimates of the measured absorbances. Inaccuracy in pipetting can also lead to changes in the slope of the standard curves, affecting their accuracy.

An obvious example of error is seen in figure 6.2(a), where the detected strepta-

vidin concentration in the type A and type B 0 Gy samples differs. The concentration of these samples should both be approximately 0.005μg/mL, as that is the nominal concentration used for the unirradiated samples. The detected streptavidin concentration for the type A and B 0 Gy samples do overlap each other in figure 6.2(b), likely due to more accurate pipetting, however the concentration is approximately 0.006 μg/mL instead of 0.005 μg/mL. While the results of figure 6.2(b) are still an improvement, if high precision results are required in the future it will be necessary to repeat each ELISA multiple times. However, as the purpose of the experiments described in this chapter was to observe general trends, the results are still very useful.

6.2 Results of Second Series of ELISA Experiments

The second ELISA experiment was designed to verify the results of the first experiment (section 6.1), and also to irradiate the samples to a wider variety of doses. For experiment # 2, eight solutions of 5μg/mL streptavidin in PBS (type A) were prepared, as were four solutions of 5μg/mL strepavidin in PBS with 3.5% BSA (type B). As in the first experiment, one of each set of solutions was left as an unirradiated control (0 Gy). For the type A solution, samples were irradiated to either 5, 10, 20, 40, 60, 80 or 120 Gy. Type B samples were irradiated to 0, 60, 120, or 240 Gy. Due to the lack of dose response of the type B samples in experiment # 1, the doses to the type B samples in the second experiment remained coarsely spaced but included a very high maximum dose.

Section 6.2.1 presents the results of direct sandwich ELISAs performed 2 and 30 hrs post-irradiation on the type A and B samples, and the results of direct ELISAs performed 2 and 30 hrs post-irradiation are shown in section 6.2.2. A discussion of the results follows in section 6.2.3. As with the first experiment, the sandwich ELISA tests the ability of the streptavidin in the irradiated type A and B samples to bind to biotin, and the direct ELISA tests the ability of anti-streptavidin to bind to streptavidin from the irradiated samples.

6.2.1 Biotin ELISA to test binding of Irradiated Streptavidin

A schematic of the plates for the direct sandwich ELISAs performed both 2 and 30hrs after the irradiations are shown in table 6.3. Both plates are very similar, but in the

ZOOM

	1	2	3	4	5	6	7	8	9	10
A	0.005 µg/mL strep. 0 Gy	0.005 µg/mL strep. 0 Gy	0.005 µg/mL strep. 0 Gy	0.005 µg/mL strep. 0 Gy	Control No strep.	Control No strep.	0.005 µg/mL strep. 0 Gy	0.005 µg/mL strep. 0 Gy	Control No strep.	Control No strep.
B	0.005 µg/mL strep. 5 Gy	0.005 µg/mL strep. 5 Gy	0.005 µg/mL strep. 5 Gy	0.005 µg/mL strep. 5 Gy	0.001 µg/mL strep.	0.001 µg/mL strep.	0.005 µg/mL strep. 0 Gy	0.005 µg/mL strep. 0 Gy	0.001 µg/mL strep.	0.001 µg/mL strep.
C	0.005 µg/mL strep. 10 Gy	0.005 µg/mL strep. 10 Gy	0.005 µg/mL strep. 10 Gy	0.005 µg/mL strep. 10 Gy	0.0025 µg/mL strep.	0.0025 µg/mL strep.	0.005 µg/mL strep. 60 Gy	0.005 µg/mL strep. 60 Gy	0.0025 µg/mL strep.	0.0025 µg/mL strep.
D	0.005 µg/mL strep. 20 Gy	0.005 µg/mL strep. 20 Gy	0.005 µg/mL strep. 20 Gy	0.005 µg/mL strep. 20 Gy	0.005 µg/mL strep.	0.005 µg/mL strep.	0.005 µg/mL strep. 60 Gy	0.005 µg/mL strep. 60 Gy	0.005 µg/mL strep.	0.005 µg/mL strep.
E	0.005 µg/mL strep. 40 Gy	0.005 µg/mL strep. 40 Gy	0.005 µg/mL strep. 40 Gy	0.005 µg/mL strep. 40 Gy	0.0075 µg/mL strep.	0.0075 µg/mL strep.	0.005 µg/mL strep. 120 Gy	0.005 µg/mL strep. 120 Gy	0.0075 µg/mL strep.	0.0075 µg/mL strep.
F	0.005 µg/mL strep. 60 Gy	0.005 µg/mL strep. 60 Gy	0.005 µg/mL strep. 60 Gy	0.005 µg/mL strep. 60 Gy	0.01 µg/mL strep.	0.01 µg/mL strep.	0.005 µg/mL strep. 120 Gy	0.005 µg/mL strep. 120 Gy	0.01 µg/mL strep.	0.01 µg/mL strep.
G	0.005 µg/mL strep. 80 Gy	0.005 µg/mL strep. 80 Gy	0.005 µg/mL strep. 80 Gy	0.005 µg/mL strep. 80 Gy	0.0125 µg/mL strep.	0.0125 µg/mL strep.	0.005 µg/mL strep. 240 Gy	0.005 µg/mL strep. 240 Gy	0.0125 µg/mL strep.	0.0125 µg/mL strep.
H	0.005 µg/mL strep. 120 Gy	0.005 µg/mL strep. 120 Gy	0.005 µg/mL strep. 120 Gy	0.005 µg/mL strep. 120 Gy	0.015 µg/mL strep.	0.015 µg/mL strep.	0.005 µg/mL strep. 240 Gy	0.005 µg/mL strep. 240 Gy	0.015 µg/mL strep.	0.015 µg/mL strep.

(a)

	1	2	3	4	5	6	7	8	9	10	11	12
A	0.005 µg/mL strep. 0 Gy	0.005 µg/mL strep. 0 Gy	0.005 µg/mL strep. 0 Gy	0.005 µg/mL strep. 0 Gy	Control No strep.	Control No strep.	Control No strep.	0.005 µg/mL strep. 0 Gy	0.005 µg/mL strep. 0 Gy	Control No strep.	Control No strep.	Control No strep.
B	0.005 µg/mL strep. 5 Gy	0.005 µg/mL strep. 5 Gy	0.005 µg/mL strep. 5 Gy	0.005 µg/mL strep. 5 Gy	0.001 µg/mL strep.	0.001 µg/mL strep.	0.001 µg/mL strep.	0.005 µg/mL strep. 0 Gy	0.005 µg/mL strep. 0 Gy	0.001 µg/mL strep.	0.001 µg/mL strep.	0.001 µg/mL strep.
C	0.005 µg/mL strep. 10 Gy	0.005 µg/mL strep. 10 Gy	0.005 µg/mL strep. 10 Gy	0.005 µg/mL strep. 10 Gy	0.0025 µg/mL strep.	0.0025 µg/mL strep.	0.0025 µg/mL strep.	0.005 µg/mL strep. 60 Gy	0.005 µg/mL strep. 60 Gy	0.0025 µg/mL strep.	0.0025 µg/mL strep.	0.0025 µg/mL strep.
D	0.005 µg/mL strep. 20 Gy	0.005 µg/mL strep. 20 Gy	0.005 µg/mL strep. 20 Gy	0.005 µg/mL strep. 20 Gy	0.005 µg/mL strep.	0.005 µg/mL strep.	0.005 µg/mL strep.	0.005 µg/mL strep. 60 Gy	0.005 µg/mL strep. 60 Gy	0.005 µg/mL strep.	0.005 µg/mL strep.	0.005 µg/mL strep.
E	0.005 µg/mL strep. 40 Gy	0.005 µg/mL strep. 40 Gy	0.005 µg/mL strep. 40 Gy	0.005 µg/mL strep. 40 Gy	0.0075 µg/mL strep.	0.0075 µg/mL strep.	0.0075 µg/mL strep.	0.005 µg/mL strep. 120 Gy	0.005 µg/mL strep. 120 Gy	0.0075 µg/mL strep.	0.0075 µg/mL strep.	0.0075 µg/mL strep.
F	0.005 µg/mL strep. 60 Gy	0.005 µg/mL strep. 60 Gy	0.005 µg/mL strep. 60 Gy	0.005 µg/mL strep. 60 Gy	0.01 µg/mL strep.	0.01 µg/mL strep.	0.01 µg/mL strep.	0.005 µg/mL strep. 120 Gy	0.005 µg/mL strep. 120 Gy	0.01 µg/mL strep.	0.01 µg/mL strep.	0.01 µg/mL strep.
G	0.005 µg/mL strep. 80 Gy	0.005 µg/mL strep. 80 Gy	0.005 µg/mL strep. 80 Gy	0.005 µg/mL strep. 80 Gy	0.0125 µg/mL strep.	0.0125 µg/mL strep.	0.0125 µg/mL strep.	0.005 µg/mL strep. 240 Gy	0.005 µg/mL strep. 240 Gy	0.0125 µg/mL strep.	0.0125 µg/mL strep.	0.0125 µg/mL strep.
H	0.005 µg/mL strep. 120 Gy	0.005 µg/mL strep. 120 Gy	0.005 µg/mL strep. 120 Gy	0.005 µg/mL strep. 120 Gy	0.015 µg/mL strep.	0.015 µg/mL strep.	0.015 µg/mL strep.	0.005 µg/mL strep. 240 Gy	0.005 µg/mL strep. 240 Gy	0.015 µg/mL strep.	0.015 µg/mL strep.	0.015 µg/mL strep.

(b)

Table 6.3: Schematic of the ELISA plate for the Sandwich ELISA performed (a) 2hrs and (b) 30hrs post-irradiation. White wells contained streptavidin dissolved in PBS (type A), and green wells contained streptavidin dissolved in PBS w/ 3.5% PBS (type B).

ELISA performed 30 hrs post-irradiation (figure 6.3(b)), two of the unfilled columns in figure 6.3(a) were used for extra duplicates of the standard streptavidin dilutions. As such, columns 5 and 6 were type A duplicates for the 2hr ELISA (figure 6.3(a)) and columns 5-7 were duplicates for the 30hr ELISA (figure 6.3(b)). The absorbances of the duplicate columns were averaged along the rows to generate the points for the standard curve of the type A samples 2hrs (figure 6.4(a)) and 30 hrs post-irradiation (figure 6.4(b)). The data points for the standard curves of the type B samples were generated using the averaged absorbances of columns 9 and 10 for the 2hr ELISA (figure 6.3(a)) and columns 10-12 for the 30hr ELISA (figure 6.3(b)). The standard curve for the 2hr ELISA is shown in figure 6.4(c) and the curve for the 30hr ELISA is shown in figure 6.4(d). Each set of data points in figure 6.4 were fit with a line using the least-squares fit algorithm in Matlab.

The wells containing the irradiated streptavidin samples are shown in columns 1-4 (type A) and 7-8 (type B) of table 6.3(a) (2hr ELISA) and columns 1-4 (type A) and 8-9 (type B) of table 6.3(b) (30hr ELISA). All irradiated samples were diluted to 0.005 μg/mL before being added to the ELISA plate. For both the type A and type B samples, there were four duplicate wells at each of the dose points, and the mean absorbance and standard deviation of each set of wells were calculated. Using the standard curves of figure 6.4 all absorbance values were converted to streptavidin concentration. The concentration of bound streptavidin as a function of dose for the type A samples is shown in figure 6.5(a) for the 2hr-ELISA and figure 6.5(b) for the 30hr-ELISA. Similarly, the corresponding curves for the type B samples are shown in figures 6.6 (a) and (b).

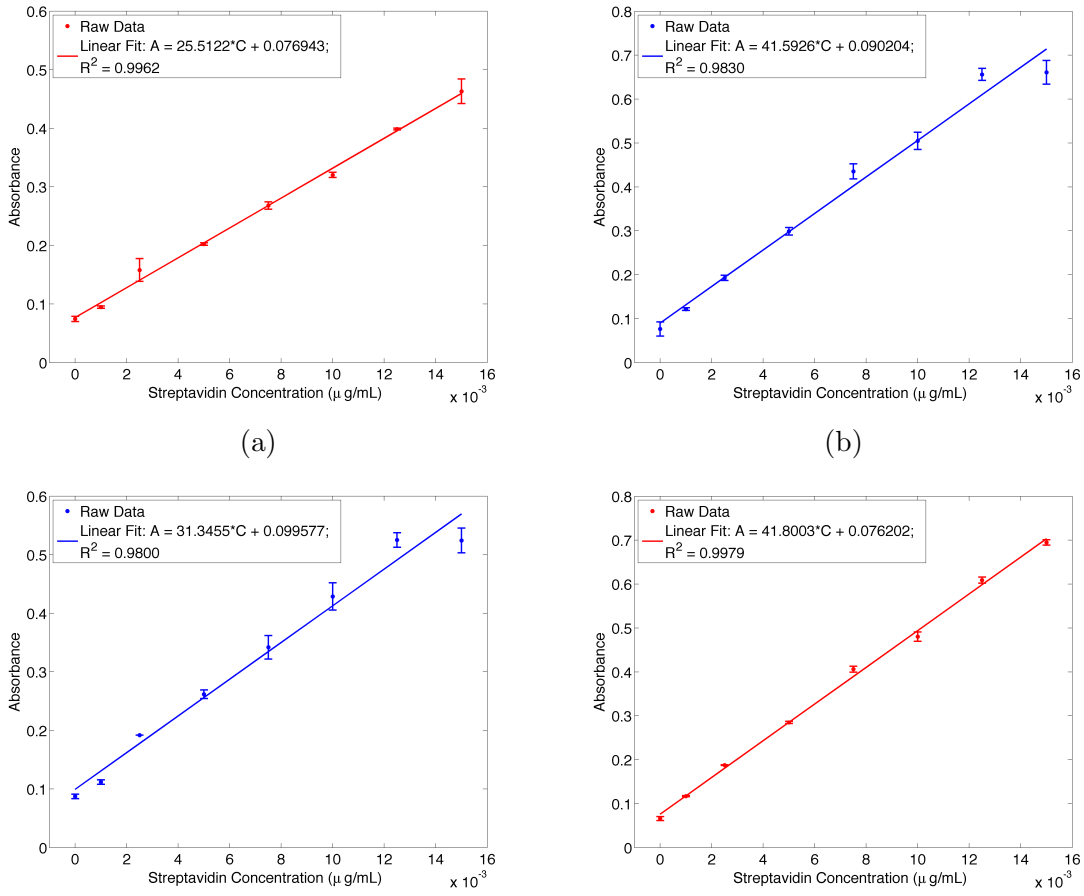

Figure 6.4: Standard Curves for the Sandwich ELISA done (a) 2hrs post-irradiation with streptavidin in PBS (type A); (b) 30hrs post-irradiation with streptavidin in PBS (type A); (c) 2hrs post-irradiation with streptavidin in PBS w/ 3.5% BSA (type B); and (d) 30hrs post-irradiation with streptavidin in PBS w/ 3.5% BSA (type B).

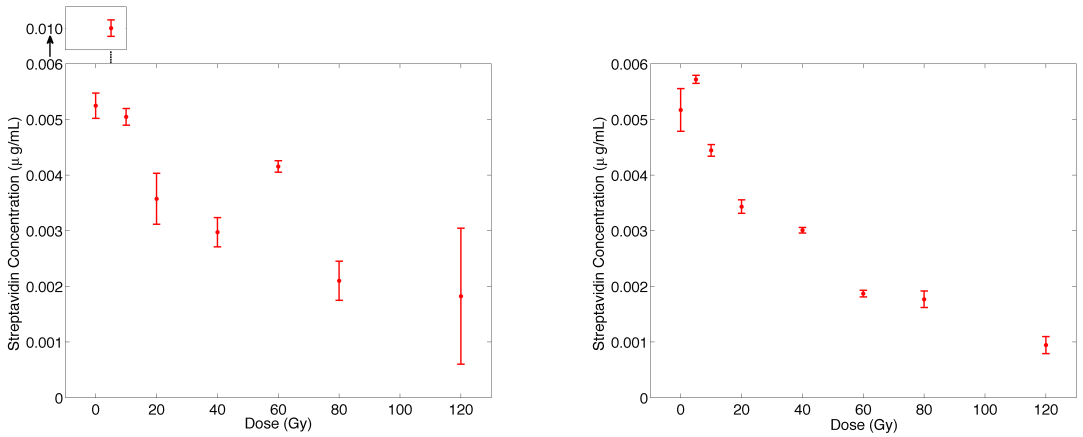

(a) (b)

Figure 6.5: Concentration of streptavidin in PBS (type A) detected in the direct Sandwich ELISA (a) 2 hrs and (b) 30 hrs after irradiation to various doses.

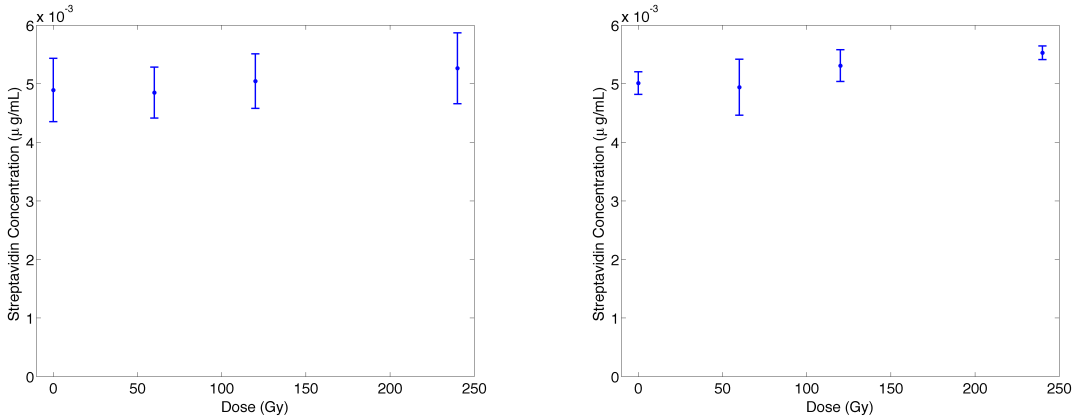

(a) (b)

Figure 6.6: Concentration of streptavidin in PBS w/ 3.5% BSA (type B) detected in the direct Sandwich ELISA (a) 2 hrs and (b) 30 hrs after irradiation to various doses.

6.2.2 Irradiated Streptavidin ELISA to test binding of Anti-Streptavidin

ZOOM

	1	2	3	4	5	6
A	Plate 5 µg/mL step irrad. to 0 Gy	Plate 5 µg/mL step irrad. to 0 Gy	Plate 5 µg/mL step irrad. to 0 Gy	Plate 5 µg/mL step irrad. to 0 Gy	Plate 5 µg/mL step irrad. to 0 Gy	Plate 5 µg/mL step irrad. to 0 Gy
B	Plate 5 µg/mL step irrad. to 5 Gy	Plate 5 µg/mL step irrad. to 5 Gy	Plate 5 µg/mL step irrad. to 5 Gy	Plate 5 µg/mL step irrad. to 5 Gy	Plate 5 µg/mL step irrad. to 0 Gy	Plate 5 µg/mL step irrad. to 0 Gy
C	Plate 5 µg/mL step irrad. to 10 Gy	Plate 5 µg/mL step irrad. to 10 Gy	Plate 5 µg/mL step irrad. to 10 Gy	Plate 5 µg/mL step irrad. to 10 Gy	Plate 5 µg/mL step irrad. to 60 Gy	Plate 5 µg/mL step irrad. to 60 Gy
D	Plate 5 µg/mL step irrad. to 20 Gy	Plate 5 µg/mL step irrad. to 20 Gy	Plate 5 µg/mL step irrad. to 20 Gy	Plate 5 µg/mL step irrad. to 20 Gy	Plate 5 µg/mL step irrad. to 60 Gy	Plate 5 µg/mL step irrad. to 60 Gy
E	Plate 5 µg/mL step irrad. to 40 Gy	Plate 5 µg/mL step irrad. to 40 Gy	Plate 5 µg/mL step irrad. to 40 Gy	Plate 5 µg/mL step irrad. to 40 Gy	Plate 5 µg/mL step irrad. to 120 Gy	Plate 5 µg/mL step irrad. to 120 Gy
F	Plate 5 µg/mL step irrad. to 60 Gy	Plate 5 µg/mL step irrad. to 60 Gy	Plate 5 µg/mL step irrad. to 60 Gy	Plate 5 µg/mL step irrad. to 60 Gy	Plate 5 µg/mL step irrad. to 120 Gy	Plate 5 µg/mL step irrad. to 120 Gy
G	Plate 5 µg/mL step irrad. to 80 Gy	Plate 5 µg/mL step irrad. to 80 Gy	Plate 5 µg/mL step irrad. to 80 Gy	Plate 5 µg/mL step irrad. to 80 Gy	Plate 5 µg/mL step irrad. to 240 Gy	Plate 5 µg/mL step irrad. to 240 Gy
H	Plate 5 µg/mL step irrad. to 120 Gy	Plate 5 µg/mL step irrad. to 120 Gy	Plate 5 µg/mL step irrad. to 120 Gy	Plate 5 µg/mL step irrad. to 120 Gy	Plate 5 µg/mL step irrad. to 240 Gy	Plate 5 µg/mL step irrad. to 240 Gy

Table 6.4: Schematic of the ELISA plate for the Direct ELISA. White wells contained streptavidin dissolved in PBS, and green wells contained streptavidin dissolved in PBS w/ 3.5% BSA.

For the direct ELISA performed 2hrs and 30hrs post-irradiation to test the ability of plated irradiated streptavidin to bind to anti-streptavidin, a schematic of the ELISA plate is shown in table 6.4. The type A samples were plated in columns 1-4, and the type B samples were plated in columns 5 and 6. Each well was plated with a 5μg/mL sample solution for 60 minutes, as described in section 3.5.3. For both the type A and B samples, there were four duplicate wells for each of the irradiated solutions. The absorbance of each set of duplicate wells was averaged and the standard deviation was calculated.

For the type A samples, the absorbance as a function of dose is shown in figure 6.7(a) as determined from the 2hr-ELISA, and in figure 6.7(b) as determined from

the 30hr-ELISA. Figure 6.8(a) shows the absorbance as a function of dose for the type B samples in the 2hr-ELISA, and figure 6.8(b) shows the same for the type B samples in the 30hr-ELISA.

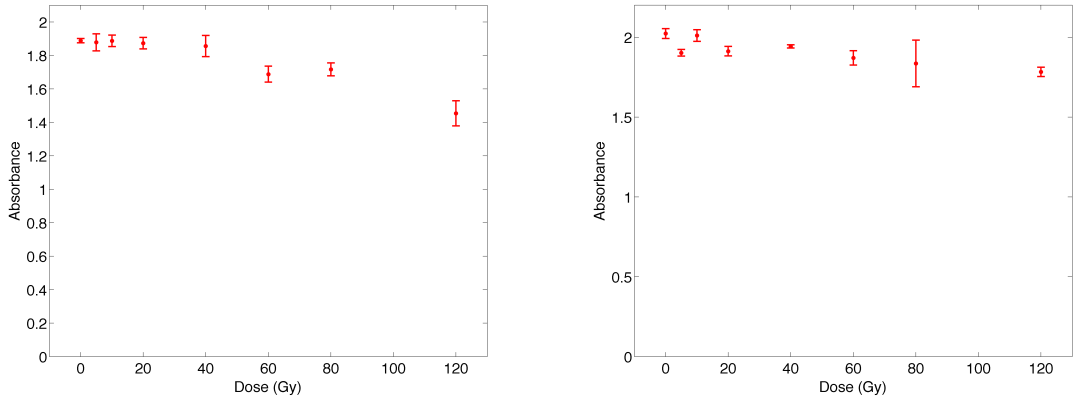

(a) (b)

Figure 6.7: Absorbance of streptavidin in PBS (type A) detected in the direct Standard ELISA (a) 2 hrs and (b) 30 hrs after irradiation to various doses.

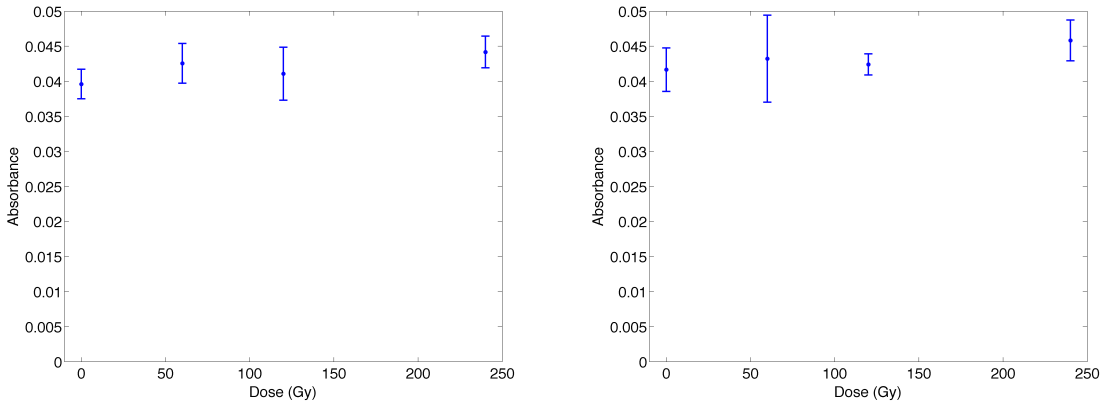

(a) (b)

Figure 6.8: Absorbance of streptavidin in PBS w/ 3.5% BSA (type B) detected in the direct Standard ELISA (a) 2 hrs and (b) 30 hrs after irradiation to various doses.

6.2.3 Discussion of Results

As with the first experiment, the standard curves shown in figure 6.4 for the ELISAs performed as part of the second experiment are all well represented with a linear fit.

Despite small fluctuations in the points, likely due to pipetting errors (as described in section 6.1.4), a linear fit is accurate with the R^2 values (shown in figure 6.4) all very close to unity. The accuracy of the standard curves is further reflected in the fact that the bound streptavidin concentrations for both the unirradiated type A (figure 6.5) and B (figure 6.6) samples in the 2hr and 30hr ELISAs are within uncertainty of 0.005 μg/mL, which is the nominal concentration of solution added to each well. Since the streptavidin in the unirradiated samples has experienced no ionizing radiation-induced damage, a concentration of 0.005 μg/mL is expected as all of the streptavidin in the solutions should bind to the biotin in the wells.

With increasing dose, the type A and type B samples show trends similar to those identified in the first experiment (section 6.1). For the type A samples, in both the ELISAs performed 2hrs (figure 6.5(a)) and 30hrs (figure 6.5(b)) after irradiation, the amount of bound streptavidin detected clearly decreases with increasing dose. In figure 6.5(b), the trend is more clear, likely due to improved experimental technique. While the data points in figure 6.5(a) do also show a decrease in bound streptavidin with increasing dose, there is more fluctuation in the points, and the error bars are larger, indicating less consistent pipetting during the ELISA. The detected streptavidin concentration at 5 Gy in figure 6.5(a) is a significant outlier, with a concentration much higher than that at 0 Gy. It is not expected that the detected streptavidin concentration would increase as the irradiation dose increases, and the significant increase between the 0 and 5 Gy doses is not seen in figure 6.5(b). Aside from errors in technique, there is no reason for a difference between figures 6.5(a) and (b), so it is likely that the sharp increase seen in figure 6.5(a) is inaccurate. While there is a small increase in streptavidin concentration between the 0 Gy and 5 Gy points in figure 6.5(b), the increase is likely a result of a slight error in experimental technique, as ionizing radiation-induced damage to the streptavidin is expected to reduce the binding ability of the protein. It may be possible that changes in protein conformation caused by low doses of radiation could potentially cause streptavidin to bind more readily to biotin, but such a conclusion could not be drawn without confirmation by further experiments. In general, both figures 6.5(a) and (b) show a decrease in the binding ability of streptavidin as the dose increases.

The behaviour of the type B samples are much more consistent between the 2 and 30 hr ELISAs shown in figure 6.6, with the detected bound streptavidin concentration remaining essentially at 0.005 μg/mL (the nominal concentration) for all doses. The result is consistent with the findings of the first experiment (section 6.1), and

further confirms the effective "shielding" of the streptavidin by the surrounding BSA molecules.

As for the results of the direct ELISA, which investigates the effect of ionizing radiation on the ability of streptavidin to be detected by anti-streptavidin, significant results can only be inferred for the type A samples (figure 6.7). The results for the type B samples are shown in figure 6.8, and as with the blue data points of figure 6.3 from the first experiment, all absorbance values are very low, implying that there is no streptavidin plated on the surface of the wells. Again, the lack of streptavidin is due to the high concentration of BSA in the type B solution sticking to the wells of the Maxisorp™ plate and leaving no space for streptavidin.

In figure 6.7, the absorbance values are 50x higher than in figure 6.8, and streptavidin from the type A samples was clearly present in the wells of the corresponding ELISA plates. The results are again presented as absorbances since no calibration curve was generated for the direct ELISAs. For the direct ELISA of the type A samples performed 2hrs post-irradiation (figure 6.7(a)), the amount of anti-streptavidin that binds to the plated streptavidin appears to remain relatively constant until there is a slight drop at 60 Gy, and then again at 120 Gy. The results of the 30hr ELISA shown in figure 6.7(b) are similar, but show a more gradual decrease in absorbance with dose. Also, the error bars of the absorbance detected from the type A sample irradiated to 80 Gy in figure 6.7(b) essentially encompass the absorbances at all dose points. The large error bar of the 80Gy point may be due to pipetting error, and as such, it is also possible that the absorbance fluctuations observed in figure 6.7 may all be related to experimental technique and not ionizing radiation-induced damage to the plated streptavidin. Compared to the changes in absorbance detected in the results of the sandwich ELISAs for the type A samples (maximum % difference of $\sim$ 60%; calculated from the raw absorbance data), the fluctuations of figure 6.7 (maximum % difference of $\sim$ 20%) are relatively minor. Nonetheless, it is possible that there is a decrease in the ability of anti-streptavidin to bind to streptavidin after exposure of the streptavidin to ionizing radiation, but as was found in the first experiment, it appears to be less significant than the effect that the radiation has on the ability of streptavidin to bind to biotin.

6.3 Summary of Results and Future Work

When considering the results of both experiments as a whole, it is clear that the ELISA is an effective technique in observing ionizing radiation-induced effects on the bonding ability of streptavidin. Using a direct sandwich ELISA, a decrease in the amount of detected streptavidin with dose can be identified. A statistically significant decrease in streptavidin from the type A samples can be identified at doses as low as 10 Gy (figure 6.5(b)), and the decrease continues steadily up to 120 Gy. When streptavidin is irradiated as part of a solution containing BSA at a physiological total protein concentration (type B), no significant change in the binding ability of streptavidin is detected. In the streptavidin/BSA solution, free radicals generated by the ionizing radiation are much more likely to interact with a BSA molecule rather than streptavidin, due to the high concentration of BSA relative to streptavidin in the solution (7000:1). Effectively, the streptavidin is shielded by the surrounding BSA, in a manner somewhat analogous to the radiation-shielding of DNA by surrounding protein in DNA-protein complexes [63, 65].

The fact that radiation damage to streptavidin in the BSA solution is not detectable by ELISA is also significant, because it implies that identifying radiation damage to a particular type of protein in a sample containing other proteins using the ELISA technique may be challenging. Ideally, it would be useful to analyze ionizing radiation-induced damage to particular proteins in a sample taken from living tissue in order to better understand the response of the body to ionizing radiation. However, unless the protein of interest was particularly sensitive to radiation, or was present in large quantities in the body, it may not be possible to identify ionizing radiation-induced changes to one protein in a multi-protein solution using an ELISA. At the same time, there is no reason that the technique could not be used in determining radiation-induced damage to a protein of interest that has been isolated and irradiated independently. Depending on the protein bonds investigated by the ELISA, such studies could provide highly specific information about the nature of radiation damage to proteins which could be pieced together to provide a better picture of the radio-response of proteins as a whole in living tissue.

As identified in this chapter, however, if a direct sandwich ELISA is used to determine the effect of ionizing radiation on the ability of a protein to bind to a complementary protein, it will be necessary to also consider the effect of radiation on the ability of the protein to bind to its detection antibody. In the work presented in

this chapter, the sandwich ELISA was meant to observe any changes in the binding of streptavidin and biotin due to ionizing radiation, but the effect on the binding ability of streptavidin and anti-streptavidn also had to be considered using a direct standard ELISA. Fortunately, polyclonal detection antibodies recognize multiple epitopes on the protein, and as such are expected to be able to bind to even highly damaged proteins. In this work, it was found that only small decreases in the amount of anti-streptavidin that was able to bind to irradiated streptavidin were found as the dose increased. As seen in figures 6.3 and 6.7, significant changes in the amount of bound anti-streptavidin were only noticeable when doses increased beyond 60 Gy. Typically, clinically relevant studies of ionizing radiation-induced damage would only investigate doses less than or equal to about 60 Gy, as prescribed doses rarely exceed 60 Gy in radiation treatment. As a result, in such studies, any proteins that were studied would likely remain intact enough to be identified by a polyclonal detection antibody, as was the streptavidin in this experiment.

In summary, the use of ELISA appears to show promise in the investigation of ionizing radiation-induced damage to proteins due to clinically relevant doses. However, before significant conclusions can be made about the results of the study presented here, it will be necessary to perform repeat experiments in order to minimize fluctuations due to error in technique. Future work could then focus on other proteins and their interactions with various complementary proteins. Of particular interest may be proteins involved in the cellular DNA repair response, and other proteins whose correct functionality is essential to cell survival.

Chapter 7

Conclusions

The work presented in this thesis looks to assess the feasibility of using protein-targeted SERS probes in the analysis of ionizing radiation-induced damage to cells. Efforts initially focused on the development of a reproducible technique for cell culture, incubation with SERS probes and SERS mapping with a Raman microscope. Two different types of SERS probe were studied, both comprised of a gold nanoparticle core. In Type I probes, a detection antibody was linked to the gold nanoparticle by the molecule DSNB, while the antibody was linked to the gold through a polyethylene glycol shell in the Type II probes. Initially, the Type I probes were targeted to the TACSTD2 protein of CaOV3 cancer cells using an antibody specific to the protein that was provided by the DRC at BCCA-VIC. However, due to a lack of characteristic SERS signal identified in SERS maps, and the limited knowledge of the distribution of the TACSTD2 protein on CaOV3 cells, a simplified experiment was developed. In the revised experiment, biotin was artificially coated on the surface of OVCAR5 cells and was targeted by gold nanoparticle probes conjugated to streptavidin. Also, focus shifted to the Type-II SERS probes due to the known reduction in non-specific binding provided by the PEG coating.

Unfortunately, two-dimensional SERS maps displayed very few spectra containing the characteristic SERS signal of the probes. In order to verify the components of the experiment, both fluorescence microscopy, and a biotin-coated gold slide were utilized. After incubating biotinylated cells with fluorescent streptavidin, images obtained by a fluorescence microscope confirmed the presence of biotin on the cell surface membrane. Further, SERS maps of a gold slide coated with a biotin monolayer and incubated with Type-II streptavidin SERS probes displayed SERS signal covering the slide surface. However, despite the fact that the biotinylation process and the

functionality of the SERS probes had been verified, SERS mapping of biotinylated cells incubated with targeted SERS probes remained unsuccessful.

Despite difficulties encountered in the SERS mapping of cells, the success of the SERS probes on the biotinylated gold slides provided a unique opportunity to characterize the highly variable enhancement typically provided by SERS probes. Four biotinylated gold slides were incubated with Type-II SERS probes for different times (1hr, 2hr, 3hr, 12hr) allowing for the formation of differently size clusters of probes on the slide surfaces. Randomly selected regions on each slide were then imaged with a Raman microscope and a SEM, and the physical distribution of the probes on the slides was related to the spectral distribution through a series of equations. As a result, a simple polynomial relationship between SERS intensity and the size of the SERS probe cluster providing the enhancement was determined. The smooth polynomial differed from the expected sharp, somewhat constant enhancement found previously for clusters of two NPs or more. It is believed that the PEG coating of the Type-II SERS probes separates the NP cores of the probes enough to prevent the formation of "hot spots" that result in highly variable SERS enhancements. Without "hot spots" the Type-II SERS probes exhibit less significant SERS enhancement, but the smooth polynomial relationship between cluster size and intensity will be beneficial in the future development of quantifiable SERS measurements.

Due to the continuing difficulties with the SERS mapping of cells incubated with targeted SERS probes, an independent experiment was devised to test whether ionizing radiation-induced damage to proteins would result in a detectable change in the distribution of SERS probes on the cell surface. A series of ELISAs were performed to determine whether exposure to ionizing radiation would affect the ability of solutions of streptavidin to bind to biotin. It was found that an appreciable drop in the concentration of streptavidin able to bind to biotin was noticed at doses as low as 10 Gy. However, if the solutions of streptavidin contained BSA at a physiological total protein concentration, no change in the binding ability of streptavidin was detected. It is believed that the large number of BSA molecules in the solution act to shield the streptavidin from the free radicals generated by ionizing radiation.

In conclusion, the Type II SERS probes show great promise as tools for targeted SERS mapping of cells. Also, the relationship between SERS intensity and the SERS probe cluster size determined in this work allows for the measured SERS intensity to be related back to the number of probes at the point illuminated by the excitation laser, leading to quantifiable SERS measurements. Despite the remaining difficulty

to detect SERS signal after incubating the probes with fixed cells, the Type II SERS probes have demonstrated functionality, and a well-characterized manufacturing process. Further, the results of the ELISA tests show that clinically relevant doses of ionizing radiation will lead to changes in the ability of a protein to bind to its complement. As a result, it will be possible to detect a difference in protein distribution between irradiated and unirradiated cells using targeted SERS imaging following the development of a suitable probe incubation procedure in future experiments.

Bibliography

[1] D. S. Grubisha, R. J. Lipert, H.-Y. Park, J. Driskell, and M. D. Porter, "Femtomolar Detection of Prostate-Specific Antigen: An Immunoassay Based on Surface-Enhanced Raman Scattering and Immunogold Labels," *Analytical Chemistry (Washington, DC, United States)*, vol. 75, pp. 5936–5943, Nov. 2003.

[2] X. Qian, X.-H. Peng, D. O. Ansari, Q. Yin-Goen, G. Z. Chen, D. M. Shin, L. Yang, A. N. Young, M. D. Wang, and S. Nie, "In vivo tumor targeting and spectroscopic detection with surface-enhanced Raman nanoparticle tags," *Nature biotechnology*, vol. 26, no. 1, pp. 83–90, 2008.

[3] D. C. Rizzo, *Fundamentals of Anatomy and Physiology*. Clifton Park, NY, USA: Thomson Delmar Learning, second ed., 2006.

[4] A. Campion and P. Kambhampati, "Surface-enhanced Raman scattering," *Chemical Society Reviews*, vol. 27, no. 4, pp. 241–250, 1998.

[5] J. R. Lombardi, R. L. Birke, T. Lu, and J. Xu, "Charge-transfer theory of surface enhanced Raman spectroscopy: Herzberg–Teller contributions," *The Journal of Chemical Physics*, vol. 84, no. 8, p. 4174, 1986.

[6] P. P. Connell and S. Hellman, "Advances in Radiotherapy and Implications for the Next Century: A Historical Perspective," *Cancer Research*, vol. 69, pp. 383–392, Jan. 2009.

[7] H. E. Johns and J. R. Cunningham, *The Physics of Radiology*. Springfield, Illinois, USA: Charles C. Thomas Publisher, fourth ed., 1983.

[8] F. M. Khan, *The Physics of Radiation Therapy*. Philadelphia, PA, USA: Lippincott Williams & Wilkins, fourth ed., Mar. 2012.

[9] J. T. Bushberg, J. A. Seibert, E. M. Leidholdt, and J. M. Boone, *The Essential Physics of Medical Imaging*. Philadelphia, PA, USA: Lippincott Williams & Wilkins, third ed., Dec. 2011.

[10] N. Chawapun, "Update on clinical radiobiology," *Biomedical Imaging and Intervention Journal*, vol. 2, no. 1, 2006.

[11] K. Harrington, P. Jankowska, and M. Hingorani, "Molecular biology for the radiation oncologist: the 5Rs of radiobiology meet the hallmarks of cancer.," *Clinical oncology (Royal College of Radiologists (Great Britain))*, vol. 19, pp. 561–571, Oct. 2007.

[12] R. D. Stewart and X. A. Li, "BGRT: Biologically guided radiation therapy—The future is fast approaching!," *Medical Physics*, vol. 34, no. 10, p. 3739, 2007.

[13] P. Symonds and D. Jones, "Advances in Clinical Radiobiology.," *Clinical oncology (Royal College of Radiologists (Great Britain))*, July 2013.

[14] J. S. Good and K. J. Harrington, "The Hallmarks of Cancer and the Radiation Oncologist: Updating the 5Rs of Radiobiology.," *Clinical oncology (Royal College of Radiologists (Great Britain))*, July 2013.

[15] M. Jioner and A. van der Kogel, *Basic Clinical Radiobiology*. Great Britain: Hodder Arnold, fourth ed., May 2009.

[16] G. G. Steel, T. J. McMillan, and J. H. Peacock, "The 5Rs of Radiobiology," *International Journal of Radiation Biology*, vol. 56, no. 6, pp. 1045–1048, 1989.

[17] G. H. Fletcher, "Regaud lecture perspectives on the history of radiotherapy," *Radiotherapy And Oncology*, vol. 12, no. 4, pp. 253–271, 1988.

[18] M. Krause, D. Zips, H. D. Thames, J. Kummermehr, and M. Baumann, "Preclinical evaluation of molecular-targeted anticancer agents for radiotherapy," *Radiotherapy And Oncology*, vol. 80, pp. 112–122, Aug. 2006.

[19] J. A. Bonner, P. M. Harari, J. Giralt, N. Azarnia, D. M. Shin, R. B. Cohen, C. U. Jones, R. Sur, D. Raben, J. Jassem, R. Ove, M. S. Kies, J. Baselga, H. Youssoufian, N. Amellal, E. K. Rowinsky, and K. K. Ang, "Radiotherapy plus Cetuximab for Squamous-Cell Carcinoma of the Head and Neck," *New England Journal of Medicine*, vol. 354, pp. 567–578, Feb. 2006.

[20] S. R. McKeown, R. L. Cowen, and K. J. Williams, "Bioreductive Drugs: from Concept to Clinic," *Clinical Oncology*, vol. 19, pp. 427–442, Aug. 2007.

[21] M. R. Horsman and D. W. Siemann, "Pathophysiologic Effects of Vascular-Targeting Agents and the Implications for Combination with Conventional Therapies," *Cancer Research*, vol. 66, pp. 11520–11539, Dec. 2006.

[22] S. M. Bentzen, "Preventing or reducing late side effects of radiation therapy: radiobiology meets molecular pathology.," *Nature Reviews Cancer*, vol. 6, pp. 702–713, Sept. 2006.

[23] D. M. Brizel, "Pharmacologic Approaches to Radiation Protection," *Journal of Clinical Oncology*, vol. 25, pp. 4084–4089, Sept. 2007.

[24] J. E. Moulder and E. P. Cohen, "Future strategies for mitigation and treatment of chronic radiation-induced normal tissue injury.," *Seminars in radiation oncology*, vol. 17, pp. 141–148, Apr. 2007.

[25] J. S. Greenberger, "Gene therapy approaches for stem cell protection," *Gene Therapy*, vol. 15, pp. 100–108, Aug. 2007.

[26] M. T. Genot-Klastersky, J. Klastersky, F. Awada, A. Awada, P. Crombez, M. D. Martinez, M. F. Jaivenois, M. Delmelle, G. Vogt, N. Meuleman, and M. Paesmans, "The use of low-energy laser (LEL) for the prevention of chemotherapy- and/or radiotherapy-induced oral mucositis in cancer patients: results from two prospective studies.," *Supportive care in cancer : official journal of the Multinational Association of Supportive Care in Cancer*, vol. 16, pp. 1381–1387, Dec. 2008.

[27] J. S. Greenberger and M. W. Epperly, "Review. Antioxidant gene therapeutic approaches to normal tissue radioprotection and tumor radiosensitization.," *In Vivo*, vol. 21, pp. 141–146, Mar. 2007.

[28] K. E. Rieger, "Portrait of transcriptional responses to ultraviolet and ionizing radiation in human cells," *Nucleic acids research*, vol. 32, pp. 4786–4803, Sept. 2004.

[29] C. M. L. West, M. J. McKay, T. Hölscher, M. Baumann, I. J. Stratford, R. G. Bristow, M. Iwakawa, T. Imai, S. M. Zingde, M. S. Anscher, J. Bourhis, A. C.

Begg, K. Haustermans, S. M. Bentzen, and J. H. Hendry, "Molecular markers predicting radiotherapy response: report and recommendations from an International Atomic Energy Agency technical meeting.," in *International Journal of Radiation Oncology, Biology, Physics*, pp. 1264–1273, Academic Department of Radiation Oncology, The University of Manchester, Christie Hospital NHS Trust, Withington, Manchester, UK., Aug. 2005.

[30] S. Eschrich, H. Zhang, H. Zhao, D. Boulware, J.-H. Lee, G. Bloom, and J. F. Torres-Roca, "Systems biology modeling of the radiation sensitivity network: a biomarker discovery platform.," *International Journal of Radiation Oncology, Biology and Physics*, vol. 75, pp. 497–505, Oct. 2009.

[31] J. H. Oh, H. P. Wong, X. Wang, and J. O. Deasy, "A bioinformatics filtering strategy for identifying radiation response biomarker candidates.," *PLoS ONE*, vol. 7, no. 6, p. e38870, 2012.

[32] M. De Palma and D. Hanahan, "The biology of personalized cancer medicine: Facing individual complexities underlying hallmark capabilities," *Molecular oncology*, vol. 6, no. 2, pp. 111–127, 2012.

[33] H. F. Lodish, A. Berk, C. A. Kaiser, M. Krieger, and M. P. Scott, *Molecular Cell Biology*. New York, NY: W H Freeman & Company, sixth ed., 2008.

[34] T. D. Pollard, W. C. Earnshaw, and J. Lippincott-Schwartz, *Cell Biology*. Philadelphia, Pennsylvania: Saunders Elsevier, second ed., 2007.

[35] E. J. Hall and A. J. Giaccia, *Radiobiology for the Radiologist*. Philadelphia: Lippincott Williams & Wilkins, sixth ed., 2006.

[36] D. T. Goodhead, "Energy deposition stochastics and track structure: what about the target?," *Radiation protection dosimetry*, vol. 122, no. 1-4, pp. 3–15, 2006.

[37] R. L. Warters and K. G. Hofer, "Radionuclide toxicity in cultured mammalian cells. Elucidation of the primary site for radiation-induced division delay.," *Radiation Research*, vol. 69, pp. 348–358, Feb. 1977.

[38] R. L. Warters, K. G. Hofer, C. R. Harris, and J. M. Smith, "Radionuclide toxicity in cultured mammalian cells: elucidation of the primary site of radiation

damage.," *Current topics in radiation research quarterly*, vol. 12, pp. 389–407, Jan. 1978.

[39] S. Matsuoka, B. A. Ballif, A. Smogorzewska, E. R. McDonald, K. E. Hurov, J. Luo, C. E. Bakalarski, Z. Zhao, N. Solimini, Y. Lerenthal, Y. Shiloh, S. P. Gygi, and S. J. Elledge, "ATM and ATR substrate analysis reveals extensive protein networks responsive to DNA damage.," *Science (New York, NY)*, vol. 316, pp. 1160–1166, May 2007.

[40] P. Fortini and E. Dogliotti, "Base damage and single-strand break repair: mechanisms and functional significance of short- and long-patch repair subpathways.," *DNA Repair*, vol. 6, pp. 398–409, Apr. 2007.

[41] M. Stucki and S. P. Jackson, "GammaH2AX and MDC1: Anchoring the DNA-Damage-Response Machinery to Broken Chromosomes.," *DNA Repair*, vol. 5, pp. 534–543, May 2006.

[42] J. Falck, J. Coates, and S. P. Jackson, "Conserved modes of recruitment of ATM, ATR and DNA-PKcs to sites of DNA damage.," *Nature*, vol. 434, pp. 605–611, Mar. 2005.

[43] S. C. West, "Molecular views of recombination proteins and their control.," *Nature reviews. Molecular cell biology*, vol. 4, pp. 435–445, June 2003.

[44] P. Tamulevicius, M. Wang, and G. Iliakis, "Homology-directed repair is required for the development of radioresistance during S phase: interplay between double-strand break repair and checkpoint response.," *Radiation Research*, vol. 167, pp. 1–11, Jan. 2007.

[45] M. R. Lieber, "The mechanism of human nonhomologous DNA end joining.," *The Journal of biological chemistry*, vol. 283, pp. 1–5, Jan. 2008.

[46] P. A. Jeggo and M. Lobrich, "Artemis links ATM to double strand break rejoining.," *Cell cycle (Georgetown, Tex.)*, vol. 4, pp. 359–362, Mar. 2005.

[47] M. Garcia-Barros, "Tumor Response to Radiotherapy Regulated by Endothelial Cell Apoptosis," *Science (New York, NY)*, vol. 300, pp. 1155–1159, May 2003.

[48] U. S. Kumta and A. L. Tappel, "Radiation damage to proteins," *Nature*, vol. 191, pp. 1304–1305, Sept. 1961.

[49] K. S. Ambe, U. S. Kumta, and A. L. Tappel, "Radiation Damage to Cytochrome c and Hemoglobin," *Radiation Research*, vol. 15, p. 709, Dec. 1961.

[50] K. J. Davies, "Protein damage and degradation by oxygen radicals. I. general aspects.," *The Journal of biological chemistry*, vol. 262, no. 20, pp. 9895–9901, 1987.

[51] S. P. Verma, A. SINGHAL, and N. Sonwalkar, "Ionizing Radiation Target Groups of Band 3 Inserted into Egg Lecithin Liposomes as Determined by Raman Spectroscopy," *International Journal of Radiation Biology*, vol. 63, pp. 279–288, Jan. 1993.

[52] E. S. Kempner, "Damage to proteins due to the direct action of ionizing radiation.," *Quarterly reviews of biophysics*, vol. 26, pp. 27–48, Feb. 1993.

[53] O. Guipaud, V. Vereycken-Holler, J. Vinh, and M. Benderitter, "Identification of differentially expressed proteins in serums of skin-irradiated mice; Characterization of potential ionising radiation biomarkers," *Molecular & Cellular Proteomics*, vol. 4, no. 8, pp. S150–S150, 2005.

[54] O. Guipaud, V. Holler, V. Buard, G. Tarlet, N. Royer, J. Vinh, and M. Benderitter, "Time-course analysis of mouse serum proteome changes following exposure of the skin to ionizing radiation," *Proteomics*, vol. 7, no. 21, pp. 3992–4002, 2007.

[55] O. Guipaud and M. Benderitter, "Protein Biomarkers for Radiation Exposure: Towards a Proteomic Approach as a New Investigation Tool," *Annali dell'Istituto Superiore di Sanita*, vol. 45, no. 3, pp. 278–286, 2009.

[56] L. J. Kuo and L.-X. Yang, "Gamma-H2AX - A Novel Biomarker for DNA Double-Strand Breaks," *In Vivo*, vol. 22, no. 3, pp. 305–309, 2008.

[57] M. Lassmann, H. Haenscheid, D. Gassen, J. Biko, V. Meineke, C. Reiners, and H. Scherthan, "In Vivo Formation of gamma-H2AX and 53BP1 DNA Repair Foci in Blood Cells After Radioiodine Therapy of Differentiated Thyroid Cancer," *Journal of Nuclear Medicine*, vol. 51, no. 8, pp. 1318–1325, 2010.

[58] T. Tanaka, X. Huang, H. D. Halicka, H. Zhao, F. Traganos, A. P. Albino, W. Dai, and Z. Darzynkiewicz, "Cytometry of ATM activation and histone

H2AX phosphorylation to estimate extent of DNA damage induced by exogenous agents," *Cytometry Part A*, vol. 71A, no. 9, pp. 648–661, 2007.

[59] A. Kinner, W. Wu, C. Staudt, and G. Iliakis, "gamma-H2AX in recognition and signaling of DNA double-strand breaks in the context of chromatin," *Nucleic acids research*, vol. 36, no. 17, pp. 5678–5694, 2008.

[60] S. V. Costes, I. Chiolo, J. M. Pluth, M. H. Barcellos-Hoff, and B. Jakob, "Spatiotemporal characterization of ionizing radiation induced DNA damage foci and their relation to chromatin organization," *Mutation Research-Reviews in Mutation Research*, vol. 704, no. 1-3, pp. 78–87, 2010.

[61] A. Krisko and M. Radman, "Protein damage and death by radiation in Escherichia coli and Deinococcus radiodurans.," *Proceedings of the National Academy of Sciences of the United States of America*, vol. 107, pp. 14373–14377, Aug. 2010.

[62] I. Shuryak and D. J. Brenner, "Mechanistic analysis of the contributions of DNA and protein damage to radiation-induced cell death.," *Radiation Research*, vol. 178, pp. 17–24, July 2012.

[63] V. Stísová, S. Goffinont, M. Spotheim-Maurizot, and M. Davídková, "Radiation damage to DNA-protein specific complexes: estrogen response element-estrogen receptor complex.," *Radiation protection dosimetry*, vol. 122, no. 1-4, pp. 106–109, 2006.

[64] S. Mazier, S. Villette, S. Goffinont, S. Renouard, J. C. Maurizot, D. Genest, and M. Spotheim-Maurizot, "Radiation damage to a DNA-binding protein. Combined circular dichroism and molecular dynamics simulation analysis.," *Radiation Research*, vol. 170, pp. 604–612, Nov. 2008.

[65] M. Spotheim-Maurizot and M. Davídková, "Radiation damage to DNA in DNA-protein complexes.," *Mutation research*, vol. 711, pp. 41–48, June 2011.

[66] S. P. Verma and A. Rastogi, "Role of proteins in protection against radiation-induced damage in membranes.," *Radiation Research*, vol. 122, pp. 130–136, May 1990.

[67] H. Okada and T. W. Mak, "Pathways of apoptotic and non-apoptotic death in tumour cells," *Nature Reviews Cancer*, vol. 4, pp. 592–603, Aug. 2004.

[68] R. C. Taylor, S. P. Cullen, and S. J. Martin, "Apoptosis: controlled demolition at the cellular level.," *Nature reviews. Molecular cell biology*, vol. 9, pp. 231–241, Mar. 2008.

[69] D. J. Klionsky, "Autophagy: from phenomenology to molecular understanding in less than a decade.," *Nature reviews. Molecular cell biology*, vol. 8, pp. 931–937, Nov. 2007.

[70] D. C. Rubinsztein, J. E. Gestwicki, L. O. Murphy, and D. J. Klionsky, "Potential therapeutic applications of autophagy.," *Nature reviews. Drug discovery*, vol. 6, pp. 304–312, Apr. 2007.

[71] J. Campisi and F. d'Adda di Fagagna, "Cellular senescence: when bad things happen to good cells.," *Nature reviews. Molecular cell biology*, vol. 8, pp. 729–740, Sept. 2007.

[72] L. Hayflick, "The limited in vitro lifetime of human diploid cell strains," *Experimental cell research*, vol. 37, pp. 614–636, Mar. 1965.

[73] J. M. Brown and L. D. Attardi, "The role of apoptosis in cancer development and treatment response.," *Nature Reviews Cancer*, vol. 5, pp. 231–237, Mar. 2005.

[74] K. Chu, N. Teele, M. W. Dewey, N. Albright, and W. C. Dewey, "Computerized Video Time Lapse Study of Cell Cycle Delay and Arrest, Mitotic Catastrophe, Apoptosis and Clonogenic Survival in Irradiated 14-3-3σ and CDKN1A (p21) Knockout Cell Lines," *Radiation Research*, vol. 162, pp. 270–286, Sept. 2004.

[75] R. A. McGrath and R. W. Williams, "Reconstruction in vivo of irradiated Escherichia coli deoxyribonucleic acid; the rejoining of broken pieces.," *Nature*, vol. 212, pp. 534–535, Oct. 1966.

[76] J. T. Lett, I. Caldwell, C. J. Dean, and P. Alexander, "Rejoining of x-ray induced breaks in the DNA of leukaemia cells.," *Nature*, vol. 214, pp. 790–792, May 1967.

[77] K. W. Kohn, "Principles and practice of DNA filter elution.," *Pharmacology & therapeutics*, vol. 49, no. 1-2, pp. 55–77, 1991.

[78] M. C. Elia, J. G. DeLuca, and M. O. Bradley, "Significance and measurement of DNA double strand breaks in mammalian cells.," *Pharmacology & therapeutics*, vol. 51, no. 3, pp. 291–327, 1991.

[79] E. R. Blazek and J. G. Peak, "Filter elution assays for DNA damage: practical and mechanistic significance of the DNA in the filter support wash.," *Radiation Research*, vol. 130, pp. 384–388, June 1992.

[80] J. Lu, M. R. Kaeck, C. Jiang, G. Garcia, and H. J. Thompson, "A Filter Elution Assay for the Simultaneous Detection of DNA Double and Single Strand Breaks.," *Analytical Biochemistry*, vol. 235, pp. 227–233, Mar. 1996.

[81] P. L. Olive, "The Role of DNA Single- and Double-Strand Breaks in Cell Killing by Ionizing Radiation," *Radiation Research*, vol. 150, p. S42, Nov. 1998.

[82] G. Rudinger and E. R. Blazek, "Fluid mechanics of DNA double-strand filter elution.," *Biophysical journal*, vol. 82, pp. 19–28, Jan. 2002.

[83] D. D. Ager, W. C. Dewey, K. Gardiner, W. Harvey, R. T. Johnson, and C. A. Waldren, "Measurement of radiation-induced DNA double-strand breaks by pulsed-field gel electrophoresis," *Radiation Research*, vol. 122, pp. 181–187, May 1990.

[84] S. J. Whitaker and T. J. McMillan, "Pulsed-field gel electrophoresis in the measurement of DNA double-strand break repair in xrs-6 and CHO cell lines: DNA degradation under some conditions interferes with the assessment of double-strand break rejoining," *Radiation Research*, vol. 130, no. 3, pp. 389–392, 1992.

[85] B. Rydberg and B. Rydberg, "Clusters of DNA Damage Induced by Ionizing Radiation: Formation of Short DNA Fragments. II. Experimental Detection," *Radiation Research*, vol. 145, p. 200, Feb. 1996.

[86] K. S. Haveles, A. G. Georgakilas, E. G. Sideris, and V. Sophianopoulou, "Effects of radical scavengers on radiation-induced DNA double strand breaks," *International Journal of Radiation Biology*, vol. 76, no. 1, pp. 51–59, 2000.

[87] B. M. Sutherland, "Clustered DNA damages induced in isolated DNA and in human cells by low doses of ionizing radiation," *Proceedings of the National Academy of Sciences*, vol. 97, pp. 103–108, Jan. 2000.

[88] E. Gajewski, G. Rao, Z. Nackerdien, and M. Dizdaroglu, "Modification of DNA bases in mammalian chromatin by radiation-generated free radicals," *Biochemistry*, vol. 29, pp. 7876–7882, Aug. 1990.

[89] M. Dizdaroglu, "Application of Capillary Gas Chromatography-Mass Spectrometry to Chemical Characterization of Radiation-Induced Base Damage of DNA: Implications for Assessing DNA Repair Processes," *Analytical Biochemistry*, vol. 144, pp. 593–603, Feb. 1985.

[90] O. Carugo and K. Djinović Carugo, "When X-rays modify the protein structure: radiation damage at work.," *Trends in biochemical sciences*, vol. 30, pp. 213–219, Apr. 2005.

[91] N. Shimizu, K. Hirata, K. Hasegawa, G. Ueno, and M. Yamamoto, "radiation damage," *J. Synchrotron Rad (2007). 14, 4-10 [doi:10.1107/S0909049506049296]*, pp. 1–7, Dec. 2006.

[92] J. Kmetko, M. Warkentin, U. Englich, and R. E. Thorne, "Can Radiation Damage to Protein Crystals be Reduced Using Small-Molecule Compounds?," *Acta Crystallographica, Section D: Biological Crystallography*, vol. 67, pp. 881–893, Sept. 2011.

[93] G. D. Fasman, *Circular Dichroism and the Conformational Analysis of Biomolecules*. The Language of Science Series, Springer, 1996.

[94] B. Rupp, *Biomolecular Crystallography: Principles, Practice, and Application to Structural Biology*. New York, NY: Garland Science, first ed., Oct. 2009.

[95] R. Henderson, "Cryo-Protection of Protein Crystals against Radiation Damage in Electron and X-Ray Diffraction," *Proceedings of the Royal Society B: Biological Sciences*, vol. 241, pp. 6–8, July 1990.

[96] E. F. Garman and T. R. Schneider, "Macromolecular Cryocrystallography," *Journal of Applied Crystallography*, vol. 30, pp. 211–237, June 1997.

[97] E. F. Garman and R. L. Owen, "Cryocooling and Radiation Damage in Macromolecular Crystallography.," *Acta Crystallographica, Section D: Biological Crystallography*, vol. 62, pp. 32–47, Jan. 2006.

[98] R. L. Owen, E. Rudiño-Piñera, and E. F. Garman, "Experimental determination of the radiation dose limit for cryocooled protein crystals.," *Proceedings of the National Academy of Sciences of the United States of America*, vol. 103, pp. 4912–4917, Mar. 2006.

[99] T. T. Puck and P. I. Marcus, "Action of x-rays on mammalian cells," *The Journal of experimental medicine*, vol. 103, pp. 653–666, May 1956.

[100] E. P. Malaise, B. Fertil, N. Chavaudra, and M. Guichard, "Distribution of radiation sensitivities for human tumor cells of specific histological types: Comparison of in vitro to in vivo data," *International Journal of Radiation Oncology, Biology and Physics*, vol. 12, pp. 617–624, Apr. 1986.

[101] T. T. Puck, D. MORKOVIN, P. I. Marcus, and S. J. CIECIURA, "Action of x-rays on mammalian cells. II. Survival curves of cells from normal human tissues," *The Journal of experimental medicine*, vol. 106, pp. 485–500, Oct. 1957.

[102] M. Bergqvist, D. Brattström, M. Stålberg, H. Vaghef, O. Brodin, and B. Hellman, "Evaluation of radiation-induced DNA damage and DNA repair in human lung cancer cell lines with different radiosensitivity using alkaline and neutral single cell gel electrophoresis," *Cancer letters*, vol. 133, pp. 9–18, Nov. 1998.

[103] F. B. Geara, L. J. Peters, K. Kian Ang, J. L. Wike, and W. A. Brock, "Prospective comparison of in vitro normal cell radiosensitivity and normal tissue reactions in radiotherapy patients," *International Journal of Radiation Oncology, Biology and Physics*, vol. 27, pp. 1173–1179, Dec. 1993.

[104] L. Peters, "Radiation therapy tolerance limits - For one or for all? Janeway lecture," *Cancer*, vol. 77, pp. 2379–2385, 1996.

[105] W. K. Sinclair and R. A. Morton, "X-ray sensitivity during the cell generation cycle of cultured Chinese hamster cells," *Radiation Research*, vol. 29, pp. 450–474, Nov. 1966.

[106] W. K. Sinclair, "Cyclic x-ray responses in mammalian cells in vitro," *Radiation Research*, vol. 33, pp. 620–643, Mar. 1968.

[107] T. Terasima and L. J. Tolmach, "Variations in several responses of HeLa cells to x-irradiation during the division cycle.," *Biophysical journal*, vol. 3, pp. 11–33, Jan. 1963.

[108] E. Smith and G. Dent, *Modern Raman Spectroscopy: A Practical Approach*. West Sussex, England: John Wiley and Sons, Ltd., 2005.

[109] R. L. McCreery, *Raman Spectroscopy for Chemical Analysis*, vol. 157 of *Chemical Analysis: A Series of Monographs of Analytical Chemistry and its Applications*. New York: John Wiley and Sons, Inc., 2000.

[110] J. R. Ferraro and K. Nakamoto, *Introductory Raman Spectroscopy*. San Diego, CA: Academic Press, Inc., 1994.

[111] K. Sailer, "Radiation-induced structural modifications in dsDNA analysed by FT-Raman spectroscopy," *International Journal of Radiation Biology*, vol. 69, pp. 601–613, May 1996.

[112] C. P. Shaw and A. Jirasek, "The Use of Ultraviolet Resonance Raman Spectroscopy in the Analysis of Ionizing-Radiation-Induced Damage in DNA," *Applied Spectroscopy*, vol. 63, pp. 412–422, Apr. 2009.

[113] S. P. Verma and N. Sonwalkar, "Structural Changes in Plasma Membranes Prepared from Irradiated Chinese Hamster V79 Cells as Revealed by Raman Spectroscopy ," *Radiation Research*, vol. 126, pp. 27–35, Dec. 1991.

[114] K. Sailer, S. Viaggi, and M. Nüsse, "Kinetics of radiation- and cytochrome c-induced modifications in liposomes analysed by FT-Raman spectroscopy.," *Biochimica et biophysica acta*, vol. 1329, pp. 259–268, Oct. 1997.

[115] C. Ferreri, I. Manco, M. R. Faraone-Mennella, A. Torreggiani, M. Tamba, and C. Chatgilialoglu, "A Biomimetic Model of Tandem Radical Damage Involving Sulfur-Containing Proteins and Unsaturated Lipids," *ChemBioChem*, vol. 5, pp. 1710–1712, Nov. 2004.

[116] A. Torreggiani, M. Tamba, I. Manco, M. R. Faraone-Mennella, C. Ferreri, and C. Chatgilialoglu, "Investigation of radical-based damage of RNase A in aqueous solution and lipid vesicles.," *Biopolymers*, vol. 81, no. 1, pp. 39–50, 2005.

[117] A. Torreggiani, M. Tamba, I. Manco, M. R. Faraone-Mennella, C. Ferreri, and C. Chatgilialoglu, "Radiation damage of lysozyme in a biomimetic model: some insights by Raman spectroscopy," *Journal of Molecular Structure*, vol. 744-747, pp. 767–773, June 2005.

[118] A. Synytsya, P. Alexa, J. de Boer, M. Loewe, M. Moosburger, M. Würkner, and K. Volka, "Raman spectroscopic study of serum albumins: an effect of proton- and γ-irradiation," *Journal of Raman Spectroscopy*, vol. 38, no. 12, pp. 1646–1655, 2007.

[119] A. Synytsya, P. Alexa, J. de Boer, M. Loewe, M. Moosburger, M. Würkner, and K. Volka, "Raman spectroscopic study of calf thymus DNA: an effect of proton- and γ-irradiation," *Journal of Raman Spectroscopy*, vol. 38, no. 11, pp. 1406–1415, 2007.

[120] A. Torreggiani, M. Tamba, and C. Ferreri, "Radical damage involving sulfur-containing enzymes and membrane lipids.," *Protein and peptide letters*, vol. 14, no. 7, pp. 716–722, 2007.

[121] S. P. Verma, "Low levels of irradiation modify lipid domains in model membranes: a laser Raman study.," *Radiation Research*, vol. 107, pp. 183–193, Aug. 1986.

[122] R. Lakshmi, V. Kartha, C. Krishna, J. Solomon, G. Ullas, and P. Devi, "Tissue Raman spectroscopy for the study of radiation damage: Brain irradiation of mice," *Radiation Research*, vol. 157, no. 2, pp. 175–182, 2002.

[123] A. Synytsya, P. Alexa, J. Besserer, J. De Boer, S. Froschauer, R. Gerlach, M. Loewe, M. Moosburger, I. Obstová, P. Quicken, B. Sosna, K. VOLKA, and M. Würkner, "Raman spectroscopy of tissue samples irradiated by protons," *International Journal of Radiation Biology*, vol. 80, pp. 581–591, Aug. 2004.

[124] J. De Boer, A. Synytsya, P. Alexa, J. Besserer, S. Froschauer, M. Loewe, M. Moosburger, K. VOLKA, and M. Würkner, "The effect of proton-irradiation on the Raman spectroscopy of tissue samples," *Radiotherapy And Oncology*, vol. 73, pp. S102–S104, Dec. 2004.

[125] P. Alexa, A. Synytsya, K. VOLKA, J. De Boer, J. Besserer, S. Froschauer, M. Loewe, M. Moosburger, and M. Würkner, "Raman Spectroscopy of Irradi-

ated Tissue Samples," *Capture Gamma-Ray Spectroscopy and Related Topics*, vol. 1, pp. 621–624, 2003.

[126] M. S. Vidyasagar, K. Maheedhar, B. M. Vadhiraja, D. J. Fernendes, V. B. Kartha, and C. M. Krishna, "Prediction of radiotherapy response in cervix cancer by Raman spectroscopy: A pilot study," *Biopolymers*, vol. 89, no. 6, pp. 530–537, 2008.

[127] Q. Matthews, A. Brolo, J. Lum, X. Duan, and A. Jirasek, "Raman spectroscopy of single human tumour cells exposed to ionizing radiation in vitro.," *Physics In Medicine And Biology*, vol. 56, pp. 19–38, Jan. 2011.

[128] Q. Matthews, A. Jirasek, J. J. Lum, and A. G. Brolo, "Biochemical signatures of in vitro radiation response in human lung, breast and prostate tumour cells observed with Raman spectroscopy.," *Physics In Medicine And Biology*, vol. 56, pp. 6839–6855, Nov. 2011.

[129] G. J. Puppels, J. H. Olminkhof, G. M. Segers-Nolten, C. Otto, F. F. de Mul, and J. Greve, "Laser irradiation and Raman spectroscopy of single living cells and chromosomes: sample degradation occurs with 514.5 nm but not with 660 nm laser light," *Experimental cell research*, vol. 195, pp. 361–367, Aug. 1991.

[130] I. Notingher, S. Verrier, H. Romanska, A. E. Bishop, J. M. Polak, and L. L. Hench, "In situ characterisation of living cells by Raman spectroscopy," *Spectroscopy-An International Journal*, vol. 16, no. 2, pp. 43–51, 2002.

[131] I. Notingher, S. Verrier, S. Haque, J. M. Polak, and L. L. Hench, "Spectroscopic study of human lung epithelial cells (A549) in culture: Living cells versus dead cells," *Biopolymers*, vol. 72, no. 4, pp. 230–240, 2003.

[132] I. Notingher and L. L. Hench, "Raman microspectroscopy: a noninvasive tool for studies of individual living cells in vitro," *Expert review of medical devices*, vol. 3, pp. 215–234, Mar. 2006.

[133] N. Uzunbajakava, A. Lenferink, Y. Kraan, B. Willekens, G. Vrensen, J. Greve, and C. Otto, "Nonresonant Raman imaging of protein distribution in single human cells," *Biopolymers*, vol. 72, no. 1, pp. 1–9, 2003.

[134] C. Krafft, T. Knetschke, A. Siegner, R. Funk, and R. Salzer, "Mapping of single cells by near infrared Raman microspectroscopy," *Vibrational Spectroscopy*, vol. 32, pp. 75–83, 2003.

[135] S. Verrier, I. Notingher, J. M. Polak, and L. L. Hench, "In situ monitoring of cell death using Raman microspectroscopy," *Biopolymers*, vol. 74, pp. 157–162, May 2004.

[136] Y.-S. Huang, T. Karashima, M. Yamamoto, and H.-o. Hamaguchi, "Molecular-level investigation of the structure, transformation, and bioactivity of single living fission yeast cells by time- and space-resolved Raman spectroscopy," *Biochemistry*, vol. 44, pp. 10009–10019, Aug. 2005.

[137] K. Hamada, K. Fujita, N. Smith, M. Kobayashi, Y. Inouye, and S. Kawata, "Raman microscopy for dynamic molecular imaging of living cells," *Journal of Biomedical Optics*, vol. 13, p. 4, Aug. 2008.

[138] J. T. Motz, M. Hunter, L. H. Galindo, J. A. Gardecki, J. R. Kramer, R. R. Dasari, and M. S. Feld, "Optical Fiber Probe for Biomedical Raman Spectroscopy.," *Applied Optics*, vol. 43, pp. 542–554, Jan. 2004.

[139] G. J. Puppels, F. F. de Mul, C. Otto, J. Greve, M. Robert-Nicoud, D. J. Arndt-Jovin, and T. M. Jovin, "Studying single living cells and chromosomes by confocal Raman microspectroscopy.," *Nature*, vol. 347, pp. 301–303, Sept. 1990.

[140] J. R. Mourant, J. Dominguez, S. Carpenter, K. W. Short, T. M. Powers, R. Michalczyk, N. Kunapareddy, A. Guerra, and J. P. Freyer, "Comparison of vibrational spectroscopy to biochemical and flow cytometry methods for analysis of the basic biochemical composition of mammalian cells," *Journal of Biomedical Optics*, vol. 11, no. 6, p. 064024, 2006.

[141] K. Kneipp, H. Kneipp, and J. Kneipp, "Surface-Enhanced Raman Scattering in Local Optical Fields of Silver and Gold Nanoaggregates-From Single-Molecule Raman Spectroscopy to Ultrasensitive Probing in Live Cells," *Accounts Of Chemical Research*, vol. 39, pp. 443–450, July 2006.

[142] P. L. Stiles, J. A. Dieringer, N. C. Shah, and R. P. Van Duyne, "Surface-Enhanced Raman Spectroscopy," *Annual Review of Analytical Chemistry*, vol. 1, pp. 601–626, July 2008.

[143] J. A. Dieringer, K. L. Wustholz, D. J. Masiello, J. P. Camden, S. L. Kleinman, G. C. Schatz, and R. P. Van Duyne, "Surface-Enhanced Raman Excitation Spectroscopy of a Single Rhodamine 6G Molecule," *Journal of the American Chemical Society*, vol. 131, no. 2, pp. 849–854, 2009.

[144] X.-M. Qian and S. M. Nie, "Single-molecule and single-nanoparticle SERS: from fundamental mechanisms to biomedical applications," *Chemical Society Reviews*, vol. 37, pp. 912–920, May 2008.

[145] J. Kneipp, H. Kneipp, and K. Kneipp, "SERS–a single-molecule and nanoscale tool for bioanalytics," *Chemical Society Reviews*, vol. 37, pp. 1052–1060, May 2008.

[146] M. D. Porter, R. J. Lipert, L. M. Siperko, G. Wang, and R. Narayanan, "SERS as a bioassay platform: fundamentals, design, and applications," *Chemical Society Reviews*, vol. 37, pp. 1001–1011, May 2008.

[147] K. Hering, D. Cialla, K. Ackermann, T. Dörfer, R. Möller, H. Schneidewind, R. Mattheis, W. Fritzsche, P. Rösch, and J. Popp, "SERS: A Versatile Tool in Chemical and Biochemical Diagnostics," *Analytical and Bioanalytical Chemistry*, vol. 390, no. 1, pp. 113–124, 2008.

[148] S. D. Hudson and G. Chumanov, "Bioanalytical Applications of SERS (Surface-Enhanced Raman Spectroscopy)," *Analytical and Bioanalytical Chemistry*, vol. 394, pp. 679–686, June 2009.

[149] X. X. Han, B. Zhao, and Y. Ozaki, "Surface-Enhanced Raman Scattering for Protein Detection," *Analytical and Bioanalytical Chemistry*, vol. 394, pp. 1719–1727, Aug. 2009.

[150] K. Kneipp, A. Haka, H. Kneipp, K. Badizadegan, N. Yoshizawa, C. Boone, K. Shafer-Peltier, J. Motz, R. Dasari, and M. Feld, "Surface-enhanced Raman Spectroscopy in Single Living Cells Using Gold Nanoparticles," *Applied Spectroscopy*, vol. 56, no. 2, pp. 150–154, 2002.

[151] C. E. Talley, L. Jusinski, C. W. Hollars, S. M. Lane, and T. Huser, "Intracellular pH Sensors Based on Surface-Enhanced Raman Scattering," *Analytical Chemistry (Washington, DC, United States)*, vol. 76, pp. 7064–7068, Dec. 2004.

[152] J. Kneipp, H. Kneipp, W. L. Rice, and K. Kneipp, "Optical Probes for Biological Applications Based on Surface-Enhanced Raman Scattering from Indocyanine Green on Gold Nanoparticles," *Analytical Chemistry (Washington, DC, United States)*, vol. 77, pp. 2381–2385, Apr. 2005.

[153] M. Wabuyele, F. Yan, G. Griffin, and T. Vo-Dinh, "Hyperspectral surface-enhanced Raman imaging of labeled silver nanoparticles in single cells," *Review Of Scientific Instruments*, vol. 76, no. 6, p. 063710, 2005.

[154] C. Eliasson, A. Loren, J. Engelbrektsson, M. Josefson, J. Abrahamsson, and K. Abrahamsson, "Surface-enhanced Raman scattering imaging of single living lymphocytes with multivariate evaluation," *Spectrochim Acta, Part A*, vol. 61, no. 4, pp. 755–760, 2005.

[155] J. Kneipp, H. Kneipp, M. McLaughlin, D. Brown, and K. Kneipp, "In vivo molecular probing of cellular compartments with gold nanoparticles and nanoaggregates," *Nano Letters*, vol. 6, pp. 2225–2231, Oct. 2006.

[156] Y. Wang, D. Li, P. Li, W. Wang, W. Ren, S. Dong, and E. Wang, "Surface enhanced Raman scattering of brilliant green on ag nanoparticles and applications in living cells as optical probes," *Journal Of Physical Chemistry C*, vol. 111, no. 45, pp. 16833–16839, 2007.

[157] A. Shamsaie, M. Jonczyk, J. Sturgis, J. P. Robinson, and J. Irudayaraj, "Intracellularly grown gold nanoparticles as potential surface-enhanced Raman scattering probes," *Journal of Biomedical Optics*, vol. 12, no. 2, p. 020502, 2007.

[158] H.-W. Tang, X. B. Yang, J. Kirkham, and D. A. Smith, "Chemical Probing of Single Cancer Cells with Gold Nanoaggregates by Surface-Enhanced Raman Scattering," *Applied Spectroscopy*, vol. 62, pp. 1060–1069, Oct. 2008.

[159] J. Kneipp, H. Kneipp, A. Rajadurai, R. W. Redmond, and K. Kneipp, "Optical probing and imaging of live cells using SERS labels," *Journal of Raman Spectroscopy*, vol. 40, no. 1, pp. 1–5, 2009.

[160] J. TANG and A. ALBRECHT, "STUDIES IN RAMAN INTENSITY THEORY," *Journal Of Chemical Physics*, vol. 49, no. 3, pp. 1144–&, 1968.

[161] H. A. Szymanski, "Raman Spectroscopy: Theory and Practice," *Raman Spectroscopy: Theory and Practice*, vol. 1 and 2, 1967.

[162] T. R. Gilson and P. J. Hendra, *Laser Raman Spectroscopy*. Chichester: John Wiley and Sons, Ltd., Jan. 1970.

[163] K. R. Spring and M. W. Davidson, *Basic Concepts and Formulas in Microscopy*. Tallahassee, FL: Molecular Expressions, 2008.

[164] D. W. Piston, "Choosing objective lenses: The importance of numerical aperture and magnification in digital optical microscopy," *Biological Bulletin*, vol. 195, pp. 1–4, Aug. 1998.

[165] M. Abramowitz, K. R. Spring, H. E. Keller, and M. W. Davidson, "Basic principles of microscope objectives," *Biotechniques*, vol. 33, pp. 772–781, Oct. 2002.

[166] C. Dyer and B. J. E. Smith, "Application of continuous extended scanning techniques to the simultaneous detection of Raman scattering and photoluminescence from calcium disilicates using visible and near-infrared excitation," *Journal of Raman Spectroscopy*, vol. 26, no. 8-9, pp. 777–785, 1995.

[167] J. E. PEMBERTON, R. L. SOBOCINSKI, and G. R. SIMS, "The Effect of Charge Traps on Raman-Spectroscopy Using a Thomson-CSF Charge Coupled Device Detector," *Applied Spectroscopy*, vol. 44, pp. 328–330, Feb. 1990.

[168] M. Fleischmann, P. J. Hendra, and A. J. McQuillan, "Raman spectra of pyridine adsorbed at a silver electrode," *Chemical Physics Letters*, vol. 26, no. 2, pp. 163–166, 1974.

[169] M. Moskovits, "Surface-enhanced Raman spectroscopy: a brief retrospective," *Journal of Raman Spectroscopy*, vol. 36, pp. 485–496, June 2005.

[170] T. E. Brown, H. E. LeMay, and B. E. Bursten, *Chemistry: The Central Science*. Prentice Hall, tenth ed., 2006.

[171] R. F. Aroca, R. A. Alvarez-Puebla, N. Pieczonka, S. Sanchez-Cortez, and J. V. Garcia-Ramos, "Surface-enhanced Raman scattering on colloidal nanostructures," *Advances in Colloid and Interface Science*, vol. 116, pp. 45–61, Nov. 2005.

[172] K. Kim and K. S. Shin, "Surface-Enhanced Raman Scattering: A Powerful Tool for Chemical Identification," *Analytical Sciences*, vol. 27, no. 8, pp. 775–783, 2011.

[173] X.-M. Lin, Y. Cui, Y.-H. Xu, B. Ren, and Z.-Q. Tian, "Surface-Enhanced Raman Spectroscopy: Substrate-Related Issues," *Analytical and Bioanalytical Chemistry*, vol. 394, pp. 1729–1745, Aug. 2009.

[174] M. K. Hossain, Y. Kitahama, G. G. Huang, X. Han, and Y. Ozaki, "Surface-Enhanced Raman Scattering: Realization of Localized Surface Plasmon Resonance Using Unique Substrates and Methods," *Analytical and Bioanalytical Chemistry*, vol. 394, pp. 1747–1760, Aug. 2009.

[175] M. J. Banholzer, J. E. Millstone, L. Qin, and C. A. Mirkin, "Rationally designed nanostructures for surface-enhanced Raman spectroscopy," *Chemical Society Reviews*, vol. 37, no. 5, pp. 885–897, 2008.

[176] M. Fan, G. F. S. Andrade, and A. G. Brolo, "A Review on the Fabrication of Substrates for Surface Enhanced Raman Spectroscopy and their Applications in Analytical Chemistry.," *Analytica Chimica Acta*, vol. 693, pp. 7–25, May 2011.

[177] K. L. Wustholz, A.-I. Henry, J. M. McMahon, R. G. Freeman, N. Valley, M. E. Piotti, M. J. Natan, G. C. Schatz, and R. P. Van Duyne, "Structure-Activity Relationships in Gold Nanoparticle Dimers and Trimers for Surface-Enhanced Raman Spectroscopy," *Journal of the American Chemical Society*, vol. 132, pp. 10903–10910, Aug. 2010.

[178] J. M. McMahon, A.-I. Henry, K. L. Wustholz, M. J. Natan, R. G. Freeman, R. P. Van Duyne, and G. C. Schatz, "Gold Nanoparticle Dimer Plasmonics: Finite Element Method Calculations of the Electromagnetic Enhancement to Surface-Enhanced Raman Spectroscopy," *Analytical and Bioanalytical Chemistry*, vol. 394, pp. 1819–1825, Aug. 2009.

[179] J. Beermann, S. M. Novikov, K. Leosson, and S. I. Bozhevolnyi, "Surface enhanced Raman imaging: periodic arrays and individual metal nanoparticles," *Optics Express*, vol. 17, pp. 12698–12705, July 2009.

[180] S. Mahajan, J. J. Baumberg, A. E. Russell, and P. N. Bartlett, "Reproducible SERRS from structured gold surfaces," *Physical Chemistry Chemical Physics*, vol. 9, no. 45, pp. 6016–6020, 2007.

[181] J. D. Driskell, R. J. Lipert, and M. D. Porter, "Labeled Gold Nanoparticles Immobilized at Smooth Metallic Substrates: Systematic Investigation of Surface Plasmon Resonance and Surface-Enhanced Raman Scattering," *Journal Of Physical Chemistry B*, vol. 110, pp. 17444–17451, Sept. 2006.

[182] C. E. Talley, J. B. Jackson, C. Oubre, N. K. Grady, C. W. Hollars, S. M. Lane, T. R. Huser, P. Nordlander, and N. J. Halas, "Surface-Enhanced Raman Scattering from Individual Au Nanoparticles and Nanoparticle Dimer Substrates," *Nano Letters*, vol. 5, pp. 1569–1574, Aug. 2005.

[183] E. Tourwe and A. Hubin, "Preparation of SERS-active electrodes via ex situ electrocrystallization of silver in a halide free electrolyte," *Vibrational Spectroscopy*, vol. 41, no. 1, pp. 59–67, 2006.

[184] N. Pazos-Perez, C. S. Wagner, J. M. Romo-Herrera, L. M. Liz-Marzán, F. J. García de Abajo, A. Wittemann, A. Fery, and R. A. Alvarez-Puebla, "Organized Plasmonic Clusters with High Coordination Number and Extraordinary Enhancement in Surface-Enhanced Raman Scattering (SERS).," *Angewandte Chemie, International Edition in English*, vol. 51, pp. 12688–12693, Dec. 2012.

[185] G. A. Baker and D. S. Moore, "Progress in Plasmonic Engineering of Surface-Enhanced Raman-Scattering Substrates Toward Ultra-Trace Analysis.," *Analytical and Bioanalytical Chemistry*, vol. 382, pp. 1751–1770, Aug. 2005.

[186] M. Kahl, E. Voges, S. Kostrewa, C. Viets, and W. Hill, "Periodically structured metallic substrates for SERS," *Sensors and Actuators B: Chemical*, vol. 51, pp. 285–291, Aug. 1998.

[187] A. G. Brolo, E. Arctander, R. Gordon, B. Leathem, and K. L. Kavanagh, "Nanohole-Enhanced Raman Scattering," *Nano Letters*, vol. 4, pp. 2015–2018, Oct. 2004.

[188] R. Gordon, D. Sinton, K. L. Kavanagh, and A. G. Brolo, "A New Generation of Sensors Based on Extraordinary Optical Transmission," *Accounts Of Chemical Research*, vol. 41, pp. 1049–1057, Aug. 2008.

[189] G. Frens, "Controlled Nucleation for the Regulation of Particle Size in Monodisperse Gold Suspensions," *Nature Physical Science*, vol. 241, pp. 20–22, 1973.

[190] Y. Xia, Y. Xiong, B. Lim, and S. E. Skrabalak, "Shape-Controlled Synthesis of Metal Nanocrystals: Simple Chemistry Meets Complex Physics?," *Angewandte Chemie, International Edition in English*, vol. 48, no. 1, pp. 60–103, 2009.

[191] P. C. Lee and D. Meisel, "Adsorption and surface-enhanced Raman of dyes on silver and gold sols," *The Journal of Physical Chemistry*, vol. 86, pp. 3391–3395, Aug. 1982.

[192] B. Nikoobakht and M. A. El-Sayed, "Preparation and Growth Mechanism of Gold Nanorods (NRs) Using Seed-Mediated Growth Method," *Chemistry Of Materials*, vol. 15, pp. 1957–1962, May 2003.

[193] T. C. R. Rocha and D. Zanchet, "Growth aspects of photochemically synthesized silver triangular nanoplates.," *Journal of nanoscience and nanotechnology*, vol. 7, pp. 618–625, Feb. 2007.

[194] J. E. Millstone, S. J. Hurst, G. S. Métraux, J. I. Cutler, and C. A. Mirkin, "Colloidal gold and silver triangular nanoprisms.," *Small (Weinheim an der Bergstrasse, Germany)*, vol. 5, pp. 646–664, Mar. 2009.

[195] S. E. Skrabalak and Y. Xia, "Pushing Nanocrystal Synthesis Toward Nanomanufacturing.," *ACS nano*, vol. 3, pp. 10–15, Jan. 2009.

[196] K. C. Grabar, K. J. Allison, B. E. Baker, R. M. Bright, K. R. Brown, R. G. Freeman, A. P. Fox, C. D. Keating, M. D. Musick, and M. J. Natan, "Two-Dimensional Arrays of Colloidal Gold Particles: A Flexible Approach to Macroscopic Metal Surfaces," *Langmuir*, vol. 12, pp. 2353–2361, Jan. 1996.

[197] R. G. Freeman, K. C. Grabar, K. J. Allison, R. M. Bright, J. A. Davis, A. P. Guthrie, M. B. Hommer, M. A. Jackson, P. C. Smith, D. G. Walter, and M. J. Natan, "Self-Assembled Metal Colloid Monolayers: An Approach to SERS Substrates.," *Science (New York, NY)*, vol. 267, pp. 1629–1632, Mar. 1995.

[198] S. Zakel, O. Rienitz, B. Güttler, and R. Stosch, "Double Isotope Dilution Surface-Enhanced Raman Scattering as a Reference Procedure for the Quantification of Biomarkers in Human Serum," *Analyst (Cambridge, United Kingdom)*, vol. 136, no. 19, pp. 3956–3961, 2011.

[199] P. D. O'neal, G. L. Coté, M. Motamedi, J. Chen, and W.-C. Lin, "Feasibility study using surface-enhanced Raman spectroscopy for the quantitative detection of excitatory amino acids," *Journal of Biomedical Optics*, vol. 8, no. 1, pp. 33–39, 2003.

[200] J. D. Driskell, K. M. Kwarta, R. J. Lipert, M. D. Porter, J. D. Neill, and J. F. Ridpath, "Low-Level Detection of Viral Pathogens by a Surface-Enhanced Raman Scattering Based Immunoassay," *Analytical Chemistry (Washington, DC, United States)*, vol. 77, pp. 6147–6154, Oct. 2005.

[201] J.-H. Kim, J.-S. Kim, H. Choi, S.-M. Lee, B.-H. Jun, K.-N. Yu, E. Kuk, Y.-K. Kim, D. H. Jeong, M.-H. Cho, and Y.-S. Lee, "Nanoparticle Probes with Surface Enhanced Raman Spectroscopic Tags for Cellular Cancer Targeting," *Analytical Chemistry (Washington, DC, United States)*, vol. 78, pp. 6967–6973, Oct. 2006.

[202] L. Sun, K.-B. Sung, C. Dentinger, B. Lutz, L. Nguyen, J. Zhang, H. Qin, M. Yamakawa, M. Cao, Y. Lu, A. J. Chmura, J. Zhu, X. Su, A. A. Berlin, S. Chan, and B. Knudsen, "Composite Organic-Inorganic Nanoparticles as Raman Labels for Tissue Analysis," *Nano Letters*, vol. 7, pp. 351–356, Feb. 2007.

[203] K. R. Strehle, D. Cialla, P. Rösch, T. Henkel, M. Köhler, and J. Popp, "A Reproducible Surface-Enhanced Raman Spectroscopy Approach. Online SERS Measurements in a Segmented Microfluidic System," *Analytical Chemistry (Washington, DC, United States)*, vol. 79, pp. 1542–1547, Feb. 2007.

[204] C.-C. Lin, Y.-M. Yang, Y.-F. Chen, T.-S. Yang, and H.-C. Chang, "A new protein A assay based on Raman reporter labeled immunogold nanoparticles," *Biosensors & Bioelectronics*, vol. 24, pp. 178–183, Oct. 2008.

[205] H.-W. Cheng, W.-Q. Luo, G.-L. Wen, S.-Y. Huan, G.-L. Shen, and R.-Q. Yu, "Surface-Enhanced Raman Scattering Based Detection of Bacterial Biomarker and Potential Surface Reaction Species," *Analyst (Cambridge, United Kingdom)*, vol. 135, no. 11, pp. 2993–3001, 2010.

[206] N. N. Yazgan, I. H. Boyaci, E. Temur, U. Tamer, and A. Topcu, "A high sensitive assay platform based on surface-enhanced Raman scattering for quantification of protease activity," *Talanta*, vol. 82, pp. 631–639, July 2010.

[207] B. Guven, N. Basaran-Akgul, E. Temur, U. Tamer, and İ. H. Boyac, "SERS-Based Sandwich Immunoassay Using Antibody Coated Magnetic Nanoparticles for Escherichia Coli Enumeration," *Analyst (Cambridge, United Kingdom)*, vol. 136, no. 4, pp. 740–748, 2011.

[208] R. Stosch, A. Henrion, D. Schiel, and B. Güttler, "Surface-Enhanced Raman Scattering Based Approach for Quantitative Determination of Creatinine in Human Serum," *Analytical Chemistry (Washington, DC, United States)*, vol. 77, pp. 7386–7392, Nov. 2005.

[209] F. Yaghobian, T. Weimann, B. Güttler, and R. Stosch, "On-chip approach for traceable quantification of biomarkers based on isotope-dilution surface-enhanced Raman scattering (IDSERS)," *Lab on a Chip*, vol. 11, no. 17, pp. 2955–2960, 2011.

[210] P.-G. Yin, L. Jiang, X.-F. Lang, L. Guo, and S. Yang, "Quantitative analysis of mononucleotides by isotopic labeling surface-enhanced Raman scattering spectroscopy," *Biosensors & Bioelectronics*, vol. 26, pp. 4828–4831, Aug. 2011.

[211] A. Lee, G. F. S. Andrade, A. Ahmed, M. L. Souza, N. Coombs, E. Tumarkin, K. Liu, R. Gordon, A. G. Brolo, and E. Kumacheva, "Probing Dynamic Generation of Hot-Spots in Self-Assembled Chains of Gold Nanorods by Surface-Enhanced Raman Scattering," *Journal of the American Chemical Society*, vol. 133, pp. 7563–7570, May 2011.

[212] M. Fan and A. G. Brolo, "Silver nanoparticles self assembly as SERS substrates with near single molecule detection limit," *Physical Chemistry Chemical Physics*, vol. 11, no. 34, pp. 7381–7389, 2009.

[213] M. Fan and A. G. Brolo, "Self-Assembled Au Nanoparticles as Substrates for Surface-Enhanced Vibrational Spectroscopy: Optimization and Electrochemical Stability.," *ChemPhysChem*, vol. 9, pp. 1899–1907, Sept. 2008.

[214] C. J. Addison and A. G. Brolo, "Nanoparticle-Containing Structures as a Substrate for Surface-Enhanced Raman Scattering," *Langmuir*, vol. 22, pp. 8696–8702, Oct. 2006.

[215] J. C. Giddings, F. J. Yang, and M. N. Myers, "Flow Field-Flow Fractionation: A Versatile New Separation Method.," *Science (New York, NY)*, vol. 193, pp. 1244–1245, Sept. 1976.

[216] R. L. Garrell, "Surface-Enhanced Raman Spectroscopy," *Analytical Chemistry (Washington, DC, United States)*, vol. 61, no. 6, pp. 401A–411A, 1989.

[217] R. L. Garrell, T. M. Herne, A. M. Ahern, and E. L. Sullenberger, "Surface-enhanced Raman spectroscopy of peptides," in *Proceedings of SPIE* (A. Katzir, ed.), pp. 451–460, SPIE, July 1990.

[218] T. M. Herne, A. M. Ahern, and R. L. Garrell, "Surface-Enhanced Raman Spectroscopy of Tripeptides Adsorbed on Colloidal Silver," *Analytica Chimica Acta*, vol. 246, no. 1, pp. 75–84, 1991.

[219] T. M. Herne, A. Ahern, and R. L. Garrell, "Surface-enhanced Raman spectroscopy of peptides: preferential N-terminal adsorption on colloidal silver," *Journal of the American Chemical Society*, vol. 113, pp. 846–854, Jan. 1991.

[220] S. Stewart and P. M. Fredericks, "Surface-enhanced Raman spectroscopy of peptides and proteins adsorbed on an electrochemically prepared silver surface," *Spectrochimica Acta Part A: Molecular and Biomolecular Spectroscopy*, vol. 55, no. 7, pp. 1615–1640, 1999.

[221] S. Stewart and P. M. Fredericks, "Surface-enhanced Raman spectroscopy of amino acids adsorbed on an electrochemically prepared silver surface," *Spectrochimica Acta Part A: Molecular and Biomolecular Spectroscopy*, vol. 55, no. 7, pp. 1641–1660, 1999.

[222] T. Vo-Dinh, K. Houck, and D. L. Stokes, "Surface-Enhanced Raman Gene Probes," *Analytical Chemistry (Washington, DC, United States)*, vol. 66, pp. 3379–3383, Oct. 1994.

[223] S. E. J. Bell and N. M. S. Sirimuthu, "Surface-Enhanced Raman Spectroscopy (SERS) for Sub-Micromolar Detection of DNA/RNA Mononucleotides," *Journal of the American Chemical Society*, vol. 128, pp. 15580–15581, Dec. 2006.

[224] C. Burda, X. Chen, R. Narayanan, and M. El-Sayed, "Chemistry and properties of nanocrystals of different shapes," *Chemical Reviews*, vol. 105, no. 4, pp. 1025–1102, 2005.

[225] C. Murphy, T. San, A. Gole, C. Orendorff, J. Gao, L. Gou, S. Hunyadi, and T. Li, "Anisotropic metal nanoparticles: Synthesis, assembly, and optical applications," *Journal Of Physical Chemistry B*, vol. 109, no. 29, pp. 13857–13870, 2005.

[226] L. Hirsch, J. Jackson, A. Lee, N. Halas, and J. West, "A Whole Blood Immunoassay using Gold Nanoshells," *Analytical Chemistry (Washington, DC, United States)*, vol. 75, no. 10, pp. 2377–2381, 2003.

[227] K. Nithipatikom, M. J. McCoy, S. R. Hawi, K. Nakamoto, F. Adar, and W. B. Campbell, "Characterization and Application of Raman Labels for Confocal Raman Microspectroscopic Detection of Cellular Proteins in Single Cells," *Analytical Biochemistry*, vol. 322, no. 2, pp. 198–207, 2003.

[228] S. Lee, S. Kim, J. Choo, S. Y. Shin, Y. H. Lee, H. Y. Choi, S. Ha, K. Kang, and C. H. Oh, "Biological Imaging of HEK293 Cells Expressing PLCgamma1 Using Surface-Enhanced Raman Microscopy," *Analytical Chemistry (Washington, DC, United States)*, vol. 79, pp. 916–922, Feb. 2007.

[229] Q. Hu, L.-L. Tay, M. Noestheden, and J. P. Pezacki, "Mammalian Cell Surface Imaging with Nitrile-Functionalized Nanoprobes: Biophysical Characterization of Aggregation and Polarization Anisotropy in SERS Imaging," *Journal of the American Chemical Society*, vol. 129, pp. 14–15, Jan. 2007.

[230] B. Chithrani, A. Ghazani, and W. Chan, "Determining the size and shape dependence of gold nanoparticle uptake into mammalian cells," *Nano Letters*, vol. 6, no. 4, pp. 662–668, 2006.

[231] B. D. Chithrani and W. C. W. Chan, "Elucidating the mechanism of cellular uptake and removal of protein-coated gold nanoparticles of different sizes and shapes," *Nano Letters*, vol. 7, no. 6, pp. 1542–1550, 2007.

[232] E. E. Connor, J. Mwamuka, A. Gole, C. J. Murphy, and M. D. Wyatt, "Gold Nanoparticles Are Taken Up by Human Cells but Do Not Cause Acute Cyto-

toxicity," *Small (Weinheim an der Bergstrasse, Germany)*, vol. 1, pp. 325–327, Mar. 2005.

[233] C. Freese, C. Uboldi, M. I. Gibson, R. E. Unger, B. B. Weksler, I. A. Romero, P.-O. Couraud, and C. J. Kirkpatrick, "Uptake and cytotoxicity of citrate-coated gold nanospheres: Comparative studies on human endothelial and epithelial cells.," *Particle and Fibre Toxicology*, vol. 9, p. 23, 2012.

[234] A. M. Alkilany and C. J. Murphy, "Toxicity and cellular uptake of gold nanoparticles: what we have learned so far?," *Journal of Nanoparticle Research*, vol. 12, pp. 2313–2333, Apr. 2010.

[235] T. Mironava, M. Hadjiargyrou, M. Simon, V. Jurukovski, and M. H. Rafailovich, "Gold nanoparticles cellular toxicity and recovery: Effect of size, concentration and exposure time," *Nanotoxicology*, vol. 4, pp. 120–137, Mar. 2010.

[236] E.-J. Park, J. Yi, Y. Kim, K. Choi, and K. Park, "Toxicology in Vitro," *Toxicology in Vitro*, vol. 24, pp. 872–878, Apr. 2010.

[237] O. Bar-Ilan, R. M. Albrecht, V. E. Fako, and D. Y. Furgeson, "Toxicity Assessments of Multisized Gold and Silver Nanoparticles in Zebrafish Embryos," *Small (Weinheim an der Bergstrasse, Germany)*, vol. 5, pp. 1897–1910, Aug. 2009.

[238] P. V. AshaRani, G. Low Kah Mun, M. P. Hande, and S. Valiyaveettil, "Cytotoxicity and Genotoxicity of Silver Nanoparticles in Human Cells," *ACS nano*, vol. 3, pp. 279–290, Feb. 2009.

[239] Y. Pan, S. Neuss, A. Leifert, M. Fischler, F. Wen, U. Simon, G. Schmid, W. Brandau, and W. Jahnen-Dechent, "Size-Dependent Cytotoxicity of Gold Nanoparticles," *Small (Weinheim an der Bergstrasse, Germany)*, vol. 3, pp. 1941–1949, Nov. 2007.

[240] C. J. Murphy, A. M. Gole, J. W. Stone, P. N. Sisco, A. M. Alkilany, E. C. Goldsmith, and S. C. Baxter, "Gold Nanoparticles in Biology: Beyond Toxicity to Cellular Imaging.," *Accounts Of Chemical Research*, vol. 41, pp. 1721–1730, Dec. 2008.

[241] Y. Wang, J. L. Seebald, D. P. Szeto, and J. Irudayaraj, "Biocompatibility and Biodistribution of Surface-Enhanced Raman Scattering Nanoprobes in Zebrafish Embryos: In vivoand Multiplex Imaging," *ACS nano*, vol. 4, pp. 4039–4053, July 2010.

[242] R. Shukla, V. Bansal, M. Chaudhary, A. Basu, R. R. Bhonde, and M. Sastry, "Biocompatibility of gold nanoparticles and their endocytotic fate inside the cellular compartment: a microscopic overview.," *Langmuir*, vol. 21, pp. 10644–10654, Nov. 2005.

[243] P. V. AshaRani, Y. lianwu, Z. Gong, and S. Valiyaveettil, "Comparison of the toxicity of silver, gold and platinum nanoparticles in developing zebrafish embryos," *Nanotoxicology*, vol. 5, pp. 43–54, Mar. 2011.

[244] A. G. Tkachenko, H. Xie, Y. Liu, D. Coleman, J. Ryan, W. R. Glomm, M. K. Shipton, S. Franzen, and D. L. Feldheim, "Cellular trajectories of peptide-modified gold particle complexes: comparison of nuclear localization signals and peptide transduction domains.," *Bioconjugate chemistry*, vol. 15, pp. 482–490, May 2004.

[245] J. M. de la Fuente and C. C. Berry, "Tat peptide as an efficient molecule to translocate gold nanoparticles into the cell nucleus.," *Bioconjugate chemistry*, vol. 16, pp. 1176–1180, Sept. 2005.

[246] K. C. Grabar, R. G. Freeman, M. B. Hommer, and M. J. Natan, "Preparation and Characterization of Au Colloid Monolayers," *Analytical Chemistry (Washington, DC, United States)*, vol. 67, pp. 735–743, Feb. 1995.

[247] W. S. Sutherland and J. D. Winefordner, "Colloid Filtration: A Novel Substrate Preparation Method for Surface-Enhanced Raman Spectroscopy," *Journal of colloid and interface science*, vol. 148, no. 1, pp. 129–141, 1992.

[248] Brookhaven Instruments Corporation, *90Plus/BI-MAS Multi Angle Particle Sizing Option Operation Manual*. Holtsville, NY, USA, Jan. 1995.

[249] M. Fan, P. Wang, C. Escobedo, D. Sinton, and A. G. Brolo, "Surface-enhanced Raman scattering (SERS) optrodes for multiplexed on-chip sensing of nile blue A and oxazine 720," *Lab on a Chip*, vol. 12, no. 8, p. 1554, 2012.

[250] Q. Matthews, A. Jirasek, J. Lum, X. Duan, and A. G. Brolo, "Variability in Raman Spectra of Single Human Tumor Cells Cultured in Vitro: Correlation with Cell Cycle and Culture Confluency," *Applied Spectroscopy*, vol. 64, no. 8, pp. 871–887, 2010.

[251] Q. Matthews, *Development of a Raman microscope for applications in radiobiology*. PhD thesis, University of Victoria, University of Victoria / British Columbia Cancer Agency - Vancouver Island Centre, 2008.

[252] E. Gazi, J. Dwyer, N. Lockyer, J. Miyan, P. Gardner, C. Hart, M. Brown, and N. Clarke, "Fixation protocols for subcellular imaging by synchrotron-based Fourier transform infrared microspectroscopy," *Biopolymers*, vol. 77, no. 1, pp. 18–30, 2005.

[253] J. Ramos-Vara, "Technical aspects of immunohistochemistry," *Veterinary Pathology*, vol. 42, no. 4, pp. 405–426, 2005.

[254] D. B. Murphy and M. W. Davidson, *Fundamentals of Light Microscopy and Electronic Imaging*. Hoboken, New Jersey: John Wiley and Sons, Inc., second ed., 2012.

[255] B. A. Forbes, K. D. Blaney, M. L. Turge, L. A. Kaplan, and C. A. Burtis, *Tietz Textbook of Clinical Chemistry and Molecular Diagnostics*. Philadelphia, PA: Saunders Elsevier, fifth ed., Oct. 2012.

[256] R. A. McPherson and M. R. Pincus, *Henry's Clinical Diagnosis and Management by Laboratory Methods*. Philadephia, PA: Saunders Elsevier, twenty-second ed., Aug. 2011.

[257] A. Ferrari and J. Robertson, "Resonant Raman spectroscopy of disordered, amorphous, and diamondlike carbon," *Physical Review B*, vol. 64, p. 075414, July 2001.

[258] A. Ferrari, S. Rodil, and J. Robertson, "Interpretation of infrared and Raman spectra of amorphous carbon nitrides," *Physical Review B*, vol. 67, p. 155306, Apr. 2003.

[259] R. Galli, O. Uckermann, E. F. Andresen, K. D. Geiger, E. Koch, G. Schackert, G. Steiner, and M. Kirsch, "Intrinsic Indicator of Photodamage during

Label-Free Multiphoton Microscopy of Cells and Tissues," *PLoS ONE*, vol. 9, p. e110295, Oct. 2014.

[260] N. M. Green, "Avidin and Streptavidin," *Methods in Enzymology*, vol. 184, pp. 51–67, 1990.

[261] N. M. Green, "Avidin.," *Advances in Protein Chemistry*, vol. 29, pp. 85–133, 1975.

[262] L.-S. Jang and H.-K. Keng, "Modified fabrication process of protein chips using a short-chain self-assembled monolayer," *Biomedical Microdevices*, vol. 10, pp. 203–211, Apr. 2008.

[263] G. F. S. Andrade, M. Fan, and A. G. Brolo, "Multilayer silver nanoparticles-modified optical fiber tip for high performance SERS remote sensing," *Biosensors & Bioelectronics*, vol. 25, pp. 2270–2275, June 2010.

[264] C. M. S. Izumi, M. G. Moffitt, and A. G. Brolo, "Statistics on Surface-Enhanced Resonance Raman Scattering from Single Nanoshells," *Journal Of Physical Chemistry C*, vol. 115, pp. 19104–19109, Oct. 2011.

[265] C. P. Shaw, M. Fan, C. Lane, G. Barry, A. I. Jirasek, and A. G. Brolo, "Statistical Correlation Between SERS Intensity and Nanoparticle Cluster Size," *Journal Of Physical Chemistry C*, vol. 117, pp. 16596–16605, Aug. 2013.

[266] A. Agresti and B. A. Coull, "Approximate is Better than "Exact" for Interval Estimation of Binomial Proportions," *American Statistician*, vol. 52, no. 2, pp. 119–126, 1998.

[267] L. D. Brown, T. T. Cai, and A. DasGupta, "Interval Estimation for a Binomial Proportion," *Statistical Science*, vol. 16, pp. 101–133, 2001.

[268] D. P. Doane and L. E. Seward, "Measuring Skewness: A Forgotten Statistic?," *Journal of Statistics Education*, vol. 19, no. 2, pp. 1–18, 2011.

[269] N. A. Campbell and J. B. Reece, *Biology*. San Francisco: Pearson/Benjamin Cummings, seventh ed., 2005.

[270] N. M. Green and M. D. MELAMED, "Optical Rotatory Dispersion Circular Dichroism and Far-Ultraviolet Spectra of Avidin and Streptavidin," *Biochemical Journal*, vol. 100, no. 3, pp. 614–&, 1966.

[271] J. DeChancie and K. N. Houk, "The Origins of Femtomolar ProteinLigand Binding: Hydrogen-Bond Cooperativity and Desolvation Energetics in the Biotin(Strept)Avidin Binding Site," *Journal of the American Chemical Society*, vol. 129, pp. 5419–5429, May 2007.

[272] Y. Lindqvist and G. Schneider, "Protein-biotin interactions," *Current Opinion in Structural Biology*, vol. 6, pp. 798–803, Dec. 1996.

[273] P. C. Weber, J. J. Wendoloski, M. W. Pantoliano, and F. R. Salemme, "Crystallographic and thermodynamic comparison of natural and synthetic ligands bound to streptavidin," *Journal of the American Chemical Society*, vol. 114, no. 9, pp. 3197–3200, 1992.

[274] S. MIYAMOTO and P. A. KOLLMAN, "Absolute and Relative Binding Free-Energy Calculations of the Interaction of Biotin and Its Analogs with Streptavidin Using Molecular-Dynamics Free-Energy Perturbation Approaches," *Proteins-Structure Function and Genetics*, vol. 16, pp. 226–245, July 1993.

[275] A. Chilkoti, P. H. Tan, and P. S. Stayton, "Site-directed mutagenesis studies of the high-affinity streptavidin-biotin complex: contributions of tryptophan residues 79, 108, and 120.," *Proceedings of the National Academy of Sciences of the United States of America*, vol. 92, pp. 1754–1758, Feb. 1995.

[276] D. E. Hyre, P. S. Stayton, I. L. Trong, S. Freitag, and R. E. Stenkamp, "Ser45 plays an important role in managing both the equilibrium and transition state energetics of the streptavidin-biotin system," *Protein Science*, vol. 9, no. 5, pp. 878–885, 2000.

[277] L. A. Klumb, V. Chu, and P. S. Stayton, "Energetic Roles of Hydrogen Bonds at the Ureido Oxygen Binding Pocket in the StreptavidinBiotin Complex ," *Biochemistry*, vol. 37, pp. 7657–7663, May 1998.

[278] S. Freitag, V. Chu, J. E. Penzotti, L. A. Klumb, R. To, D. Hyre, I. Le Trong, T. P. Lybrand, R. E. Stenkamp, and P. S. Stayton, "A structural snapshot of an intermediate on the streptavidin-biotin dissociation pathway," *Proceedings of the National Academy of Sciences*, vol. 96, pp. 8384–8389, July 1999.

[279] I. Le Trong, S. Freitag, L. A. Klumb, V. Chu, P. S. Stayton, and R. E. Stenkamp, "Structural Studies of Hydrogen Bonds in the High-Affinity Streptavidin-Biotin

Complex: Mutations of Amino Acids Interacting with the Ureido Oxygen of Biotin," *Acta Crystallographica, Section D: Biological Crystallography*, vol. 59, no. 9, pp. 1567–1573, 2003.

[280] C.-S. Goh, D. Milburn, and M. Gerstein, "Conformational changes associated with protein–protein interactions," *Current Opinion in Structural Biology*, vol. 14, pp. 104–109, Feb. 2004.

[281] R. GRUNBERG, J. LECKNER, and M. NILGES, "Complementarity of structure ensembles in protein-protein binding," *Structure*, vol. 12, pp. 2125–2136, Dec. 2004.

[282] G. R. Smith, M. J. E. Sternberg, and P. A. Bates, "The Relationship between the Flexibility of Proteins and their Conformational States on Forming Protein–Protein Complexes with an Application to Protein–Protein Docking," *Journal of Molecular Biology*, vol. 347, pp. 1077–1101, Apr. 2005.

[283] R. GRUNBERG, M. NILGES, and J. LECKNER, "Flexibility and Conformational Entropy in Protein-Protein Binding," *Structure*, vol. 14, pp. 683–693, Apr. 2006.

[284] M.-H. Seo, J. Park, E. Kim, S. Hohng, and H.-S. Kim, "Protein conformational dynamics dictate the binding affinity for a ligand," *Nature Communications*, vol. 5, Apr. 2014.

[285] J. Wilting, W. F. van der Giesen, L. H. Janssen, M. M. Weideman, M. Otagiri, and J. H. Perrin, "The effect of albumin conformation on the binding of warfarin to human serum albumin. The dependence of the binding of warfarin to human serum albumin on the hydrogen, calcium, and chloride ion concentrations as studied by circular dichroism, fluorescence, and equilibrium dialysis.," *The Journal of biological chemistry*, vol. 255, pp. 3032–3037, Apr. 1980.

[286] A. A. ELBARY, J. J. VALLNER, and C. W. WHITWORTH, "Effect of Albumin Conformation on the Binding of Phenylbutazone and Oxyphenbutazone to Human-Serum Albumin," *Journal of Pharmaceutical Sciences*, vol. 71, no. 2, pp. 241–244, 1982.

[287] B. Ahmad, S. Parveen, and R. H. Khan, "Effect of Albumin Conformation on the Binding of Ciprofloxacin to Human Serum Albumin: A Novel Approach

Directly Assigning Binding Site," *Biomacromolecules*, vol. 7, pp. 1350–1356, Apr. 2006.